Crystallographic Investigations of Respiratory Proteins

Thesis by Tina Michelle Iverson

In Partial Fulfillment of the Requirements
for the Degree of Doctor of Philosophy

California Institute of Technology
Pasadena, California
2000
(Submitted May 5, 2000)

© 2000
Tina Michelle Iverson
All Rights Reserved

Acknowledgements

I'd like to thank:

Doug for financial and intellectual support

Glenn for emotional support

Amy, Eric, Grandma and Grandpa

And all the lab members, collaborators, and others I've met along the way that have made this a truly fun experience.

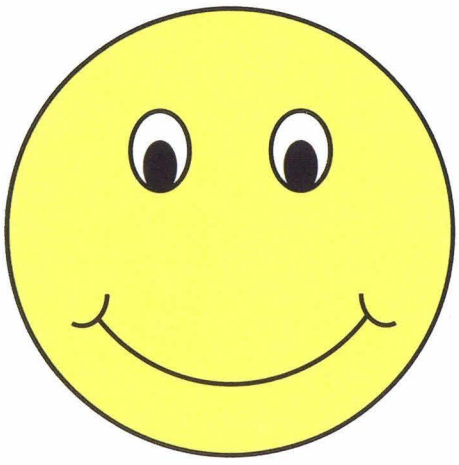

Abstract

All organisms require a respiratory process to produce energy. In eukaryotes, this process occurs in the mitochondria, and requires a respiratory chain of four integral membrane proteins as well as a membrane-soluble quinone pool and cytochrome *c*. The respiratory proteins transfer electrons to oxygen as the terminal electron acceptor with the electron transfer coupled to the translocation of protons across the mitochondrial membrane. Not all organisms use oxygen as the terminal electron acceptor of their electron transport chain. One of the more common alternative electron acceptors is fumarate, but other common electron acceptors include nitrogen-containing compounds, the transformation of which represents an important step in the biological nitrogen cycle. This thesis discusses the structural investigations of proteins involved in diverse respiratory processes. The crystal structure of the *Escherichia coli* fumarate reductase, an integral-membrane enzyme complex involved in anaerobic respiration with fumarate as the terminal electron acceptor, has been solved. This structure both suggests the mechanism of the terminal step of anaerobic fumarate respiration and gives a model for the function of the homologous protein succinate dehydrogenase from mitochondrial respiration. The crystal structure of cytochrome c554 from the chemoautotrophic nitrifer *Nitrosomonas europaea* shows a heme-packing motif that may be important in respiratory pathways that require the simultaneous transfer of multiple electrons.

Table of Contents

List of Figures

Chapter 1:

Chapter 2:

Chapter 3:

Chapter 4:

Chapter 5:

Chapter 6:

Chapter 7:

Chapter 8:

Appendix A-1:

Appendix A-2:

Appendix A-3:

Appendix A-4:

List of Tables

Appendix 2:

Appendix 3:

Appendix 4:

Chapter 1: Mitochondrial Aerobic Respiration and Bacterial Anaerobic Respiration with Fumarate as the Terminal Electron Acceptor

Mitochondrial Aerobic Respiration

Almost four billion years ago, some unicellular organisms developed the ability to harvest light energy from the sun *(1)*. As water is exceedingly stable and therefore plentiful, the primitive photosynthetic organisms evolved mechanisms to oxidize water to gaseous O_2. The evolutionary consequences of oxygen-evolving photosynthesis were tremendous, as a reducing atmosphere became oxidizing, and strategies for dealing with a new, reactive environment had to be developed *(2)*. Unlike water, oxygen is capable of participating in catastrophic reactions that can lead to disruption of cellular processes and cell death. On the other hand, the appearance of a significant amount of O_2 in the atmosphere must have exerted a very strong evolutionary pressure favoring organisms able to utilize O_2 as an oxidant of foodstuffs, as much more energy can be released with O_2 than with less effective oxidants.

Dioxygen has been harnessed effectively as the terminal oxidant in aerobic respiration. One of the cornerstones of biology involves understanding oxidative phosphorylation, the process that couples generation of adenine triphosphate (ATP) to oxygen reduction through a transmembrane proton gradient. In mammalian aerobic respiration, this process occurs at the inner membrane of the mitochondria and involves four transmembrane respiratory complexes (complexes I - IV), the soluble protein

cytochrome *c* and membrane soluble ubiquinone molecules, as well as the ATP synthase (complex V; Fig. 1.1). The electron transfer steps catalyzed by complexes I-IV each harvest energy by coupling the electron transfer to cofactors of increasingly higher reduction potential to the formation of a proton gradient across the membrane. The electron transfer requires a variety of redox-active cofactors associated with each complex. As endergonic tunneling of electrons occurs at physiologically relevant rates when the cofactor separation is < ~14 Å, each of these large respiratory complexes requires multiple redox-active centers for efficient transfer of the electron from the cytoplasm to the membrane.

All of the respiratory complexes are large, transmembrane molecules. One theme evident in the organization of these complexes is that they are often modular structures arising from the conjunction of different proteins during evolution. This modular complex formation may be an evolutionarily efficient mechanism for an organism to respond to the various chemicals that can be used as electron donors and acceptors in respiration. Ferredoxin folds are commonly seen in proteins joining a catalytic domain and a transmembrane domain. Additionally, the catalytic domain often exhibits folds seen in other proteins.

Complex I

Complex I (NADH-ubiquinone oxidoreductase; NUO) represents the largest, most complicated, and least understood of all the respiratory enzymes *(3-5)*. The oxidation of NADH by this enzyme couples the transfer of two electrons to the ubiquinone pool to the vectorial translocation of $4H^+$ *(6-9)* across the mitochondrial membrane. Bovine mitochondrial complex I is composed of at least 43 different

subunits, *(10-13)* seven of which are mitochondrially encoded *(14)*, while bacterial homologues of complex I contain 13 to 14 subunits *(15-18)* that form the functional core of the enzyme. Electron microscopy of complex I from *Escherichia coli* and *Neurospora crassa* shows that complex I forms an L-shaped overall structure *(19, 20)* (Fig. 1.2). This structure can be divided into two major parts: the membrane arm that extends 180 Å within the membrane and the peripheral arm that protrudes 80 Å from the mitochondrial membrane. The peripheral arm can be biochemically divided into two subcomplexes: the flavoprotein (Fp) and the iron protein (Ip) *(21)*. The flavoprotein is composed of three subunits of molecular weight 51 kD, 24 kD and 10 kD and contains noncovalently-associated flavin mononucleotide (FMN) as well as several [Fe:S] clusters. The Ip subcomplex contains six subunits of molecular weights 75 kD, 49 kD, 30 kD, 18 kD, 15 kD, and 13 kD as well as nonheme iron and acid-labile sulfur, suggesting the presence of iron-sulfur clusters. The sequence similarity between the Fp of complex I and the NAD-reducing hydrogenase from *Alcalugenes eutrophus (22)*, the sequence similarity between the Ip and ferredoxins, and the ability to resolve complex I into several independently folding subcomplexes *(21)*, suggest complex I has a modular structure resulting from its evolutionary origins. Respiratory complex II, hydrogenase and formate dehydrogenase, described below, similarly appear to have evolved from smaller subcomponents; thus, modular complex formation represents a theme in the evolution of many respiratory enzymes.

Associated with the peripheral arm of complex I is at least one flavin mononucleotide (FMN) *(23)* that likely forms the active site for NADH oxidation. Until the recent discovery of spectroscopic signals arising from two [4Fe:4S] clusters associated with a truncated form of the complex I homologue from *Paracoccus denitrificians (24)*, electron paramagnetic resonance (EPR) had shown the presence of

only six distinct [Fe:S] clusters associated with complex I *(25-28)* despite the presence of eight consensus [Fe:S] cluster sequences *(11, 15-17)*. All the [Fe:S] clusters are believed to be associated with the peripheral arm of the complex or lie at the interface between the peripheral arm and the membrane arm. Standard nomenclature defined by Ohnishi *(29)* labels the six well-studied [Fe:S] clusters N1a, N1b, N2, N3, N4 and N5 in order of increasing spin relaxation rates; the two recently discovered [4Fe:4S] clusters have not yet been assigned specific nomenclature. Of the [Fe:S] clusters that have been identified, two (N1a, N1b) have EPR spectra characteristic of [2Fe:2S] clusters, three (N3, N4, N5) exhibit classic [4Fe:4S] spectra, and one (N2) is believed to be a [4Fe:4S] with pH dependent EPR spectra.

Associated with the membrane arm of complex I are at least two ubiquinone-binding sites that have been identified by the presence of two distinct semiquinone signals in the EPR spectra *(30, 31)* that are quenched by different quinone-binding inhibitors *(32-34)*. The presence of additional quinone binding sites in complex I is debated *(35)*. A model for the functional core of complex I, including the putative cofactor locations, is shown in Fig. 1.3.

Theories of proton translocation by complex I cannot fully explain the experimentally observed proton to electron stoichiometry of $4H^+/2e^-$ *(21, 33, 36)*. However, proton pumping may include a combination of vectorial translocation involving the N2 [4Fe:4S] cluster and a modification of the quinone-cycling (Q-cycling) mechanism *(37)* described in detail below for complex III, as well as an additional undetermined mechanism. Cluster N2 has been proposed to play an important role for energy conservation in complex I *(29, 37)* since it exhibits several unique properties. First, it has the highest E_m value of all the clusters that have been observed so far in

complex I *(25, 38)* suggesting it is the last [Fe:S] cluster to be reduced before the electrons are passed to the quinones. Second, its one electron reduction or oxidation is coupled with the binding and release of one proton in the physiological pH range (Fig. 1.4) *(3, 25, 38-40)*. Third, the location of the cluster N2 is likely near the interface between the peripheral arm *(24)* and the membrane arm. Both EPR interactions showing a distance of < 11 Å from one of the semiquinone species *(31, 41)* and the observation that delipidation of purified complex I affects the reduction potential of cluster N2 *(42)* suggest this interface position. A location at the membrane interface allows cluster N2 to be optimally positioned for involvement in proton translocation.

Complex II

Complex II (succinate-quinone oxidoreductase; SQR) oxidizes succinate to fumarate at a flavin adenine dinucleotide (FAD) and transports the electrons generated from this process into the ubiquinone pool *(43, 44)*. By catalyzing oxidation of succinate and participating in electron transfer, complex II acts as important member of both the Krebs cycle and the mitochondrial aerobic respiratory chain (Figures 1.1; 1.2 *(45)*). Complex II is organized into four polypeptide chains *(43)*: the flavoprotein (Mr ~60 kD) contains the covalently-linked active site FAD; the iron protein (Mr ~25kD) covalently links one [2Fe:2S] *(46)*, one [3Fe:4S] *(47)*, and one [4Fe:4S] center *(48)*; and the membrane anchors (Mr ~13 kD and ~11 kD) bind one *b*-type heme and are associated with ubiquinone molecules.

Like complex I, sequence and biochemical analyses of complex II suggest the structure has evolved as a conjunction of modules *(49)*. Indeed, complex II can be

biochemically resolved into a membrane-spanning domain and a soluble domain; the soluble domain containing the flavoprotein and the iron protein retains catalytic activity in succinate oxidation under appropriate conditions *(50)*. The flavoprotein exhibits significant sequence similarity to soluble flavocytochrome c3 fumarate reductases *(51-53)*, L-aspartate oxidase *(54-60)*, a protein involved in the biosynthesis of NADH, 3-ketosteroid-delta-1-dehydrogenase *(61-63)* a protein involved in the first step of steroid catabolism, and an osmotic regulatory protein from yeast *(64, 65)*. Similarly, the N-terminus of the iron protein has sequence similar to [2Fe:2S] plant-type ferredoxins, while the C-terminus contains [Fe:S] binding cysteine motifs identical to those seen in bacterial ferredoxins *(43)*.

All of the flavin and iron-sulfur cluster prosthetic groups of complex II are located in the soluble domain of the complex. The reduction potentials of each prosthetic group are tuned to catalyze the oxidation of succinate and to facilitate the transfer of electrons into the ubiquinone molecules associated with the membrane anchors (Table 1.1). However, under appropriate conditions the enzyme can also act in the reduction of fumarate *(66, 67)*. Because of the redox couple between succinate and fumarate (+25 mV), electron transfer to a non-covalently attached FAD (<-200 mV) would be extremely unfavorable. Site-directed mutagenesis altering the histidine that forms the covalent linkage to the FAD results in an enzyme that cannot catalyze the oxidation of succinate *(68)*, but can function in the reduction of fumarate *(69)*, which is opposite of the physiological direction of the reaction in mitochondria. The 8α-FAD covalent attachment to the Nε of a histidine *(70)* raises the reduction potential to -79 mV. Transfer of an electron from succinate to the FAD still appears somewhat unfavorable; however this energy barrier can be overcome during reaction turnover. By analogy, chemical

reactions can overcome the barrier of high energy intermediates during the formation of lower energy products.

Based on a sequence identity of ~40% between the soluble domain of complex II and the soluble domain of bacterial anaerobic homologues of complex II, the fold of the soluble domain should be nearly identical between the two complexes. Recent crystallographic analysis of the anaerobic homologue of complex II *(71, 72)* has confirmed the modular nature of the enzyme and the similar fold of the flavoprotein and soluble homologues *(73-76)* as well as the iron protein and bacterial ferredoxins. In contrast, the membrane transmembrane anchors between complex II and bacterial homologues have virtually no sequence similarity. However, both complexes are believed to associate with quinone molecules in a similar fashion *(77)*. Complex II is predicted to be associated with at least two quinone molecules situated on opposite sides of the membrane *(78-81)* in a fashion reminiscent of that utilized for the Q-cycle mechanism of complex III *(82-84)*. Recent crystallographic studies of the anaerobic complex II homologue from *E. coli (71)* confirm the transmembrane positions of two quinone molecules. Despite this suggestive arrangement of quinones, it has long been held that complex II is not energy coupled. Calculations suggest that the energetics of proton translocation by complex II would be unfavorable during aerobic respiration *(85)*.

Complex III

Complex III (cytochrome bc_1; ubiquinol:cytochrome *c* oxidoreductase) accepts electrons from the reduced ubiquinol pool and transfers them to the soluble cytochrome *c* with the concomitant generation of a proton gradient across the mitochondrial membrane. Complex III is composed of a functional core containing cytochrome *b*, cytochrome c_1,

and the Rieske [2Fe:2S] iron-sulfur protein. Essential for the function of the complex are the cofactors associated with these subunits: two *b*-type hemes (b_L and b_H); one *c*-type heme; the Rieske [2Fe:2S] center; and the binding sites for two ubiquinone molecules *(86, 87)*. Mitochondrial complex III contains additional subunits not present in bacterial complexes that may be involved in mitochrondrial targeting and processing *(88-90)*. Based on the organization of cofactors seen in the crystal structure as well as the buried surface area between monomers *(82-84)*, complex III functions as a physiological dimer (Fig. 1.2).

The protonmotive quinone cycle (Q-cycle) originally proposed by Peter Mitchell *(91)* best explains the experimental results on electron transfer through the redox centers of complex III. The Q-cycle requires two separate quinone binding sites (Q_o and Q_i) positioned on opposite sides of the membrane with a bifurcated electron flow from the Q_o quinone bound near the intermembrane space (positive side of the membrane; Fig. 1.5). The unique bifurcated oxidation of ubiquinol at Q_o of complex III is the reaction within the Q-cycle reaction scheme that is most critical for the link between electron transfer and vectorial proton translocation *(92)*. Bifurcated electron flow occurs during hydroquinone oxidation at the Q_o site *(93)*, with one electron transferred through a high-potential chain involving the Rieske [2Fe:2S] cluster and heme c_1 to cytochrome *c*, while the second electron is transferred by the two *b*-type hemes across the membrane to reduce the quinone bound to the Q_i site *(94-98)*. Oxidation of reduced quinone (hydroquinone; QH_2) to ubiquinol (Q) requires the release of the two protons that are transferred to the intermembrane space. Likewise, the reduction of quinone in the Q_i site occurs with the uptake of two protons from the matrix. The resultant H^+/e^- stoichiometry of the Q-cycle is $2H^+$ translocated for each electron that reduces cytochrome *c*.

While there is a general consensus about the overall reaction at Q_o, the nature of the intermediates and the way the reaction is controlled to ensure obligatory bifurcation is still controversial *(99)*. Crystallographic studies of complex III *(83, 84, 100)* suggest that the bifurcated pathway of electron transfer is associated with physical movement of the Rieske iron-sulfur protein *(101, 102)*. A hinge rotation around two β-strands combined with the isomerization of Pro 175 *(84)* can shift the location of the Rieske [2Fe:2S] cluster over 15 Å *(83, 84)*. In one stabilized position, the cluster lies in close contact to the Q_o site, in a second position, the cluster is proximal to heme c_1, and in a third position the Rieske iron-sulfur protein is found at an intermediate location (Fig. 1.6).

In addition to the movement by the Rieske iron-sulfur protein, the binding sites stabilizing the quinones are critical for function of complex III. The Q_i site must preferentially bind fully oxidized quinone and stabilize a ubisemiquinone species after the transfer of one electron from the Q_o site. After reduction by the second electron and the uptake of two protons, binding to the hydroquinone species must weaken such that it is released back into the Q-pool.

Several mechanisms have been suggested to explain the bifurcated electron flow from the Q_o site *(103-106)*. The proposal by Brandt and von Jagow *(104, 105)* of a "catalytic switch" mechanism perhaps agrees best with the recent crystallographic data. Crystallographic studies of complex III have not yet shown the presence of a quinone in the Q_o site, but its location has been mapped by inhibitors. The inhibitor binding sites show a bi-lobed pocket for quinone binding *(107, 108)*, and the position of the Rieske iron-sulfur protein is dependent upon the lobe in which the inhibitor binds *(107)*. This would suggest that hydroquinone would bind at Q_o triggering the conformation of the Rieske iron-sulfur protein to shift to a location proximal to the quinone *(97)*. Before QH_2

can be oxidized by the Reiske iron-sulfur cluster, it must first be deprotonated to QH^-, which represents the activation barrier of hydroquinone oxidation *(109)*. This is believed to occur through the conserved His 161 and Glu 272 residues that make hydrogen-bonding contacts to polar groups of inhibitor molecules *(100, 110)*. Upon oxidation, the newly formed ubisemiquinone shifts into a second site *(97)*, concomitantly pushing the Rieske protein away to interact with cytochrome c_1 (Fig. 1.7). QH^- is deprotonated to a ubisemiquinone species (SQ•) before electron transfer fully oxidizes the quinone by the low potential pathway. The time scale of the movement of the Rieske iron sulfur protein may be slow enough to prevent both of the electrons from being transferred from the Q_o site by the high-potential pathway, but is not thought to be a rate-limiting step in the Q-cycle *(111)*. Rather, the reaction rate is limited by the ubihydroquinone deprotonation *(109)* or the stability of the semiquinone intermediate *(97)*.

Complex IV

Complex IV (cytochrome *c* oxidase; CcO) catalyzes the final step in the electron transport chain *(112-115)* by accepting electrons from the soluble cytochrome *c* and using them to reduce molecular dioxygen to water, with the concomitant vectorial translocation of four protons *(116-119)*, such that the overall reaction is:

$$O_2 + 8H^+_{in} + 4e^- \rightarrow 2H_2O + 4H^+_{out}$$

where H^+_{in} and H^+_{out} indicate protons that are taken up and released vectorially with respect to the respiratory membrane. Complex IV, an aa_3-type cytochrome *c* oxidase, resides in a superfamily of terminal oxidases *(120, 121)* including the cytochrome bo_3

complexes and the aa_3-type cytochrome *c* oxidases, that require similar cofactors for reaction turnover. Complex IV from all organisms is comprised of at least two integral-membrane subunits *(122, 123)* that contain a di-nuclear copper center (Cu_A) and a low-spin six-coordinate *a*-type heme (heme *a*) that mediate electron input to a heme-copper dioxygen activating and reduction center (heme a_3 - Cu_B). Crystal structures of bacterial *(124, 125)* and mitochondrial *(126-128)* complex IV (Fig. 1.2) have shown that the Cu_A is located in core subunit II while the rest of the cofactors known to be essential for catalytic activity are located in core subunit I *(129)*. This functional core appears capable of independently catalyzing the reduction of molecular oxygen in bacterial systems. The peripheral subunits of mitochondrial complex IV form binding sites for zinc, sodium, and magnesium *(126-128, 130)* and may be necessary for assembly of the complex *(131)* or for allosteric regulation of activity by ATP *(127, 132, 133)*. Site directed mutagenesis of the side chains that bind the peripheral metals *(134, 135)* suggest they are necessary for catalysis in the mitochondria *(136)*, but it is possible that these metals merely serve a structural role.

Electrons enter complex IV from reduced cytochrome *c*, which binds above Cu_A and heme *a (137-139)*, and proceed to the active site. The active site of complex IV, often called the binuclear center, is composed of heme a_3-Cu_B. Heme a_3 is a five-coordinate heme with the open ligation site suggested to be the dioxygen binding site. Cu_B lies 4.9 Å away from the heme iron in the unliganded form of the enzyme and 5.3 Å away if the enzyme is bound to molecular dioxygen, cyanide, or azide. The change in distance is associated with movement of the Cu_B center *(128)*, while the heme position remains fixed, regardless of the oxidation state of the enzyme. Cu_B forms a bond to the substrate or substrate analog bound to the heme iron *(124, 128)*, changing the coordination from trigonal planar to square planar. Near the active site, a catalytically

essential tyrosine *(140)* (Tyr 244 using bovine numbering) appears to make a covalent bond to one of the histidine ligands (His 240) to the Cu_B center (Fig. 1.8) in both the bacterial *(125)* and mitochondrial complexes *(128)*. This covalent bond may raise the pK_a of the tyrosine hydroxyl to a value that would function in proton shuttling to the oxygen species bound at the active site.

The catalytic cycle of complex IV appears to have multiple intermediates (Fig. 1.9). In the first step, the oxidized enzyme accepts two electrons and pumps two protons. The second step binds molecular oxygen to the active site at the binuclear center. One oxygen atom forms a double bond to the iron of heme a_3 in what is historically known as the peroxy (P) intermediate. The other oxygen atom associates with Cu_B. During the peroxy intermediate, Tyr 244 donates a proton to Cu_B forming a tyrosyl radical (•O-Tyr) and a Cu_B bound to -OH. It is thought that the spectral signals arising from the tyrosyl radical have mistakenly caused the interpretation of this state being a peroxy radical. Coupled to the uptake of one electron and the pumping of one proton, the next step in the catalytic cycle, called ferry (F) reprotonates Tyr 244, such that both Cu_B and Tyr 244 are both protonated, and the iron is in a ferroxy state. With the pumping of a final proton and reduction by a fourth electron, the oxidative (O) state is formed. In this state, all of the catalytically active species are bound to hydroxide. The correlation of proton translocation to the catalytic cycle is highly controversial. Recent electrometric measurements suggest that protons may be pumped in other phases of the catalytic cycle *(141)*.

No channel providing access for the substrate molecular oxygen has been observed in the crystal structure, as is the case for hemoglobin and myoglobin *(142)*. In analogy to these globins, the conformation for an open O_2 channel may be attained

through transient conformational changes. A candidate that could serve as a water channel for the removal of the product may lie between subunit I and II *(127)*. Residues lining this channel have been shown by site-directed mutagenesis to be necessary for enzyme function and are highly conserved.

Complex IV is not associated with quinones, excluding a Q-cycling mechanism for proton pumping. Thus channels for proton uptake and translocation are essential for enzyme function. It is proposed that two separate proton channels are present *(143, 144)*. One pathway delivers protons from the negative side of the membrane to the active site to combine with the reduced oxygen substrate. A second pathway is utilized for vectorial proton translocation and requires a full pathway through the complex. Based on the structure of complex IV (Fig. 1.2) three compelling candidates for the proton channels have been proposed *(127)*. Two of these candidates, dubbed the H-channel and D-channel for the conserved external residues lining the channel (His and Asp respectively) have been suggested as candidates for vectorial proton translocation. Site-directed mutagenesis shows the D-channel is absolutely required for activity *(145)*, making it a stronger candidate for proton translocation. The third channel, dubbed the K-channel for the lysine residue positioned at its exterior, likely delivers protons into the bi-nuclear active site. Despite the seemingly few possible proton transfer routes, no consensus on the mechanism of proton translocation through complex IV has been reached, and currently, different models are intensely debated *(123, 141, 145-149)*.

Complex V

Complex V (F_oF_1 ATP synthase) catalyzes the formation of ATP from the precursor components adenine diphosphate (ADP) and inorganic phosphate (Pi) *(150)*.

The complex is formed from a soluble domain (F_1) and a membrane-spanning domain (F_o; Fig. 1.2). The functional core of F_o portion consists of three types of subunits in bacteria: a, b, and c. It is believed that one a-subunit, two b-subunits, and ten c-subunits are present *(151)*. In contrast, the more complex mitochondrial F_o has additional subunits. The F_1 part of the ATP synthase consists of five types of subunits: α, β, γ, δ, and ε. While there are three each of α and β, there is only one of each of the others. Despite the sequence similarity between the α and β subunits, ATP synthesis only occurs in the β subunits. The most detailed studies of ATP synthesis have highlighted the F_1 part of the complex *(152, 153)*. It is now widely accepted that the asymmetric γ, δ, and ε subunits rotate in a cylinder formed of alternating α and β subunits *(152)* (Fig. 1.10). This rotational catalysis has been recently confirmed by visualization of the F_1 subunit rotating an actin filament *(154-156)*.

The transmembrane proton gradient achieved by the oxidation-reduction reactions catalyzed by complexes I-IV in the electron transport chain drives the rotation of the F_1 subunit *(91)*. The membrane-spanning F_o subunit forms a proton channel between the a-subunit and the ring of ten c-subunits. Each c-subunit is composed of two membrane-spanning helices *(157)*. Protons are delivered to a conserved carboxylate side chain (Asp 61 in *E. coli* and Glu 59 in *S. cerevisiae*) by subunit a, resulting in a neutral state of the side chain that is stable in the center of the membrane. The uptake of each proton and concomitant release of a proton on the other side of the membrane adds torque to the central γ-subunit (Fig. 1.11). After three to four protons have been passed back along their gradient, enough torque has built up on the γ-subunit to force its rotation within the α and β subunits, causing a change in conformation in this α/β subunit cylinder *(158)*. This conformational change sterically forces ADP and Pi together in the binding pocket of the β subunit to form ATP (Fig. 1.12) in what is referred to as the binding change

mechanism *(159)*. This binding change mechanism facilitates release of the tightly bound ATP after formation.

Bacterial Anaerobic Respiration with Fumarate as the Terminal Electron Acceptor

Not all organisms require oxygen to produce ATP *(160)*. In facultative anaerobes, like *E. coli*, the switch from aerobic respiration to anaerobic respiration requires the expression of a variety of proteins dedicated to anaerobic respiration and the repression of proteins involved in aerobic respiration. In the 1970s, the characterization of mutants that failed to carry out anaerobic respiration by fumarate and nitrate reduction were designated FNR mutants *(161)*. Since then, it has been determined that FNR is a single protein that is a global regulator responsible for controlling the anaerobic-aerobic regulation of over 120 target genes in *E. coli (162)*. Under anaerobic conditions, FNR exists as a homodimeric transcription factor with each monomer containing a [4Fe:4S] cluster *(163, 164)* (Fig. 1.13). A growth shift from anaerobic to aerobic conditions causes the [4Fe:4S] clusters to disassemble rapidly to form two [2Fe:2S] clusters *(165, 166)*. The loss of the [4Fe:4S] clusters converts FNR from a homodimer with high DNA-binding affinity to a monomer with low DNA-binding affinity.

One important switch that occurs during the transition from aerobic to anaerobic respiration involves the identity of the quinone acting as the membrane-soluble electron carrier between respiratory complexes. Aerobic respiration usually utilizes ubiquinone, while menaquinone molecules mediate most anaerobic respiration (Fig. 1.14). This switch results in the use of quinone molecules that exhibit midpoint potentials less than that of the terminal electron acceptor, facilitating the directional electron transfer.

Ubiquinone has a resting potential of +70 mV, while menaquinone has a potential of -74 mV. Although the potentials may be modulated when bound to the protein complexes, the resting potential generally indicate the direction the reaction will proceed *in vivo*.

Many different primary electron donors and terminal electron acceptors can be used in the absence of oxygen *(167)*(Table 1.2). One of the more common terminal electron acceptors in anaerobic respiration is fumarate *(43, 44)*, which is reduced to succinate by the quinol-fumarate reductase (QFR) complex located in the periplasmic membrane. The electrons required for fumarate reduction are supplied by a reduced menaquinol pool. A membrane-bound hydrogenase and formate dehydrogenase *(168-170)* can supply all of the reducing equivalents necessary in both *W. succinogenes* and *E. coli* and represents one of the simplest systems for anaerobic respiration (Fig. 1.15). During this type of anaerobic respiration, the transmembrane proton gradient used to drive ATP synthesis is generated by selective catalysis of reactions on opposite sides of the membrane, where formate dehydrogenase and hydrogenase release protons on one side of the membrane *(171)*, while QFR utilizes protons on the other.

Hydrogenase

The capacity to oxidize molecular hydrogen is a central metabolic feature of a wide variety of microorganisms *(172-177)*. Hydrogenases can be classified into four types according to metal composition *(178)*: the iron-only, or Fe-hydrogenases; Ni-Fe hydrogenases; Ni-Fe-Se hydrogenases; and one enzyme that does not contain any bound transition metals. The membrane-bound Ni-Fe hydrogenases act in anaerobic respiration when fumarate is the terminal electron acceptor and contain three redox active iron-sulfur clusters, two [4Fe:4S] clusters and one [3Fe:4S] cluster, as well the Ni-Fe binuclear

center at the active site (Fig. 1.16). A high-resolution crystal structure of the purified soluble domain of the Ni-Fe hydrogenase from *Desulfovibrio gigas (179)* shows the Ni-Fe binuclear center as ligated to the protein by four cysteine ligands, two to the nickel, and two that bridge the nickel and iron; three diatomic ligands stabilize the iron. Additionally, the binuclear center is bridged by an unassigned mononuclear ligand *(180)*, the position of which is believed to be the binding site for hydrogen during reaction turnover.

The periplasmically-located soluble domain of the Ni-Fe hydrogenase contains two subunits of molecular weights 63 kD and 29 kD, with the active site Ni-Fe center covalently bound to the large subunit. The small subunit of the Ni-Fe hydrogenase contains the ligands to the [Fe:S] clusters that form a linear chain for electron transfer *(180)*. Hydrophobic analysis and sequence similarity to the hydrophobic membrane anchors of complex I suggest six different proteins are capable of forming the membrane-anchors in *E. coli (170)*. Since *E. coli* contains genes for three isozymes of hydrogenase, it is thought that each isozyme is exclusively associated with two membrane anchors. However, the properties exhibited by the membrane anchors have not been well characterized.

Formate dehydrogenase

Formate dehydrogenase oxidizes formate to carbon dioxide at a molybdopterin guanine dinucleotide (MGD) cofactor *(181, 182)*. The fold of the 79 kD soluble subunit contains four domains *(183)* (Fig. 1.16) and exhibits high structural similarity to DMSO reductase *(184, 185)*, which also contains an MGD cofactor and can act as a terminal electron acceptor during anaerobic respiration in the presence of DMSO *(186)*.

Interestingly, a nonsense (UGA) codon is present at a position corresponding to amino acid 140 of the polypeptide *(187)*. This codon is required for cotranslational incorporation of selenocysteine into formate dehydrogenase *(188)*. The crystal structure of the soluble domain *(183)* showed that this selenocysteine acts as a ligand to the molybdenum in the MGD cofactor. The gene cluster for formate dehydrogenase additionally contains two peripheral proteins that are believed to be responsible for membrane association. These two genes encode an [Fe:S] protein and a cytochrome *b* like polypeptide.

Quinol-fumarate reductase

During anaerobic respiration with fumarate as the terminal electron acceptor, the quinol-fumarate reductase (QFR) complex is expressed and catalyzes the reduction of fumarate to succinate, which is opposite of the reaction catalyzed by complex II during aerobic respiration. QFR and complex II exhibit significant sequence similarity, thus the structure of either complex provides information about both aerobic and anaerobic respiration. The structure of the *Escherichia coli* QFR respiratory complex has been solved at 3.3 Å resolution *(69)* using the method of mulitwavelength anomalous dispersion. Analysis of this structure has revealed insights into the formation of the complex, catalysis, and the potential role this enzyme might play in energy coupling. Structural aspects of this complex as well as mechanistic implications for both aerobic and anaerobic respiration will be discussed in detail in the next three chapters.

Fig. 1.1: Mitochondrial electron transport chain. The electron transport chain is initiated at either complex I (NADH ubiquinone oxidoreductase; NUO) or complex II (succinate-quinone oxidoreductase; SQR), which reduce the ubiquinone pool. Electron transport by complex I is coupled to proton translocation across the mitochondrial membrane. Reduced ubiquinol then binds to complex III (cytochrome bc_1), which uses a Q-cycling mechanism to translocate protons across the mitochondrial membrane. Electrons are transferred from complex III to complex IV (cytochrome *c* oxidase; CcO) with the soluble cytochrome *c* as the intermediate electron carrier. Complex IV catalyzes the final step in respiration by transferring electrons to molecular dioxygen, thus reducing it to water. Fig. adapted from *(83)*.

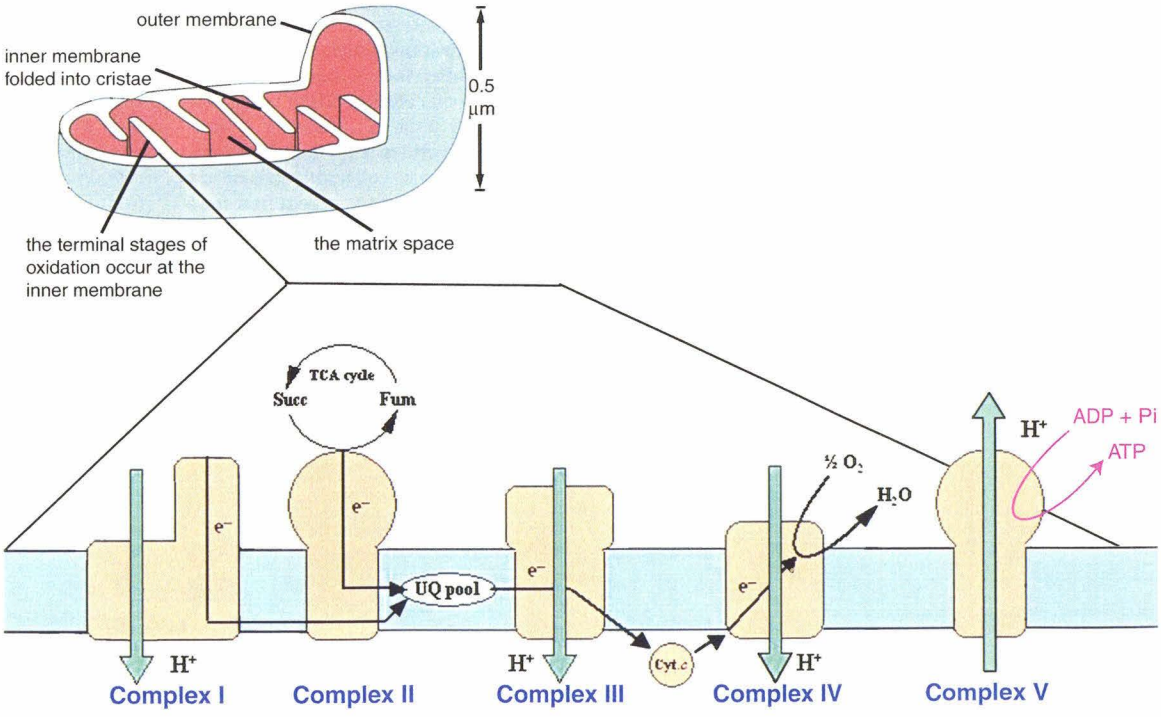

Fig. 1.2: The structural understanding the mitochondrial respiratory chain. Complexes I, III, and IV pump protons out of the mitochondrial matrix to form a transmembrane proton gradient. Following this, complex V (the ATP synthase) couples the favorable process of bringing a proton back along its gradient with the unfavorable process of ATP synthesis. Complex I has been solved to ~35 Å resolution by electron microscopy and exhibits an L-shaped structure both in mitochondria and bacteria. The remaining complexes have been solved to atomic resolution by x-ray diffraction. Only bacterial homologues of complex II have been solved (*Escherichia coli* and *Wolinella succinogenes*). Complex III has been solved from the mitochondria (bovine and chicken). Complex IV has been solved from both bacterial and mitochondrial sources (*Paracoccus denitrificians* and bovine). Complex V has been solved from yeast mitochondria and the F_1 portion has been solved from bovine. In all cases, the structures have revealed insights into the mechanism of function by the respiratory complex. The structures that have been solved from multiple sources have agreed in the overall fold, but yielded complementary insight into function.

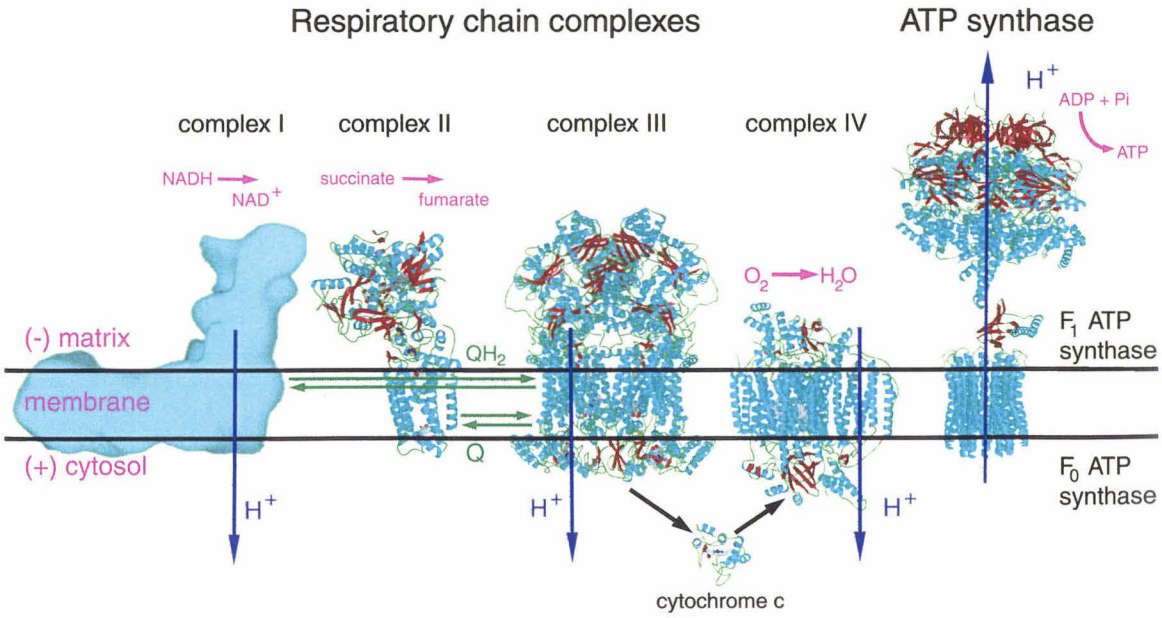

Fig. 1.3: Topological prediction and cluster location of complex I. Only the functional core of the enzyme is shown with the subunits labeled according to the nomenclature used for the *E. coli* enzyme.

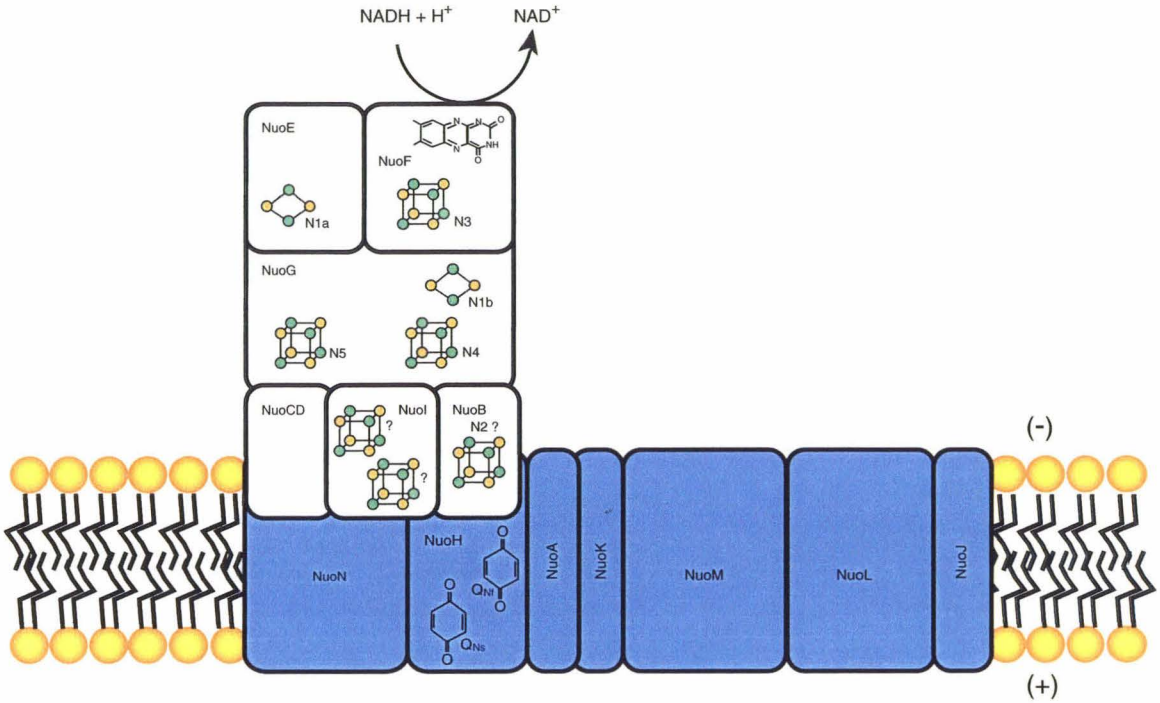

Fig. 1.4: The pH dependent midpoint of cluster N2 in complex I. It is believed that cluster N2 is protonated upon reduction and may play a role in proton translocation. The limits for the pK_A and E_m values were estimated from experimental data given in *(36)*.

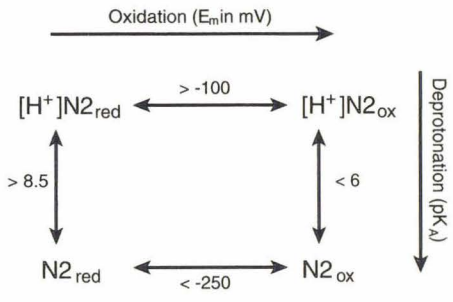

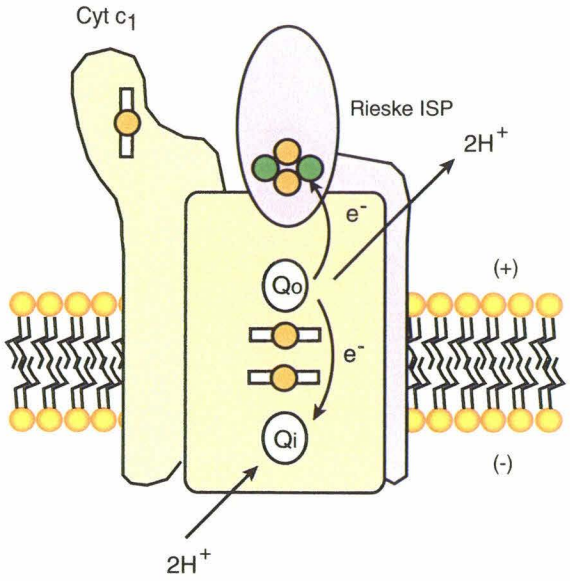

Fig. 1.5: Q-cycling by cytochrome bc_1 requires bifurcated electron flow at the Q_o binding site. As the quinone changes its oxidation state, protons must disassociate (when quinone is oxidized) or associate (when quinone is reduced) to form a stable molecule. The quinones found at the membrane interface will acquire or deposit protons into the adjacent solvent when driven by the bifurcated electron transfer shown.

Fig. 1.6: Movement of the Rieske iron-sulfur protein (ISP) is required for catalysis of partial reactions during the Q-cycle. When interacting with either ubiquinone or heme c_1, hydrogen bonds are formed between the ISP and the cofactor binding site, while the intermediate state does not make specific interactions with either the cofactors or the other proteins in the complex. Although crystal contacts have stabilized an intermediate position of the Rieske ISP, the binding switch between ubiquinone and heme c_1 may involve random exploration of three-dimensional space rather than discrete movement. The binding of the ubiquinone likely depends on whether the quinone is in the QH^- or SQ• oxidation state.

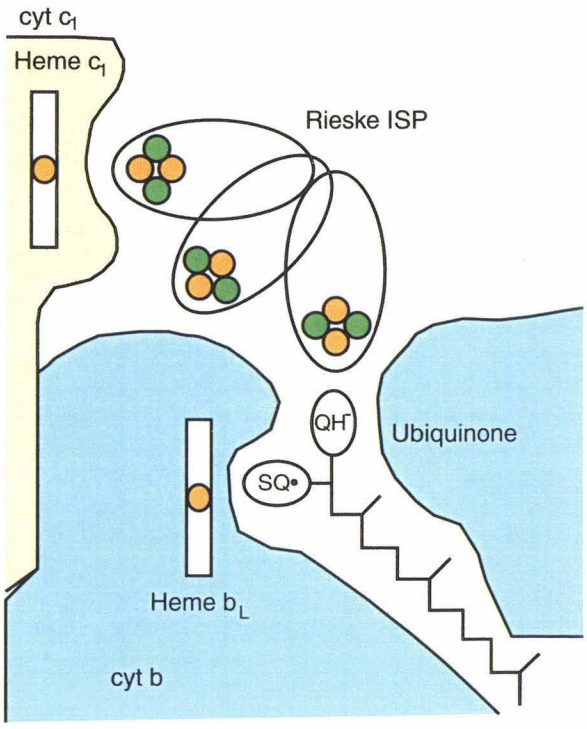

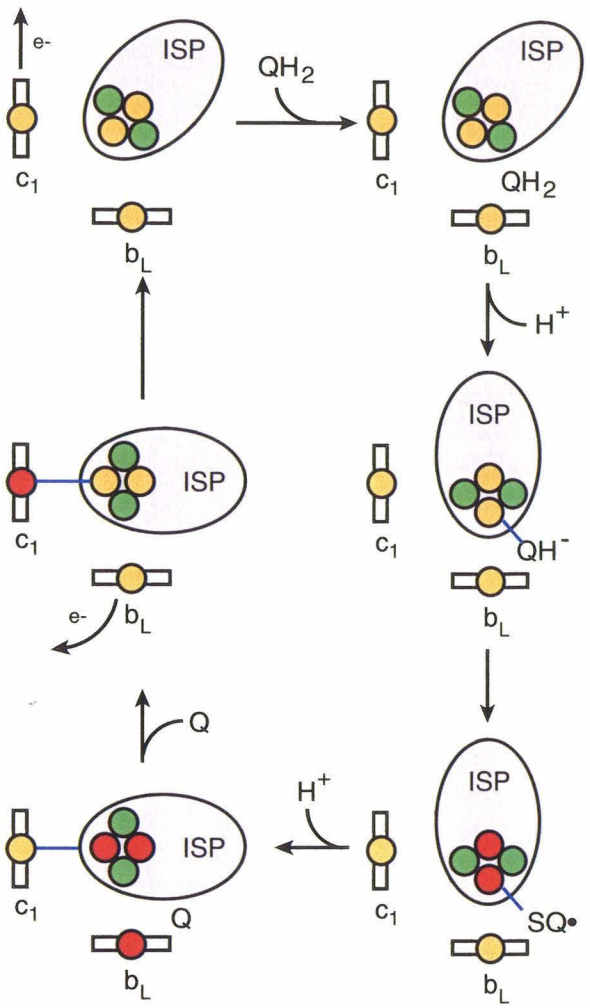

Fig. 1.7: Proposed mechanism of hydroquinone oxidation at the Q_o site of the bc_1 complex based on the multiple conformations of the Rieske ISP. Red iron cofactors are reduced while orange iron cofactors are oxidized. The ISP starts at an intermediate position with the Q_o binding site unoccupied (step 1; upper left). Hydroquinone (QH_2) binds to Q_o (step 2), followed by ionization with the proton shuttled to the intermembrane space. The resultant QH^- forms a hydrogen-bond to the shifted position of the ISP (step 3), stabilizing the protein in that conformation while an electron is transferred to the Rieske [2Fe:2S] cluster, forming an unstable semiquinone (SQ•; step 4). The ISP changes conformations and is stabilized by hydrogen bonds to the cytochrome c_1 protein subunit, while a second hydrogen is lost from the SQ• species, with the concomitant transfer of an electron to b_L (step 5). The ISP then reduces heme c_1 (step 6) as the electron is passed from b_L to b_H (not shown). As the reduced cytochrome c_1 passes the electron to cytochrome *c*, the starting state is regenerated.

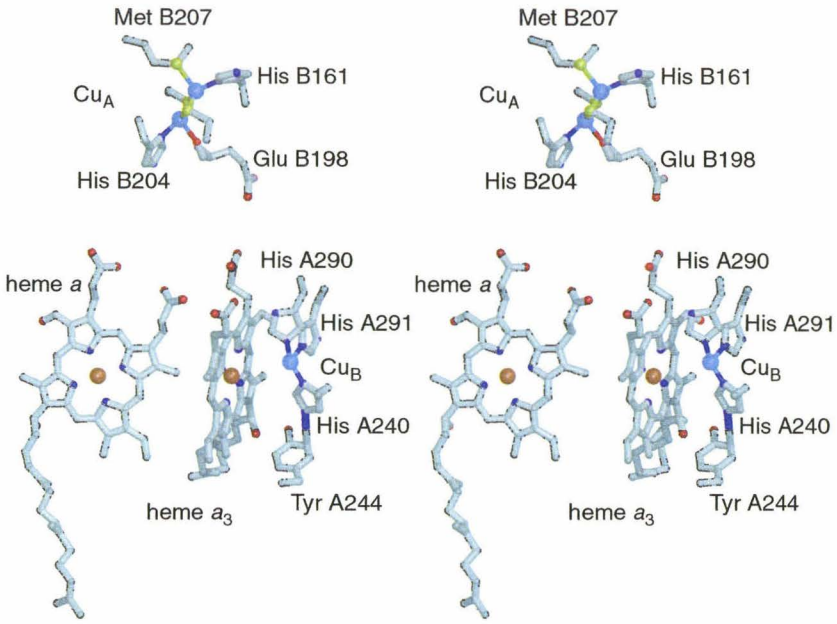

Fig. 1.8: A stereoview of the cofactors of complex IV and their ligands. Electrons enter complex IV above the Cu_A copper center. Since Cu_A is equidistant between heme *a* and heme a_3, it is unclear how the electron proceeds to the active site heme a_3-Cu_B. O_2 is believed to bind at the open site of heme a_3 in contact with Cu_B.

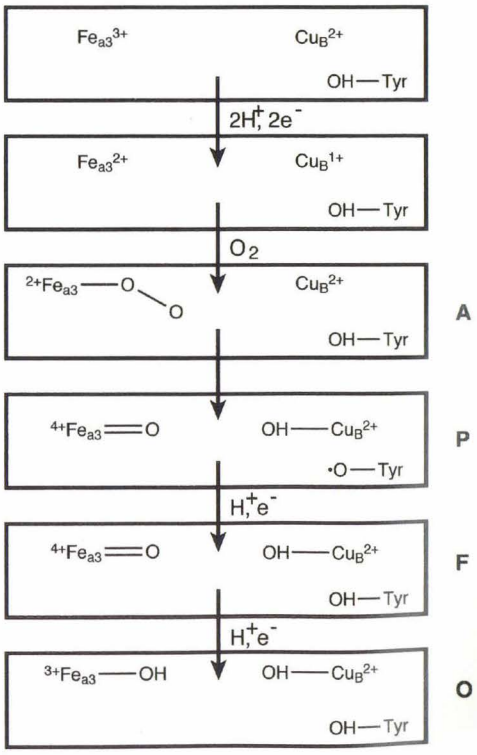

Fig. 1.9: The catalytic cycle of complex IV. Although portions are widely debated, the catalytic cycle of complex IV has several generally accepted intermediates that have been characterized. Four protons are vectorially translocated during the catalytic cycle (shown over the reaction arrows). In addition, four protons are combined with one molecule of oxygen to form water (shown in boxes).

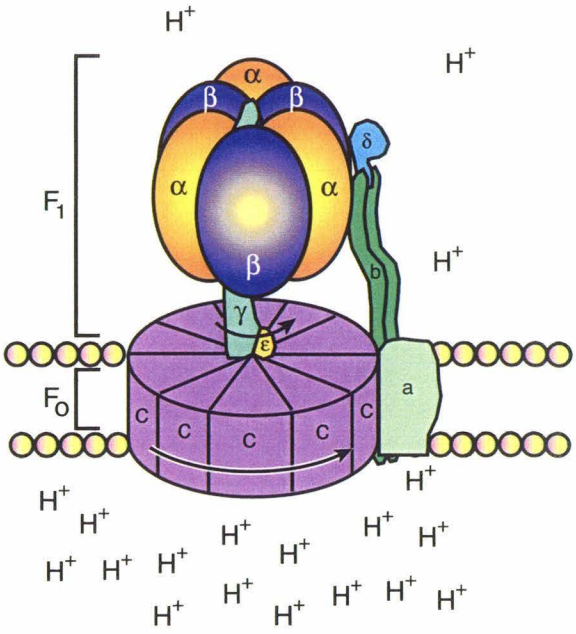

Fig. 1.10: Schematic drawing of the F_1F_o ATP synthase. The F_o portion (a subunit in light green, b subunit in green and c subunits in lavender) is located in the membrane, while the F_1 portion is located in the mitochondrial matrix. Protons that flow through the cylindrical c subunits forces a rotation of the c subunits as well as γ, while the a, b, and δ subunits stabilize the α/β heterotrimer. The rotation of the asymmetric γ subunit within the stationery α/β heterotrimer forces conformational changes within the α and β subunits. The conformational changes in the active site of the β subunit result in the formation of ATP.

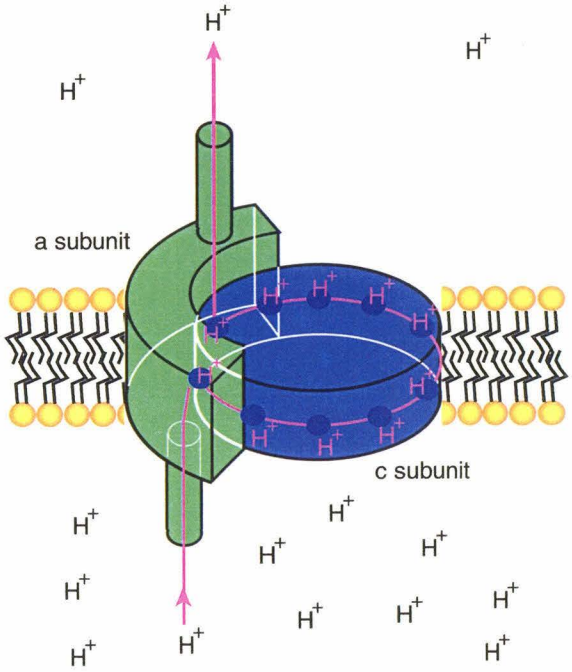

Fig. 1.11: Model for the generation of rotation by proton transport through the F_o portion of the ATPase. The central cylinder (blue) consists of ten c subunits while the external part (green) is composed of a single a subunit. The magenta arrow indicates the path of proton transfer. The flow of protons allows the c subunit to rotate with respect to the a subunit. This rotation continues through the γ subunit of the F_1 portion.

Fig. 1.12: Binding change mechanism of the ATP synthase. The F_1 ATP synthase is represented as a circle with alternating α and β subunits at four different stages of ATP synthesis. The asymmetric γ subunit causes the conformational changes in the α and β subunits, as shown in the center in yellow. The three different conformational states of the β subunit are termed open (β_o), loose (β_L), and tight (β_T). In the first step, an ATP molecule is bound to β_T, while β_o and β_L are empty. The ATP synthase then binds to ADP and Pi. After an input of energy by the F_o subunit, the F_1 part rotates 120° around the asymmetric γ subunit causing conformational changes in the β subunits such that the ADP and Pi are now bound in β_T and ATP is bound to β_o. The β_o conformation has a low affinity for ATP, which is released in the final step, regenerating the initial state.

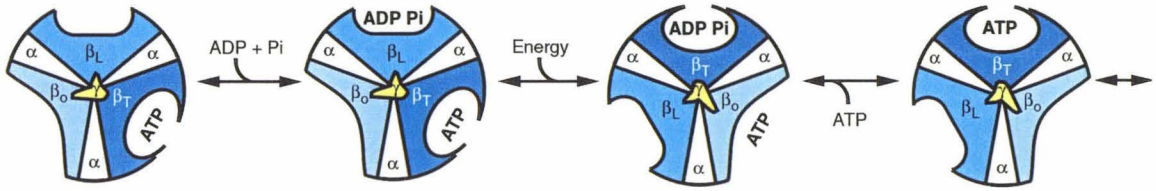

Fig. 1.13: Model for the control of the FNR transcription factor in response to the presence of O_2. DNA binding of FNR is promoted by the formation of a homodimer with each monomer containing a single [4Fe:4S] cluster. Within minutes of oxidation, the homodimer is converted to monomers, with the [4Fe:4S] clusters oxidized to [2Fe:2S] clusters. After several hours in oxidizing conditions, the [2Fe:2S] clusters are also lost.

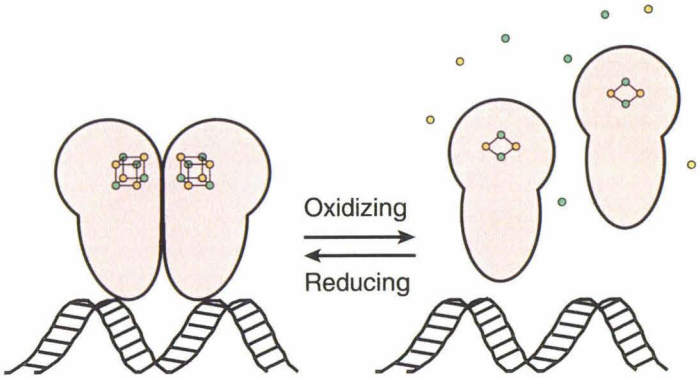

Fig. 1.14: Structures of menaquinone and ubiquinone cofactors. In the membrane, the menaquinone has a hydrophobic tail contains seven isoprenol groups while ubiquinone has ten.

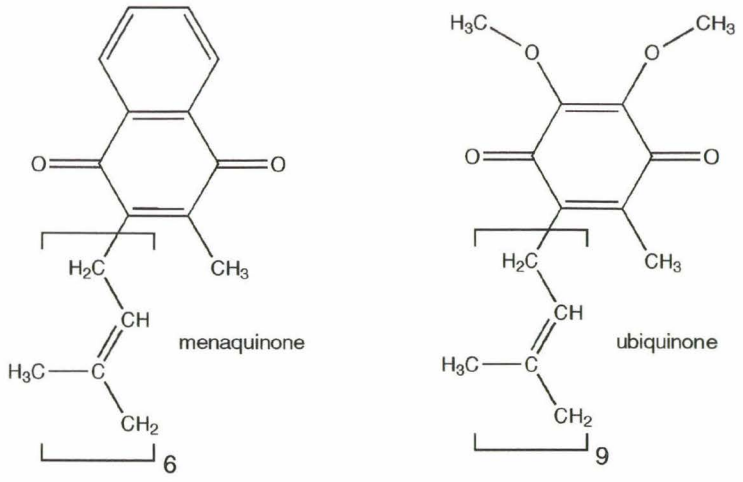

Fig. 1.15: Schematic representation of anaerobic respiration with formate and hydrogen as the electron donors and fumarate as the terminal electron acceptor. Anaerobic respiration occurs in the periplasmic membrane in bacteria. Formate dehydrogenase and hydrogenase catalyze the oxidation of formate and hydrogen, respectively, and transfer the electrons through the membrane-soluble menaquinone pool to quinol-fumarate reductase. Fig. adapted from *(83)*.

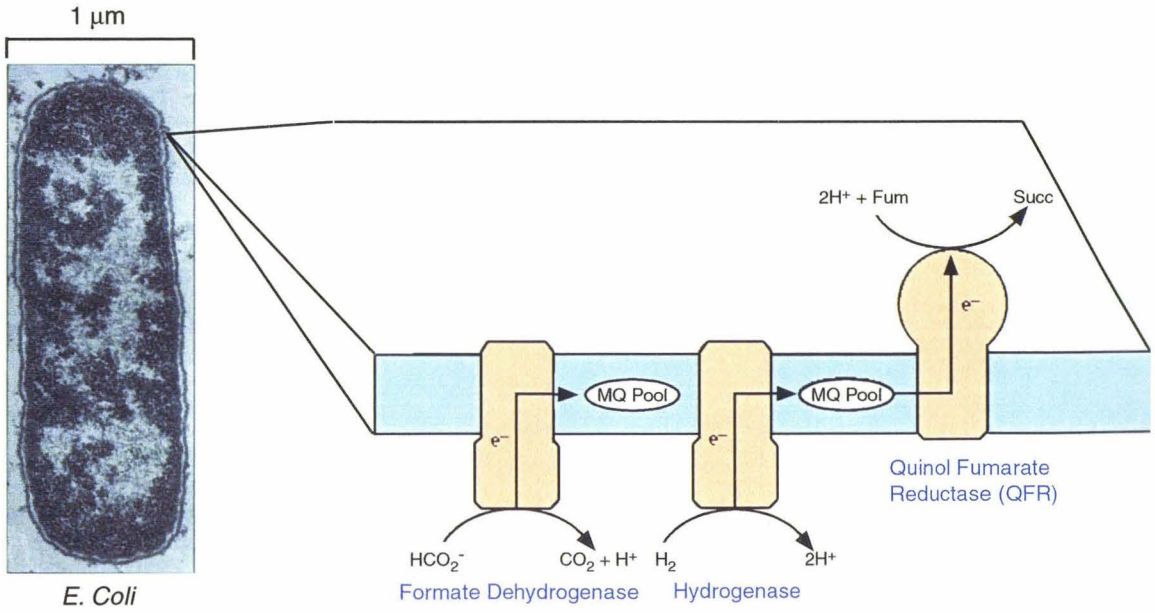

Fig. 1.16: The structural understanding of anaerobic respiration with fumarate as the terminal electron acceptor. The soluble domain of the Ni-Fe hydrogenase has been solved from *Desulfovibrio gigas*, and the soluble domain from formate dehydrogenase has been solved from *Escherichia coli*. The complex II homologue quinol-fumarate reductase has been solved from *Escherichia coli* and *Wolinella succinogenes*.

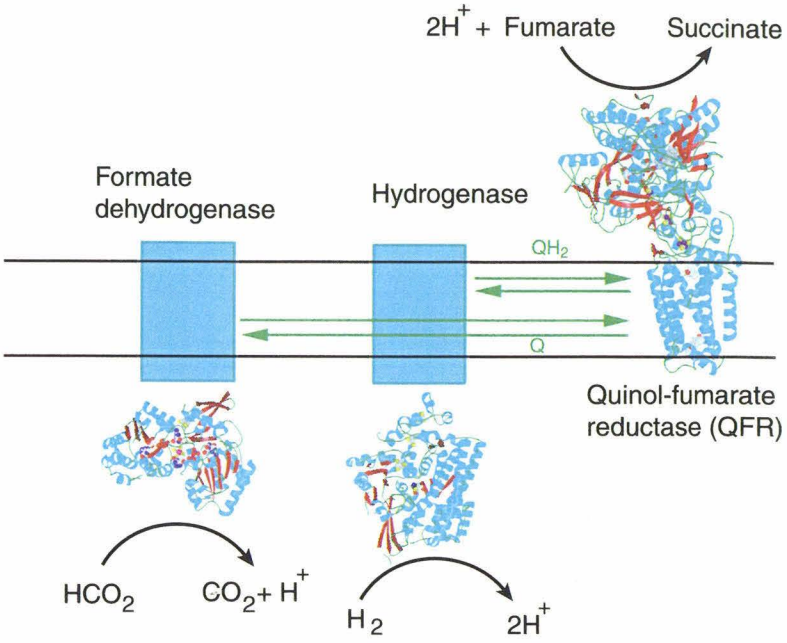

Table 1.1: Reduction potentials for *Bos taurus* mitochondrial complex II

succinate	+25 mV
FAD	-79 mV
[2Fe:2S]	0 mV
[4Fe:4S]	-260 mV
[3Fe:4S]	+60mV
heme *b*	-185 mV
ubiquinone	+113 mV

Table 1.2: Oxido-reductases of the anaerobic respiratory chains of *Escherichia coli*

Enzyme	Redox couple pair	E_m(V)
Primary electron donors		
Formate dehydrogenase	$HCO_3^-/CO_2 + H^+$	-0.43
Hydrogenase	H_2/H^+	-0.42
NADH dehydrogenase	NAD^+/NADH	-0.32
Glycerol 3-P dehydrogenase	DHAP/Gly-3-P	-0.19
Pyruvate oxidase	acetate + CO_2/pyruvate	
Lactate dehydrogenase	pyruvate/lactate	-0.19
Glucose dehydrogenase	glucose/gluconate	-0.14
Succinate dehydrogenase	succinate/fumarate	+0.03
Termainal reductases		
Nitrate reductase	NO_3^-/NO_2^-	+0.42
Nitrite reductase	NO_2^-/NH_4^+	+0.36
DMSO reductase	DMSO/DMS	+0.16
TMAO reductase	TMAO/TMA	+0.13
Fumarate reductase	fumarate/succinate	+0.03

REFERENCES

1. Szalai, A., and Brudvig, G. W. (1998) *American Scientist 86*, 542-551.

2. Babcock, G. T. (1999) *Proc. Natl. Acad. Sci. USA 96*, 12971-12973.

3. Brandt, U. (1997) *Biochim. Biophys. Acta 1318*, 79-91.

4. Friedrich, T., Steinmutter, K., and Weiss, H. (1995) *FEBS Lett. 367*, 107-111.

5. Walker, J. E., Skehel, J. M., and Buchanan, S. K. (1995) *Methods Enzymol. 260*, 14-34.

6. Vercesi, A., Reynafarje, B., and Lehninger, A. L. (1978) *J. Biol. Chem. 253*, 6379-6385.

7. DiVirgilio, F., and Azzone, G. F. (1982) *J. Biol. Chem. 257*, 4106-4113.

8. Wikström, M. (1984) *FEBS Lett. 169*, 300-304.

9. Brown, G. C., and Brand, M. D. (1988) *Biochem. J. 252*, 473-479.

10. Walker, J. E. (1992) *Q. Rev. Biophys. 25*, 253-324.

11. Fearnley, I. M., and Walker, J. E. (1992) *Biochim. Biophys Acta 1140*, 105-134.

12. Buchanan, S. K., and Walker, J. E. (1996) *Biochem. J. 318*, 343-349.

13. Skehel, J. M., Fearnley, I. M., and Walker, J. E. (1998) *FEBS Lett. 438*, 301-305.

14. Chomyn, A., Cleeter, M. W. J., Ragan, C. I., Riley, M., Doolittle, R. F., and Attardi, G. (1986) *Science 234*, 614-618.

15. Weidner, U., Geier, S., Ptock, A., Friedrich, T., Leif, H., and Weiss, H. (1993) *J. Mol. Biol. 233*, 109-122.

16. Yagi, T., Yano, T., and Matsunoyagi, A. (1993) *J. Bioenerg. Biomembr. 25*, 339-345.

17. Yano, T., Chu, S. S., Sled, V. D., Ohnishi, T., and Yagi, J. (1997) *J. Biol. Chem. 272*, 4201-4211.

18. Blattner, F. R., Plunkett, G., Bloch, C. A., Perna, N. T., Burland, V., Riley, M., Collado-Vides, J., Glasner, J. D., Rode, C. K., Mayhew, G. A. F., Gregor, J., Davis, N.

W., Kirkpatrick, H. A., Goeden, M. A., Rose, D. J., Mau, B., and Shao, Y. (1997) *Science 277*, 1453-1474.

19. Guenebaut, V., Vincentelli, R., Mills, D., Weiss, H., and Leonard, K. R. (1997) *J. Mol. Biol. 265*, 409-418.

20. Guenebaut, V., Schlitt, A., Weiss, H., Leonard, K., and Friedrich, T. (1998) *J. Mol. Biol. 276*, 105-112.

21. Ragan, C. I. (1987) *Curr. Top. Bioenerg. 15*, 1-36.

22. Pilkington, S. J., Skehel, J. M., Gennis, R. B., and Walker, J. E. (1991) *Biochemistry 30*, 2166-2175.

23. Rao, N. A., Felton, S. P., Huennekens, F. M., and Mackler, B. (1963) *J. Biol. Chem. 238*, 449-455.

24. Yano, T., and Yani, T. (1999) *J. Biol. Chem. 274*, 28606-28611.

25. Ohnishi, T. (1979) in *membrane proteins in energy transduction* (Capaldi, R. A., Ed.), Marcel Dekker, New York.

26. Ohnishi, T., and Salerno, J. C. (1982) in *Iron-sulfur proteins* (Spiro, T. G., Ed.), Wiley, New York.

27. Beinert, H., and Albracht, S. P. J. (1982) *Biochim. Biophys. Acta 683*, 245-277.

28. Yano, T., Magnitsky, S., Sled, V. D., Ohnishi, T., and Yagi, T. (1999) *J. Biol. Chem. 274*, 28598-28605.

29. Ohnishi, T. (1998) *Biochim. Biophys. Acta 1364*, 186-206.

30. Suzuki, H., and King, T. E. (1983) *J. Biol. Chem. 268*, 352-358.

31. Vinogradov, A. D., Sled, V. D., Burbaev, D. S., Grivennikova, V. G., Moroz, I. A., and Ohnishi, T. (1995) *FEBS Lett. 370*, 83-87.

32. Burbaev, D. S., Moroz, I. A., Kotlyar, A. B., Sled, V. D., and Vinogradov, A. D. (1989) *FEBS Lett. 254*, 47-51.

33. Kotlyar, A. B., Sled, V. D., D.S., B., Moroz, I. A., and Vinogradov, A. D. (1990) *FEBS Lett. 264*, 17-20.

34. Ohnishi, T., Magnitsky, S., Toulokhonova, L., Yano, T., Yagi, T., Burbaev, D. S., and Vinogradov, A. D. (1999) *Biochem. Soc. T. 27*, 586-591.

35. Albracht, S. P. J., Mariette, A., and deJong, P. (1997) *Biochim. Biophys. Acta 1318*, 92-106.

36. Krishnamoorthy, G., and Hinkle, P. C. (1988) *J. Biol. Chem. 263*, 17566-17575.

37. Dutton, P. L., Moser, C. C., Sled, V. D., Daldal, F., and Ohnishi, T. (1998) *Biochim. Biophys. Acta 1364*, 245-257.

38. Ingledew, W. J., and Ohnishi, T. (1980) *Biochem. J. 186*, 111-117.

39. Gutman, M., T.P., S., and Beinert, H. (1972) *Biochemistry 11*, 556-562.

40. Sled, V. D., Friedrich, T., Leif, H., Weiss, H., Meinhardt, S. W., Fukumori, Y., Calhoun, M. W., Gennis, R. B., and Ohnishi, T. (1993) *J. Bioenerg. Biomembr. 25*, 347-356.

41. Salerno, J. C., Blum, H., and Ohnishi, T. (1979) *Biochim. Biophys. Acta 547*, 270-281.

42. Ohnishi, T., Leigh, J. S., Ragan, C. I., and Racker, E. (1974) *Biochem. Biophys. Res. Commun. 56*, 775-782.

43. Ackrell, B. A. C., Johnson, M. K., Gunsalus, R. P., and Cecchini, G. (1992) *Chemistry and biochemistry of flavoenzymes*, Vol. 3, CRC Press, Boca Raton.

44. Hägerhäll, C. (1997) *Biochim. Biophys. Acta 1320*, 107-141.

45. Guest, J. R., and Russell, G. C. (1992) *Curr. Top. Cell. Regul. 33*, 231-247.

46. Kowal, A. T., Werth, M. T., Moanodori, A., Cecchini, G., Schröder, I., Gunsalus, R. P., and Johnson, M. K. (1995) *Biochemsitry 34*, 12284-12293.

47. Morningstar, J. E., Johnson, M. K., Cecchini, G., Ackrell, B. A. C., and Kearney, E. B. (1985) *J. Biol. Chem. 260*, 3631-3638.

48. Cammack, R., Patil, D. S., and Weiner, J. H. (1986) *Biochim. Biophys. Acta 870*, 545-551.

49. Gest, H. (1980) *FEMS Lett. 7*, 73-77.

50. Singer, T. P., Kearney, E. B., and Kenney, W. C. (1973) *Adv. Enzymol. 37*, 189-272.

51. Pealing, S. L., Black, A. C., Manson, F. D., Ward, F. B., Chapman, S. K., and Reid, G. A. (1992) *Biochemistry 31*, 12132-12140.

52. Simon, J., Gross, R., Klimmek, O., Ringel, M., and Kroger, A. (1998) *Arch. Microbiol. 169*, 424-433.

53. Pealing, S. L., Lysek, D. A., Taylor, P., Alexeev, D., Reid, G. A., Chapman, S. K., and Walkinshaw, M. D. (1999) *J. Structu. Biol. 127*, 76-78.

54. Flachmann, R., Kunz, N., Seifert, J., Gutlich, M., Wientjes, F. J., Laufer, A., and Gassen, H. G. (1988) *Eur. J. Biochem. 175*, 221-228.

55. Sun, D., and Setlow, P. (1993) *J. Bacteriol. 175*, 1423-1432.

56. Kaneko, T., Sato, S., Kotani, H., Tanaka, A., Asamizu, E., Nakamura, Y., Miyajima, N., Hirosawa, M., Sugiura, M., Sasamoto, S., Kimura, T., Hosouchi, T., Matsuno, A., Muraki, A., Nakazaki, N., Naruo, K., Okumura, S., Shimpo, S., Takeuchi, C., Wada, T., Watanabe, A., Yamada, M., Yasuda, M., and Tabata, S. (1996) *DNA Res. 3*, 109-136.

57. Cole, S. T., Brosch, R., Parkhill, J., Garnier, T., Churcher, C., Harris, D., Gordon, S. V., Eiglmeier, K., Gas, S., Barry, C. E. I. I. I., Tekaia, F., Badcock, K., Basham, D., Brown, D., Chillingworth, T., Connor, R., Davies, R., Devlin, K., Feltwell, T., Gentles, S., Hamlin, N., Holroyd, S., Hornsby, T., Jagels, K., Krogh, A., McLean, J., Moule, S., Murphy, L., Oliver, S., Osborne, J., Quail, M. A., Rajandream, M. A., Rogers, J., Rutter, S., Seeger, K., Skelton, S., Squares, S., Sqares, R., Sulston, J. E., Taylor, K., Whitehead, S., and Barrell, B. G. (1998) *Nature 393*, 537-544.

58. Deckert, G., Warren, P. V., Gaasterland, T., Young, W. G., Lenox, A. L., Graham, D. E., Overbeek, R., Snead, M. A., Keller, M., Aujay, M., Huber, R., Feldman, R. A., Short, J. M., Olson, G. J., and Swanson, R. V. (1998) *Nature 392*, 353-358.

59. Redenbach, M., Kieser, H. M., Denapaite, D., Eichner, A., Cullum, J., Kinashi, H., and Hopwood, D. A. (1996) *Mol. Microbiol. 21*, 77-96.

60. Tettelin, H., Saunders, N. J., Heidelberg, J., Jeffries, A. C., Nelson, K. E., Eisen, J. A., Ketchum, K. A., Hood, D. W., Peden, J. F., Dodson, R. J., Nelson, W. C., Gwinn, M. L., DeBoy, R., Peterson, J. D., Hickey, E. K., Haft, D. H., Salzberg, S. L., White, O., Fleischmann, R. D., Dougherty, B. A., Mason, T., Ciecko, A., Parksey, D. S., Blair, E., Cittone, H., Clark, E. B., Cotton, M. D., Utterback, T. R., Khouri, H., Qin, H., Vamathevan, J., Gill, J., Scarlato, V., Masignani, V., Pizza, M., Grandi, G., Sun, L., Smith, H. O., Fraser, C. M., Moxon, E. R., Rappuoli, R., and Venter, J. C. (2000) *Science 287*, 1809-1815.

61. Plesiat, P., Grandguillot, M., Harayama, S., Vragar, S., and Michel-Briand, Y. (1991) *J. Bacteriol. 173*, 7219-7227.

62. Morii, S., Fujii, C., Miyoshi, T., Iwami, M., and Itagaki, E. (1998) *J. Biochem. 124*, 1026-1032.

63. Molnar, I., Choi, K. P., Yamashita, M., and Murooka, Y. (1995) *Mol. Microbiol. 15*, 895-905.

64. Galibert, F., Alexandraki, D., Baur, A., Boles, E., Chalwatzis, N., Chuat, J. C., Coster, F., Cziepluch, C., De Haan, M., Domdey, H., Durand, P., Entian, K. D., Gatius, M., Goffeau, A., Grivell, L. A., Hennemann, A., Herbert, C. J., Heumann, K., Hilger, F., Hollenberg, C. P., Huang, M. E., Jacq, C., Jauniaux, J. C., Katsoulou, C., and Karpfinger-Hartl, L. e. a. (1996) *EMBO J. 15*, 2031-2049.

65. Goffeau, A., Barrell, B. G., Bussey, H., Davis, R. W., Dujon, B., Feldmann, H., Galibert, F., Hoheisel, J. D., Jacq, C., Johnston, M., Louis, E. J., Mewes, H. W.,

Murakami, Y., Philippsen, P., Tettelin, H., and Oliver, S. G. (1996) *Science 274*, 546-550.

66. Maklashina, E., Berthold, D. K., and Cecchini, G. (1998) *J. Bacteriol. 180*, 5989-5996.

67. Pershad, H. R., Hirst, J., Cochran, B., Ackrell, B. A. C., and Armstrong, F. A. (1999) *Biochim. Biophys. Acta 1412*, 262-272.

68. Blaut, M., Whittaker, K., Valdovinos, A., Ackrell, B. A. C., Gunsalus, R. P., and Cecchini, G. (1989) *J. Biol. Chem. 264*, 13599-13604.

69. Robinson, K. M., Rothery, R. A., Weiner, J. H., and Lemire, B. D. (1994) *Eur. J. Biochem. 222*, 983-990.

70. Walker, W. H., and Singer, T. P. (1970) *J. Biol. Chem. 245*, 4224-4225.

71. Iverson, T. M., Luna-Chavez, C., Cecchini, G., and Rees, D. C. (1999) *Science 284*, 1961-1966.

72. Lancaster, C. R. D., Kröger, A., Auer, M., and Michel, H. (1999) *Nature 402*, 377-385.

73. Matttevi, A., Tedeschi, G., Bacchella, L., Coda, A., Negri, A., and Ronchi, S. (1999) *Structure 7*, 745-756.

74. Bamford, V., Dobbin, P. S., Richardson, D. J., and Hemmings, A. M. (1999) *Nat. Struct. Biol. 6*, 1104-1109.

75. Leys, D., Tsapin, A. S., Nealson, K. H., Meyer, T. E., Cusanovich, M. A., and VanBeeumen, J. J. (1999) *Nat. Struct. Biol. 6*, 1113-1117.

76. Taylor, P., Pealing, S. L., Reid, G. A., Chapman, S. K., and Walkinshaw, M. D. (1999) *Nat. Struct. Biol. 6*, 1108-1112.

77. Hägerhäll, C., and Hederstedt, L. (1996) *FEBS Lett. 389*, 25-31.

78. Westenberg, D. J., Gunsalus, R. P., Ackrell, B. A. C., Sices, H., and Cecchini, G. (1993) *J. Biol. Chem. 268*, 815-822.

79. Lee, G. Y., He, D. Y., Yu, L., and Yu, C. A. (1995) *J. Biol. Chem. 270*, 6193-6198.

80. Shenoy, S. K., Yu, L., and Yu, C. A. (1997) *J. Biol. Chem. 272*, 17867-17872.

81. Hägerhäll, C., Magnitsky, S., Sled, V. D., Schröder, I., Gunsalus, R. P., Cecchini, G., and Ohnishi, T. (1999) *J. Biol. Chem. 274*, 26157-26164.

82. Xia, D., Yu, C., Kim, H., Xia, J., Kachurin, A. M., Zhang, L., L. Yu, and Deisenhofer, J. (1997) *Science 277*, 60-66.

83. Zhang, Z. (1998) *Nature 392*, 677-684.

84. Iwata, S., Lee, J. W., Okada, K., Lee, J. K., Iwata, M., Rasmussen, B., Link, T. A., Ramaswamy, S., and Jap, B. K. (1998) *Science 281*, 64-71.

85. Ohnishi, T., Moser, C. C., Page, C. C., Dutton, P. L., and Yano, T. (2000) *Structure 8*, R23-R32.

86. Yang, X. H., and Trumpower, B. L. (1986) *J. Biol. Chem. 262*, 8702-8706.

87. Robertson, D. E., Ding, H. G., Chelminski, P. R., Slaughter, C., Hsu, J., Moomaw, C., Tokito, M., Daldal, F., and Dutton, P. L. (1993) *Biochemistry 32*, 1310-1317.

88. Schägger, H., Brandt, U., Gencic, S., and von Jagow, G. (1995) *Method. Enzymol. 260*, 82-96.

89. Braun, H. P., and Schmitz, U. K. (1997) *Int. J. Biochem. Cell. B. 29*, 1043-1045.

90. Glaser, E., and Dessi, P. (1999) *J. Bioenerg. Biomemb. 31*, 259-274.

91. Mitchell, P. (1961) *Nature 191*, 144-148.

92. Cramer, W. A., and Soriano, G. M. (1999) *Biofactors 2*, 81-6.

93. Wikström, M. K., and Berden, J. A. (1972) *Biochim. Biophys. Acta 283*, 403-407.

94. Trumpower, B. L. (1990) *J. Biol. Chem. 265*, 11409-11412.

95. Brandt, U., and Trumpower, B. (1994) *Crit. Rev. Biochem. Mol. 29*, 165-197.

96. Brandt, I. (1996) *FEBS Lett. 387*, 1-6.

97. Link, T. A. (1997) *FEBS Lett 412*, 257-264.

98. Brandt, U. (1998) *Biochim. Biophys. Acta 1365*, 261-268.

99. Brandt, U. (1999) *J. Bioenerg. Biomembr. 31*, 243-250.

100. Crofts, A. R., Barquera, B., Gennis, R. B., Kuras, R., Guergova-Kuras, M., and Berry, E. A. (1999) *Biochemistry 38*, 15807-15926.

101. Yu, C. A., Zhang, L., Deng, K. P., Tian, H., Xia, D., Kim, H., Deisenhofer, J., and Yu, L. (1999) *Biofactors 9*, 103-109.

102. Brugna, M., Rodgers, S., Schricker, A., Montoya, G., Kazmeier, M., Nitschke, W., and Sinning, I. (2000) *Proc. Natl. Acad. Sci. USA 97*, 2069-2074.

103. Crofts, A. R., and Wang, Z. G. (1989) *Photosynth. Res. 22*, 69-87.

104. Brandt, U., and vonJargow, G. (1991) *Eur. J. Biochem. 195*, 163-170.

105. Brandt, U., Haase, U., Schägger, H., and vonJargow, G. (1991) *J. Biol. Chem. 266*, 19958-19964.

106. Ding, H., Moser, C. C., Robertson, D. E., Tokito, M. K., Daldal, F., and Dutton, P. L. (1995) *Biochemistry 34*, 15979-15996.

107. Kim, H., Xia, D., Yu, C., Xia, J., Kachurin, A. M., Zhang, L., Yu, L., and Deisenhofer, J. (1998) *Proc. Natl. Acad. Sci. USA 95*, 8026-8033.

108. Crofts, A. R., Barquera, B., Gennis, R. B., Kuras, R., Guergova-Kuras, M., and Berry, E. A. (1999) *Biochemistry 38*, 15807-15826.

109. Brandt, U., and Okun, J. G. (1997) *Biochemistry 36*, 11234-11240.

110. Iwata, S. (personal communication) .

111. Crofts, A. R., Hong, S., Zhang, Z., and Berry, E. A. (1999) *Biochemistry 38*, 15827-15839.

112. Saraste, M. (1990) *Q. Rev. Biophys. 23*, 331-366.

113. Babcock, G. T., and Wikström, M. (1992) *Nature 356*, 301-309.

114. Calhoun, M. W., Thomas, J. W., and Gennis, R. B. (1994) *Trends. Biochem. Sci. 19*, 325-330.

115. Ferguson-Miller, S., and Babcock, G. T. (1996) *Chem. Rev. 96*, 2889-2907.

116. Wikström, M. (1977) *Nature 266*, 271-273.

117. Solioz, M., Carafoli, E., and Ludwig, B. (1982) *J. Biol. Chem. 257*, 1579-1582.

118. Sone, N., and Hinkle, P. C. (1982) *J. Biol. Chem. 257*, 2600-2604.

119. Puustinen, A., Finel, M., Virkki, M., and Wikström, M. (1989) *FEBS Lett. 249*, 163-167.

120. Musser, S. M., and Chan, S. I. (1998) *J. Mol. Evol. 46*, 508-520.

121. Garcia-Horsman, J. A., Barquera, B., Rumbley, J., Ma, J. X., and Gennis, R. B. (1994) *J. Bacteriol. 176*, 5587-5600.

122. Kadenbach, B., Kuhnnentwig, L., and Buge, U. (1987) *Curr. Top. Bioenerg. 15*, 113-161.

123. Musser, S. M., Stowell, M. H. B., and Chan, S. I. (1995) *Adv. Enzymol. RAMB 71*, 79-208.

124. Iwata, S., Ostermeier, C., Ludwig, B., and Michel, H. (1995) *Nature 376*, 660-669.

125. Ostermeier, C., Harrenga, A., Ermler, U., and Michel, H. (1997) *Proc. Natl. Acad. Sci. USA 94*, 10547-10553.

126. Tsukihara, T., Aoyama, H., Yamashita, E., Tomizaki, T., Yamaguchi, H., Shinzawa-Itoh, K., Nakashima, R., Yaono, R., and Yoshikawa, S. (1995) *Science 269*, 1069-1074.

127. Tsukihara, T., Aoyama, H., Tomizaki, E. Y. Y., Yamaguchi, H., Shinzawa-Itoh, K., Nakashima, R., Yaono, R., and Yoshikawa, S. (1996) *Science 272*, 1136-1144.

128. Yoshikawa, S., Shinzawa-Itoh, K., Nakashima, R., Yaono, R., Yamashita, E., Inoue, N., Yao, M., Fie, M. J., Libeu, C. P., Mizushima, T., Yamaguchi, H., Tomizaki, T., and Tsukihara, T. (1998) *Science 280*, 1723-1729.

129. Müller, M., Schläpfer, B., and Azzi, A. (1988) *Proc. Natl. Acad. Sci. USA 85*, 6647-6651.

130. Yoshikawa, S., Tera, T., Takahashi, Y., T., T., and Caughey, W. S. (1988) *Proc. natl. Acad. Sci. USA 85*, 1354-1358.

131. Hiser, L., Di Valentin, M., Hamer, A. G., and Hosler, J. P. (2000) *J. Biol. Chem. 275*, 619-623.

132. Napiwotzki, J., Shinzawa-Itoh, K., Yoshikawa, S., and Kadenbach, B. (1997) *Biol. Chem. 378*, 1013-1021.

133. Bender, E., and Kadenbach, B. (2000) *FEBS Lett. 466*, 130-134.

134. Hosler, J. P., Espe, M. P., Zhen, Y. J., Babcock, G. T., and Ferguson-Miller, S. (1995) *Biochemistry 34*, 7586-7592.

135. Espe, M. P., Hosler, J. P., Ferguson-Miller, S., Babcock, G. T., and McCracken, J. (1995) *Biochemistry 34*, 7593-7602.

136. Kelly, M., Lappalainen, P., Talbo, G., Haltia, T., Vanderoost, J., and Saraste, M. (1993) *J. Biol. Chem. 268*, 16781-16787.

137. Zhen, Y. J., Hoganson, C. W., Babcock, G. T., and Ferguson-Miller, S. (1999) *J. Biol. Chem. 274*, 38032-38041.

138. Wang, K. F., Zhen, Y. J., Sadoski, R., Grinnell, S., Geren, L., G., Ferguson-Miller, S., Durham, B., and Millett, F. (1999) *J. Biol. Chem. 274*, 38042-38050.

139. Roberts, V. A., and Pique, M. E. (1999) *J. Biol. Chem. 274*, 38051-38060.

140. Thomas, J. W., Calhoun, M. W., Lemieux, L. J., Puutstinen, A., Wikström, M., Alben, J. O., and Gennis, R. B. (1994) *Biochemistry 33*, 13013-13021.

141. Verkhovsky, M. I., Jasaitis, A., Verkovskaya, M. L., Morgan, J. E., and Wikström, M. (1999) *Nature 400*, 480-483.

142. Perutz, M. F. (1990) *Mechanism of Cooperativity and Allosteric Regulation in Proteins*, Cambridge University Press, Cambridge.

143. Williams, R. J. P. (1995) *Nature 376*, 643-643.

144. Gennis, R., and S., F.-M. (1995) *Science 269*, 1063-1064.

145. Mitchell, D. M., Fetter, J. R., Mills, D. A., Adelroth, P., Pressler, M. A., Kim, Y., Aasa, R., Brzezinski, P., Malmstrom, B. G., Alben, J. O., Babcock, G. T., FergusonMiller, S., and Gennis, R. B. (1996) *Biochemistry 35*, 13089-13093.

146. Michel, H. (1998) *Proc. Natl. Acad. Aci. USA 95*, 107-112.

147. Michel, H. (1999) *Biochemistry 38*, 15129-15140.

148. Michel, H. (1999) *Nature 402*, 602-603.

149. Verkhovsky, M. I., Jasaitis, A., Verkhovskaya, M. L., Morgan, J. E., and Wikström, M. (1999) *Nature 402*.

150. Boyer, P. D. (1997) *Annu. Rev. Biochem. 66*, 717-749.

151. Stock, D., Leslie, A. G. W., and Walker , J. E. (1999) *Science 286*, 1700-1705.

152. Abrahams, J. P., Leslie, A. G. W., Lutter, R., and Walker, J. E. (1994) *Nature 370*, 621-628.

153. Shirakihara, Y., Leslie, A. G. W., Abrahams, J. P., Walker, J. E., Ueda, T., Sekimoto, Y., Kambara, M., Saika, K., Kagawa, Y., and Yoshida, M. (1997) *Structure 5*, 825-836.

154. Noji, H., Yasuda, R., Yoshida, M., and Kinoshita, K. (1997) *Nature 386*, 8215-8221.

155. Yasuda, R., Noji, H., Kinosita, K., and Yoshida, M. (1998) *Cell 93*, 1117-1124.

156. Sambongi, Y., Iko, Y., Tanabe, M., Omote, H., Iwamoto-Kigara, A., Ueda, I., Yanagida, T., Wada, Y., and Futai, M. (1999) *Science 286*, 1722-1724.

157. Girvin, M. E., Rastogi, V. K., Abildgaard, F., Markley, J. L., and Fillingame, R. H. (1998) *Biochemistry 37*, 8817-8824.

158. Sabbert, D., Engelbrecht, S., and Junge, W. (1996) *Nature 381*, 623-625.

159. Boyer, P. D. (1993) *Biochim. Biophys. Acta 1140*, 215-250.

160. Bauer, C. E., Elsen, S., and Bird, T. H. (1999) *Annu. Rev. Microbiol. 53*, 495-523.

161. Guest, J. R., and Lambden, P. R. (1976) *J. Gen. Microbiol. 180.*

162. Sawers, R. G., Zalelein, E., and Böck, A. (1988) *Arch. Microbiol. 149*, 240-244.

163. Khoroshilova, N., Beinert, H., and Kiley, P. J. (1995) *Proc. Natl. Acad. Sci. USA 92*, 2499-2503.

164. Lazazzera, B. A., Beinert, H., Khoroshilova, N., Kennedy, M. C., and Kiley, P. J. (1996) *J. Biol. Chem. 271*, 2762-2768.

165. Khoroshilova, N., Popescu, C., Münck, E., Beinert, H., and Kiley, P. J. (1997) *Proc. Natl. Acad. Sci. USA 94*, 6087-6092.

166. Popescu, C., Bates, D. M., Beinert, H., Münck, E., and Kiley, P. J. (1998) *Proc. Natl. Acad. Sci. USA 95*, 13431-13435.

167. Unden, G., and Bongaerts, J. (1997) *Biochim. Biophys. Acta 1320*, 217-234.

168. Mell, H., Bronder, M., and Kröger, A. (1982) *Arch. Microbiol. 131*, 224-228.

169. Kröger, A., Geisler, V., Lemma, E., Theis, F., and Lenger, R. (1992) *Arch. Microbiol. 158*, 477-483.

170. Sawers, G. (1994) *Anton van Leeuwenhoek 66*, 57-88.

171. Geisler, V., Ullmann, R., and Kröger, A. (1994) *Biochim. Biophys. Acta 1184*, 219-226.

172. Stephenson, M., and Stickland, L. H. (1931) *Biochem. J. 25*.

173. Adams, M. M. W. (1990) *Biochim. Biophys. Acta 1020*, 115-145.

174. Pryzbyla, A. E., Robbins, J., Menon, N., and Peck, H. D. (1992) *FEMS Microbiol. Rev. 88*, 109-135.

175. Wu, L. F., and Mandrand, M. A. (1993) *FEMS Microbiol. Rev. 104*, 243-270.

176. Schauder, R., and Kröger, A. (1993) *Arch. Microbiol. 159*, 238-242.

177. Hedderich, R., Klimmek, O., Kröger, A., Dirmeier, R., Keller, M., and Stetter, K. O. (1999) *FEMS Microbiol. Rev. 22*, 353-381.

178. Reeve, J. N., and Beckler, G. S. (1990) *FEMS Microbiol. Rev. 87*, 419-424.

179. Higuchi, Y., Yagi, T., and Yasuoka, N. (1997) *Structure 5*, 1671-1680.

180. Volbeda, A., Charon, M. H., Piras, C., Hatchiikian, E. C., Frey, M., and Fontecilla-Camps, J. C. (1995) *Nature 373*, 580-587.

181. Axley, M. J., Grahame, D. A., and Stadtman, T. C. (1990) *J. Biol. Chem. 265*, 18213-18218.

182. Gladyshev, V. N., Khangulov, S. V., Axley, M. J., and Stadtman, T. C. (1994) *Proc. Natl. Acad. Sci. USA 91*, 7708-7711.

183. Boyington, J. C., Gladyshev, V. N., Khangolov, S. V., Stadtman, T. C., and Sun, P. D. (1997) *Science 275*, 1305-1308.

184. Schindelin, H., Kisker, C., Hilton, J., Rajagopalan, K. V., and Rees, D. C. (1996) *Science 272*, 1615-1621.

185. Schneider, F., Löwe, J., Huber, R., Schindelin, H., Kisker, C., and Knäblein, J. (1996) *J. Mol. Biol. 263*, 53-69.

186. McEwan, A. G. (1994) *Anton. van Leeuwenhoek 66*, 151-164.

187. Zinoni, F., Birkmann, A., Stadtman, T. C., and Böck, A. (1986) *Proc. Natl. Acad. Sci. USA 83*, 4650-4654.

188. Zinoni, F., Birkmann, A., Leinfelder, W., and Böck, A. (1987) *Proc. Natl. Acad. Sci. USA 84*, 3156-3160.

Chapter 2

Luna-Chavez, C., Iverson, T.M., Rees, D.C., Cecchini, G. (2000) Overexpression, Purification and Crystallization of the Membrane-bound Fumarate Reductase from *Escherichia coli. Protein Exp. Pur.*, in press.

Overexpression, Purification and Crystallization of the Membrane-bound Fumarate Reductase from *Escherichia coli*

Running Title: Crystallization of Fumarate Reductase

César Luna-Chavez,[1] Tina M. Iverson,[2] Douglas C. Rees,[3] and Gary Cecchini[1*]

[1]Molecular Biology Division (151-S), VA Medical Center, San Francisco, CA 94121 and Department of Biochemistry and Biophysics, University of California, San Francisco, CA 94143

[2]Graduate Option in Biochemistry, 147-75CH, California Institute of Technology, Pasadena, CA 91125

[3]Howard Hughes Medical Institute, Division of Chemistry and Chemical Engineering, 147-75CH, California Institute of Technology, Pasadena, CA 91125

[*]To whom correspondence should be addressed at Molecular Biology Div. (151-S), VA Medical Center, 4150 Clement Street, San Francisco, CA 94121. Telephone: (415) 752-9676, FAX: (415) 750-6959, E-mail: **ceccini@itsa.ucsf.edu**.

Key Words: Fumarate reductase, succinate dehydrogenase, crystallography, membrane proteins.

[4] Abbreviations used: Ap^r, ampicillin resistant; CHAPS, (3-[(3-cholamidopropyl) dimethylammonio]-1-propane-sulfonate; cmc, critical micelle concentration; DCIP, 2,6-dichlorophenolindophenol; Fp, flavoprotein subunit; GuHCl, guanidinium hydrochloride; Ip, iron-sulfur protein subunit; LB, Luria-Bertani; PEG, polyethylene glycol; PES, phenazine ethosulfate; QFR, quinol:fumarate reductase; SQR, succinate:quinone reductase

ABSTRACT

Quinol-fumarate reductase (QFR) from *Escherichia coli* is a membrane-bound four subunit respiratory protein that shares many physical and catalytic properties with succinate-quinone oxidoreductase (SQR) (EC 1.3.99.1) commonly referred to as complex II. The *E. coli* QFR has been overexpressed using plasmid vectors so that more than 50% of the cytoplasmic membrane fraction is composed of the four subunit enzyme complex. The growth characteristics required for optimal levels of expression with minimal degradation by host cell proteases and oxidation factors were determined for the strains harboring the recombinant plasmid. The enzyme is extracted from the enriched membrane fraction using the non-ionic detergent Thesit (polyoxyethylene(9)dodecyl ether) in a monodisperse form and then purified by a combination of anion exchange, perfusion, and gel filtration chromatography. The purified enzyme is highly active and contains all types of redox cofactors expected to be associated with the enzyme. Crystallization screening of the purified QFR by vapor diffusion resulted in the formation of crystals within 24 hours using a sodium citrate buffer and polyethylene glycol precipitant. The crystals contain the complete four subunit QFR complex, diffract to 3.3 Å resolution and were found to be in space group $P2_12_12_1$ with unit cell dimensions a=96.6 Å, b=138.1 Å, and c=275.3 Å. The purification and crystallization procedures are

highly reproducible and the general procedure may prove useful for complex II's from other sources.

INTRODUCTION

Complex II's (succinate:quinone reductase, SQR and quinol:fumarate reductase, QFR)[4] are structurally and functionally similar membrane-bound enzymes involved in aerobic and anaerobic respiration, respectively. The enzymes catalyze the oxidation of succinate or the reduction of fumarate in the mitochondrial matrix or bacterial cytoplasm and the reduction or oxidation of quinone/quinol in the membrane. All complex II enzymes are composed of a large flavoprotein subunit (Fp, 66-70 kDa) which contains an 8α-N(3)-histidyl-FAD cofactor and the dicarboxylate-binding site and an iron-sulfur protein subunit (Ip, ~27 kDa) containing three distinct iron-sulfur clusters (1, 2). The Fp and Ip catalytic dimer is linked to the membrane in most cases by two hydrophobic polypeptides. The membrane anchor domain of the enzyme (FrdC/SdhC and FrdD/SdhD) is more varied in composition and in some cases consists of only one polypeptide. Depending on the species from which the enzyme is isolated, the membrane anchors also may contain and also may contain zero, one, or two *b* hemes. The primary amino acid sequence similarity is lower in the membrane domain; however, evidence indicates that the membrane anchors have a conserved general structure (2, 3). The membrane anchor domain of complex II also provides binding sites for quinones as has been demonstrated in SQR/QFR by various methods (4-8).

Purified preparations of SQR (9) and QFR (10) in a membrane-bound form have been achieved for a number of years; however, the enzymes were often isolated under

harsh conditions that gave varied stoichiometry of subunits and cofactors (1, 11). The SQR and QFR complexes from *Escherichia coli* have been cloned and overexpressed and this has proven useful in obtaining highly purified preparations (12,13). The *E. coli* complexes have the additional advantage for studying the properties of complex II that they are easily genetically manipulated. In many respects this has made them the model systems of choice for investigating complex II structure and the function of the various redox cofactors from the complex.

In the past few years high resolution structures for several of the membrane-bound electron transport chain respiratory complexes have become available (14-19). Nevertheless, the number of membrane proteins that have been crystallized in forms that diffract to high resolution remains relatively small in comparison to the number of soluble proteins for which there are well-ordered crystals. There are a number of reasons for the lack of high resolution crystals structures for membrane proteins. These include the fact that many are relatively unstable when extracted from their native membrane environment by the use of detergents where they become exposed to conditions quite different than their native environment (20). Membrane proteins also are often difficult to overexpress often becoming toxic to host cells or forming inclusion bodies. The most recent x-ray structures that have become available for membrane-bound electron transport proteins are the four-subunit non-heme containing fumarate reductase from *E. coli* (21) and the three subunit diheme enzyme from *Wolinella succinogenes* (22). This

manuscript describes the modified and improved procedures that were used to achieve expression and purification of *E. coli* QFR that resulted in a protein complex that was amenable to crystallization and also contains two tightly bound menaquinone molecules.

MATERIALS AND METHODS

Materials. "Complete" protease inhibitor cocktail tablets, the detergent Thesit (polyoxyethylene(9)dodecyl ether), and the perfusion chromatography anion exchange column, POROS 50HQ were obtained from Roche Molecular Biochemicals (Indianapolis, IN). DEAE Sepharose Fast Flow, Sephacryl S-300, PhastGel isoelectrofocusing gels, and high and low molecular weight protein standards were obtained from Amersham Pharmacia Biotech (Piscataway, NJ). SDS-PAGE (10-20%) and native PAGE precast Tris-HCl gels were obtained from Bio-Rad (Hercules, CA). Protein concentration was accomplished with YM30 membranes and Centriprep-30 concentrators from Amicon (Bradford, MA). The Membfac screening kit from Hampton Research (Laguna Hills, CA) was used for crystallization trials. Reagents used for optimization of crystallization conditions were from Fluka (Milwaukee, WI), and all other reagents were analytical grade and obtained from Sigma (St. Louis, MO). Double distilled water was used for preparing all solutions.

Growth and overexpression of recombinant QFR. The construction of *E. coli* strain DW35 (Δ*frdABCD sdhC::kan*) has been described elsewhere (7) and this strain is

completely deficient in both fumarate reductase and succinate dehydrogenase activity. Plasmid pH3 (Ap^r) encodes wild type *E. coli* fumarate reductase (*frdA*$^+$*B*$^+$*C*$^+$*D*$^+$) and is a derivative of pBR322 (23). Growth of bacteria was initiated from a single colony of DW35 transformed with pH3 by transferring to 5-ml of LB medium containing 100 μg ampicillin/ml and growing overnight with shaking at 275 rpm at 37 °C. A 3-ml inoculum from the overnight culture was then added to 50-ml of LB medium plus ampicillin and grown as above for 6 h. Appropriate inocula ($25/OD_{600}$ = ml per 20-liter carboy flask) were then added to 20-liters of anaerobic growth medium contained in a 20-liter carboy filled to the neck. The growth medium contained glycerol-fumarate medium (24) minus manganese, 35 μg ampicillin/ml, and 0.2% (w/v) and 0.1% (w/v) tryptone and yeast extract, respectively. The cells were grown anaerobically with slow stirring overnight at 37 °C. The cells were harvested by continuous flow centrifugation at 4 °C when they had reached late log phase (OD_{600} = 1.1-1.2, ~ 17 h) and then kept on ice for immediate preparation of crude membranes. Typically the yield of cells (wet wt.) is 1.5 g per liter of culture.

Preparation of membranes. All subsequent steps are done at 4 °C. Crude membrane fractions enriched in *E. coli* inner membranes and fumarate reductase containing tubules were prepared as follows: 90 g of cells were resuspended by homogenization in 300-ml of buffer A (100 mM potassium phosphate, 0.1 mM EDTA, pH 6.8) and in the presence of small amounts of DNAse, RNAse, and six Complete

protease inhibitor tablets and then ruptured by two passages through a French pressure cell at 15,000 p.s.i. The cell lysate was centrifuged at 10,000 x g for 15 min. The supernatant was carefully removed and centrifuged for 1 hour at 120,000 x g. The pellets from this centrifugation were resuspended in 180-ml of buffer A containing 3 protease inhibitor tablets and centrifuged for 15 min at 10,000 x g to remove any remaining cellular debris. A final centrifugation for 1 h at 120,000 x g yielded a dark brown membrane fraction enriched for QFR. The membrane fraction contained about one gram of total protein and the QFR is approximately 30-50% pure. The membranes could be stored at –80 °C for use within one month.

Solubilization of QFR. The membranes described above were resuspended in 120 ml of buffer B (20 mM Tris-HCl, 0.1 mM EDTA, pH 7.4) with 3 Complete protease inhibitor tablets. Thesit was added from a 20% (w/v) stock to give a final concentration of 2% and 5-10 mg protein/ml. Fresh detergent stock was prepared for each enzyme preparation and used within 7-10 days. The membrane suspension was stirred briefly and then centrifuged at 100,000 x g for 30 min. The supernatant containing the solubilized QFR was filtered using a 0.2 μm nylon filter and kept at 4 °C for immediate chromatography.

FPLC Chromatography for purification of QFR. The dark brownish supernatant from the previous step was applied to a DEAE Sepharose FF column (3.6 x 30 cm, 300-ml bed volume) previously equilibrated with buffer C (20 mM Tris-HCl, 0.1 mM EDTA,

0.05% (w/v) Thesit, pH 7.4). The column was then washed with two bed volumes of buffer C followed by two bed volumes of the same buffer containing 0.1 M NaCl. The QFR complex was eluted with seven bed volumes of buffer C using a linear gradient from 0.1 – 0.25 M NaCl at a flow rate of 2 ml/min. The eluant peak containing QFR appears between 0.11 – 0.25 M NaCl as a broad peak; however, only the central fractions of these samples were pooled for subsequent steps. The salt background of the pooled samples was reduced by repeated exchange in an Amicon stirred cell with a YM30 membrane against buffer C to a final concentration of less than 50 mM NaCl, and concentrated for the next step. The pooled and concentrated fractions were further purified by perfusion chromatography using a POROS 50HQ column using a strategy identical to that described for the DEAE Sepharose FF column. The fractionation obtained during this step, although modest, is important since the protein obtained from the NaCl gradient contains the material that can be successfully crystallized. Minimal enzyme activity was recovered from material that remains bound to the column and eluted with high salt; such material contains QFR fragments or other denatured proteins (data not shown). The pooled fractions from the center of the peak from the POROS column are subsequently purified on a Sephacryl S-300 gel filtration column. Fractions containing excess detergent aggregates elute slightly earlier than the QFR containing fractions as confirmed by passing detergent alone through the column and analysis for the presence of detergent (data not shown). The dark brown QFR containing fraction was

pooled, concentrated, filtered by passage through 0.2 μm nylon filters and finally concentrated using sterile Centiprep-30 concentrators to a final concentration of 30-40 mg protein/ml.

Characterization of QFR. Protein determination was performed according to Markwell *et al.,* (25). The enzyme was judged to be >95% pure according to native PAGE and SDS-PAGE using both the methods of von Jagow/Schagger and Laemmli (26,27). The homogeneity of the QFR preparation was also checked by isoelectrofocusing. Protein was stained using coomassie blue R-250 and gels were permanently stained and fixed with 5% (w/v) acetic acid. Enzyme activity was measured as previously described (28). Endogenous lipids were measured by the method of Bartlett (29).

Fluorescence spectroscopy. Relative changes in the environment of the tryptophan residues of QFR were followed by monitoring variation in the maximum emission wavelength (λ_{max}) as previously described (30) using a Hitachi F-4010 fluorescence spectrophotometer. The excitation wavelength was 286 nm with a bandwidth of 5 nm for both excitation and emission slits. All measurements were done at a concentration of 50 μg protein/ml in 30 mM $NaHCO_3$, 45 mM NaCl, at pH 8.5. Various concentrations of detergent and guanidinium hydrochloride (GuHCl) were added to the enzyme and then incubated for 72 h at 4 °C prior to measurement of changes in

fluorescence. Similar results were seen if the samples were incubated briefly or overnight.

Crystallization of QFR. The initial search for suitable crystallization conditions of QFR was performed by vapor diffusion using the Hampton sparse matrix screening kit. A droplet of 5 µl protein and 5 µl reservoir solution were mixed and equilibrated against 0.8 ml of a reservoir solution. The final protein concentration was 30 mg/ml. Several screening solutions gave growth of crystals; however, the crystals that were optimized from starting conditions containing 12% (w/v) PEG 12K and 100 mM sodium citrate, pH 5.8 eventually displayed the highest resolution diffraction. Crystallization using PEG 12K was very reproducible. Nevertheless, a further screening of precipitant molecular weight was carried out. A screen of different detergent and divalent cation additives produced crystals with varying degrees of resolution. Consequently, hanging drop vapor-diffusion experiments were performed using 12-20% (w/v) PEG in the average molecular weight range of 4-20K. The crystallization conditions resulting in the best diffracting crystals were buffered using sodium citrate in the pH range of 5.8-6.2 and included 85 mM magnesium acetate, 0.1 mM EDTA and 60 µM dithiothreitol. Under these conditions, crystal growth can be observed overnight and mature within 3-10 days. For cryoprotection experiments crystals were soaked in the mother liquor solutions containing 30% (v/v) ethylene glycol.

RESULTS AND DISCUSSION

Production of recombinant QFR. Expression of the membrane-bound fumarate reductase has been amplified more than 30-fold over native levels of the enzyme utilizing a recombinant plasmid carrying the *frdA*$^+$*B*$^+$*C*$^+$*D*$^+$ operon as has been previously described (12,28). The enzyme can account for up to 60% of the total crude membrane protein fraction when cells are allowed to grow until late stationary phase (12). This very high level of overexpression has been shown to result in the formation of tubular structures branching from the cytoplasmic membrane that are composed of the four subunit QFR complex and phospholipid, primarily cardiolipin (31). A growth profile for *E. coli* cells overexpressing QFR (Fig. 2.1A) is shown with the hatched region indicating where cells can be harvested and the resulting isolated enzyme proving amenable to crystallization. Although intracellular lipid-protein tubules enriched in QFR are produced in late-log phase (Fig. 2.1B.1) their concentration is less than in stationary phase cells (Fig. 2.1B.2). SDS-PAGE and enzyme specific activity analyses of QFR produced from late stationary phase cells indicates that the enzyme has become partially degraded (Fig. 2.2). A specific proteolytic fragment of the flavoprotein (Fp) subunit can be identified of approximately 50 kDa. A smaller fragment of approximately 15 kDa contains covalently bound flavin. Analysis of the larger peptide showed that proteolytic cleavage occurs between a pair of arginine residues (residues 114 and 115) in the Fp sequence. The concentration of this proteolytic peptide increases the later in stationary phase the cells were harvested (Fig. 2.2). In order to minimize the *in vivo* proteolysis of

QFR it was necessary to harvest cells in log phase or as they approached stationary phase. This approach yielded enzyme with the highest specific activity (Table 2.1). A significant decrease in the microheterogeneity and proteolytic nicking of the enzyme was observed when the membranes were prepared from fresh rather than frozen cells harvested at late log phase. The observations are consistent with those of others showing that protein microheterogeneity can occur as a result of protein degradation during growth or purification (32). Figure 2.2 shows an SDS-PAGE profile of membranes prepared from late stationary phase (lane 2) and the late log phase membranes (lane 3) that proved best for enzyme that was amenable to crystallization (lane 7). The preparation of inner-membranes from late-log phase cells yielded a membrane fraction that contained 50-60% of its protein as QFR (Table 2.1, Fig. 2.2). Extraction of the enzyme from the membrane using the non-ionic detergent Thesit readily solubilizes the enzyme complex in a stable form as determined by enzyme activity measurements.

Purification and characterization of QFR. QFR from the Thesit extract was purified by a combination of ion exchange and gel filtration chromatography. The Thesit extraction is done using 2% (w/v) detergent, however, during elution of the enzyme from the DEAE Sepharose FF column the concentration of Thesit which results in the best resolution of QFR is 0.05% (Fig. 2.3A). The specific fumarate reductase/succino-oxidase activity of the QFR eluted from column both to the left and right of the arrows shown in Fig. 2.3A was very similar to the specific activity between the arrows, however,

only the protein fractions located between the arrows resulted in enzyme that was amenable to crystallization. On this basis it appears that specific enzyme activity is not a key criterion for discrimination of samples with the ability to crystallize. The material eluting between the arrows in Fig. 2.3A was then subjected to a second ion exchange step using perfusion chromatography media (POROS 50HQ). Fig. 2.3B shows that this perfusion chromatography step separates the enzyme into three major fractions with the major peak located between the arrows providing enzyme suitable for crystallization. The peak eluting at 1 M NaCl contains material that is less pure (observed by SDS-PAGE) and is rich in endogenous lipid (data not shown). Trials with other purification resins indicated that this step using the perfusion media was required in order to obtain enzyme that crystallizes. The QFR protein from the central peak in Fig. 2.3B was then concentrated and applied to a Sephacryl S-300 gel filtration column. The resultant elution profile (Fig. 2.3C) shows a major protein peak with shoulders on both sides. The material in the shoulders appears to be degraded enzyme based on SDS-PAGE. The central fraction, however, produces protein that is highly active (Fig. 2.4) and amenable to crystallization. Figure 2.4 also shows that the initial anion exchange chromatography step removes most of the endogenous lipids associated with the protein complex and they are apparently completely removed by the final gel filtration step. The data show that considerable amounts of phospholipids are present in the enzyme complex during the extraction process, however, they are removed during the subsequent purification

process. The enzyme activity of isolated QFR (Fig. 2.4) does not appear dependent upon the presence of phospholipids. It was also found that the purified enzyme would not crystallize if it contained significant amounts of the native lipids.

The purified QFR complex was found to be >95% pure based on densitometer analysis of SDS-PAGE, native gel electrophoresis and isoelectric focusing (data not shown). The purified enzyme shows a single band during native gel electrophoresis, which was found necessary for subsequent crystallization. The purified QFR complex following extensive dialysis, to remove excess detergent present following concentration of the protein, was found to have pI of 4.8.

The purified enzyme was evaluated as to its stability by determining effects of various detergents and the chaotrope guanidinium hydrochloride on enzyme activity and conformation of the enzyme based on tryptophan fluorescence. As shown in Fig. 2.5 the purified QFR complex is much more stable in guanidinium hydrochloride than is the soluble domain (FrdAB) (28 and manuscript in preparation) of fumarate reductase. The FrdCD hydrophobic peptides stabilize the QFR complex and appear to protect the [3Fe-4S] cluster from the oxidative denaturation of the enzyme that occurs when this iron-sulfur cluster is destroyed (1,12,28). The slow unfolding of QFR is indicative of irreversible non-cooperative denaturation due to strong hydrophobic interactions in the complex (33). Table 2.2 shows the change in tryptophan fluorescence maximum wavelength (λ_{max}) (30) of QFR as a function of different detergents. Moderate unfolding

of the complex is observed using 0.05% Thesit as is the case for the majority of other detergents. As shown in Table2.2, the specific activity of QFR is enhanced by the presence of Thesit in the assay mixture. By contrast the detergents, octylglucoside, CHAPS, and sodium cholate all inhibited enzyme activity to varying extents while 0.2% (w/v) SDS inactivated the enzyme almost completely. Similar effects on protein conformation and enzyme activity have been shown for membrane-bound proteins in the presence of detergents or chaotropes (34,35).

Crystallization of QFR. Crystallization trials using standard screens in vapor-diffusion experiments yielded a number of conditions producing QFR crystals. As shown in Fig. 2.6, the crystals were dark brown, birefringent, and assumed a uniform shape with distinct edges and vertices. For all protein preparations, crystals grown in 100 mM sodium citrate, pH 5.8, 85 mM magnesium acetate, 0.1 mM EDTA, and 60 μM dithiothreitol provided the highest resolution diffraction. In contrast, the molecular weight of the polyethylene glycol that grew the best diffracting crystals varied from preparation to preparation. A concentration of 30 mg protein/ml in the final droplet was also required for optimal crystal growth. SDS-PAGE analysis of serially washed crystals showed four distinct bands of the correct molecular size representative of the FrdABCD subunits. Crystal growth was apparent within 24 hours and crystals 24-72 hours old gave the best diffraction. Crystals used for the initial structure determination were obtained

from crystals grown from 10K PEG with ethylene glycol as cryoprotectant and immediate cryo-cooling in liquid nitrogen. The QFR structure has been solved to 3.3 Å using these crystals with the space group symmetry $P2_12_12_1$ with a=96.6 Å, b=138.1 Å, and c=275.3 Å (21). The presence of Thesit in concentrations of 140-fold above its cmc does not prevent growth of crystals as has been shown for other proteins (36). The concentration of micelles in the solvent was about 0.6 per protein molecule (mol/mol) with no excess of "empty" micelles (37) that might otherwise inhibit the growth of crystals. At least one molecule of Thesit is found per QFR monomer from the structure of the protein complex (21). The refined structure suggests that the FrdAB soluble domain constitute the largest part of the structure as compared to the detergent coated hydrophobic (FrdCD) domain (21). The QFR complex essentially may behave as a soluble protein with the colloidal state becoming crucial when upon assembly of the crystal lattice the detergent coats come into close contact (38). This arrangement is atypical of either type I or type II crystals (39,40). Unlike prostaglandin H synthase (41), where the relative protein mass located on the cytoplasmic side of the membrane is 90% and in bacteriorhodopsin is as low as 10%; in QFR 75% of the complex is a rather extensive globular domain projecting from the membrane to make the necessary interlayer interactions in the crystal lattice.

The technique described above for optimizing preparations of highly pure QFR and its crystallization has been highly reproducible. Although variation of crystallization conditions yielded various crystal shapes, the space group remained the same. The isolated and crystallized enzyme show the same subunit stoichiometry and contains all types of redox cofactors known to be present in *E. coli* QFR (1-3) including two molecules of menaquinone. The general procedures described above may be applicable to the isolation and crystallization of other membrane-bound QFR's and SQR's.

ACKNOWLEDGMENTS

This work was supported by the Department of Veterans Affairs, and grants from the NIH (HL-16251 and GM45162), the NSF (MCB-9728778), and the Howard Hughes Medical Institute. T.M.I. is supported by an NIH training grant. C.L.C. would like to acknowledge the support and continuing mentorship of Professor Alex V. Nichols and his helpful discussions and suggestions and Dr. Ciarán N. Cronin for useful discussions.

Figure 2.1: *Optimization of bacterial growth.* **A.** *E. coli* strain DW35 transformed with the QFR encoding plasmid pH3 was grown anaerobically as described in Materials and Methods. The hatched regions between points II and III produced cells containing QFR that were amenable to crystallization. Growth of cells beyond point III although producing even greater quantities of QFR results in enzyme that does not crystallize. **B.** Thin section electron micrographs of longitudinal cross sections of *E. coli* DW35 transformed with pH3 grown to (B1) late log phase and (B2) late stationary phase. The tubules produced in the cell are composed almost entirely of QFR and cardiolipin as shown in Refs.12 and 31.

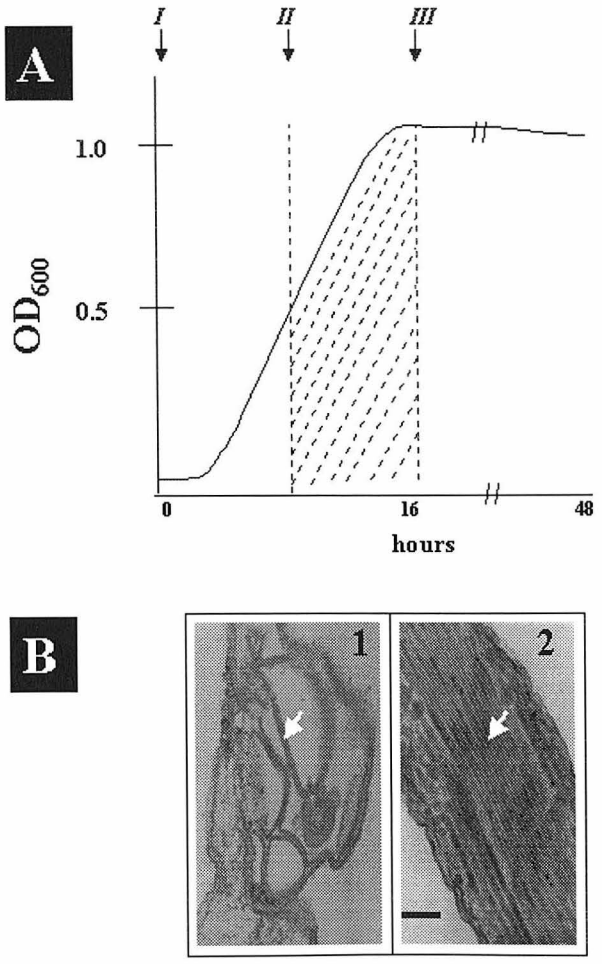

Figure 2.2: *SDS-PAGE analysis of E. coli QFR enriched membranes and purified protein.* SDS-PAGE were performed with 10-20% polyacrylamide gels and stained with Coomassie brilliant blue. The amount of protein loaded ranged from 25 to 30 µg for lanes 2 and 3 and 10 to 15 µg for lanes 4-7. Lane 1, molecular markers; lane 2, membrane preparations from late stationary phase; lane 3, membranes from late log phase; lane 4, Thesit extract; lane 5, DEAE Sepharose FF fraction; lane 6, POROS 50HQ chromatography fraction; lane 7, purified QFR from Sephacryl S-300 column.

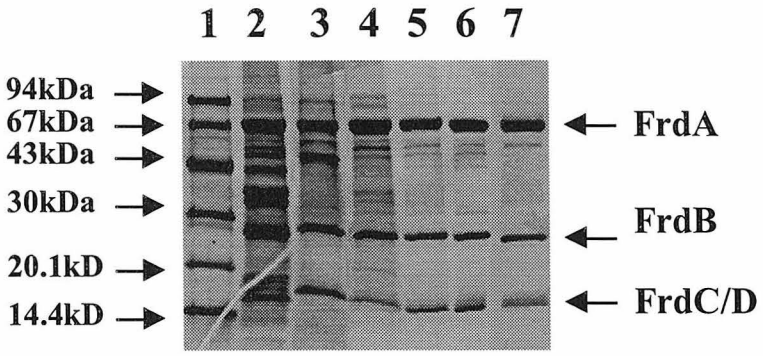

Figure 2.3: *Chromatograms of Thesit solubilized QFR.* **A.** DEAE Sepharose FF chromatography showing effect of different concentrations of Thesit used in elution buffer. Equivalent amounts of protein were loaded and elution carried out at 4 °C with 0% (dashed line, ---), 0.05% (solid line, _), and 0.8% (dotted line, ...), (w/v) Thesit included in the elution buffer. The gradient of 100-250 mM NaCl is indicated by the hatched line. The QFR elutes at approximately 125-175 mM NaCl. The solid arrows in all chromatograms (⬇) indicate the beginning and end points of the fractions of QFR that were isolated and pooled for subsequent steps. **B.** Perfusion chromatography with POROS 50HQ ion exchange of the isolated QFR from the previous step. Conditions as described in Materials and Methods. **C.** Sephacryl S-300 gel filtration chromatography of QFR from step B. The area between the arrows indicates QFR that is amenable to crystallization.

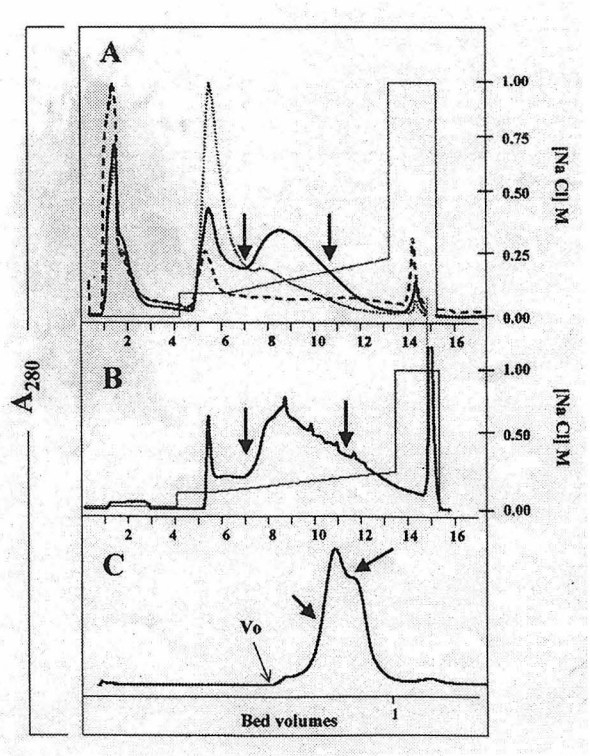

Figure 2.4: *Phospholipid concentration and QFR activity during purification.* CM refers to membrane fraction; TE, Thesit extract; and DEAE, POROS, and Sephacryl, refer to the respective chromatography steps. The open rectangles (□) indicate enzyme activity and the solid diamonds (◆) indicate the percent of the original fraction of lipids remaining. The lipid concentration and enzyme activity measurements were as described in Methods.

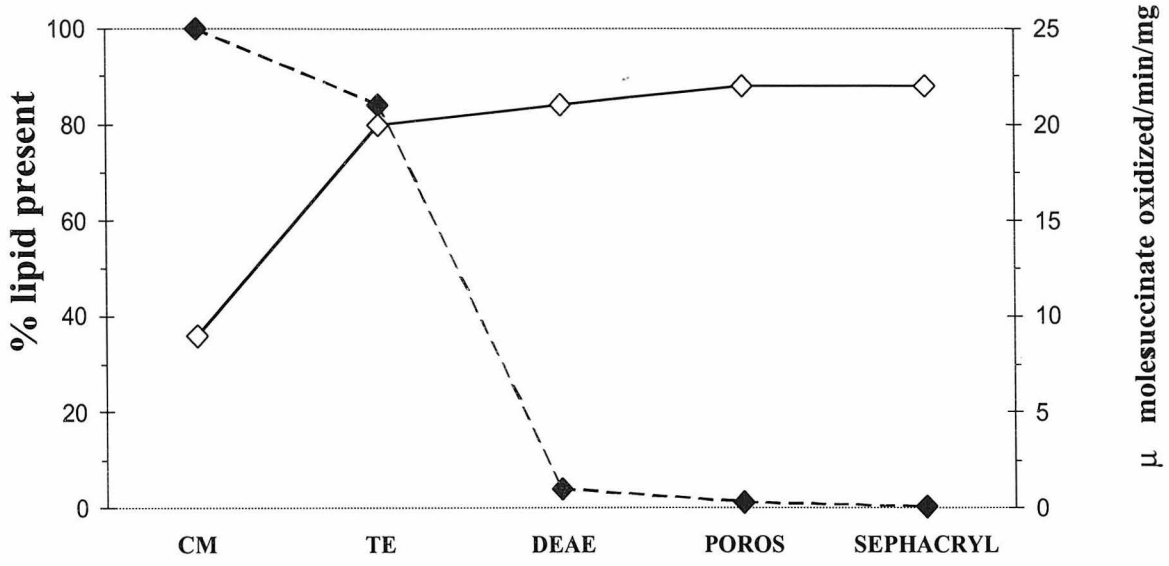

Figure 2.5: *Effect of guanidinium hydrochloride (GuHCl) on tryptophan fluorescence maximum emission wavelength (λ_{max})* (30). Soluble fumarate reductase (FrdAB subunits) (28) is shown by the solid circle (•). QFR is indicated by the open circle (o). The concentration used during analysis was 50 μg protein/ml in both cases. The final GuHCl concentration in the samples was obtained by addition of 8 M GuHCl. Samples were incubated for 72 h at 4 °C prior to fluorescence measurement. Excitation wavelength was 286 nm.

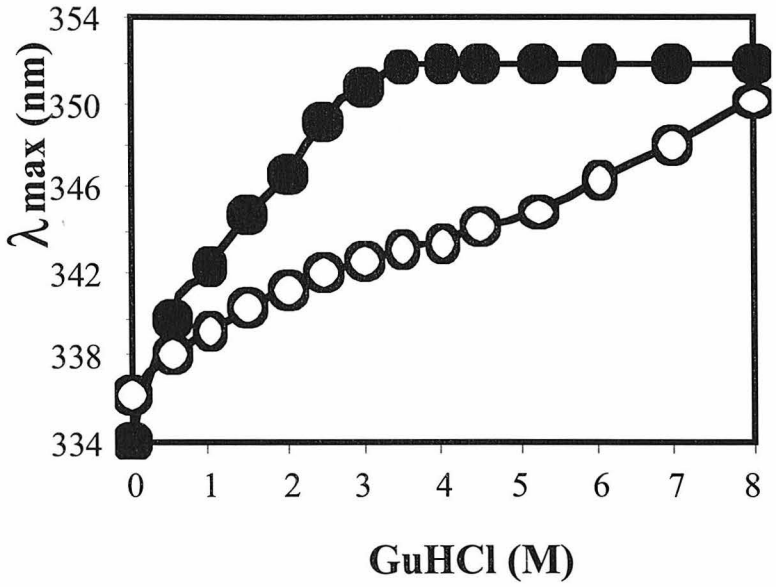

Figure 2.6: *Crystals obtained from purified QFR*. Protein concentration was 30 mg/ml. Crystals were grown for 48 h in 100 mM sodium citrate, pH 5.8, 85 mM magnesium acetate, 0.1 mM EDTA, and 60 μM dithiothreitol with 10 kDa polyethylene glycol as the precipitating agent.

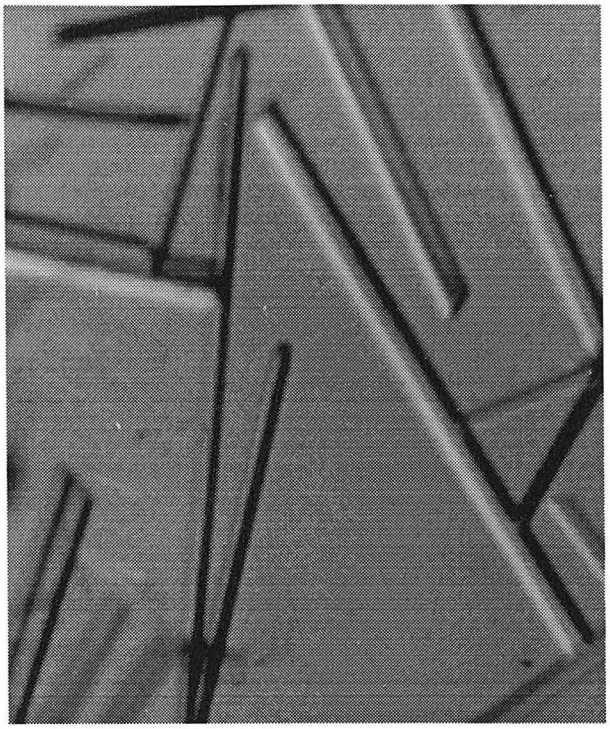

Table 2.1

Purification of QFR Complex from *Escherichia coli*[a]

	Total Protein (mg)	Total Activity[b] µmol/min	Specific Activity µmol/min/mg	Fold[c] purific.	% yield
Membranes	742	4,600	9	2-3	100
Thesit extract	384	2,600	20	4.4	56
DEAE Seph FF	129	2,300	21	4.7	49
POROS 50HQ	112	2,300	22	4.9	49
Sephacryl S-300	20	220	22	4.9	5

[a] 90 g wet weight of anaerobically grown *E. coli* DW35 containing plasmid pH3.

[b] Enzyme activity was determined by following the succinate:phenazine ethosulfate (PES) reaction in the presence of dicholorphenolindophenol (DCIP) (ε^{600}= 21.8 mM^{-1} cm^{-1}) using 1.5 mM PES and 50 µM DCIP at 37 °C as previously described (28).

[c] Washing of membranes to remove light brownish material prior to extraction improves the initial yield of QFR some 2-3 fold, thus the initial purification is greater than 1-fold.

Table 2.2

Effect of detergents[a] on enzyme activity and fluorescence emission.

Detergent Type	% ($\Delta\lambda_{max}$)[b]	Specific Activity[c]	cmc (mM)[d]	Micellar M_r[e]
None[f]	0	25±3	---	---
0.05% Thesit	14	33±2	0.1	~64,000
0.1% Triton X-100	n.d.	22±1	0.3	~90,000
0.09% Dodecylmaltoside	4	27±1	0.2	~50,000
0.8% Octylglucoside	13	4±1	15	8,800-29,200
0.5% CHAPS	16	9±2	4-6	~6,200
0.6% Sodium cholate	16	13±2	3-10	800-2,000
0.2% SDS	20	0.2±0.1	8.1	17,000-28,800

[a] The concentration of detergent used was 3-10 fold above their corresponding cmc.

[b] Relative change of λ_{max} at 286 nm of a 50 μg/ml sample, calculated as % change to QFR in the absence of detergent. Detergent was incubated with sample for 72 h at 4 °C.

[c] Specific activity determined as in Table 2.1.

[d] The data for cmc are taken from tables reported by Roche Molecular Biochemicals.

[e] The average micellar molecular weights are as reported by Roche Molecular Biochemicals.

[f] Although QFR is purified in the presence of Thesit no additional detergent was added to sample prior to measurement.

n.d. = not determined

REFERENCES

1. Ackrell, B.A.C., Johnson, M.K., Gunsalus, R.P., and Cecchini, G. (1992) Structure and function of succinate dehydrogenase and fumarate reductase *in* "Chemistry and Biochemistry of Flavoenzymes" (Müller, F., Ed.), pp. 229-297, CRC Press, Inc., Boca Raton.

2. Hägerhäll, C. (1997) Succinate:quinone oxidoreductases; variations on a conserved theme. *Biochim. Biophys. Acta* **1320,** 107-141.

3. Hägerhäll, C., and Hederstedt, L. (1996) A structural model for the membrane-integral domain of succinate:quinone oxidoreductases. *FEBS Lett.* **389,** 25-31.

4. Ruzicka, F.J., Beinert, H., Schepler, K.L., Dunham, W.R., and Sands, R.H. (1975) Interaction of ubisemiquinone with a paramagnetic component in heart tissue. *Proc. Natl. Acad. Sci. USA* **72,** 2886-2890.

5. Yu, C.-A., and Yu, L. (1982) Specific interaction between protein and ubiquinone in succinate-ubiquinone reductase. *J. Biol. Chem.* **257,** 6127-6131.

6. Yang, X., Yu, L., He, D., and Yu, C.-A. (1998) The quinone-binding site in succinate-ubiquinone reductase from *Escherichia coli*. *J. Biol. Chem.* **273,** 31916-31923.

7. Westenberg, D.J., Gunsalus, R.P., Ackrell, B.A.C., Sices, H., and Cecchini, G. (1993) *Escherichia coli* fumarate reductase *frdC* and *frdD* mutants. *J. Biol. Chem.* **268,** 815-822.

8. Yankovskaya, V., Sablin, S.O., Ramsay, R.R., Singer, T.P., Ackrell, B.A.C., Cecchini, G., and Miyoshi, H. (1996) Inhibitor probes of the quinone binding sites of mammalian complex II and *Escherichia coli* fumarate reductase. *J. Biol. Chem.* **271,** 21020-21024.

9. Ziegler, D.M., and Doeg, K.A. (1959) Studies on the electron transport system: XLIII. The isolation of a succinate-coenzyme Q reductase from beef heart mitochondria. *Biochem. Biophys. Res. Commun.* **1,** 344-349.

10. Unden, G., Hackenberg, H., and Kröger, A. (1980) Isolation and functional aspects of the fumarate reductase involved in the phosphorylative electron transport of *Vibrio succinogenes*. *Biochim. Biophys. Acta* **591,** 275-288.

11. Singer, T.P., and Johnson, M.K. (1985) The prosthetic groups of succinate dehydrogenase: 30 years from discovery to identification. *FEBS Lett.* **190,** 189-198.

12. Lemire, B.D., and Weiner, J.H. (1986) Fumarate reductase of *Escherichia coli*. *Methods Enzymol.* **126,** 377-386.

13. Kita, K., Vibat, C.R., Meinhardt, S., Guest, J.R., and Gennis, R.B. (1989) One-step purification from *Escherichia coli* of complex II (succinate:ubiquinone

oxidoreductase) associated with succinate-reducible cytochrome b_{556}. *J. Biol. Chem.* **264,** 2672-2677.

14. Iwata, S., Ostermeier, C., Ludwig, B., and Michel, H. (1995) Structure at 2.8 Å resolution of cytochrome *c* oxidase from *Paracoccus denitrificans*. *Nature* **376,** 660-669.

15. Tsukihara, T., Aoyama, H., Yamashita, E., Tomizaki, T., Yamaguchi, H., Shinzawa-Itoh, K., Nakashima, R., Yaono, R., and Yoshikawa, S. (1996) The whole structure of the 13-subunit oxidized cytochrome *c* oxidase at 2.8 Å. *Science* **272,** 1136-1144.

16. Yoshikawa, S., Shinzawa-Itoh, K., Nakashima, R., Yaono, R., Yamashita, E., Inoue, N., Yao, M., Fei, M.J., Libeu, C.P., Mizushima, T., Yamaguchi, H., Tomizaki, T., and Tsukihara, T. (1998) Redox-coupled crystal structural changes in bovine heart cytochrome *c* oxidase. *Science* **280,** 1723-1729.

17. Xia, D., Yu, C.-A., Kim, H., Xia, J.Z., Kachurin, A.M., Zhang, L., Yu, L., and Deisenhofer, J. (1997) Crystal structure of the cytochrome bc_1 complex from bovine heart mitochondria. *Science* **277,** 60-66.

18. Zhang, Z., Huang, L., Shulmeister, V.M., Chi, Y.I., Kim, K.K., Hung, L.W., Crofts, A.R., Berry, E.A., and Kim, S.H. (1998) Electron transfer by domain movement in cytochrome bc_1. *Nature* **392,** 677-684.

19. Iwata, S., Lee, J.W., Okada, K., Lee, J.K., Iwata, M., Rasmussen, B., Link, T.A., Ramaswamy, S., and Jap, B.K. (1998) Complete structure of the 11-subunit bovine mitochondrial cytochrome bc_1 complex. *Science* **281,** 64-71.

20. Stowell, M.H. and Rees, D.C. (1995) Structure and stability of membrane proteins. *Adv. Protein Chem.* **46,** 279-311.

21. Iverson, T.M., Luna-Chavez, C., Cecchini, G., and Rees, D.C. (1999) Structure of the *Escherichia coli* fumarate reductase respiratory complex. *Science* **284,** 1961-1966.

22. Lancaster, C.R.D., Kröger, A., Auer, M., and Michel, H. (1999) Structure of fumarate reductase from *Wolinella succinogenes* at 2.2 Å resolution. *Nature* **402,** 377-385.

23. Blaut, M., Whittaker, K., Valdovinos, A., Ackrell, B.A.C., Gunsalus, R.P., and Cecchini, G. (1989) Fumarate reductase mutants of *Escherichia coli* that lack covalently bound flavin. *J. Biol. Chem.* **264,** 13599-13604.

24. Spencer, M.E., and Guest, J.R. (1973) Isolation and properties of fumarate reductase mutants of *Escherichia coli*. *J. Bacteriol.* **114,** 563-570.

25. Markwell, M.A., Haas, S.M., Bieber, L.L., and Tolbert, N.E. (1978) A modification of the Lowry procedure to simplify protein determination in membrane and lipoprotein samples. *Anal. Biochem.* **87,** 206-210.

26. von Jagow, G., and Schagger, H. (1994) *in* "A practical guide to membrane protein purification." Academic Press, San Diego, CA.

27. Laemmli, U.K. (1970) Cleavage of structural proteins during the assembly of the head of bacteriophage T4. *Nature* **227,** 680-685.

28. Cecchini, G., Ackrell, B.A.C., Deshler, J.O., and Gunsalus, R.P. (1986) Reconstitution of quinone reduction and characterization of *Escherichia coli* fumarate reductase activity. *J. Biol. Chem.* **261,** 1808-1814.

29. Bartlett, G.F. (1959) Phosphorus assay in column chromatography. *J. Biol. Chem.* **234,** 466-468.

30. Luna-Chavez, C., Gong, E.L., Forte, T.M., and Nichols, A.V. (1994) Sodium oleate-facilitated reassembly of apolipoprotein A-I with phosphatidylcholine. *Biochim. Biophys. Acta* **1215,** 141-149.

31. Weiner, J.H., Lemire, B.D., Elmes, M.L., Bradley, R.D., and Scraba, D.G. (1984) Overproduction of fumarate reductase in *Escherichia coli* induces a novel intracellular lipid-protein organelle. *J. Bacteriol.* **158,** 590-596.

32. Park, J.-I., Grant, C.M., Davies, M.J., and Dawes, I.W. (1998) The cytoplasmic Cu,Zn superoxide dismutase of *Saccharomyces cerevisiae* is required for resistance to freeze-thaw stress. *J. Biol. Chem.* **273,** 22921-22928.

33. Yeates, T. (1993) *in* "Thermodynamics of Membrane Receptors and Channels" (Jackson, M.D., Ed.), pp. 1-25, CRC Press, Inc., Boca Raton.

34. Yun, C.-H., Song, M., and Kim, H. (1997) Conformational change of cytochrome P450 1A2 induced by phospholipids and detergents. *J. Biol. Chem.* **272,** 19725-19730.

35. Ushakova, A.V., Grivennikova, V.G., Ohnishi, T., and Vinogradov, A.D. (1999) Triton X-100 as a specific inhibitor of the mammalian NADH-ubiquinone oxidoreductases (complex I). *Biochim. Biophys. Acta* **1409,** 143-153.

36. Garavito, R.M., Picot, D., and Loll, P.J. (1996) Strategies for crystallizing membrane proteins. *J. Bioenerget. Biomemb.* **28,** 13-27.

37. Song, L., and Gouaux, J.E. (1997) Membrane protein crystallization: Application of sparse matrices to the α-hemolysin heptamer. *Methods Enzymol.* **276,** 60-74.

38. Zulauf, M. (1990) *in* "Crystallization of membrane proteins" (Michel, H., ed.), pp. 53-72, CRC Press, Boca Raton.

39. Michel, H. (1983) Crystallization of membrane proteins. *Trends Biochem. Sci.* **8,** 56-59.

40. Ostermeier, C., and Michel, H. (1997) Crystallization of membrane proteins. *Curr. Op. Str. Biol.* **7,** 697-701.

41. Picot, D., Loll, P.J., and Garavito, R.M. (1994) The x-ray crystal structure of the membrane protein prostaglandin H2 synthase-1. *Nature* **367,** 243-249.

Chapter 3

Reprinted with permission from:

Iverson, T.M., Luna-Chavez, C., Cecchini, G., Rees, D.C. (1999) Structure of the *Escherichia coli* Fumarate Reductase Respiratory Complex, *Science* **284**: 1961-1966.

Copyright 1999, American Association for the Advancement of Science

Structure of the *Escherichia coli* Fumarate Reductase Respiratory Complex

Tina M. Iverson,[1] César Luna-Chavez,[2] Gary Cecchini,[2]* Douglas C. Rees[3]*

The integral membrane protein fumarate reductase catalyzes the final step of anaerobic respiration when fumarate is the terminal electron acceptor. The homologous enzyme succinate dehydrogenase also plays a prominent role in cellular energetics as a member of the Krebs cycle and as complex II of the aerobic respiratory chain. Fumarate reductase consists of four subunits that contain a covalently linked flavin adenine dinucleotide, three different iron-sulfur clusters, and at least two quinones. The crystal structure of intact fumarate reductase has been solved at 3.3 angstrom resolution and demonstrates that the cofactors are arranged in a nearly linear manner from the membrane-bound quinone to the active site flavin. Although fumarate reductase is not associated with any proton-pumping function, the two quinones are positioned on opposite sides of the membrane in an arrangement similar to that of the Q-cycle organization observed for cytochrome bc_1.

Because oxygen has a high affinity for electrons, aerobic respiration represents a very favorable form of energy metabolism. However, in the absence of oxygen, many microorganisms can obtain energy through anaerobic respiratory processes that result in the reduction of alternate terminal acceptors (*1*). One of the most widespread acceptors is fumarate (*2*), which is reduced to succinate by fumarate reductase, an integral membrane protein containing flavin adenine dinucleotide (FAD) and iron-sulfur clusters (*3*). The electron donor for this reaction is reduced menaquinone, which commonly serves as a membrane-soluble, mobile electron carrier between respiratory complexes. The most extensively characterized fumarate reductase, from *Escherichia coli*, has a total molecular mass of 121 kD in four subunits. It consists of two water-soluble subunits, the flavoprotein (66 kD) and iron-sulfur protein (27 kD) subunits, and two membrane anchor subunits (15 and 13 kD), which are the products of the *frdABCD* genes, respectively (*4*). The flavoprotein (Fp) subunit contains the catalytic site for fumarate reduction and succinate oxidation at a covalently linked FAD (*5*), while the iron-sulfur protein subunit (Ip) contains three different types of iron-sulfur clusters, [2Fe:2S], [4Fe:4S], and [3Fe:4S], which have been spectroscopically characterized (*6*). At least two sites associated with the membrane anchor subunits have been proposed to bind the quinones that are involved in electron transfer reactions of the enzyme (*7*).

Fumarate reductase catalyzes the reverse reaction of succinate dehydrogenase, which participates in both the aerobic respiratory chain as complex II and in the Krebs cycle (*3*). These two proteins exhibit substantial similarities in amino acid sequence, cofactor composition, and mechanism. Indeed, under certain conditions, one enzyme can functionally replace the other and support bacterial growth (*8*). Because of the central role of fumarate reductase and succinate dehydrogenase in respiration, mutations in these complexes can have substantial metabolic consequences. In bacteria, mutations in fumarate reductase can significantly retard growth under appropriate conditions (*9*). In higher organisms, mutations of succinate dehydrogenase have been linked to oxidative stress and aging in nematodes (*10*) and to Leigh's syndrome in humans (*11*). Historically, succinate dehydrogenase was one of the most widely studied enzymes during the development of enzymology. Early studies resulted in the discoveries of nonheme iron and covalently bound flavin in proteins (*12*). To provide a framework for addressing the functional properties of fumarate reductase and succinate dehydrogenase, we have solved the structure of the *E. coli* fumarate reductase at 3.3 Å resolution. Here we describe the fold of the polypeptides and location of the cofactors, and the functional implications of this structural arrangement.

[1]Graduate Option in Biochemistry, 147-75CH, California Institute of Technology, Pasadena, CA 91125, USA. [2]Molecular Biology Division, Department of Veterans Affairs Medical Center, San Francisco, CA 94121, and Department of Biochemistry and Biophysics, University of California, San Francisco, CA 94143, USA. [3]Howard Hughes Medical Institute, Division of Chemistry and Chemical Engineering, 147-75CH, California Institute of Technology, Pasadena, CA 91125, USA.

*To whom correspondence should be addressed. E-mail: ceccini@itsa.ucsf.edu; dcrees@caltech.edu

Structure Determination and Overall Fold

Fumarate reductase from *E. coli* was purified and crystallized in the presence of the non-ionic detergent Thesit (*13*). The structure was solved by multiple wavelength anomalous diffraction (MAD), with data collected at three wavelengths near the Fe K edge (*14*) (Table 1). The iron-sulfur clusters and transmembrane helices were striking in the initial maps calculated at 4 Å resolution, and the structure was solved by iterative combination of density modification, noncrystallographic symmetry averaging, model building, and refinement (*15*). The final model has been refined to values of R_{cryst} of 22.2% and R_{free} of 29.2% at 3.3 Å resolution with reasonable stereochemistry (*15, 16*).

The four subunits in fumarate reductase are arranged in a complex resembling the letter "q," with the top of the "q" generated by the Fp and Ip subunits (diameter ~70 Å), while the tail of the "q" (length 110 Å) contains the membrane anchor subunits (Fig. 1, A and B). The orientation of fumarate reductase in the cell membrane is such that the Fp and Ip subunits are located in the cytoplasm (equivalent to the mitochrondrial matrix for succinate dehydrogenase). In these crystals, two fumarate reductase complexes, which are related by a twofold axis approximately parallel to the membrane normal, are present per asymmetric unit. These two complexes associate through their transmembrane regions. Contacts with neighboring molecules related by crystallographic symmetry also occur in the membrane-spanning region, creating a continuous membrane-spanning region throughout the crystal (Fig. 1C). Despite the suggestiveness of this arrangement, there is no evidence that a dimer is physiologically relevant, unlike the situation with cytochrome bc_1 (*17*). Additionally, the contact region between fumarate reductase molecules in the crystals is relatively small (~325 Å^2) (*18*) and is unlikely to support formation of a stable dimer (Fig. 1B).

The Fp (FrdA) subunit is organized around an FAD/NAD(P) (nicotinamide adenine dinucleotide phosphate) binding domain formed by residues A1 to A50, A130 to A231, and A354 to A414 (Fig. 2A). This domain structure includes a Rossmann-type fold that provides the binding site for FAD. The FAD is further associated with the flavoprotein through a covalent bond between the flavin C8A methyl group and the Nε atom of the side chain of His A44. The remaining residues of this subunit, A51 to A129, A232 to A353, and A415 to A575, are inserted into

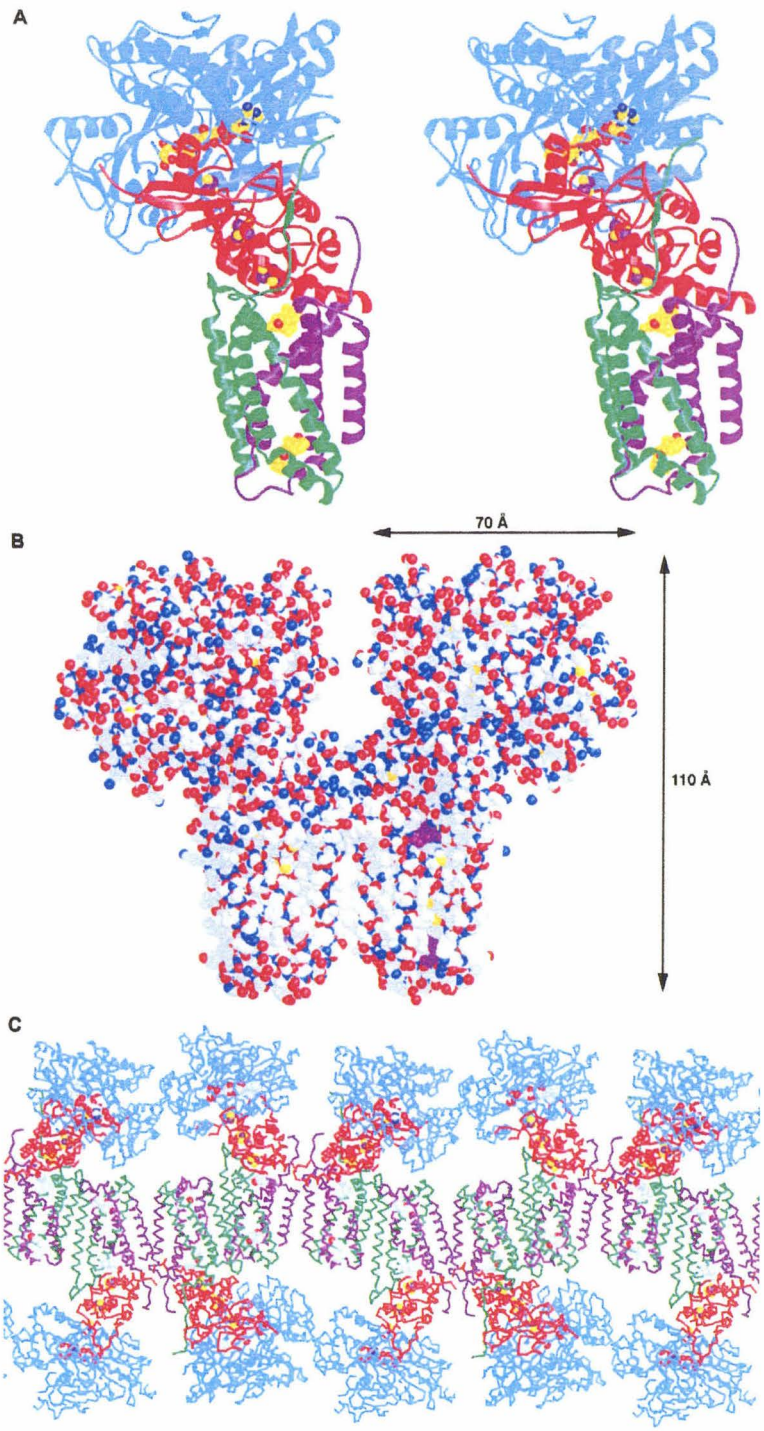

Fig. 1. Structure of fumarate reductase. (**A**) Stereoview of a fumarate reductase monomer. The flavoprotein is in blue, the iron protein is in red, and the membrane anchors are in green (FrdC) and purple (FrdD). The [Fe:S] clusters are shown as purple (Fe atoms) and yellow (S atoms), while the menaquinones and FAD are shown in yellow. (**B**) Space-filling model of fumarate reductase showing the crystal contacts between the two complexes in the membrane-spanning portion. In the fumarate reductase complex, oxygen atoms are shown in red, nitrogen atoms are shown in blue, sulfur atoms are shown in yellow. Menaquinone molecules are shown in magenta (see right-hand monomer). The location of the membrane-spanning region can be inferred from the coloring of the atoms in this representation. The more hydrophilic (soluble) region contains many polar oxygen and nitrogen atoms (red and blue) while the hydrophobic (membrane-spanning) region contain mostly apolar carbon atoms (gray). (**C**) Crystal packing of fumarate reductase is through the transmembrane regions of the protein (green and purple) and forms a continuous membrane-spanning portion in the crystal (*36*). In this representation, the FAD and menaquinone are shown in gray (*37*).

the core FAD binding domain and adopt compact folds that do not exhibit significant structural similarities to known folds in the Protein Data Bank, as assessed by the DALI server (*19*).

Fumarate reductase contains three iron-sulfur clusters that are coordinated by cysteine residues in the Ip (FrdB) subunit as follows: [2Fe:2S] (Cys residues B57, B62, B65, and B77); [4Fe:4S] (Cys B148, B151, B154, and B214); and [3Fe:4S] (Cys B158, B204, and B210). Consistent with the conclusions of sequence and electron paramagnetic resonance (EPR) analyses (*3*, *6*), the Ip subunit is organized into two domains (Fig. 2B), one characteristic of [2Fe:2S]-containing ferredoxins (residues B1 to B91) and the other characteristic of bacterial ferredoxins that contain [3Fe:4S] or [4Fe:4S] type clusters (residues B145 to B221). The [2Fe:2S] domain superimposes closely with plant-type ferredoxins, while more substantial changes have occurred in the bacterial ferredoxin domain. Although bacterial ferredoxins containing both a [3Fe:4S] and a [4Fe:4S] cluster are relatively common, the cysteine ligands for the [3Fe:4S] cluster always appear first in the protein sequence. As anticipated from sequence analyses, the cluster arrangement in fumarate reductase is reversed relative to these ferredoxins. In addition, the four-stranded antiparallel β sheet found on one side of the clusters in ferredoxins has been replaced by a helical hairpin in fumarate reductase.

The two membrane anchor subunits, FrdC and FrdD, exhibit similar folds, each with three transmembrane helices connected by extra-membrane loops (Fig. 2C). These helices, designated I to VI (*3*), consist of residues C22 to C49, which is actually composed of two kinked, helical segments, C66 to C90, C105 to C128, D9 to D35, D61 to D89, and D97 to D115, and are in reasonable agreement with transmembrane segments predicted by hydropathy analysis and mutagenesis (*20*). Helices I, II, IV, and V are tilted ~30° to 40° from the membrane normal, as defined by the dimer twofold axis, and are arranged in a right-handed, helical bundle, with helix crossing angles of ~120°. In contrast, helices III and VI are more parallel to the membrane normal with a tilt of ~10° to 25°. The NH_2- and COOH-termini are on opposite sides of the membrane-spanning region, which correspond to the cytoplasm and periplasm, respectively. The overall arrangement is such that the two subunits could be covalently connected upon deletion of helix III, consistent with the observation that homologous enzymes have been identified that contain only a single transmembrane domain with five membrane-spanning helices (*20*).

Two menaquinone molecules, which are located on opposite sides of the membrane-spanning region, are present in this fumarate reductase structure. The menaquinone (Q_P) positioned proximal to the [3Fe:4S] cluster of the Ip subunit binds in a relatively polar pocket formed by helices I, II, IV, and V, while the second menaquinone (Q_D) distal to this cluster, is positioned ~27 Å from the first and binds in a relatively hydrophobic pocket near the other ends of helices I, II, IV, and V. Site-directed mutagenesis and labeling with azido-quinones have implicated residues in both these regions as involved in quinone binding in both fumarate reductase and succinate dehydrogenase (*9*, *21*). Although evidence suggests that complex II contains a stabilized semiquinone pair in close proximity to the [3Fe-4S] cluster with the quinone rings perpendicular to the membrane plane (*7*, *22*), only single quinone molecules were identified at the spatially distinct Q_P and Q_D sites in the fumarate reductase structure. In the absence of a conformational rearrangement of the protein in the Q_P region, it does not appear that this site can accommodate more than one quinone molecule.

Redox Centers and Electron Transfer Pathway

The six redox cofactors of fumarate reductase are organized into a chain with the sequence FAD-[2Fe:2S]-[4Fe:4S]-[3Fe:4S]-Q_P-Q_D (Fig. 3). With the exception of the ~27 Å spacing between the two menaquinones, the redox cofactors are all separated by ~11 to 14 Å center-to-center distances, which are common cofactor separation distances observed in multicentered electron transfer proteins. In its physiologically relevant reaction, electrons enter fumarate reductase in the form of reduced menaquinone, although the enzyme will physiologically reduce ubiquinone at rates similar to native succinate dehydrogenase (*8*). Examination of a space-filling model of fumarate reductase indicates that both quinone binding sites are exposed and should be accessible to the exterior of the complex (Fig. 1B). Electron transfer to the iron-sulfur cluster almost certainly would occur from the Q_P site, which is adjacent to the [3Fe:4S] cluster. Although Q_P primarily interacts with residues from both membrane anchor subunits, it has limited contact with Ip through Lys B238. The polar environment of the Q_P (Fig. 4A) site resembles the Q_B site of bacterial photosynthetic reaction centers (*23*), which can accommodate all three quinone oxidation states (reduced, oxidized, and semiquinone). The Q_D site has an apolar character (Fig. 4B) that resembles the Q_A site of photosynthetic reaction centers, which can accommodate only the oxidized and semiquinone states. Indeed, residues in the Q_P and Q_D binding pockets had been identified with Q_B and Q_A, respectively, based on the consequences of residue substitution (*7*). However, the assignments of quinone oxidation states to specific binding sites during enzyme turnover cannot be unambiguously established at present.

During fumarate reduction, electrons from reduced quinone are transferred to the iron-sulfur clusters. Both the oxygen sensitivity upon removal of the membrane anchor subunits and perturbation of the EPR spectrum of the [3Fe:4S] cluster by quinone site inhibitors and mutants suggest that the [3Fe:4S] cluster interacts with the quinone binding subunits to initially accept electrons from the menaquinone (*9*, *24*). Spectroscopic studies have indicated that the [2Fe:2S] cluster is in close proximity to the FAD (*25*), and this cluster is the likely donor of electrons to the flavin. The crystallographic structure demonstrates that His A44, covalently linked to the flavin, intervenes between the flavin and [2Fe:2S] cluster. Although there was speculation that the [4Fe:4S] cluster was "off-pathway," in part due to the low reduction potential of this center, the structure confirms the proposal from EPR studies that the clusters are arranged in the sequence [3Fe:4S]-[4Fe:4S]-[2Fe:2S] (*6*). The consequences of this arrangement for kinetics of electron transfer through complex II have recently been discussed (*26*).

Many of the residues observed to participate in the binding of FAD to fumarate reductase had been previously identified from sequence analysis, and from molecular biological and biochemical studies. The binding site for fumarate can be inferred from the location of oxaloacetate observed in the structure. Oxaloacetate is a physiological inhibitor of fumarate reductase (inhibition constant $K_i < 1$ μM), and purified preparations of enzyme contain oxaloacetate that remains

Table 1. Summary of data collection and refinement statistics. Numbers in parentheses indicate values for the highest resolution bin. The figure of merit was 0.48 for all data to 4.0 Å. $R_{sym} = \Sigma|I_i - \langle I\rangle|/\Sigma[\langle I\rangle]$. Res, resolution (in angstroms); URef, number of unique reflections; and Red, redundancy. ⟨PP⟩ denotes overall phasing power to 4 Å resolution.

Energy (keV)	f'	f''	Res	URef	Red	Completeness (%)	R_{sym}	I/σ	⟨PP⟩
7.500 (high remote)	−2.2	3.6	3.3	49,332	4.4	87.2 (90.0)	0.093 (0.277)	15.1 (6.3)	2.6
7.127 (peak)	−6.6	4.5	3.5	39,139	5.3	94.1 (91.0)	0.096 (0.236)	14.5 (7.9)	2.8
7.120 (inflection)	−4.2	2.7	4.0	31,125	4.1	97.2 (97.1)	0.118 (0.269)	15.8 (10.2)	1.6

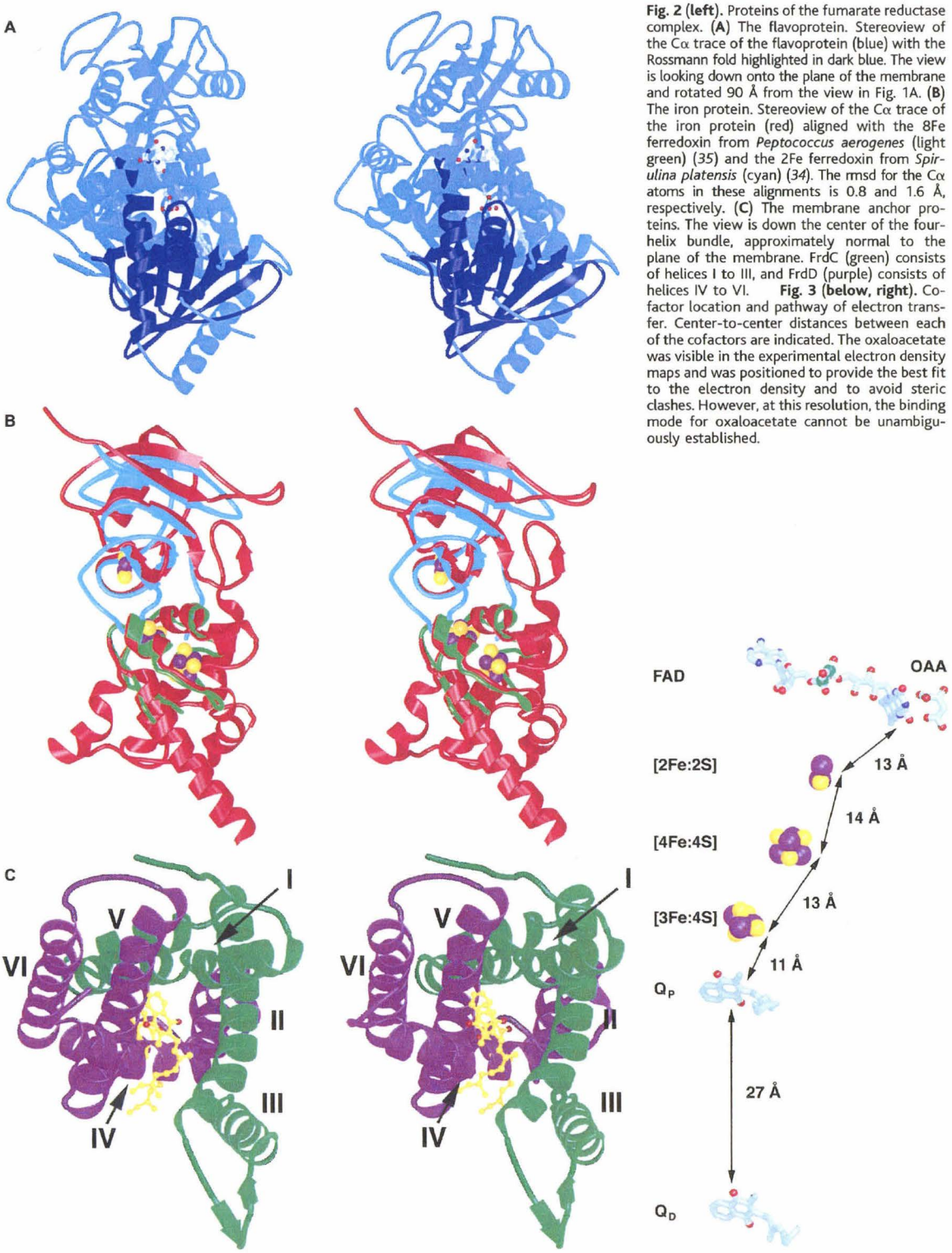

Fig. 2 (left). Proteins of the fumarate reductase complex. (**A**) The flavoprotein. Stereoview of the Cα trace of the flavoprotein (blue) with the Rossmann fold highlighted in dark blue. The view is looking down onto the plane of the membrane and rotated 90 Å from the view in Fig. 1A. (**B**) The iron protein. Stereoview of the Cα trace of the iron protein (red) aligned with the 8Fe ferredoxin from *Peptococcus aerogenes* (light green) (*35*) and the 2Fe ferredoxin from *Spirulina platensis* (cyan) (*34*). The rmsd for the Cα atoms in these alignments is 0.8 and 1.6 Å, respectively. (**C**) The membrane anchor proteins. The view is down the center of the four-helix bundle, approximately normal to the plane of the membrane. FrdC (green) consists of helices I to III, and FrdD (purple) consists of helices IV to VI. **Fig. 3 (below, right).** Cofactor location and pathway of electron transfer. Center-to-center distances between each of the cofactors are indicated. The oxaloacetate was visible in the experimental electron density maps and was positioned to provide the best fit to the electron density and to avoid steric clashes. However, at this resolution, the binding mode for oxaloacetate cannot be unambiguously established.

bound until an excess of substrate is added (*27*). Oxaloacetate interacts with a pocket of arginines and histidines near the side of the flavin opposite to the [2Fe:2S] cluster (Fig. 4C). This group is positioned near conserved residues His A232, Glu A245, and His A355, which may serve as proton donors, and the N5 of the flavin, which likely functions as a hydride donor to fumarate. Although the flavin is buried, access to the active site could take place at the interface between two domains of the Fp.

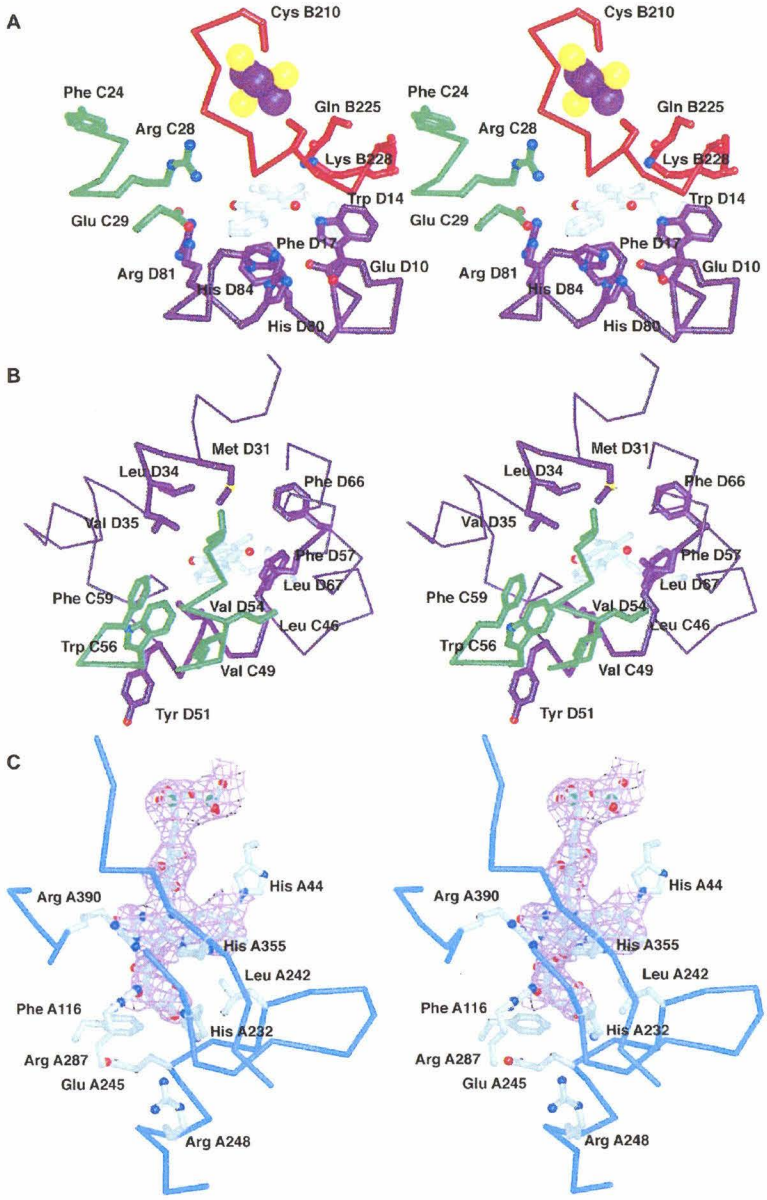

Fig. 4. Quinone binding pockets and active site residues. (**A**) Stereoview of the Q_P binding site shows Q_P is bound in a polar pocket likely positioned just above the membrane bilayer. (**B**) Stereoview of the Q_D site shows Q_D is in a relatively apolar pocket within the membrane bilayer. (**C**) Binding site for the physiological inhibitor oxaloacetate adjacent to the FAD. Oxaloacetate lies beneath the isoalloxazine ring of the flavin. The flavin ring and inhibitor are shown superimposed onto a $2|F_o| - |F_c|$ map contoured at 1σ. The adenine has been omitted for clarity. Side chains that appear to interact directly with the inhibitor are labeled.

Implications for Energy Transduction Processes in Respiration

Quinones play a central role in respiration because they serve as membrane-soluble electron carriers that can couple proton and electron transfer reactions. In the placement of quinones on opposite sides of the membrane-spanning region, fumarate reductase resembles the arrangement observed in cytochrome bc_1 (*17*) more than the photosynthetic reaction center (*23*), where the quinones are on the same side of the membrane. This distinction can be functionally significant, because the quinone arrangement in cytochrome bc_1 (*17*) allows proton translocation to be coupled to electron transfer through operation of the Q-cycle, as first recognized by Mitchell (*28*). When quinones are on opposite sides of the membrane, the Q-cycle couples oxidation at one quinone site to reduction at the second site, with the net result that protons are transported across the membrane. In contrast, if the quinones are on the same side of the membrane as in the reaction center (*23*), there may be proton release associated with hydroquinone oxidation, or proton uptake associated with quinone oxidation, but there cannot be quinone-mediated proton translocation across the membrane. In cytochrome bc_1, two heme groups are positioned between the quinone binding sites to mediate electron transfer between these centers. While the *E. coli* fumarate reductase lacks heme, other fumarate reductases and succinate dehydrogenases contain one or two b-type hemes. These hemes are likely coordinated by histidine residues positioned between the quinone sites in the membrane-spanning region. Although fumarate reductase and succinate dehydrogenase are not known to couple proton translocation to electron transfer, the similar arrangement of redox groups across the membrane like that found in the cytochrome bc_1 complex raises the possibility that at some point these enzymes may have participated in proton translocation.

Fumarate reductase and succinate dehydrogenase occupy central positions in cellular energy metabolism; fumarate reductase serves as the terminal acceptor for a major anaerobic respiratory pathway, while succinate dehydrogenase participates in both the Krebs cycle and as complex II of the aerobic respiratory chain. Although fumarate reductase and succinate dehydrogenase catalyze the same reaction (but in different physiological directions) and are predicted to have similar structures, organisms with both types of respiratory chains use distinct proteins for each purpose for reasons not understood. In terms of the overall process of respiration, exciting progress has been made recently in structurally characterizing membrane-associated members of respiratory pathways (*29*). Fumarate reductase

(complex II) now joins structures available for cytochrome bc_1 [complex III (*17*)], cytochrome c oxidase [complex IV (*30*)], and the F_1 component of the ATP synthase [complex V (*31*)]. This gives a more complete view of the respiratory chain at the atomic level and increases our understanding of one of the most fundamental processes of biological systems.

References and Notes

1. For a review, see G. Gottschalk, *Bacterial Metabolism* (Springer-Verlag, New York, ed. 2, 1986).
2. For a review, see A. Kröger, V. Geisler, E. Lemma, F. Theis, R. Lenger, *Arch. Microbiol.* **158**, 311 (1992).
3. For reviews, see B. A. C. Ackrell, M. K. Johnson, R. P. Gunsalus, G. Cecchini, in *Chemistry and Biochemistry of Flavoenzymes*, F. Müller, Ed. (CRC Press, Boca Raton, FL, 1992), vol. 3, pp. 229–297; C. Hägerhäll, *Biochim. Biophys. Acta* **1320**, 107 (1997); J. J. Van Hellemond and A. G. M. Tielens, *Biochem. J.* **304**, 321 (1994).
4. T. Grundström and B. Jaurin, *Proc. Natl. Acad. Sci. U.S.A.* **79**, 1111 (1982); S. T. Cole, *Eur. J. Biochem.* **122**, 479 (1982); ———, T. Grundström, B. Jaurin, J. J. Robinson, J. H. Weiner, *ibid.* **126**, 211 (1982).
5. W. H. Walker and T. P. Singer, *J. Biol. Chem.* **245**, 4224 (1970); J. H. Weiner and P. Dickie, *Can. J. Biochem.* **254**, 8590 (1979).
6. J. E. Morningstar, M. K. Johnson, G. Cecchini, B. A. C. Ackrell, E. B. Kearney, *J. Biol. Chem.* **260**, 13631 (1985); R. Cammack, D. S. Patil, J. H. Weiner, *Biochim. Biophys. Acta* **870**, 545 (1986); A. T. Kowal *et al.*, *Biochemistry* **34**, 12284 (1995).
7. F. J. Ruzicka, H. Beinert, K. L. Schepler, W. R. Dunham, R. H. Sands, *Proc. Natl. Acad. Sci. U.S.A.* **72**, 2886 (1975); J. C. Salerno and T. Ohnishi, *Biochem. J.* **192**, 769 (1980); D. J. Westenberg, R. P. Gunsalus, B. A. C. Ackrell, H. Sices, G. Cecchini, *J. Biol. Chem.* **268**, 815 (1993).
8. E. Maklashina, D. K. Berthold, G. Cecchini, *J. Bacteriol.* **180**, 5989 (1998); J. R. Guest, *J. Gen. Microbiol.* **122**, 171 (1981).
9. J. H. Weiner *et al.*, *Proc. Natl. Acad. Sci. U.S.A.* **83**, 2056 (1986); G. Cecchini *et al.*, *ibid.*, p. 8898; D. J. Westenberg, R. P. Gunsalus, B. A. C. Ackrell, G. Cecchini, *J. Biol. Chem.* **265**, 19560 (1990); I. Schröder, R. P. Gunsalus, B. A. C. Ackrell, B. Cochran, G. Cecchini, *ibid.* **266**, 13572 (1991).
10. N. Ishii *et al.*, *Nature* **394**, 694 (1998).
11. T. Bourgeron *et al.*, *Nature Genet.* **11**, 144 (1995).
12. T. P. Singer, *Biological Oxidations*, T. P. Singer, Ed. (Interscience, New York, 1968), pp. 339–377.
13. Fumarate reductase from *E. coli* was produced and purified as described (C. Luna-Chavez and G. Cecchini, in preparation). In brief, protein was extracted into 0.05% (w/v) Thesit (polyoxyethylene 9-dodecyl ether) and concentrated to 30 mg/ml in a buffer of 20 mM tris (pH 7.4) and 0.7% Thesit. Crystals were obtained by vapor diffusion with hanging drops equilibrated against a reservoir solution [8% PEG 10,000, 0.1 M sodium citrate (pH 5.8), 0.085 M magnesium acetate, 0.1 mM EDTA, 0.001% (w/v) dithiothreitol]. Menaquinone and oxaloacetate were not added to either the protein preparation or the crystallization conditions. Crystals grew in the space group $P2_12_12_1$ with unit cell constants a = 96.6 Å, b = 138.1 Å, and c = 275.3 Å and two complexes per asymmetric unit. The oxidation state of the enzyme cannot be clearly established in this structure.
14. Data were collected by the inverse beam method at −180°C at beam line 5.0.2 at the Advanced Light Source with an ADSC Quantum4 charge-coupled device. Wavelengths for optimal data collection were determined with a single-crystal EXAFS (extended x-ray absorption fine structure) scan. Data were processed with DENZO and scaled with SCALEPACK [Z. Otwinoski and W. Minor, *Methods Enzymol.* **276**, 307 (1997)] and the CCP4 suite of programs (*32*).
15. Sites for the iron-sulfur clusters were determined from anomalous Patterson maps calculated at 6 Å resolution with the program FFT (*32*). Positions and occupancies of the sites, as well as values for f′ and f″ for two wavelengths, were refined with the program SHARP [E. De La Fortelle and G. Bricogne, *Methods Enzymol.* **276A**, 472 (1997)] yielding initial phases. Phases were improved with solvent flattening and multiple domain noncrystallographic averaging in DM [(*32*); K. Cowtan, *Joint CCP4 EACBM Newslett. Crystallogr.* **31**, 34 (1994)] initially with the transformation matrix determined based on the positions of the iron-sulfur clusters with the program FINDNCS [G. Lu, *J. Appl. Crystallogr.* **32**, 365 (1999)]. Masks used in averaging were calculated with MAMA [G. J. Kleywegt and T. A. Jones, *Acta Crystallogr.* **D55**, 941 (1999)]. The model was built as a polyalanine chain at 4 Å resolution with the program O version 6.22 [T. A. Jones and M. Kjeldgaard, *Methods Enzymol.* **277**, 173 (1997)]. Subsequent rounds of modeling used the structures of NADH peroxidase [Protein Data Bank (PDB) accession number 1joa.pdb; the root mean square deviation (rmsd) is 1.4 Å for the 125 Cα atoms in this alignment] (*33*), the 2Fe ferredoxin from *Spirulina platensis* (accession number 4fxc.pdb) (*34*), and the 8Fe ferredoxin from *Peptococcus aerogenes* (accession number 1fdx.pdb) (*35*) as guides for structurally similar regions. This modeling used phase-combined maps produced by SIGMAA (*32*) and REFMAC [(*32*); G. N. Murshudov, A. A. Vagin, E. J. Dodson, *Acta Crystallogr.* **D53**, 240 (1997)]. Side chains were added to the model when the effective resolution reached 3.5 Å resolution and the R_{free} dropped below 40%. Side chain assignment in the iron protein was greatly aided by sequence analysis identifying the iron-sulfur cluster ligands (*3*). Side chains were initially assigned to the flavoprotein based on sequence similarity with NADH peroxidase in the flavin-binding region. Refinement was carried out with alternating cycles of REFMAC [(*32*); G. N. Murshudov, A. A. Vagin, E. J. Dodson, *Acta Crystallogr.* **D53**, 240 (1997)] and X-PLOR [N. S. Pannu and R. J. Read, *ibid.* **A52**, 659 (1996)] with tight noncrystallographic symmetry (NCS) restraints on the soluble region until the R_{free} dropped below 35%, when the NCS restraints were only loosely used. The rmsd of the soluble and membrane domains of the two NCS related complexes in the asymmetric unit is 0.85 and 0.79 Å, respectively, as determined with the program LSQKAB (*32*). To take advantage of the quality and completeness of the peak data set and the higher resolution of the high remote data set, we chose the same test set for R_{free} for these data sets and alternated refinement between them. The values for R_{cryst} and R_{free} after refinement are 22.2 and 29.2%, respectively, where $R_{cryst} = \Sigma||F_o| - |F_c||/\Sigma|F_o|$ and R_{free} is R_{cryst} for 2% of the reflections omitted from the refinement totaling 1005 Bijvoet pairs. The rmsd of bond lengths and angles is 0.02 Å and 1.9°, respectively, with less than 1% of the residues having disallowed values for the Φ and Ψ angles according to a Ramachandran diagram. The final model for each complex contains 8467 atoms in residues 1 to 575 (of 601 total residues) of FrdA, 1 to 243 (of 243 total residues) of FrdB, 1 to 130 (of 130 total residues) of FrdC, and 1 to 118 (of 118 residues) of FrdD, as well as a [2Fe:2S] cluster, a [3Fe:4S] cluster, a [4Fe:4S] cluster, a FAD, an oxaloacetate molecule, two menaquinone molecules, and one molecule of ordered detergent. The initiator methionine has been excluded from residue numbering because it is believed to be cleaved from the mature protein (*3*), consistent with the lack of electron density seen before residue 1 of each protein in the complex.
16. The coordinates have been deposited in the Protein Data Bank (accession number 1fum).
17. D. Xia *et al.*, *Science* **277**, 60 (1997); Z. Zhang *et al.*, *Nature* **392**, 677 (1998); S. Iwata *et al.*, *Science* **281**, 64 (1998).
18. Surface area calculation was done with the program GRASP [A. Nicholls, K. Sharp, B. Honig, *Proteins* **11**, 281 (1991)].
19. A search of the Protein Data Bank with the European Molecular Biology Laboratory DALI server [L. Holm and C. Sander, *J. Mol. Biol.* **233**, 123 (1993)] did not reveal significant structural similarity to any previously determined folds for domains of the flavoprotein other than the flavin binding domain mentioned in the text.
20. C. Hägerhäll and L. Hederstedt, *FEBS Lett.* **389**, 25 (1996).
21. S. K. Shenoy, L. Yu, C. A. Yu, *J. Biol. Chem.* **272**, 17867 (1997); X. D. Yang, L. Yu, D. Y. He, C. A. Yu, *ibid.* **273**, 31916 (1998).
22. J. C. Salerno, H. J. Harmon, H. Blum, J. S. Leigh, T. Ohnishi, *FEBS Lett.* **82**, 179 (1977); T. Miki, L. Yu, C.A. Yu, *Arch. Biochem. Biophys.* **293**, 61 (1992), A. R. Waldeck *et al.*, *J. Biol. Chem.* **272**, 19373 (1997).
23. J. Deisenhofer, O. Epp, K. Miki, R. Huber, H. Michel, *Nature* **318**, 618 (1985); G. Feher, J. P. Allen, M. Y. Okamura, D. C. Rees, *ibid.* **339**, 111 (1989).
24. H. Beinert, B. A. C. Ackrell, A. D. Vinogradov, E. Kearney, T. P. Singer, *Arch. Biochem. Biophys.* **182**, 95 (1977); T. Ohnishi and B. L. Trumpower, *J. Biol. Chem.* **255**, 3278 (1980).
25. T. Ohnishi *et al.*, *J. Biol. Chem.* **256**, 5577 (1981).
26. P. L. Dutton *et al.*, *Biological Electron Transfer Chains: Genetics, Composition and Mode of Operation*, G. W. Canters and E. Vijgenboom, Eds. (Kluwer, Netherlands, 1988), pp. 3–7.
27. G. Cecchini, B. A. C. Ackrell, J. O. Deshler, R. P. Gunsalus, *J. Biol. Chem.* **261**, 1808 (1986); B. A. C. Ackrell, B. Cochran, G. Cecchini, *Arch. Biochem. Biophys.* **268**, 26 (1989).
28. P. Mitchell, *Biol. Rev.* **41**, 445 (1966); For a review, see U. Brandt and B. L. Trumpower, *Crit. Rev. Biochem. Mol. Biol.* **29**, 165 (1994).
29. For a review, see M. Saraste, *Science* **283**, 1488 (1999).
30. S. Iwata, C. Ostermeier, B. Ludwig, H. Michel, *Nature*, **376**, 660 (1995); T. Tsukihara *et al.*, *Science* **269**, 1069 (1995).
31. J. P. Abrahams, A. G. W. Leslie, R. Lutter, J. E. Walker, *Nature* **370**, 621 (1994).
32. S. Bailey, *Acta Crystallogr.* **D50**, 760 (1994).
33. J. I. Yeh, A. Claiborne, W. G. Hol, *Biochemistry* **35**, 9951 (1996).
34. K. Fukuyama, N. Ueki, H. Nakamura, T. Tsukihara, H. Matsubara, *J. Biochem (Tokyo)* **117**, 1017 (1995).
35. E. T. Adman, L. T. Sieker, L. H. Jensen, *J. Biol. Chem.* **251**, 3801 (1976).
36. Crystal contacts in the membrane-spanning region of a protein are relatively unusual, but have previously been seen in the structure of the iron transporter FhuA [K. P. Locher, B. Rees, D. Moras, J. P. Rosenbusch, in *G-Protein–Coupled Receptors* T. Haga, Ed. (CRC Monographs, CRC Press, Boca Raton, FL, in press); K. P. Locher *et al.*, *Cell* **95**, 771 (1998)], porins [S. W. Cowen *et al.*, *Nature* **358**, 727 (1992)], and bacteriorhodopsin, which was crystallized in the presence of cubic lipids [E. Pebay-Peyroula, G. Rummel, J. P. Rosenbusch, E. M. Landau, *Science* **277**, 1676 (1997)].
37. All figures were made with MOLSCRIPT [P. J. Kraulis, *J. Appl. Crystallogr.* **24**, 946 (1991)] or BOBSCRIPT [R. Esnouf, *J. Mol. Graph.* **15**, 133 (1997)] and rendered with RASTER3D [E. A. Merritt and M. E. P. Murphy, *Acta Crystallogr.* **D50**, 869 (1994)].

38. Supported by the Department of Veterans Affairs, NIH, and NSF (G.C. and C.L-C.), and the Howard Hughes Medical Institute and NIH (D.C.R.). T.M.I. is supported by an NIH training grant. We thank I. Schröder, S. I. Chan, S. C. Hung, and the members of the Rees group for discussions; K. H. Tubman and T. D. Tubman for critical reading; and J. J. Ottesen and T. N. Earnest for experimental assistance. The Advanced Light Source is supported by the Director, Office of Energy Research, Office of Basic Energy Sciences, Materials Sciences Division, of the U.S. Department of Energy under Contract No. DE-AC03-76SF00098 at Lawrence Berkeley National Laboratory.

3 May 1999; accepted 21 May 1999

Chapter 4

Iverson, T.M., Luna-Chavez, C., Schröder, I., Cecchini, G., Rees, D.C. (2000) Analyzing your complexes: Structure of the quinol-fumarate reductase respiratory complex. *Curr. Op. Str. Biol.* in press.

Analyzing your complexes: Structure of the quinol-fumarate reductase respiratory complex

Tina M. Iverson[*], César Luna-Chavez[†], Imke Schröder[‡], Gary Cecchini[†], and Douglas C. Rees[§]

* Graduate Option in Biochemistry, 147-75 CH, California Institute of Technology, Pasadena, CA 91125

† Molecular Biology Division, Department of Veterans Affairs Medical Center, San Francisco, CA 91421 and the Department of Biochemistry and Biophysics, University of California, San Francisco, CA 94143

‡ Department of Microbiology and Molecular Genetics and the Molecular Biology Institute, University of California, Los Angeles, CA 90024

§ Howard Hughes Medical Institute, Division of Chemistry and Chemical Engineering, 147-75 CH, California Institute of Technology, Pasadena, CA 91125; telephone (626) 395-8393, FAX (626) 744-9524, e-mail dcrees@caltech.edu.

Abbreviations

QFR quinol-fumarate reductase

SQR succinate-quinone oxidoreductase

FAD flavin adenine dinucleotide

$\mathbf{Q_P}$ menaquinone binding site proximal to the QFR soluble domain

$\mathbf{Q_D}$ menaquinone binding site distal to the QFR soluble domain

$\mathbf{Q_i}$ quinone-reducing site from the cytochrome bc_1 complex

$\mathbf{Q_o}$ quinol-oxidizing site from the cytochrome bc_1 complex

The integral-membrane protein complex quinol-fumarate reductase (QFR) catalyzes the terminal step in a major anaerobic respiratory pathway. The homologous enzyme succinate-quinone oxidoreductase participates in aerobic respiration as both complex II and as a member of the Krebs cycle. Last year, two structures of QFRs were reported. These structures revealed the cofactor organization linking the fumarate and quinol sites and showed a cofactor arrangement across the membrane that is suggestive of a possible energy coupling function.

Introduction

Bacteria such as *Escherichia coli* can utilize multiple respiratory pathways, and although aerobic respiration is preferred due to the highly favorable energetics of oxygen reduction, respiration can proceed in the absence of oxygen [1]. Fumarate represents one of the more common alternative terminal electron acceptors [2], and is reduced to succinate during anaerobic respiration by quinol-fumarate reductase (QFR), an integral membrane protein located in the bacterial inner membrane. A pool of reduced quinones in the membrane serves as the electron source for fumarate reduction by QFR. The reduced quinones are ultimately generated through the action of an integral membrane protein donor, such as hydrogenase or a formate dehydrogenase.

For comparison, mitochondrial aerobic respiration [3] requires four integral-membrane proteins: NADH-ubiquinone oxidoreductase (NUO; complex I); succinate-quinone oxidoreductase (SQR; complex II); cytochrome bc_1 (complex III); and cytochrome *c* oxidase (complex IV); as well as the involvement of soluble cytochrome *c* and the ubiquinone pool to transport electrons between complexes. SQR and QFR represent a common element of both aerobic and anaerobic respiration since they exhibit significant sequence similarity to one another. Both complexes can catalyze either the oxidation of succinate or the reduction of fumarate [4-6], although physiologically they function to

catalyze this reaction in opposite directions [7-9]. In addition to the involvement in both aerobic and anaerobic respiration, complex II (SQR) also participates in the citric acid cycle, reflecting the central importance of this enzyme in basic metabolism [10].

QFR and SQR are composed of three or four subunits: the flavoprotein; the iron protein; and one or two membrane-bound subunits, depending on the organism. The total molecular weight of a single complex is ~120 kD. Both QFR and SQR can be separated into two components: a water-soluble domain and the membrane anchor subunit(s). The purified soluble domain consists of the flavoprotein subunit and the iron protein subunit, and retains catalytic activity for fumarate reduction when a suitable source of reducing equivalents is provided [11, 12]. The subunits of the soluble domain exhibit strong sequence conservation throughout all species and contain a variety of redox cofactors. The flavoprotein contains flavin adenine dinucleotide (FAD) covalently linked to the $N\varepsilon$ atom of a conserved histidine residue [13], while the iron protein contains three iron sulfur clusters, a [2Fe:2S] cluster, a [3Fe:4S] cluster, and a [4Fe:4S] cluster [7]. In contrast to the soluble proteins, the sequence and cofactor composition of the membrane anchors vary between different organisms and even between QFR and SQR of the same organism. These membrane anchors have been assigned to four classes [14] that differ in the number of transmembrane subunits (one or two), the number of transmembrane

helices (five or six), and the number of associated *b*-type heme moieties (zero, one, or two).

The preceding year has witnessed an explosion in the structural understanding of complex II, with structures for the complete QFR complex from both *E. coli* [15] and *Wolinella succinogenes* [16] reported. Additionally, the structures of four soluble homologs of the flavoprotein were described [17-20], which allow a detailed comparison of flavoprotein structure, and increase insight into catalysis by complex II.

Organization of the complex

As predicted from biochemical and sequence analyses, complex II exists as an essentially modular protein (Figure 1). Each subunit in the soluble domain exhibits homology to other known proteins, suggesting that the formation of this complex may have proceeded by the assembly of other proteins [21]. For example, soluble homologs of the flavoprotein have been seen in multiple pathways (NADH biosynthesis and fumarate reduction), and the iron protein has sequence and structural similarity to both plant and bacterial ferredoxins. Furthermore, the iron protein exhibits weak sequence homology and similar cluster characteristics to the iron protein subunits found in other terminal respiratory complexes, including the multi-subunit membrane-bound DMSO reductase

[22] and heterodisulfide reductase [23]. Thus, modular complex formation may represent an evolutionary mechanism to adjust to the availability of dissimilar terminal electron acceptors.

In the transmembrane region, the membrane anchor subunits of the *E. coli* and *W. succinogenes* QFR complexes are organized around a central four-helix bundle, with two or one additional helices outside this central core, respectively. The *E. coli* and *W. succinogenes* QFRs (Figure 1) contain different cofactors associated with the membrane spanning helices. In the *E. coli* QFR structure, two menaquinone molecules have been identified in the electron density, while the *W. succinogenes* enzyme contains two *b*-type hemes. As a result of the varied cofactor composition in the transmembrane region, the intercofactor distances (Figure 2) differ between the *E. coli* and *W. succinogenes* enzymes in the membrane-spanning region. This situation may be contrasted to the conserved distances between cofactors in the soluble domain.

In the crystal structures of both the *E. coli* and *W. succinogenes* QFRs, two complexes are present in the asymmetric unit that associate through their transmembrane regions in a fashion suggestive of dimer formation. In the *E. coli* structure, this crystal contact buries 325 $Å^2$ of surface area, and is mediated by two ordered detergent molecules ($C_{12}E_9$; [15]). In the *W. succinogenes* QFR structure, almost 3700 $Å^2$ of surface area is buried [16] in

this interface, suggesting this enzyme exists as a dimer. Although detergent molecules may have disassociated a physiological dimer in the *E. coli* enzyme, the $C_{12}E_9$ detergent used in crystallization yields optimal enzyme activity when used in biochemical assays [24]. Additionally, it is possible that the crystals of the *W. succinogenes* enzyme contain a deceivingly tight crystal contact, and that the enzyme is indeed a monomer. Based on the intercofactor distances of the crystal packing interaction, if the *W. succinogenes* enzyme exists as a dimer, it likely acts as a structural and not a functional dimer, unlike the situation in the cytochrome bc_1 complex [25-27].

Fumarate reduction by the flavoprotein and comparison of flavoprotein conformations

The flavoprotein subunit contains two major domains, a flavin-binding domain based on a Rossmann type fold, and a capping domain (Figure 1). The flavin-binding domain exhibits sequence and structural conservation between the two full length QFR structures, the soluble fumarate reductases [18-20], and L-aspartate oxidase (LASPO; [17]). The pairwise deviations between Cα atoms in these proteins never exceeds 1.7 Å, consistent with a sequence identity that is never less than 30%.

The flavin-binding domain and capping domain of the flavoprotein are connected by a small hinge region consisting of two β-strands, with the active site located at the interface between these two domains. An overlay of the recently solved structures containing the flavoprotein [17-20, 28] fold shows that the relative angle between the flavin-binding and capping domains can vary (Figure 3).

It is proposed that during catalysis, fumarate enters the active site, with concomitant closure of the capping domain, sterically causing a rotation of the substrate carboxylate around the double bond (Figure 4). Interaction with the protein have been shown to distort the substrate in complexes with the *W. succinogenes* enzyme [16] and the soluble *Shewanella* enzyme [19]. Fumarate reduction then proceeds by hydride transfer from the N5 of the flavin, followed by proton transfer from a nearby side chain. Four active site residues (His 232, Arg 287, His 355 and Arg 390 in the *E. coli* sequence) that directly contact substrate or inhibitor are absolutely conserved in all available sequences. Three of these residues, His 232, Arg 287 and Arg 390, have been substituted by site directed mutagenesis and are known to be critical for enzyme activity [29; Maklashina, Schröder and Cecchini, unpublished observation]. Both His 355 and Arg 390 have been suggested as proton donors for this reaction [16, 19]; however, the role each side chain plays in the reaction mechanism remains to be conclusively established.

In an overlay of the ensemble of available structures (Figure 5), the side chains of His 232, His 355 and Arg 390 appear structurally conserved both in location and conformation. In contrast, Arg 287, which is located in the capping domain, exhibits different conformations depending on the orientation of the capping domain and the nature of the species bound at the active site. This suggests Arg 287 may be involved with recruiting substrate into or moving product out of the active site.

The iron protein

As predicted by sequence similarity to plant and bacterial ferredoxins, the iron protein contains two domains. The N-terminus has a fold similar to plant-type ferredoxins surrounding the [2Fe:2S] cluster, while the C-terminal domain exhibits a core similar to bacterial ferredoxins and contains the cysteine ligands to the [4Fe:4S] and the [3Fe:4S] clusters. The C-terminal domain additionally contains several other helices that associate with the membrane anchor subunits. In agreement with EPR spectroscopy [30-33], the three clusters are arranged in a nearly linear fashion leading from the membrane anchor to the active site flavin (Figure 2). This structural organization indicates that, despite the low reduction potential of the [4Fe:4S] cluster [7, 8], it is likely that all [Fe:S] clusters participate in electron transfer between the quinone pool and fumarate [34, 44].

Organization of cofactors in the membrane: a possible role in energy transduction

Two sets of transmembrane associated cofactors are present in the two available QFR structures: two menaquinone molecules (Q_P and Q_D) are observed in the *E. coli* enzyme, while two *b*-type hemes bind to the *W. succinogenes* enzyme (Figure 1). Despite the differences in subunit composition, sequences, and cofactor components, the transmembrane anchors of the *E. coli* and *W. succinogenes* QFRs are both organized around an antiparallel four helix bundle in the membrane, with two or one additional peripheral transmembrane helices, respectively. In each structure, one of the helices of the four helix bundle contains a distinctive bend in the transmembrane section. As an ideal four-helix bundle is two-fold symmetric, the transmembrane helices of the QFR structures can be aligned in two distinct ways. In one alignment, the C-subunit of the *E. coli* enzyme is superimposed with the N-terminus of the C-subunit of the *W. succinogenes* enzyme, yielding an rms deviation of 2.4 Å for 137 C_α atoms between corresponding residues in the five transmembrane helices of the *Wolinella* enzyme and the *E. coli* enzyme. In this alignment, the connections between the transmembrane helices are similar, and the bent helices superimpose (Figure 6A). However, if the menaquinone molecules from the *E. coli* QFR were transferred into the *W. succinogenes* enzyme, they would sterically clash with the distal heme of the latter. In the second alignment, which is rotated ~180° from the first alignment, the N-terminus of the D-

subunit of the *E. coli* enzyme becomes superimposed with the N-terminus of the C-subunit of the *W. succinogenes* enzyme (Figure 6B). Although this alignment appears quantitatively inferior (2.2 Å for only 62 C_α atoms), it preserves the relative orientation between the transmembrane helices and the soluble domains in the two QFR structures. Furthermore, the Q_D menaquinone from the *E. coli* enzyme no longer sterically clashes with the distal heme, suggesting that this position might correspond to where Q_D binds in the *W. succinogenes* enzyme. Indeed, a cavity is present in the *Wolinella* QFR near this position that might represent the cofactor binding site for that complex.

The separation distance between the two menaquinone molecules in the *E. coli* enzyme (~25 Å; Figure 2) is too far to support electron transfer at physiological relevant rates [34]. While this may indicate that the Q_D site is not catalytically relevant, an alternate explanation is that a third cofactor binding site is positioned between the Q_P and Q_D sites and would be ~13 Å from each of the established quinone sites. Although the involvement of an additional cofactor cannot be conclusively proven, several factors point to its possible existence. Biochemical evidence [35-37] suggests that Q_D is necessary for physiological catalysis, and site-directed mutagenesis has implicated a cluster of residues between the two known quinone binding sites as necessary for enzyme function [35]. This cluster of residues lies near a cavity between the transmembrane helices in the *E. coli* enzyme and is associated with density from the structure

determination that could not be assigned. Spectroscopic evidence suggests that a stabilized semiquinone pair separated by ~8 Å is localized near the [3Fe:4S] cluster [33, 38-41], which could be a result of Q_P interacting with a quinone in a central binding site that could not be identified in the density. Indeed, several residues (Trp C86, Arg D51) lining the pocket of the potential quinone binding site also line the Q_P binding site. Although a menaquinone molecule could not be docked into the density observed in the *E. coli* structure determination, it is possible that this site is only partially occupied in the crystal structure.

One intriguing observation concerning the quinone locations in the *E. coli* QFR is that they are positioned on opposite sides of the membrane, as observed for the two quinone sites in the cytochrome bc_1 complex [25-27]. In cytochrome bc_1, this transmembrane arrangement is essential for proton pumping across the mitochondrial membrane via a Q-cycling mechanism [42]. In addition to the location of the quinone binding sites, the environment of the Q_P site shares certain features in common with the Q_o and Q_i sites of cytochrome bc_1. Proton translocation at the Q_o site in cytochrome bc_1 is thought to occur through His 161 and Glu 272 (bovine numbering). These two residues only form hydrogen bonds to inhibitors when the Reiske iron sulfur center is at a position near the Q_o site [43; S. Iwata, personal communication] thereby mechanically coupling proton translocation to electron transfer to the Reiske center. Analysis of the Q_i site suggests

that the conserved Asp C228 and His C201 (bovine numbering) residues, both of which form hydrogen bonds to the quinone (Figure 7A), participate in the proton translocation mechanism. In the *E. coli* QFR structure, Glu C29 and Lys B228 are each within hydrogen bonding distance of the quinone (Figure 7B). Glu C29 has been shown by site-directed mutagenesis [35] to be critical for enzyme function. Proton translocation has not been observed for QFR or SQR, although the energetics of proton translocation by QFR have been calculated to be favorable for the *W. succinogenes* complex [44]. In contrast, similar calculations indicate that energetics are less favorable for the *E. coli* enzyme. If other modular terminal respiratory acceptors, such as DMSO reductase or heterodisulfide reductase, have evolved with a similar transmembrane arrangement of quinone binding sites, it is possible that these proteins may employ a Q-cycling mechanism to pump protons.

Conclusions

Structural information is now available for most members of the aerobic respiratory chain, including atomic-level resolution crystal structures of the respiratory complexes II-IV [25-27, 45, 46], much of the ATP synthase [47, 48] and electron microscopic reconstruction of complex I [49-51] at approximately 30 Å resolution. In the last year, structures have been reported for two intact two full-length QFRs, one from *E. coli* [15]

and one from *W. succinogenes* [16], as well as several soluble homologs [17-20]. This ensemble of fumarate reductase structures allows a better understanding of the reaction mechanism catalyzed by the flavoprotein as well as an understanding of how electrons are passed from the membrane soluble quinones into the active site of the enzyme. Additionally, these structures open the question of whether QFR and SQR can potentially couple electron transfer to proton translocation, thereby representing an additional mechanism for energy conservation in respiratory chains.

Acknowledgements

This work has been supported by the Department of Veterans Affairs, and funding from HHMI (DCR), the NIH (GM45162, DCR; HL-16251, GC), and the NSF (MCB-9729778, GC). We would like to acknowledge stimulating discussions with T. Ohnishi, P. L. Dutton, H. B. Gray, and S. Iwata.

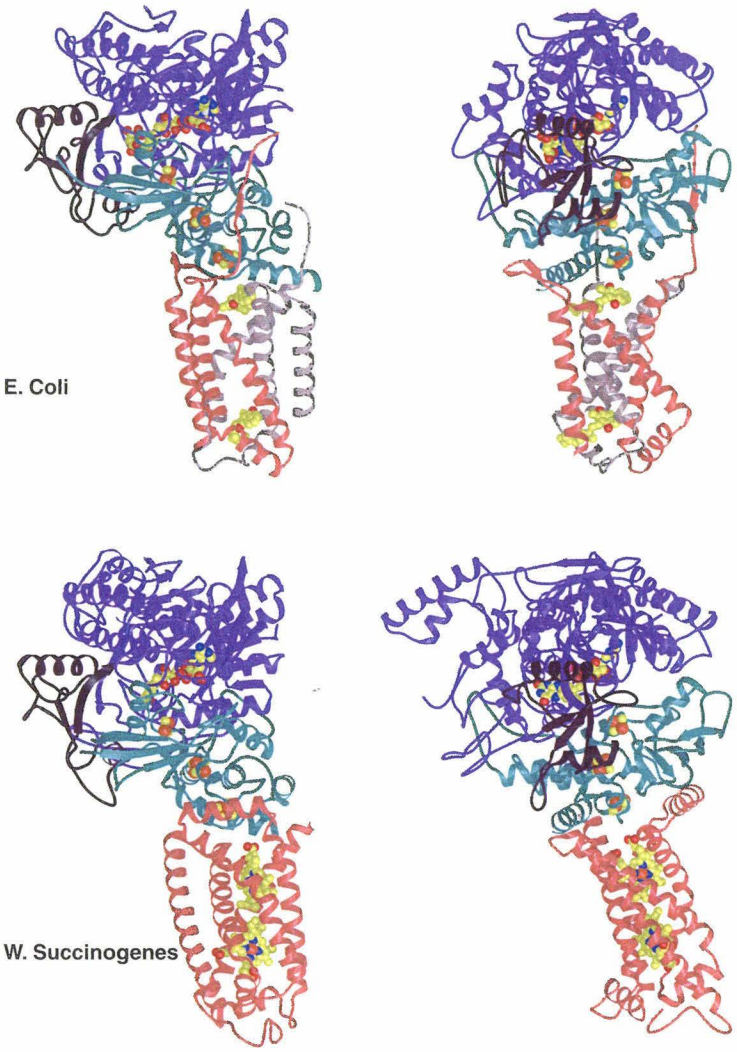

Figure 4.1: Ribbon diagrams of the *E. coli* (1FUM) and *W. succinogenes* (1QLA) QFR complexes. The flavoprotein is colored in purple, with the capping domain highlighted in dark purple; the iron protein is colored in teal; the C-subunit membrane anchor is in peach; while the D-subunit membrane anchor is in gray (*E. coli* enzyme only). The left column shows a view that is rotated 90° from the right column. The *W. succinogenes* enzyme contains a C-terminal extension of the flavoprotein (lower right figure) that was not observed in the *E. coli* structure determination. Figures 1-3 and 5-7 were made using MOLSCRIPT [52], BOBSCRIPT [53], and RASTER3D.

Figure 4.2: Distances between cofactors in the *E. coli* and *W. succinogenes* QFR complexes. Distances between redox centers are measured between the closest redox active atom of each cluster, rather than center-to-center distance as given in Iverson et al [15]. The distances to hemes are measured to the heme iron rather than the edge of the porphyrin ring. The distances between cofactors in the soluble domains ([Fe:S] clusters and FAD) are conserved, whereas the distances between the cofactors associated with the membrane anchors varies as a result of the differences in cofactor composition.

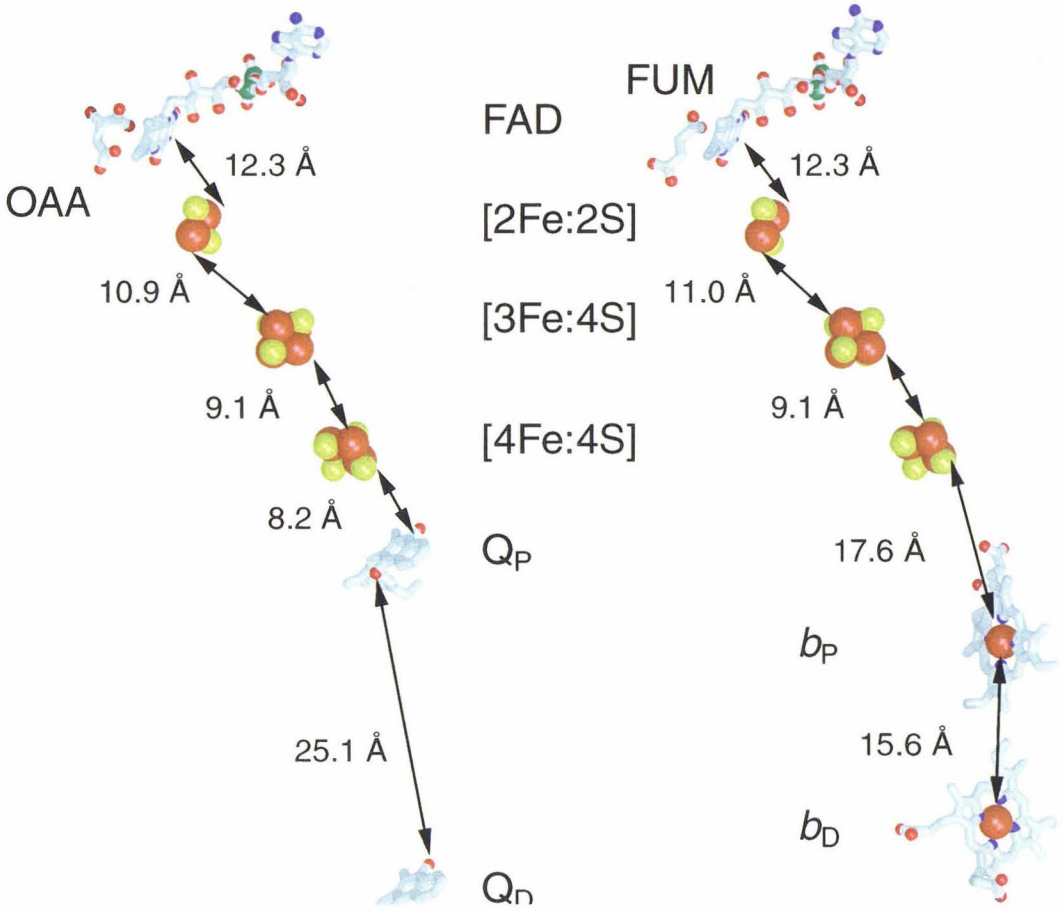

Figure 4.3: Stereoview illustrating the movement of the capping domain with respect to the flavin-binding domain in the flavoprotein. The capping domain from *S. putrefaciens* (green; 1D4D; [19]) *S. frigidimarina* (pink; 1QO8; [18]) and *W. succinogenes* (blue; 1QLA; [16]) flavoenzymes are shown relative to a least squares superposition of the flavin-binding domain (black), with the position of the FAD indicated (red). The maximal displacement for the capping domain suggests that the hinge connecting the two domains can bend over 30 °. Other flavoproteins having intermediate hinge angles have been omitted for clarity.

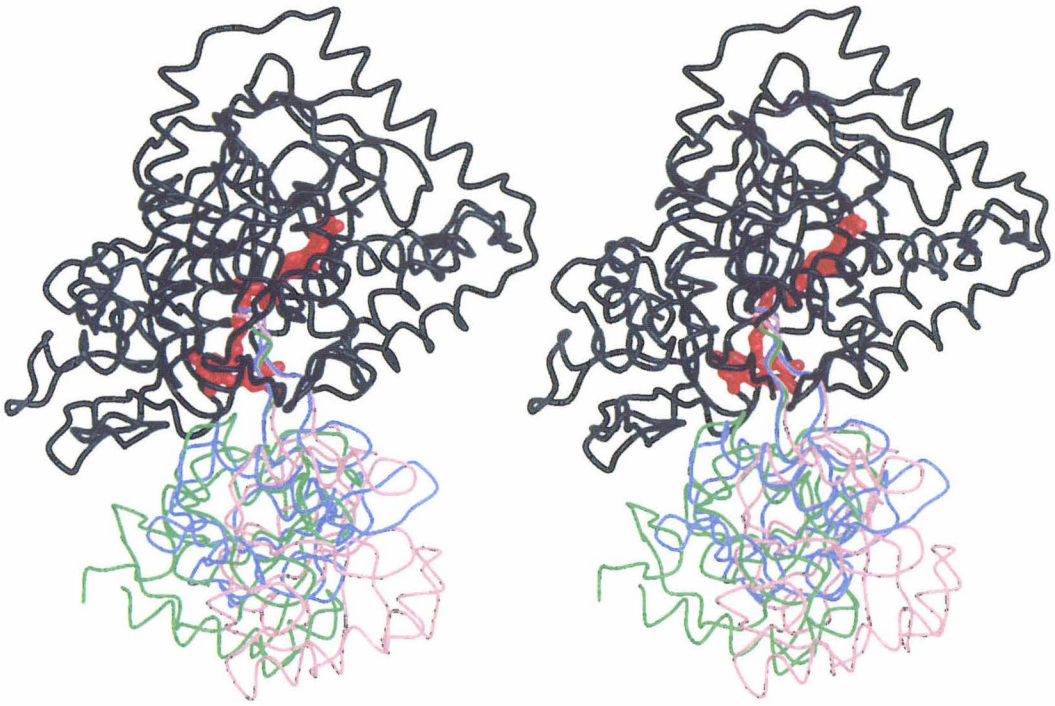

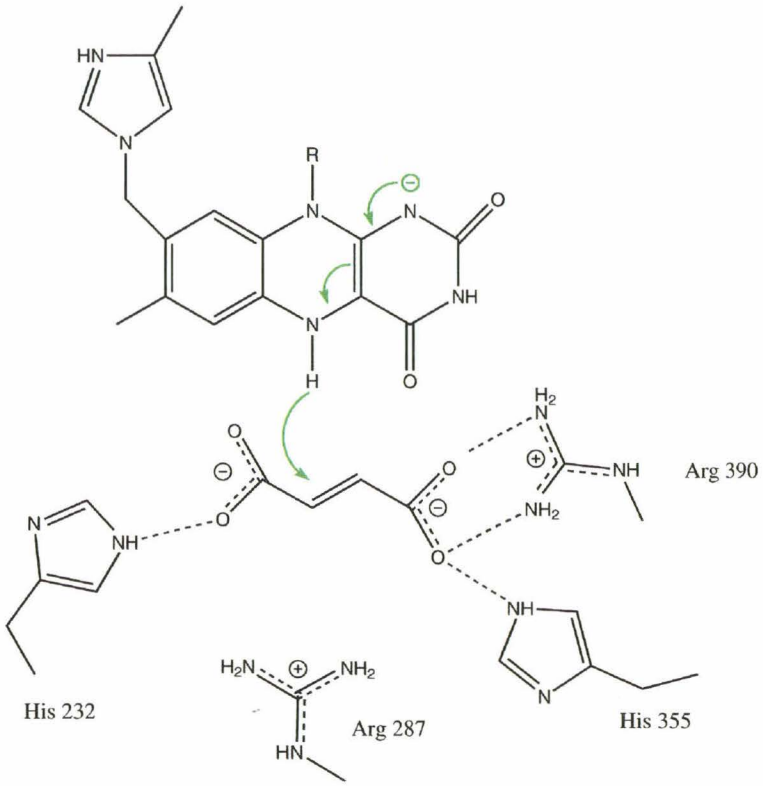

Figure 4.4: Schematic diagram of active site interactions with proposed reaction mechanism. Hydrogen bond interactions between the protein and bound ligands are indicated, with the exception of Arg 287, which exhibits significant conformational variability in the different structural determinations. Hydride transfer from the N5 of FAD (green arrows) represents the initial step of fumarate reduction, followed by proton transfer to the substrate. The side chains of His 232, Arg 287, His 355 or Arg 390 are likely candidates for the immediate proton donor. Arg 287 and Arg 390 have also been shown to be necessary for covalent attachment of the FAD to His 44 [Maklashina, Schröder and Cecchini, unpublished observation].

Figure 4.5: Stereoview illustrating the superposition of active site residues in different fumarate reductase structures. The positions of residues from the *E. coli* (1FUM) enzyme are red, from the *Wolinella* (1QLB) enzyme are orange, from L-aspartate oxidase (1CHU) are yellow, from the *S. frigidimarina* soluble fumarate reductase are green and blue (1QO8; 1QJD), and from the *S. putrefaciens* fumarate reductase (1D4D) are magenta. The cofactor FAD and substrate fumarate substrate fumarate are black and gray, respectively. Although the positions of His 232, His 355 and Arg 390 are structurally conserved, the positions of the Arg 287 side chain and the surrounding main chain are more variable.

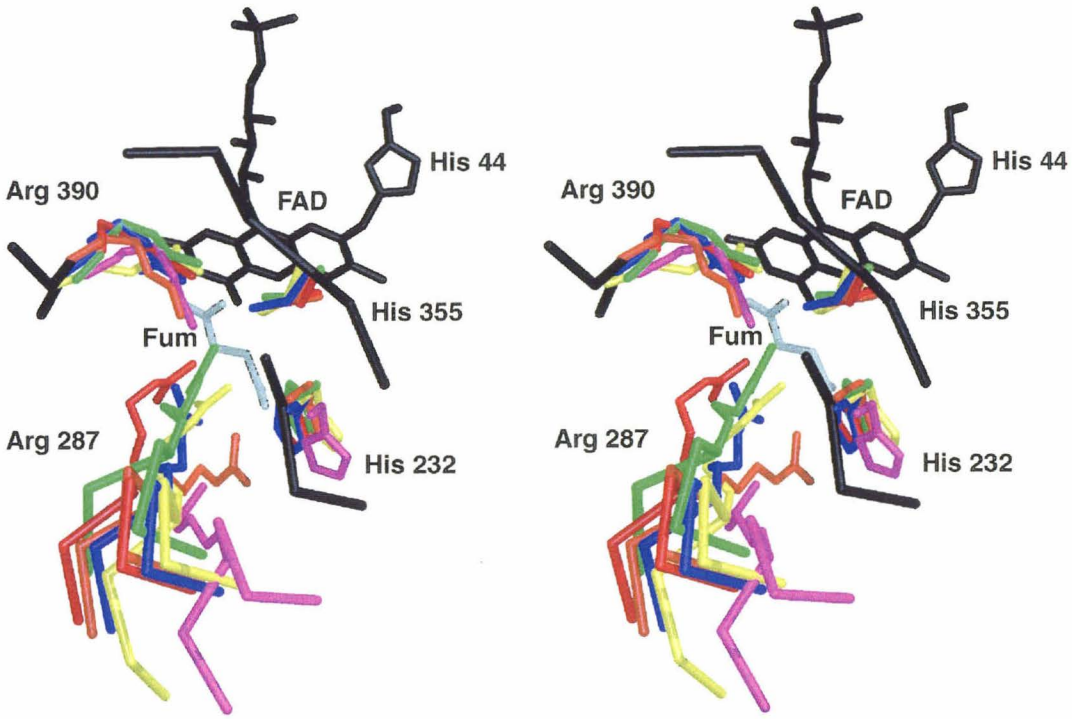

Figure 4.6: Alignment of transmembrane helices from the *E. coli* (1FUM) and *W. succinogenes* (1QLB) QFR complexes. **A**. Superposition of the transmembrane helices with the N-terminus of the C-subunit of the *E. coli* enzyme (C subunit in blue, D subunit in green) superimposed with the N-terminus from the *W. succinogenes* enzyme (pink). Quinones from the *E. coli* enzyme are shown in yellow, while the hemes from the *Wolinella* enzyme are in black. **B**. Alternate alignment superimposing the N-terminus of the *E. coli* enzyme D subunit with the N-terminus of the *W. succinogenes* C subunit. A cavity located by the program VOIDOO [55] in the *W. succinogenes* enzyme is shown in brown mesh. If this cavity represents the quinone binding site for the *Wolinella* enzyme, the location would be structurally preserved in both enzymes.

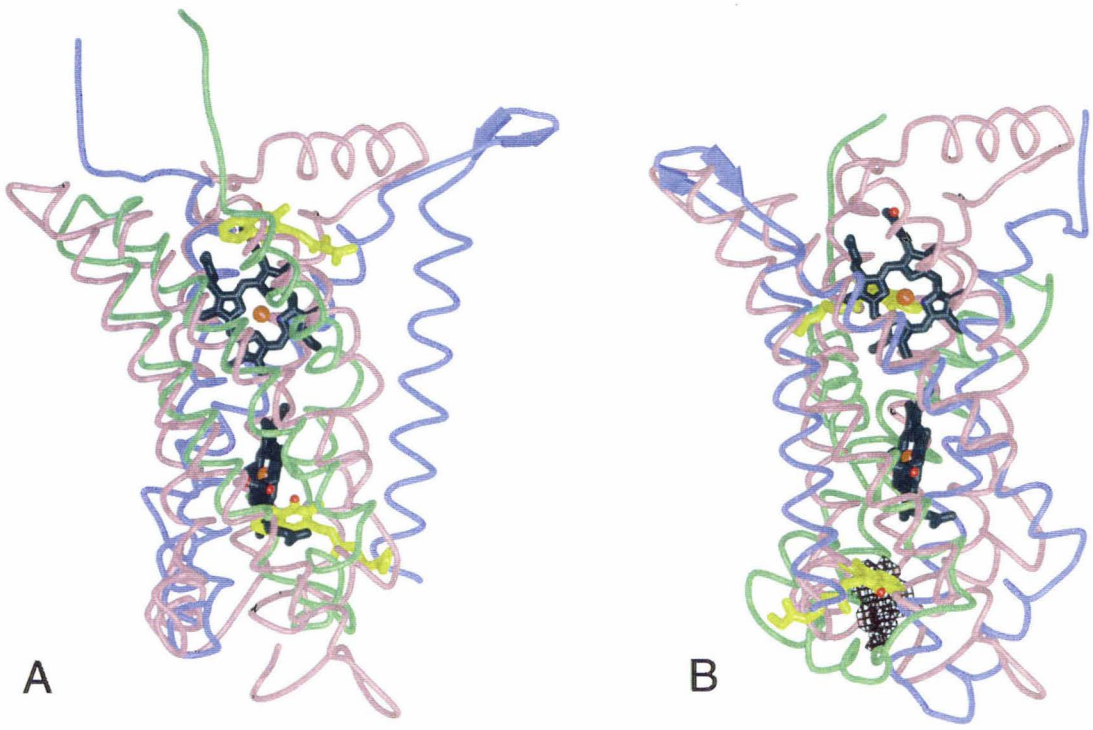

Figure 4.7: **A**. Binding pocket for Q_P in the *E. coli* QFR reductase complex. The quinone binding environment includes hydrogen bonds to the side chains of Glu C29 and Lys B228 **B.** Binding pocket for Q_O in the cytochrome bc_1 complex. The structural arrangement of the hydrogen bonds relative to the quinone is similar to those seen in the *E. coli* QFR. Additionally, several other residues (Phe D17 (QFR) and Phe C32 (bc_1); Trp D14 (QFR) and Leu C22 (bc_1); [3Fe:4S] (QFR) and heme b_H (bc_1)) are observed in conserved locations with resides of similar property in the *E. coli* enzyme.

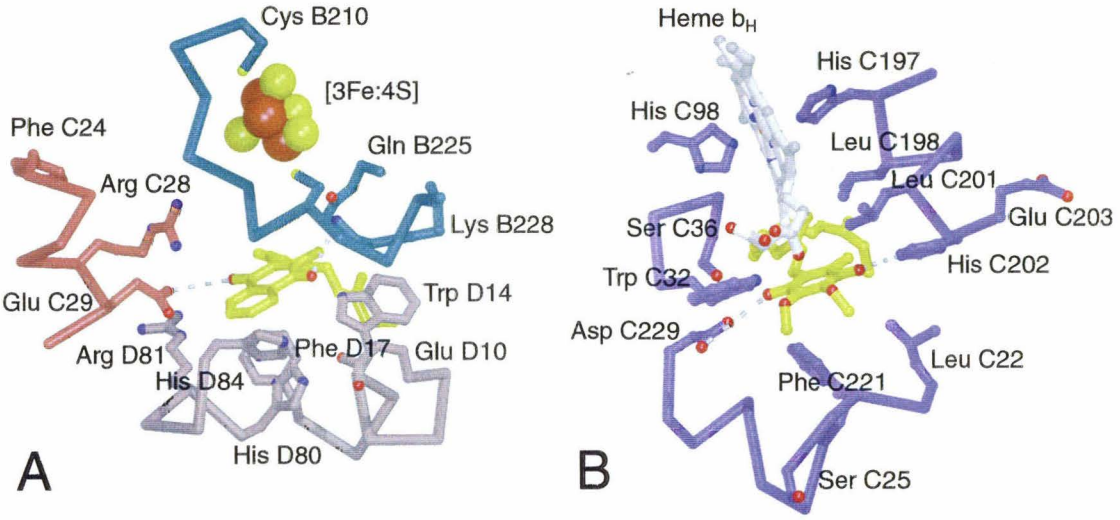

References and recommended reading

Papers of particular interest, published within the annual period of review, have been highlighted as:

• of special interest

•• of outstanding interest

1. Gottschalk, G: *Bacterial Metabolism.* New York: Springer-Verlag; 1986.

2. Kröger, A, Geisler, V, Lemma, E, Theis, F and Lenger, R: **Bacterial Fumarate Respiration.** *Arch Microbiol* 1992, **158**:311-314.

3. Saraste, M: **Oxidative phosphorylation at the fin de siecle.** *Science* 1999, **283**:1488-1493.

4. Guest, JR: **Partial replacement of succinate dehydrogenase function in phage and plasmid-specified fumarate reductase in *Escherichia coli.*** *J Gen Microbiol* 1981, **122**:171-179.

5. Maklashina, E, Berthold, DK and Cecchini, G: **Anaerobic expression of *Escherichia coli* succinate dehydrogenase: functional replacement of fumarate reductase in the respiratory chain during anaerobic growth.** *J Bacteriol* 1998, **180**:5989-5996.

6. Pershad, HR, Hirst, J, Cochran, B, Ackrell, BAC and Armstrong, FA: **Voltammeric studies of bidirectional catalytic electron transport in *Escherichia coli* succinate**

dehydrogenase: comparison with the enzyme from beef heart mitochondria. *Biochim Biophys Acta* 1999, **1412**:262-272.

7. Ackrell, BAC, Johnson, MK, Gunsalus, RP and Cecchini, G: *Chemistry and biochemistry of flavoenzymes*. Boca Raton: CRC Press; 1992.

8. Hågerhall, C: **Succinate:quinone oxidoreductases. Variations on a conserved theme.** *Biochim Biophys Acta* 1997, **1320**:107-141.

9. Hellemond, JJV and Tielens, AGM: **Expression and functional properties of fumarate reductase.** *Biochem J* 1994, **304**:321-331.

10. Guest, JR and Russell, GC: **Complexes and complexities of the citric acid cycle in *Escherichia coli*.** *Curr Top Cell Regul* 1992, **33**:231-247.

11. Singer, TP, Kearney, EB and Kenney, WC: **Succinate dehydrogenase.** *Adv Enzymol* 1973, **37**:189-272.

12. Ackrell, BAC, Kearney, EB and Singer, TP: **Mammalian succinate dehydrogenase.** *Methods Enzymol* 1978, **53**:466-483.

13. Walker, WH and Singer, TP: **Identification of the covalently-bound flavin of succinate dehydrogenas as 8α-(histidyl) flavin adenine dinucleotide.** *J Biol Chem* 1970, **245**:4224-4225.

14. Hågerhall, C and Hederstedt, L: **A general structural model for the membrane-domain of succinate:quinone oxidoreductases.** *FEBS Lett* 1996, **389**:25-31.

••15. Iverson, TM, Luna-Chavez, C, Cecchini, G and Rees, DC: **Structure of the *Escherichia coli* fumarate reductase respiratory complex.** *Science* 1999, **284**:1961-1966.

The first structural analysis of quinol-fumarate reductase details the organization of the complex and reveals bound quinones in the membrane spanning regions. The locations of these quinones are reminiscent of quinones involved in energy transduction.

••16. Lancaster, CRD, Kröger, A, Auer, M and Michel, H: **Structure of fumarate reductase from *Wolinella succinogenes* at 2.2 Å resolution.** *Nature* 1999, **402**:377-385.

The structure determination of the intact quinol-fumarate reductase from *W. succinogenes* allows analysis of *b*-type hemes bound to the membrane anchor subunit and reveals common elements of QFR structure through comparisons to the *E. coli* enzyme.

•17. Matttevi, A, Tedeschi, G, Bacchella, L, Coda, A, Negri, A and Ronchi, S: **Structure of L-aspartate oxidase: implication for the succinate dehydrogenase/fumarate reductase oxidoreductase family.** *Structure* 1999, **7**:745-756.

The first structure determination of a soluble homologue of the flavoprotein suggests flexibility exists between the flavin-binding domain and the capping domain.

•18. Bamford, V, Dobbin, PS, Richardson, DJ and Hemmings, AM: **Open conformation of a flavocytochrome c_3 fumarate reductase.** *Nat Struct Biol* 1999, **6**:1104-1109.

•19. Leys, D, Tsapin, AS, Nealson, KH, Meyer, TE, Cusanovich, MA and VanBeeumen, JJ: **Structure and Mechanism of the flavocytochrome *c* fumarate reductase of *Shewanella putrefaciens* MR-1.** *Nat Struct Biol* 1999, **6**:1113-1117.

•20. Taylor, P, Pealing, SL, Reid, GA, Chapman, SK and Walkinshaw, MD: **Structural and mechanistic mapping of a unique fumarate reductase.** *Nat Struct Biol* 1999, **6**:1108-1112.

This report and the preceding two [18, 19], structure determinations of soluble fumarate reductases, published simultaneously, provide further support for domain movement in the flavoprotein.

21. Gest, H: **The evolution of biological energy-transducing systems.** *FEMS Lett* 1980, **7**:73-77.

22. Bilous, PT, Cole, ST, Andersib, WF and Weiner, JH: **Nucleotide sequence of the dmsABC operon encoding the anaerobic dimethylsulphoxide reductase of *Escherichia coli*.** *Mol Microbiol* 1988, **2**:785-795.

23. Kunkel, A, Vaupel, M, Heim, S, Thauer, RK and Hedderich, R: **Heterodisulfide reductase from methanol-grown cells of *Methanosarcina barkeri* is not a flavoenzyme.** *Eur J Biochem* 1997, **244**:226-234.

24. Luna-Chavez, C, Iverson, TM, Rees, DC and Cecchini, G: **Overexpression, purification, and crystallization of the membrane-bound fumarate reductase from *Eschericia coli*.** *Protein Expr Purif* 2000, in press.

25. Xia, D, Yu, C, Kim, H, Xia, J, Kachurin, AM, Zhang, L, L. Yu and Deisenhofer, J: **Crystal structure of the cytochrome bc_1 complex from bovine heart mitochondria.** *Science* 1997, **277**:60-66.

26. Zhang, Z: **Electron transfer by domain movement in cytochrome bc_1.** *Nature* 1998, **392**:677-684.

27. Iwata, S, Lee, JW, Okada, K, Lee, JK, Iwata, M, Rasmussen, B, Link, TA, Ramaswamy, S and Jap, BK: **Complete structure of the 11-subunit bovine mitochondrial bc_1 complex.** *Science* 1998, **281**:64-71.

28. Ackrell, BAC: **Progress in understanding structure-function relationships in respiratory chain complex II.** *FEBS Lett* 2000, **466**:1-5.

29. Schröder, I, Gunsalus, R, Ackrell, BAC, Cochran, B and Cecchini, G: **Identification of active site residues of *Eschericia coli* fumarate reductase by site directed mutagenesis.** *J Biol Chem* 1991, **266**:13572-13579.

30. Morningstar, JE, Johnson, MK, Cecchini, G, Ackrell, BAC and Kearney, EB: **The high-potential iron-sulfur center in *Escherichia coli* fumarate reductase is a 3-iron cluster.** *J Biol Chem* 1985, **260**:3631-3638.

31. Cammack, R, Patil, DS and Weiner, JH: **Evidence that center-2 in *Escherichia coli* fumarate reductase is a [4Fe-4S] cluster.** *Biochim Biophys Acta* 1986, **870**:545-551.

32. Kowal, AT, Werth, MT, Moanodori, A, Cecchini, G, Schröder, I, Gunsalus, RP and Johnson, MK: **Effect of cysteine to serine mutation on the properties of the [4Fe-4S] center in *Escherichia coli* fumarate reductase.** *Biochemsitry* 1995, **34**:12284-12293.

33. Waldeck, AR, Stowell, MHB, Lee, HK, Hung, SC, Matsson, M, Hederstedt, L, Ackrell, BAC and Chan, SI: **Electron paramagnetic resonance studies of succinate:ubiquinone oxidoreductase from *Paracoccus denitrificans*.** *J Biol Chem* 1997, **272**:19373-19382.

••34. Page, CC, Moser, CC, Chen, X and Dutton, PL: **Natural engineering principles of electron tunneling in biological molecules.** *Nature* 1999, **402**:47-52.

This thorough compilation of electron transfer proteins discusses the mechanism of endergonic tunneling as well as explaining the biological tendency for redox cofactors to be positioned at distances ~13 Å apart in proteins.

35. Westenberg, DJ, Gunsalus, RP, Ackrell, BAC, Sices, H and Cecchini, G: ***Escherichia coli* fumarate reductase FrdC and FrdD mutants. Identification of amino acid residues involved in catalytic activity with quinones.** *J Biol Chem* 1993, **268**:815-822.

36. Lee, GY, He, DY, Yu, L and Yu, CA: **Identification of the ubiquinone-binding domain in QPs1 of succinate-ubiquinone reductase.** *J Biol Chem* 1995, **270**:6193-6198.

37. Shenoy, SK, Yu, L and Yu, CA: **The smallest membrane anchoring subunit (QPs3) of bovine heart mitochondrial succinate-ubiquinone reductase. Cloning, sequencing, topology, and Q-binding domain.** *J Biol Chem* 1997, **272**:17867-17872.

38. Salerno, JC, Harmon, HJ, Blum, H, Leigh, JS and Ohnishi, T: **A transmembrane quinone pair in the succinate dehydrogenase cytochrome *b* region.** *FEBS Lett* 1977, **82**:179-182.

39. Rich, PR, Moore, AL, Ingledew, WJ and Bonner, WDJ: **EPR studies of higher plant mitochondria. I ubisemiquinone and its relation to alternative respiratory oxidations.** *Biochim Biophys Acta* 1977, **504**:345-363.

40. Rich, PR and Bonner, WDJ: **An EPR analysis of cyanide-resistant mitochondria isolated from the mutant poky strain of *Neurospora crassa*.** *Biochim Biophys Acta* 1978, **504**:345-363.

41. Salerno, JC and Ohnishi, T: **Studies on the stabilized ubisemiquinone species in the succinate-cytochrome *c* reductasesegment of the intact mitochondrial membrane system.** *Biochem J* 1980, **192**:769-781.

42. Mitchell, P: **Coupling of phosphorylation to electron and hydrogen transfer by a chemi-osmotic type of mechanism.** *Nature* 1961, **191**:144-148.

43. Crofts, AR, Barquera, B, Gennis, RB, Kuras, R, Guergova-Kuras, M and Berry, EA: **Mechanism of ubiquinol oxidation by the bc_1 complex: different domains of the**

quinol binding pocket and their role in the mechanism and binding of inhibitors. *Biochemistry* 1999, **38**:15807-15926.

••44. Ohnishi, T, Moser, CC, Page, CC, Dutton, PL and Yano, T: **Simple redox-linked proton-transfer design: new insights from structures of quinol-fumarate reductase.** *Structure* 2000, **8**:R23-R32.

This insightful mini-review focuses on the bioenergetics of QFR and SQR.

45. Iwata, S, Ostermeier, C, Ludwig, B and Michel, H: **Structure at 2.8-Ångstrom resolution of cytochrome *c* oxidase from *Paracoccus denitrificans*.** *Nature* 1995, **376**:660-669.

46. Tsukihara, T, Aoyama, H, Tomizaki, T, Yamaguchi, H, SinzawaItoh, K, Nakashima, R, Yaono, R and Yoshikawa, S: **The whole structure of the 13-subunit oxidized cytochrome *c* oxidase at 2.8 Ångstrom.** *Science* 1996, **272**:1136-1144.

47. Abrahams, JP, Leslie, AGW, Lutter, R and Walker, JE: **Structure at 2.8-Ångstrom resolution of F1ATPase from bovine heart-mitochondria.** *Nature* 1994, **370**:621-628.

••48. Stock, D, Leslie, AGW and Walker, JE: **Molecular architecture of the rotary motor in ATP synthase.** *Science* 1999, **286**:1700-1705.

The structure determination of the c subunit of the ATP synthase shows homodecameric arrangement associated with the trimeric water soluble F1 component, suggesting a non-integral number of protons is pumped for each ATP synthesized.

49. Guénebaut, V, Vincentelli, R, Mills, D, Weiss, H and Leonard, KR: **Three dimensional structure of NADH-dehydrogenase from *Neurospora crassa* by electron microscopy and conical tilt reconstruction.** *J Mol Biol* 1997, **265**:409-418.

50. Guénebaut, V, Schlitt, A, Weiss, H, Leonard, K and Friedrich, T: **Consistent structure between bacterial and mitochondrial NADH:ubiquinone oxidoreductase (complex I).** *J Mol Biol* 1998, **276**:105-112.

51. Grigorieff, N: **Three-dimensional structure of bovine NADH:ubiquinone oxidoreductase (complex I) at 22Å in ice.** *J Mol Biol* 1998, **277**:1033-1046.

52. Kraulis, PJ: **MOLSCRIPT - a program to produce both detailed and schematic plots of protein structures.** *J Appl Cryst* 1991, **24**:946-950.

53. Esnouf, R: **BOBSCRIPT -- An extensively modified version of molscript that includes greatly enhanced coloring capabilities.** *J Mol Graph* 1997, **15**:133-138.

54. Merritt, EA and Murphy, MEP: **Raster3D Version 2.0 - a program for photorealistic molecular graphics.** *Acta Cryst* 1994, **D50**:869-873.

with a site-specific mutant. *Biochemistry* 1989, **28**:7913-7918.

55. Kleywegt, GJ and Jones, TA: **Detection, delineation, measurement and display of cavities in macromolecular structures.** *Acta Cryst* 1994, **D50**:175-185.

Chapter 5: Biological Nitrification and the Nitrogen Cycle

The biological nitrogen cycle involves a network of microorganisms that interconvert inorganic nitrogen between different redox states (+5 to -3) in five reduction reactions and three oxidation reactions *(1-3)*(Figure 5.1). Aside from the obvious ecological relevance of the biological nitrogen cycle, the application of the reactions catalyzed by the nitrogen cycle has been a major biotechnological advance in waste removal of NO_3^-, NO_2^-, and NH_4^+ *(4, 5)*. One byproduct of the nitrogen cycle, N_2O represents the third largest contributor to greenhouse gasses, following CH_4 and CO_2, and has been implicated in ozone depletion *(6)*. Further advances in microbial technology could help reduce atmospheric pollution by N_2O.

The metabolism of organisms that participate in the nitrogen cycle are relatively unusual, thus the enzymes that catalyze these reaction contain various metal cofactors that are often unique in composition, ligation, or both *(1-3)*. In particular, molybdenum-containing cofactors are used for both nitrogen fixation and nitrite reduction *(7, 8)*; stacked-heme motifs and unusual heme ligation are involved in the catalytically opposite reaction of nitrification and nitrate ammonification *(9-11)*; and novel four-copper center provides the active site for nitrous oxide reduction *(12)*. These active site architectures are discussed in detail below.

Nitrogen fixation and nitrogenase

Biological nitrogen fixation catalyzes the conversion of gaseous dinitrogen (N_2) to ammonia (NH_3) *(7, 8)*. The extremely stable triple bond of N_2 provides a kinetic challenge to oxidize or reduce. The industrial method of doing so, called the Haber-Bosch process, requires extreme temperatures (~800 K) and pressures (~500 atm) as well as an iron catalyst to drive what should be a thermodynamically favorable process *(13, 14)*. In contrast, obligate anaerobic nitrogen-fixing bacteria can accomplish this reaction at ambient temperatures and pressures using a variety of interesting iron-containing cofactors and produces a significantly greater amount of ammonia (~170×10^9 kg) per year than does the industrial process (~80×10^9 kg). Several types of nitrogenases are recognized. Although the molybdenum-containing nitrogenase, described in detail below, is by far the best-studied, some organisms have alternative nitrogenase systems containing vanadium and iron, or iron exclusively *(15)*.

The reaction catalyzed by the molybdenum-containing nitrogenase requires the input of approximately 16 ATP molecules *(16)*, but still acts as the only energy source for nitrogen-fixing bacteria (Equation 5.1).

$$N_2 + 8H^+ + 16\ MgATP \rightarrow 2NH_3 + H_2 + 16\ MgADP + 16\ Pi \qquad (5.1)$$

The molybdenum-containing nitrogenase system involves two main components: the molybdenum-iron (MoFe) protein and the iron (Fe) protein. The MoFe-protein exists as a ~300 kD $\alpha_2\beta_2$ heterotetrameric complex *(17-19)* (Figure 5.1). Two unusual iron-containing clusters are associated with the MoFe-protein: an [8Fe:7S] EPR-silent cluster (P-cluster) thought to participate in electron transfer *(20-22)*; and the active site iron-molybdenum cofactor *(20, 21)* (FeMoCo; Figure 5.2). The FeMoCo contains 7 irons, 1 molybdenum atom, 1 homocitrate, and 9 bridging sulfur atoms and is ligated to the protein by only two protein ligands, one cysteine to an iron atom and one histidine to the molybdenum. The coordination sphere of the molybdenum is octahedral, and the sphere is completed by three of the bridging sulfurs of the FeMoCo and two contacts to the homocitrate. Although it is largely accepted that the FeMoCo is the active site *(23-25)*, evidence for the catalytic roles of each of the two cofactors of the MoFe-protein remains largely circumstantial. However, changes in the cofactor or the surrounding environment of the FeMoCo can drastically affect reduction of the substrate.

The Fe-protein couples the hydrolysis of MgATP *(26, 27)* to the electron transfer to the MoFe-protein that provides the reducing equivalents necessary for the reduction of N_2. The Fe-protein acts as a homodimer with a dimeric molecular weight of ~60,000 and contains one [4Fe:4S] cluster at the dimer interface *(28)*. Two ATP molecules bind per

dimer of reduced Fe-protein, allowing a conformational change upon association with the MoFe-protein *(29)*. This necessary conformational change pushes the [4Fe:4S] cluster out so that it lies within 14 Å of the P-cluster of the MoFe-protein and the ability of the protein to drastically alter its structure may be reflected in the conformational variability of the Fe-protein *(30)*. Upon ATP hydrolysis, the complex between the MoFe-protein and Fe-protein disassociates, allowing the cycle to repeat until eight electrons are incorporated into N_2. Concomitant with the reducing equivalents is the association of the substrate with protons, however a proton channel has not yet been conclusively established in the MoFe-protein.

Nitrification and Nitrate Ammonification

Nitrification and nitrite ammonification are essentially opposite reactions interconverting NO_2^- and NH_4^+ (equation 5.2); nitrification cycles the electrons to terminal oxidases, whereas nitrite ammonification uses NO_2^- as the terminal electron acceptor in the electron transport chain.

$$NH_4^+ \rightarrow NO_2^- + 8H^+ + 6e^- \qquad (5.2)$$

Nitrification removes biologically active NH_4^+ from the soil in an obligatory aerobic process and converts it to nitrite with hydroxylamine as the intermediate. Although

farmers may resent the loss of NH_4^+-containing fertilizer by nitrification, it is necessary for the production of a second important inorganic nitrogen compound that can be readily assimilated into the biomass: NO_3^- *(31)*. The bioenergetic pathway of the organism *Nitrosomonas europaea* represents the most extensively studied system of nitrification, however gene hybridization studies *(32)* suggest that similar enzymes are used for nitrification in other nitrifying bacteria, including *Nitrobacter* and *Nitrosospira.* Two enzymes function in the nitrification pathway: hydroxylamine oxidoreductase (HAO) and ammonia monooxygenase (AMO) *(4, 33)*. The former is a trimer (Figure 5.1) containing eight hemes per monomer arranged in stacked pairs (Figure 5.3a), with the active site P460 heme covalently attached to a tyrosine *(34)*. The latter is an integral-membrane protein with sequence identity to particulate methane monooxygenase that contains copper and iron cofactors *(35-37)*. Electrons released by the oxidation of NH_4^+ are transferred by a tetraheme cytochrome *(38)* (cytochrome *c554*) and a monoheme cytochrome *(39)* (cytochrome *c552*) to the terminal oxidases of the electron transport chain *(40, 41)*. Intriguingly, the heme core of cytochrome *c554* appears to be entirely contained within its redox partner HAO despite the lack of sequence identity *(9)*(Figure 5.3b). The evolutionary relationship between HAO and cytochrome *c554* will be discussed in detail in the following three chapters.

Nitrite ammonification catalyzed by cytochrome *c* nitrite reductase requires a protein acting as a physiological dimer (Figure 5.1) with five hemes per monomer *(10)*. The hemes are stacked in the same manner as observed in hydroxylamine oxidoreductase and cytochrome *c554 (10, 11, 42)*(Figure 5.3c), suggesting evolutionary convergence between these proteins catalyzing the same reaction in opposite directions. The active site lies above a five-coordinate heme, where the fifth ligand is a lysine rather than a histidine that is normally found in the C-x-y-C-H *c*-heme binding motif *(10)*.

Nitrite oxidation

Nitrite oxidation converts NO_2^- to NO_3^-, which is more readily incorporated into the biomass (Figure 5.1). This reaction is catalyzed by an integral-membrane protein, nitrite oxidase, about which very little is known. Nitrite oxidase exhibits significant sequence similarity to a membrane-bound nitrate reductase that catalyzes the reaction in the opposite direction. As other soluble proteins are involved in nitrate reduction, most studies have focussed on these more facile systems.

Denitrification

Denitrification is the process by which bacteria that use nitrogen oxidized compounds rather than oxygen as the terminal electron acceptor in respiration. These metabolic processes return N_2 to the atmosphere, completing the nitrogen cycle. The

commercial importance of denitrification lies in the depletion of NO_3^- from fixed nitrogen fertilizer. Conversely, denitrification fulfills an important role in wastewater treatment *(43, 44)*. One disadvantage of the "leaky" denitrification process is the release of large amounts of the greenhouse gas N_2O into the atmosphere.

Denitrification occurs in both assimilatory and dissimilatory pathways *(44)*. The assimilatory pathways (Figure 5.1) reduce nitrogen oxide compounds in the physiologically opposite direction as nitrification such that the end product is NH_4^+ *(45, 46)*. The annual regeneration of NH_3 from NO_3^- and NO_2^- by assimilatory denitrification returns approximately 100 times the amount of NH_3 that is generated by nitrogen fixation *(47)*. The dissimilatory pathway of nitrification (Figure 5.1) reduces nitrogen to N_2.

Nitrate reduction

The reduction of nitrate to nitrite is catalyzed by a heterogeneous group of molybdoenzymes that are similar in active site organization. Nitrate reductases (NaR) can be broadly categorized as assimilatory and dissimilatory. The assimilatory NaRs catalyze the reduction of NO_3^- to NH_4^+. The enzyme forms homodimers with a molecular weight of ~220 kD, and contains three cofactors: a molybdenum cofactor (MoCo; Figure 5.4a), a *b*-type heme, and an FAD/$NADP^+$ binding site *(48)*. Although no structural information is available for an assimilatory nitrate reductase, sequence analyses show that

sulfite oxidase can act as a structural model for the majority of this enzyme *(49, 50)*. Sulfite oxidase contains the domains associated with the MoCo and the *b*-type heme, but does not contain the domain that binds FAD/$NADP^+$. The fold of sulfite oxidase can be divided into three domains that contain a mixed α/β fold (Figure 5.1); the first domain has structural similarity to cytochrome b_5, the second domain binding the MoCo appears structurally unique, while the third domain contains a greek-key motif *(51)*. The active site consists of a single molybdopterin bound deeply within the protein. Residues involved in cofactor binding are conserved between the sequences of nitrate reductases and sulfite oxidase, thus the active site of sulfite oxidase should represent a reasonable model for nitrate reductases. In sulfite oxidase, the substrate binds near the vicinity of the oxo-ligand to the MoCo in a positively charged pocket, suggesting its position during catalytic turnover.

In contrast, the dissimilatory nitrate reductases (Figure 5.1) catalyze the reduction of NO_3^- to NO_2^-, and have significant sequence and structural similarity to DMSO reductase *(52, 53)* and formate dehydrogenase *(54)*. The dissimilatory nitrate reductases (DNaR) act as the primary respiratory enzymes in nitrate reduction. DNaR folds into four distinct domains *(55)* with pronounced structural similarity to formate dehydrogenase (rms deviation of 1.47 Å) but exhibits a slightly more divergent fold to DMSO reductase. DNaR acts as an ~80 kD monomeric enzyme with a molybdenum

atom coordinated to a molybdopterin guanine dinucleotide (MGD) as the active site (Figure 5.4b). A [4Fe:4S] cluster positioned ~12 Å away from the molybdenum transports electrons into the active site for nitrate reduction. The reaction catalyzed by DNaR involves binding of the substrate NO_3^- to an open ligation position of the molybdenum, with the molybdenum removing one oxygen to form an oxo-ligand previously observed in several MGD containing protein structures.

Nitrite reduction

Like nitrate reduction, nitrite reduction can occur as an assimilatory or dissimilatory process. The assimilatory nitrite reductases (NiR) reduce NO_2^- to NH_4^+ in a process with no detectable intermediates, with a flavodoxin likely acting as the phsyiological electron donor. Assimilatory NiRs have an active site containing a [4Fe:4S] cluster linked to a siroheme *(56, 57)* (Figure 5.5) and share significant sequence similarity to sulfite reductases. No structural information is currently available for an assimilatory NiR, although the structure of sulfite reductase (SiR) *(58)* can yield insight into the function of the enzyme. Indeed SiR can catalyze assimilatory denitrification *(59, 60)*, albeit with a much slower rate than it catalyzes sulfite reduction or that physiological assimilatory NiRs catalyze denitrification. SiR comprises a monomer that folds into three domains with pseudo-twofold symmetry *(58)* (Figure 5.1). The non-covalently bound siroheme is positioned at the center of the three domains and acts as the active site.

The pocket surrounding the open ligation site of the five-coordinate siroheme contains numerous basic residues as well as many solvent molecules that participate in a complicated hydrogen-bonding network. This positively charged active site should have a high affinity for oxo-ligands, as reflected by the presence of a phosphate acquired from the crystallization conditions binding in the reduced form of the enzyme. In the presence of the substrate, the phosphate is replaced by sulfite.

Numerous organisms and enzymes can catalyze the dissimilatory reduction of NO_2^- to NO, and two distinct classes of nitrite oxide reductases have been recognized: the heme cd_1-containing and the copper-containing nitrite reductases *(1, 44)*. The heme cd_1-containing nitrite reductases (CDNiR) are the more abundant in nature, whereas the copper-nitrite reductases (CuNiR) are perhaps better studied.

CDNiRs are bifunctional enzymes that catalyze the one-electron reduction of nitrite to nitric oxide (equation 5.3) or the four-electron reduction of oxygen to water, however, NO_2^- reduction represents the main physiological reaction *(61)*. The physiological electron donor for this reaction appears to be cytochrome *c551 (62, 63)*.

$$NO_2^- + 2H^+ + e^- \rightarrow NO + H_2O \qquad (5.3)$$

CDNiR contains two hemes: a *c*-type and an unusual non-covalently bound d_1-type heme that acts as the active site *(61)*. The enzyme acts as a functional dimer *(64)* with each monomer containing a helical domain ligating the *c*-type heme and a β-propeller domain containing the d_1-heme *(65)*. Based on comparisons to *c*-cytochromes, the *c*-heme was predicted to have His-Met ligation. It was therefore a surprise when the crystal structure showed His-His coordination in the oxidized state. Later analysis of CDNiR under reducing conditions showed that a large conformational change occurs in the domain binding the *c*-heme, switching the distal ligand from His 17 to Met 106 *(66)* (Figure 5.6). Based on previous small angle x-ray scattering experimetns *(67)*, a large conformational change of the protein had been expected.

Like the *c*-heme, the catalytic d_1-heme undergoes ligand switching during catalysis *(66)*. The original structure determination showed that a tyrosyl phenoxy group ligated the open ligation position of the d_1-heme during the resting, oxidized state. In the presence of reaction intermediates or product, the tyrosine side chain rotates around chi1 either to stabilize the product through a hydrogen bond, or to form an alternative hydrogen bond with the side chain of a threonine when the reaction intermediates are present (Figure 5.7)

Copper-containing NiRs (CuNiRs) appear pink, blue, or green depending on the state of the enzyme and physiologically accept electrons from azurin to perform nitrite reduction *(2, 3, 44)* (equation 5.3). CuNiRs exist as trimers (monomeric molecular weight of ~35 kD) with two distinct copper centers ligated at the interface between the monomers *(68)*. Copper center 1 exhibits similar ligation as the plastocyanin or azurin copper ligation and is known as the "blue" copper *(69)*. The second, "non-blue" copper center exhibits tetrahedral coordination by three hisitidine side chains, two of which are provided by one monomer, while the third is provided by a second monomer, and a water molecule *(68)*. This second copper center is believed to represent the active site of the enzyme. Crystal structures show that NO_2^- replaces the copper-bound water molecule, changing the almost perfect tetrahedral coordination to asymmetric five-coordinate ligation through the binding of two oxygen atoms of the NO_2^- *(69-71)*. However, most proposed reaction mechanisms involve the N-bound to the active site copper. Protons that reduce the oxygen to water may be shuttled to the active site by a conserved aspartate side chain.

Nitric oxide reduction

Nitric oxide (NO) serves as a messenger molecule for a variety of biological functions, however can be toxic to cells. In lower organisms, nitric oxide levels are diminished immediately after nitrite reduction by further reduction to nitrous oxide.

Nitric oxide reduction occurs via a cytochrome *bc* complex in prokaryotes, and by a heme-containing enzyme in eukaryotic fungal systems *(44)*. The bacterial nitric oxide reductases (NORs) consist of an integral-membrane heterodimer with subunit molecular weights of 53 and 17 kD *(72-76)*, and appear to contain both low- and high-spin hemes as well as non-heme iron *(76)*. The high-spin heme is likely five-coordinate thus may serve as the active site of the enzyme. Little else is known regarding the mechanism of reduction of NO by the bacterial NOR complex

In the fungus *Fusarium oxysporum*, a monomeric water-soluble heme enzyme *(77)* with a molecular weight of 46,000 (Figure 5.1) catalyzes NO reduction (equation 5.4).

$$2NO + NADH + H^+ \rightarrow N_2O + NAD^+ + H_2O \qquad (5.4)$$

The fungal NO reductase (NOR) exhibits significant sequence and structural similarity to monooxygenase P450 superfamily *(78)*. However, compared to structures of the active site in the P450 superfamily *(79)*, the helices surrounding the open ligation site of the heme are pushed back, allowing a larger cavity for the reaction to take place *(80)*. The reduction of NO occurs at a five-coordinate heme as the active site with a cysteine thiolate as the fifth axial ligand rather than a histidine normally present in the C-x-y-C-H

c-heme binding motif. The ferric state of the enzyme appears to be a non-functional resting state, while the ferrous state forms a water molecule network between the active site heme iron and solvent, suggesting a plausible proton transfer pathway. Crystallographic investigation has implicated one of these water molecules as a proton donor to the Fe-NO moiety during catalysis *(81)*. There does not appear to be an obvious binding-site for NADH, and it has been suggested that NADH physically enters the active site after NO is bound to the heme, donating the electron directly to the substrate *(80)*.

Nitrous oxide reduction

Nitrous oxide is a major greenhouse gas *(6)*, thus understanding the biological reduction has environmental implications. The penultimate step of denitrification requires the conversion of N_2O to N_2 (equation 5.5).

$$N_2O + 2H^+ + 2e^- \rightarrow N_2 + H_2O \qquad (5.5)$$

Nitrous oxide reductase (N2OR) has long been known to contain two copper centers: Cu_A and the active site Cu_Z *(82)*. Cu_A has spectral properties similar to Cu_A from respiratory complex IV*(83, 84)*, and the sequence ligating Cu_A to N2OR shares significant similarity to the sequence that ligates Cu_A of complex IV *(85)*. It was therefore not surprising to find a similar fold associated with the ligation of Cu_A from

both proteins *(12)*. The nature of the Cu_Z copper center of N2OR has remained more mysterious. Metal quantification and spectroscopy had suggested that Cu_Z likely existed as either a mono- or bi-nuclear cluster *(86, 87)*. The novel tetra-nuclear cluster revealed by the crystal structure *(12)* was therefore a surprise. This cluster is ligated with distorted geometry to the polypeptide chain by seven conserved histidine ligands (Figure 5.8) and is associated with two additional water molecule ligands. It is believed that substrate binding occurs by replacement of one of the two water molecule ligands and that the tetra-nuclear center provides and electron-sink for catalysis.

N2OR acts as a physiological dimer with dimeric molecular weight of 130 kD. Each monomer folds into a β-propeller, however the dimeric associated is involves a rotation of the second monomer 90° with respect to that observed for dimeric association of the cytochrome cd_1 nitric oxide reductase *(65)* (Figure 5.1).

Anaerobic ammonia Oxidation (ANAMOX)

The process of anaerobic ammonia oxidation (ANAMOX) is the most recent nitrogen cycle reaction to be described *(88)*. Bacteria that can catalyze this process can grow under chemolithoautotrophic conditions using ammonia as an electron donor and nitrite as an electron acceptor (equation 5.6)

$$NH_3 + NO_2^- \rightarrow N_2 + H_2O \qquad (5.6)$$

The reaction intermediates for this pathway may include hydrazine *(89)*, and can generate transmembrane potential if hydrazine oxidation occurs at the periplasmic face of the cytoplasmic membrane. Although the ANAMOX phenomenon has been known for two years, the first organism catalyzing ANAMOX was only discovered last year *(90)* and represents a new type of bacterium. The enzymology of the reaction(s) involved remains uncertain.

The discovery of new pathways and organisms involved in the biological nitrogen cycle acts as a reminder that the current understanding of the interconversion of inorganic nitrogen may include many as yet undiscovered components.

Figure 5.1 (next page): The enzymatic components of the biological nitrogen cycle. Protein components of nitrogenase have been solved from *Azotobacter vinelandii* (1NIP, 2NIP *(28)*; 2MIN, 3MIN *(22)*; 1DE0, *(97)*), *Clostridium pasteurianum* (1MIO, *(18)*; 1CP2, *(30)*), and *Klebsiella pneumonae* (1QGU, 1QH1, 1QH8, *(19)*). The *Azotobacter vinelandii* (1N2C, *(29)*) complex is shown. Hydroxylamine oxidoreductase has been solved from *Nitrosomonas europaea* (1FGJ, *(34)*). Cytochrome *c* nitrite reductase has been solved from *Sulfurospirillum deleyianum* (1QDB, *(10)*). The assimilitory nitrite and nitrate reductases have been modeled from the structures of the *Escherichia coli* sulfite reductase (1AOP, *(58)*; 2AOP, 3AOP, 2GEP, 3GEO, 4AOP, 4GEP, 5AOP, 5GEP, 6GEP, 7GEP, 8GEP, *(96)*) and the chicken liver sulfite oxidase (1SOX, *(51)*), respectively. Nitrate reducase has been solved from *Desulfovibrio desulfuricans* (2NAP). Cytochrome cd_1 nitrite reductase has been solved from both *Thiospaera pantotropha* (1QKS, *(65)*; 1AOF, 1AOM, 1AOQ, *(66)*) and *Pseudomonas aeruginosa* (1BL9, 1NNO, *(92)*; 1N15, 1N50, 1N90, *(94)*; 1NIR, *(64)*). Copper nitrite reductases have been solved from *Alcaligenes faecalis* (1AFN, 1NTD, *(70)*; 1AQ8, 1AS6, 1AS7, 1AS8, *(91)*), *Alcaligenes xylosoxidans* (1BQ5 *(93)*; 1NDR, 1NDS, 1NDT *(71)*), and *Achromobacter cycloclastes* (1NIA, 1NIB, 1NIC, 1NID, 1NIE, 1NIF, *(95)*). Nitric oxide reductase has been solved from *Fusarium oxysporum* (1ROM, 2ROM, *(80)*; 1CL6 1CMJ, 1CMN *(81)*). Nitrous oxide reductase has been solved from *Pseudomonas nautica* (1QNI, *(12)*).

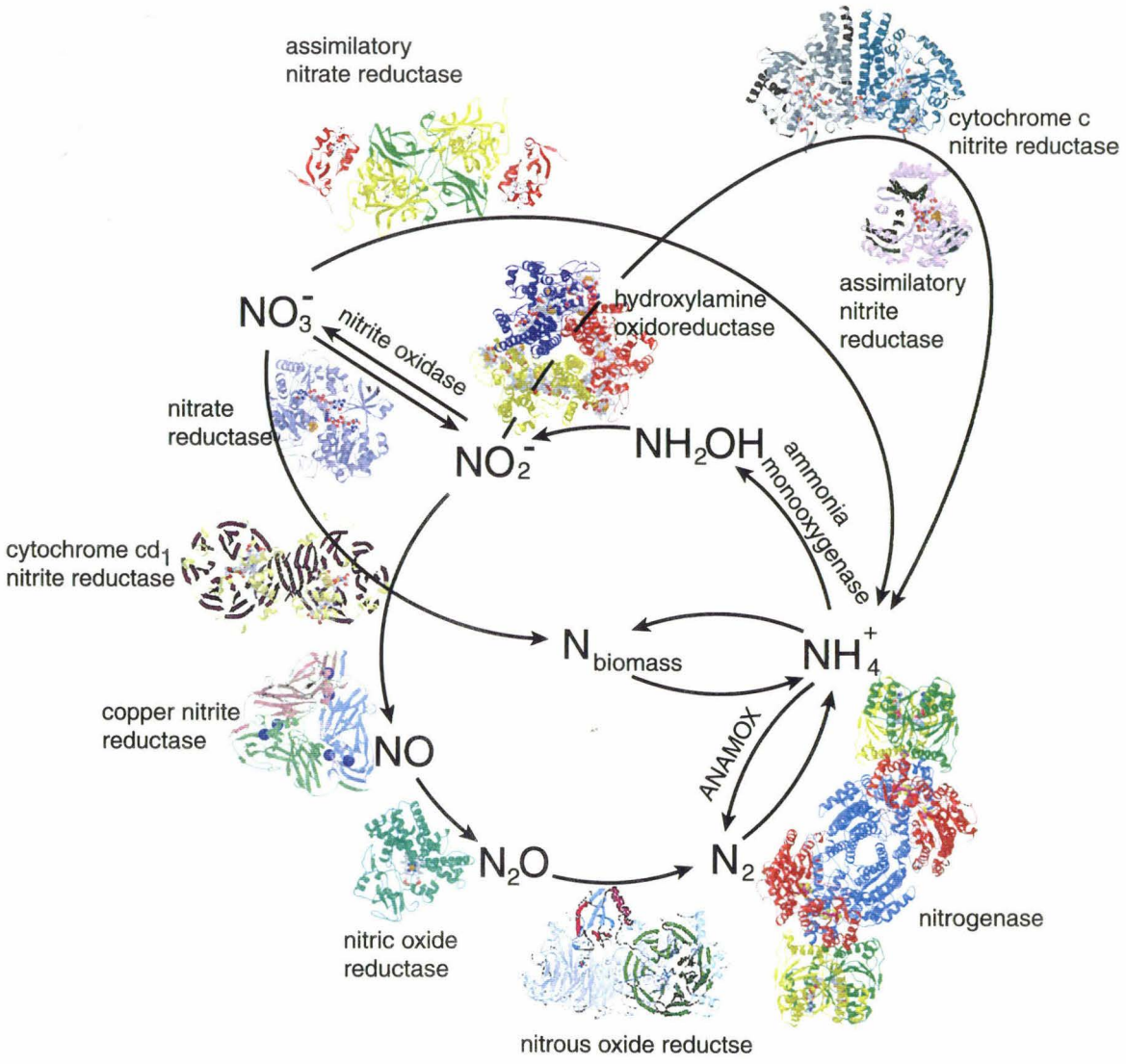

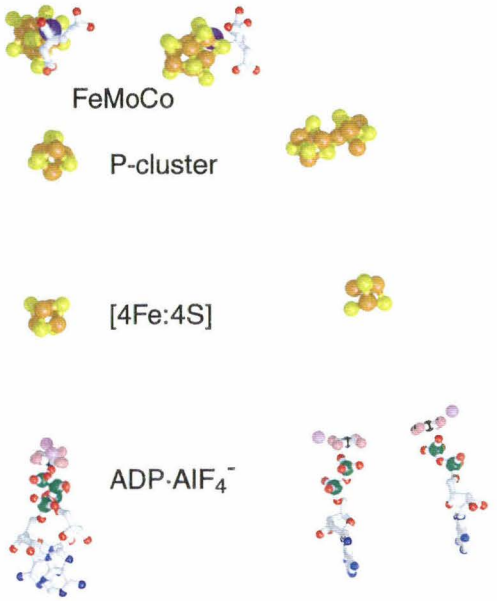

Figure 5.2: The cofactors of the nitrogenase system. The two views are separate by 90°. The FeMoCo and P-cluster are located in the Mo-Fe protein while the [4Fe:4S] cluster and ADP·ALF_4^- are located in the iron protein.

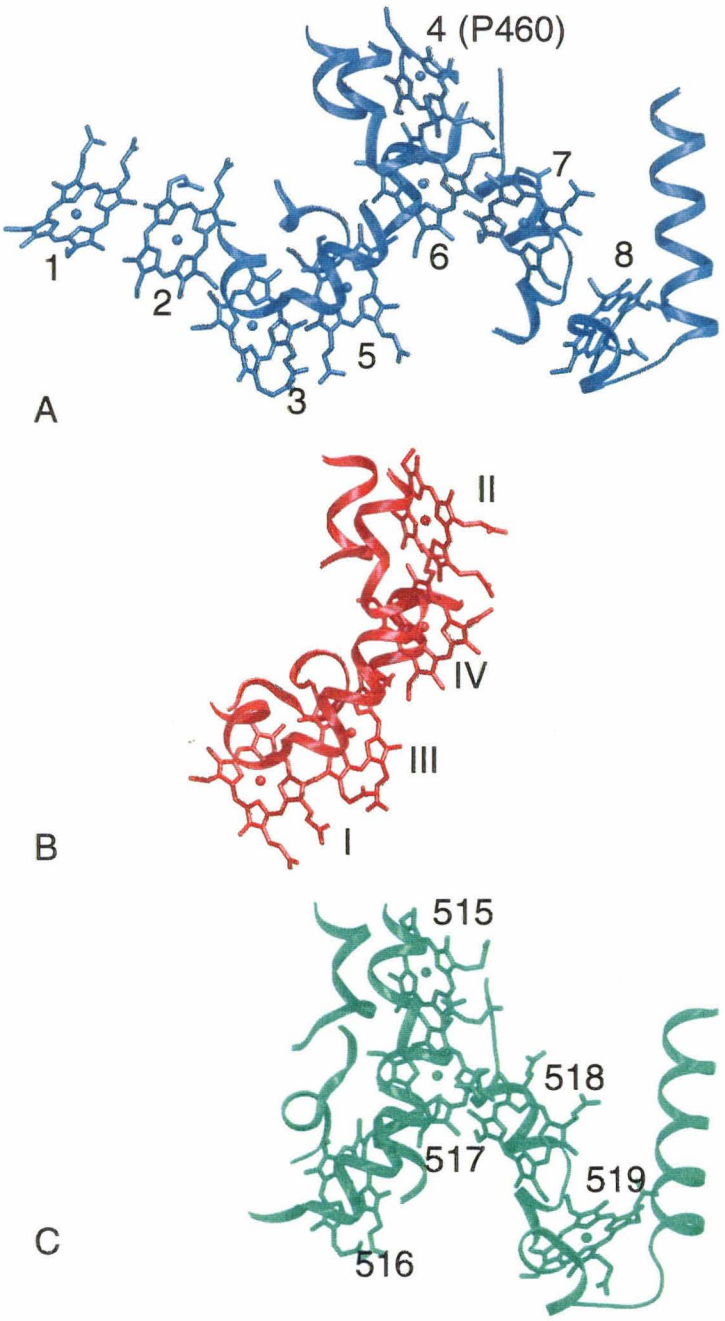

Figure 5.3: Heme-packing motifs of proteins involved in nitrification and nitrite ammonification. The hemes of each protein are labeled in the order of their ligation to the polypeptide chain using the author's numbering scheme. A. The eight hemes of HAO. B. The four hemes of cytochrome *c554*. C. The five hemes of cytochrome *c* nitrite reductase. All proteins are shown from the same relative view. Intriguingly, a five-coordinate heme aligns in each of these proteins. In HAO (heme P460) and cytochrome *c* nitrite reductase (heme 515), the five-coordinate heme is associated with catalytic activity, whereas in cytochrome *c554* (heme II), the only known function of the five-coordinate heme is in electron transfer.

Figure 5.4: Molybdenum-containing cofactors *(98)*. A. Stereoview of the molybdenum cofactor (MoCo) from sulfite oxidase. The pterin ring is highly bent. B. The MGD cofactor found in nitrate reductase requires two pterins with a nucleotide extention. The two cofactors are not shown to scale.

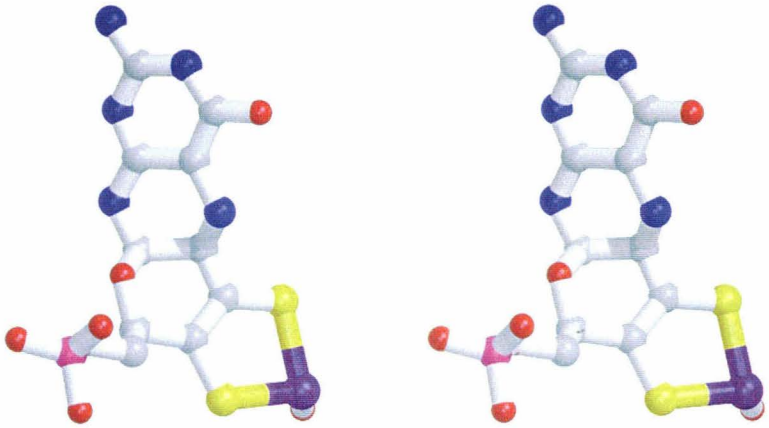

A

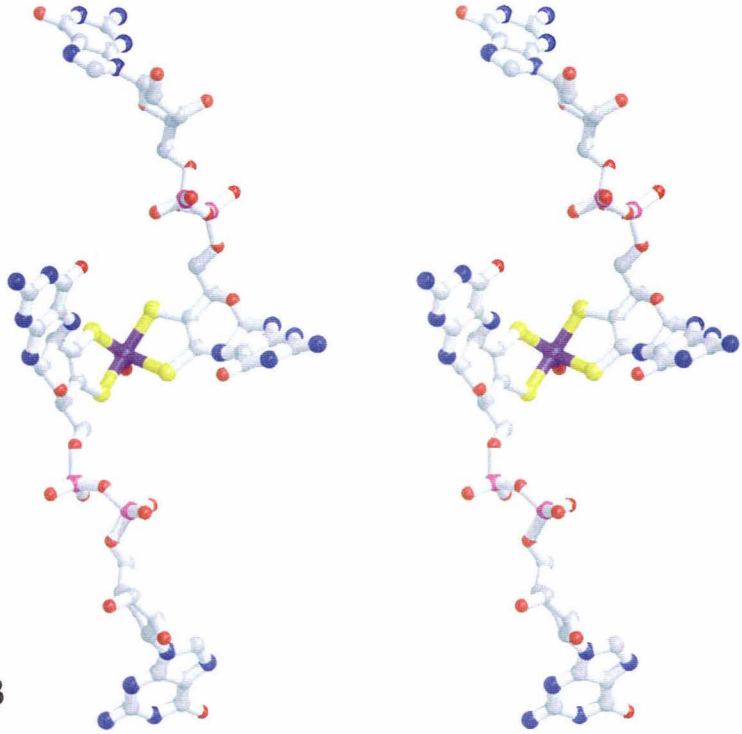

B

Figure 5.5: Stereoview of the siroheme of sulfite reductase. The structure of the cofactor will be similar to that of the assimilatory nitrite reductase. A siroheme differs from a *c*-type heme in that the pyrrole rings are saturated with dicarboxylate groups. The iron of the siroheme is bridged to the [4Fe:4S] cluster by Cys 483 of sulfite reductase. The binding of phosphate to the distal side of the siroheme shows where substrate binds.

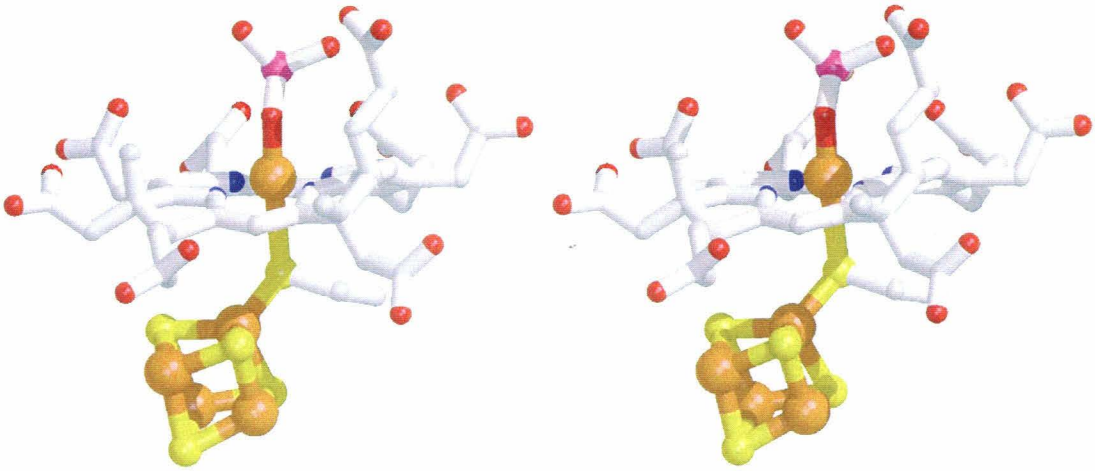

Figure 5.6: Ligand switching to the *c*-heme of the cd_1 nitrite reductase. The panel on the left shows the *c*-heme ligation under oxidizing conditions where His 17 acts as the heme iron ligand. Under reducing conditions (right panel), the long loop changes conformation with the simultaneous unfolding of the N-terminus to residue 26. Met 106 then acts and the heme iron ligand.

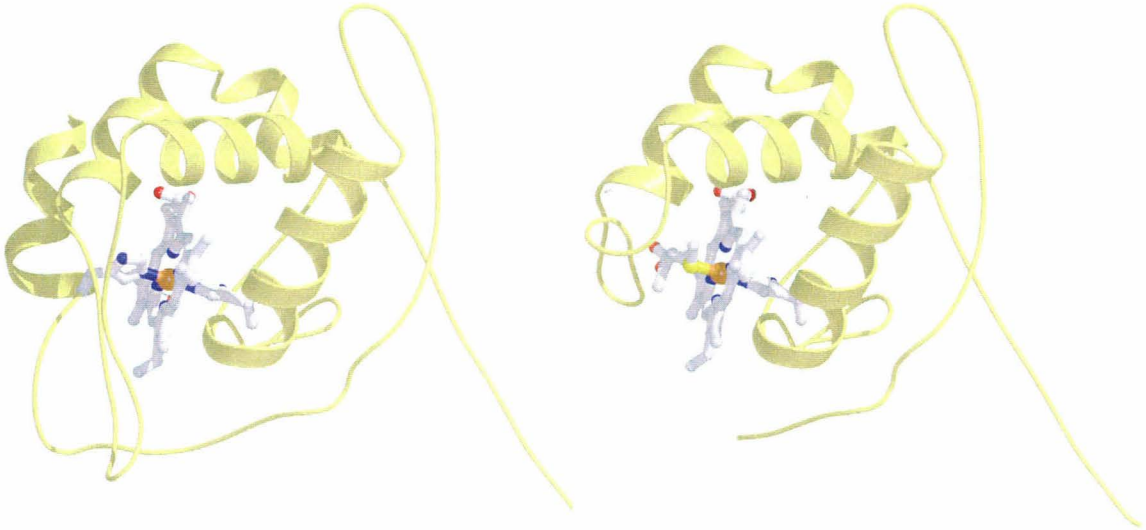

Figure 5.7: Stereoview of the movement of Tyr 25 during catalysis by cytochrome cd_1 nitrite reductase. In the oxidized form of the enzyme, Tyr 25 directly ligates the heme iron (blue position). Upon the addition of substrate, the tyrosine swings away (green position) to allow access to the binding site. During catalysis, Tyr 25 swings back such that it makes contact to the reaction intermediates (red position), possibly stabilizing the transition state.

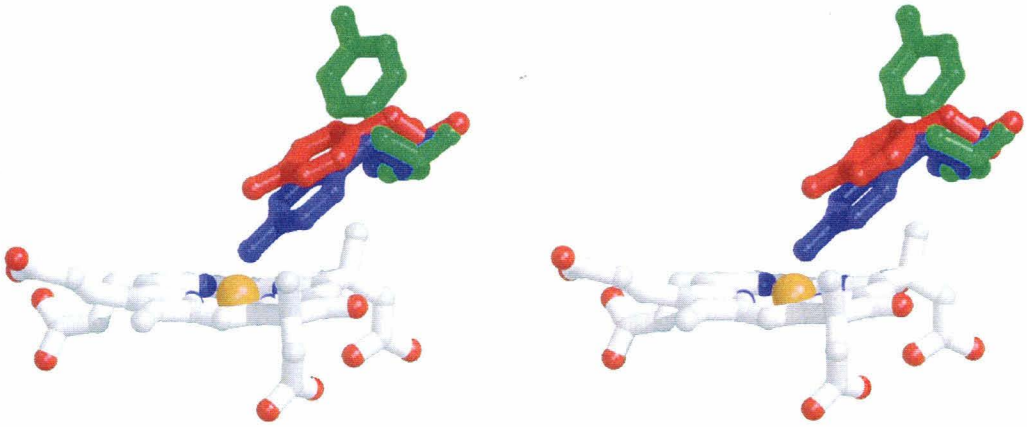

Figure 5.8: Stereoview of the Cu_Z center of nitrous oxide reductase. The four copper ions of Cu_Z form a diamond and are coordinated by seven histidine residues from the protein. The substrate N_2O has been modeled to interact with Cu IV, replacing a position filled by an ordered water molecule in the structure determination.

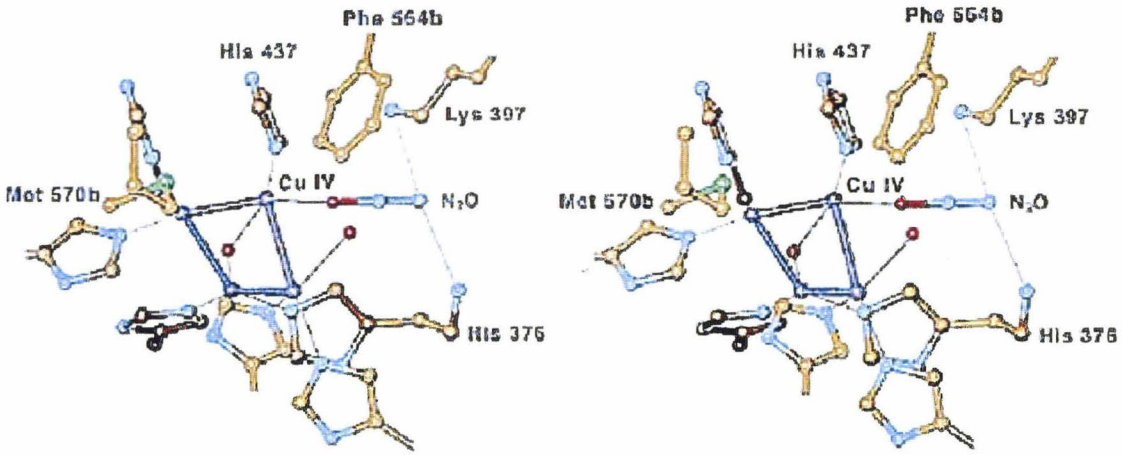

REFERENCES

1. Berks, B. C., Ferguson, S. J., Moir, J. W. B., and Richardson, D. J. (1995) *Biochim. Biophys. Acta 1231*, 97-173.

2. Ferguson, S. J. (1998) *Curr. Op. Chem. Biol. 2*, 182-193.

3. Richardson, D. J., and Watmough, N. J. (1999) *Curr. Op. Chem. Biol. 3*, 207-219.

4. Wood, P. M. (1986) in *Nitrification* (Prosser, J. I., Ed.) pp 39-62, IRL Press, Oxford.

5. Hutchins, H. (1991) *Appl. Environ. Microbiol. 57*, 2403-2407.

6. Rasmussen, R. A., and Khalil, M. A. K. (1986) *Science 232*, 1623-1624.

7. Howard, J. B., and Rees, D. C. (1996) *Chem. Rev. 96*, 2965-2982.

8. Burgess, B. K., and Lowe, D. J. (1996) *Chem. Rev. 96*, 2983-3011.

9. Iverson, T. M., Arciero, D. M., Hsu, B. T., Logan, M. S. P., Hooper, A. B., and Rees, D. C. (1998) *Nat. Struct. Biol. 5*, 1005-1012.

10. Einsle, O., Messerschmidt, A., Stach, P., Bourenkov, G. P., Bartunik, H. D., Huber, R., and Kroneck, P. M. H. (1999) *Nature 400*, 476-480.

11. Iverson, T. M., Arciero, D. M., Hooper, A. B., and Rees, D. C. (in preparation) *J. Biol. Inorg. Chem.*

12. Brown, K., Tegoni, M., Prudencio, M., Oereira, A. S., Besson, S., Moura, J. J., Moura, I., and Cambillau, C. (2000) .

13. Topham, S. A. (1985) in *Catalysis: Science and Technology* (Anderson, J. R., and Boudart, M., Eds.), Springer-Verlag, Berlin.

14. Jennings, J. R. (1991) , Plenum Press, New York.

15. Eady, R. R. (1996) *Chem. Rev. 96*, 3013-3030.

16. Alberty, R. A. (1994) *J. Biol. Chem. 269*, 7099-7102.

17. Kim, J., and Rees, D. C. (1992) *Nature 360*, 553-560.

18. Kim, J., Woo, D., and Rees, D. C. (1993) *Biochemistry 32*, 7104-7115.

19. Mayer, S. M., Lawson, D. M., Gormal, C. A., Roe, S. M., and Smith, B. E. (1999) *J. Mol. Biol. 292*, 871-891.

20. Kim, J., and Rees, D. C. (1992) *Science 257*, 1677-1682.

21. Chan, M. K., Kim, J., and Rees, D. C. (1993) *Science 260*, 792-794.

22. Peters, J. W., Stowell, M. H. B., Soltis, M., Finnegan, M. G., Johnson, M. K., and Rees, D. C. (1997) *Biochemistry 36*, 1181-1187.

23. Hawkes, T. R., Lowe, D. J., and Smith, B. E. (1983) *Biochem. J. 211*, 495-497.

24. Hawkes, T. R., McLean, P. A., and Smith, B. E. (1984) *Biochem. J. 217*, 317-321.

25. Imperial, J., Hoover, T. R., Madden, M. S., Ludden, P. W., and Shah, V. K. (1989) *Biochemistry 28*, 7796-7799.

26. Howard, J. B., and Rees, D. C. (1994) *Annu. Rev. Biochem. 63*, 235-264.

27. Seefedt, L. C., and Dean, D. R. (1997) *Acc. Chem. Res. 30*, 260-266.

28. Georgiadis, M. M., Komiya, H., Chakrabarti, P., Woo, D., Kornuc, J. J., and Rees, D. C. (1992) *Science 257*, 1653-1659.

29. Schindelin, H., Kisker, C., Schlessman, J. L., Howard, J. B., and Rees, D. C. (1997) *Nature 387*, 370-376.

30. Schlessman, J. L., Woo, D., Joshua-Tor, L., Howard, J. B., and Rees, D. C. (1998) *J. Mol. Biol. 280*, 669-685.

31. Prince, R. C., and George, G. N. (1997) *Nat. Str. Biol. 4*, 247-250.

32. Bruns, M. A., Fries, J. M., Tiedje, J. M., and Paul, E. A. (1998) *Microb. Ecol. 36*, 293-302.

33. Hooper, A. B., Vannelli, T., Bergmann, C. J., and Arciero, D. M. (1997) *Anton. van Lieuwenhoek 71*, 56-67.

34. Igarashi, N., Moriyama, H., Fujiwara, T., Fukumori, Y., and Tanaka, N. (1997) *Nat. Struct. Biol. 4*, 276-284.

35. Shears, J. H., and Wood, P. M. (1985) *Biochem. J. 226*, 499-507.

36. Zahn, J. A., and Dispirito, A. A. (1996) *J. Bacteriol. 178*, 1018-1029.

37. Zahn, J. A., Arciero, D. M., Hooper, A. B., and DiSpirito, A. A. (1996) *FEBS Lett. 397*, 35-38.

38. Andersson, K., Lipscomb, J., Valentine, M., Münck, E., and Hooper, A. (1986) *J. Biol. Chem. 261*, 1126-1138.

39. Timkovich, R., Bergmann, D., Arciero, D. M., and Hooper, A. B. (1998) *Biophys. J. 75*, 1964-1972.

40. Yamanaka, T., and Shinra, M. (1974) *J. Biochem. 75*, 1265-1273.

41. Yamanaka, T. (1996) *Plant Cell Physiol. 37*, 569-574.

42. Iverson, T. M., Hendrich, M. P., Arciero, D. M., Hooper, A. B., and Rees, D. C. (in preparation) in *Metalloprotein handbook* (Poulos, T., Ed.).

43. Mellor, R. B., Ronnenberg, J., Campbell, W. H., and Diekmann, S. (1992) *Nature 355*, 717-719.

44. Averill, B. A. (1996) *Chem. Rev. 96*, 2951-2964.

45. Cole, J. A., and Brown, C. M. (1980) *FEMS Microbiol. Lett. 7*, 65-72.

46. Wray, J. L., and Kinghorn, J. R. (1989) , Oxford Science Publications, Oxford.

47. Campbell, W. H., and Kinghorn, J. R. (1990) *Trends. Biochem. Sci. 15*, 315-319.

48. Kubo, Y., Ogura, N., and Nakagawa, H. (1988) *J. Biol. Chem. 263*, 19684-19689.

49. Neame, P. J., and Barber, M. J. (1989) *J. Biol. Chem. 264*, 20894-20901.

50. Wooton, J. C., Nicholson, R. E., Cock, J. M., Walters, D. E., Burke, J. F., Doyle, W. A., and Bray, R. C. (1991) *Biochim. Biophys. Acta 1057*, 157-185.

51. Kisker, C., Schindelin, H., Pacheco, A., Wehbi, W. A., Garrett, R. M., Rajagopalan, K. V., Enemark, J. H., and Rees, D. C. (1997) *Cell 91*, 973-983.

52. Schindelin, H., Kisker, C., Hilton, J., Rajagopalan, K. V., and Rees, D. C. (1996) *Science 272*, 1615-1621.

53. Schneider, F., Löwe, J., Huber, R., Schindelin, H., Kisker, C., and Knäblein, J. (1996) *J. Mol. Biol. 263*, 53-69.

54. Boyington, J. C., Gladyshev, V. N., Khangolov, S. V., Stadtman, T. C., and Sun, P. D. (1997) *Science 275*, 1305-1308.

55. Dias, J. M., Than, M. E., Humm, A., Huber, R., Bourenkov, G. P., Bartunik, H. D., Bursakov, S., Calvete, J., Caldeira, J., Carneiro, C., Moura, J. J. G., Moura, I., and Romao, M. J. (1999) *Structure 7*, 65-79.

56. Janick, P. A., Rueger, D. C., Krueger, R. J., Barber, M. J., and Siegel, L. M. (1982) *Biochemistry 21*, 3538-3547.

57. Wilkerson, J. O., Janick, P. A., and Siegel, L. M. (1983) *Biochemistry 22*, 5048-5054.

58. Crane, B. R., Siegel, L. M., and Getzoff, E. D. (1995) *Science 270*, 59-67.

59. Siegel, L. M., and Davis, P. S. (1974) *J. Biol. Chem. 249*, 1587-1593.

60. Janick, P. A., Rueger, D. C., Krueger, R. J., Barber, M. J., and Siegel, L. M. (1983) *Biochemistry 22*, 396-408.

61. Moir, J. W. B., Baratta, D., Richardson, D. J., and Ferguson, S. J. (1993) *Eur. J. Biochem. 212*, 377-385.

62. Greenwood, C., Barber, D., Parr, S. R., Antonini, E., Brunori, M., and Colosimo, A. (1978) *Biochem. J. 173*, 11-17.

63. Silverstrini, M. C., Tordi, M.G., Colosimo, A. A., E., and Brunori, M. (1982) *Biochem. J. 203*, 445-451.

64. Nurizzo, D., Silvestrni, M.-C., Mathieu, M., Cutruzzolá, F., Bourgeois, s. D., Fülöp, V., Hajdu, J., Brunori, M., Tegoni, M., and Cambillau, C. (1997) *Structure 5*, 1157-1171.

65. Fülöp, V., Moir, J. W. B., Ferguson, S. J., and Hajdu, J. (1995) *Cell 81*, 369-377.

66. Williams, P. A., Fülöp, V., Garman, E. F., Saunders, N. F. W., Ferguson, S. J., and Hajdu, J. (1997) *Nature 389*, 406-412.

67. Berger, H., and Wharton, D. C. (1980) *Biochim. Biophys. Acta 622*, 355-359.

68. Godden, J. W., Turley, S., Teller, D. C., Adman, E. T., Liu, M. Y., Payne, W. J., and LeGall, J. (1991) *Science 253*, 438-442.

69. Dodd, F. E., VanBeeumen, J., Eady, R. R., and Hasnain, S. S. (1998) *J. Mol. Biol. 282*, 369-382.

70. Murphy, M. E. P., Turley, S., Kukimoto, M., Nishiyama, M., Horinouchi, S., Sasaki, H., Tanokura, M., and Adman, E. T. (1995) *Biochemistry 34*, 12107-12117.

71. Dodd, F. E., Hasnain, S. S., Abraham, Z. H. L., Eady, R. R., and Smith, B. E. (1997) *Acta Cryst. D553*, 406-418.

72. Heiss, B., Frunzke, K., and Zumft, W. G. (1989) *J. Bacteriol. 171*, 3288-3297.

73. Carr, G. J., and Ferguson, S. J. (1990) *Biochem. J. 269*, 423-429.

74. Dermastia, M., Turk, T., and Hollocher, T. C. (1991) *J. Biol. Chem. 266*, 10899-10905.

75. Jones, A. M., and Hollocher, T. C. (1993) *Biochim. Biophys. Acta 1144*, 359-366.

76. Kastrau, D. H. W., Heiss, B., Kroneck, P. M. H., and Zumft, W. G. (1994) *Eur. J. Biochem. 222*, 293-303.

77. Shiro, Y., Fujii, M., Isogai, Y., Adachi, S., Iizuka, T., Obayashi, R., Makino, R., Nakahara, K., and Shoun, H. (1995) *Biochemistry 34*, 9052-9058.

78. Kizawa, H., Tomura, D., Oda, M., Fukamizu, A., Hoshino, T., Gotoh, O., Yasui, T., and Shoun, H. (1991) *J. Biol. Chem. 266*, 10632-10637.

79. Hasemann, C. A., Ravichandran, K. G., Boddupalli, S. S., Peterson, J. A., and Deisenhofer, J. (1995) *Structure 3*, 41-62.

80. Park, S.-Y., Shimizu, H., Adachi, S., Nakagawa, A., Tanaka, I., Nakahara, K., Shoun, H., Obayashi, E., Nakamura, H., Iizuka, T., and Shiro, Y. (1997) *Nat. Struct. Biol. 4*, 827-832.

81. Shimizu, H., Obayashi, E., Gomi, Y., Arakawa, H., Park, S.-Y., Nakamura, H., Adachi, S., Shoun, H., and Shiro, Y. (2000) *J. Biol. Chem. 275*, 4816-4826.

82. Zumft, W. G. (1997) *Microbiol. Mol. Biol. Rev. 61*, 533-616.

83. Kroneck, P. M. H., Antholine, W. E., Riester, J., and Zumft, W. G. (1988) *FEBS Lett. 242*, 70-74.

84. Antholine, W. E., Kastrau, D. H. W., Steffens, G. C. M., Buse, G., Zumft, W. G., and Kroneck, P. M. H. (1992) *Eur. J. Biochem. 209*, 875-881.

85. Holm, L., Saraste, M., and Wikström, M. (1987) *EMBO J. 6*, 2819-2823.

86. Farrar, J. A., Thomson, A. J., Cheesman, M. R., Dooley, D. M., and Zumft, W. G. (1991) *FEBS Lett. 294*, 11-15.

87. Farrar, J. A., Zumft, W. G., and Thomson, A. J. (1998) *Proc. Natl. Acad. Sci. USA 95*, 9891-9896.

88. Van de Graf, A., deBruijn, P., Robertson, L. A., Jetten, M. S. M., and Kuenen, J. G. (1998) *Microbiology 143*, 2415-2421.

89. Schalk, J., Outstad, H., Kuenen, J. G., and Jetten, M. S. (1998) *FEMS Microbiol. Lett. 158*, 61-67.

90. Strous, M., Fuerst, J. A., Kramer, E. H. M., Logemann, S., Muyzer, G., van de Pas-Schoonen, K. T., Webb, R., Kuenen, J. G., and Jetten, M. S. M. (1999) *Nature 400*, 446-449.

91. Murphy, M. E.P., Turley, S., Adman, E. T. (1997) *J Biol Chem 272*, 28455-28462.

92. Nurizzo, D., Cutruzzola, F., Arese, M., Bourgeois, D., Brunori, M., Cambillau, C., Tegoni, M. (1998) *Biochemistry 37,* 13987-13995.

93. Inoue, T., Gotowda, M., Deligeer, Kataoka, K., Yamaguchi, K., Suzuki, S., Watanabe, H., Gohow, M., Kai, Y. (1998) *J.Biochem.(Tokyo) 124*, 876-889.

94. Nurizzo, D., Cutruzzola, F., Arese, M., Bourgeois, D., Brunori, M., Cambillau, C., Tegoni, M. (1999) *J.Biol.Chem. 274*, 14997-15008.

95. Adman, E. T., Godden, J. W., Turley, S. (1995) *J Biol Chem 270*, 27458-27470.

96. Crane, B. R., Siegel, L. M., Getzoff, E. D. (1997) *Biochemistry 36*, 12120-12135.

97. Jang, S. B., Seefeldt, L. C., Peters, J. W. (2000) *Biochemistry 39,* 641-650.

98. Schindelin, H., Kisker, C., Rees, D.C. (1997) *J. Biol. Inorg. Chem. 2*, 773-781.

Chapter 6

Reprinted with permission from:

Iverson, T.M., Arciero, D.M., Hsu, B.T., Logan, M.S.P., Hooper, A.B., Rees, D.C. (1998) Heme-packing motifs revealed by the structure of the tetra-heme cytochrome *c554* from *Nitrosomonas europaea*. *Nat. Struct. Biol.* **5**: 1005-1012.

Copyright 1998, Nature America, Inc.

1998 Nature America Inc. • http://structbio.nature.com

Heme packing motifs revealed by the crystal structure of the tetra-heme cytochrome c554 from *Nitrosomonas europaea*

Tina M. Iverson[1], David M. Arciero[2], Barbara T. Hsu[3], Michael S.P. Logan[2,4], Alan B. Hooper[2] and Douglas C. Rees[3,5]

Cytochrome c554 (cyt c554), a tetra-heme cytochrome from *Nitrosomonas europaea*, is an essential component in the biological nitrification pathway. In *N. europaea*, ammonia is converted to hydroxylamine, which is then oxidized to nitrite by hydroxylamine oxidoreductase (HAO). Cyt c554 functions in the latter process by accepting pairs of electrons from HAO and transferring them to a cytochrome acceptor. The crystal structure of cyt c554 at 2.6 Å resolution shows a predominantly α-helical protein with four covalently attached hemes. The four hemes are arranged in two pairs such that the planes of the porphyrin rings are almost parallel and overlapping at the edge; corresponding heme arrangements are observed in other multi-heme proteins. Striking structural similarities are evident between the tetra-heme core of cyt c554 and hemes 3–6 of HAO, which suggests an evolutionary relationship between these redox partners.

1998 Nature America Inc. • http://structbio.nature.com

Cyt c554 (cyt c554) is a tetra-heme[1] cytochrome involved in the oxidation of ammonia to nitrite in the chemoautotrophic bacterium *Nitrosomonas europaea*[2]. Oxidation of ammonia is the sole energy source for *N. europaea* and the pathway by which this occurs is summarized schematically in Fig. 1. As the mobile electron carrier between hydroxylamine oxidoreductase (HAO) and the mono-heme cytochrome c552 (cyt c552)[2], cyt c554 plays a critical role in the process of nitrification in the biological nitrogen cycle.

Cyt c554 does not exhibit significant sequence homology to any other known protein, including other tetra-heme cytochromes, and is considered to be in its own class[3]. The name reflects the absorbance peak of the α-band at 554 nm in its fully reduced form[2]. Cyt c554 has unusual spectroscopic properties that change dramatically above pH 10 or below pH 4. These studies have established that three of the hemes are low-spin while the fourth is high-spin, and that the four hemes interact magnetically[1]. The reduction potentials of the four hemes at pH 7.0 have been determined[4] by a combination of voltammetry and spectroscopy, using an optically transparent thin layer electrode. The high-spin heme has a reduction potential of +47 mV, while the low-spin hemes titrate with midpoint potentials of +47 mV, -147 mV, and -276 mV. Stopped-flow kinetic studies of electron transfer at physiological pH revealed that one electron is passed from HAO to cyt c554 with a rate constant of 250–300 s^{-1}, while a second electron is passed ten times more slowly with a rate constant of 25–30 s^{-1} (ref. 5). The order of reduction of the hemes under physiological conditions is unknown.

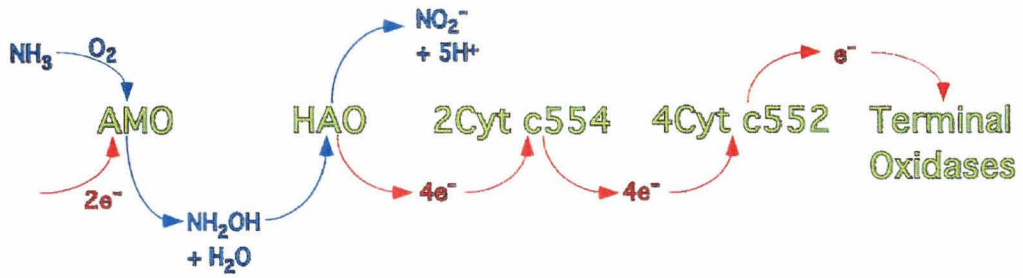

Fig. 1 The oxidation of NH_3 to NO_2^- by *Nitrosomonas europaea*. Ammonia is first oxidized to hydroxylamine (NH_2OH) by ammonia monooxygenase (AMO.) The product, NH_2OH, is oxidized to NO_2^- by HAO. The released electrons are transferred to cyt c554 (a two electron acceptor) and then possibly to cyt c552 (a one electron acceptor), which ultimately passes electrons to terminal oxidases. The electron transfer pathway following the oxidation of NH_2OH to NO_2^- is not fully understood and alternative electron transfer routes may exist[30], including the transfer of electrons from cyt c554 directly to a membrane-bound electron transport chain[31].

[1]Graduate Option in Biochemistry, 147-75 CH, California Institute of Technology, Pasadena, California 91125, USA. [2]Department of Biochemistry, University of Minnesota, St. Paul, Minnesota 55108, USA. [3]Division of Chemistry and Chemical Engineering, 147-75 CH, California Institute of Technology, Pasadena, California 91125, USA. [4]Present address: Biotechnology Center for Agriculture and the Environment, Rutgers University, New Brunswick, New Jersey 08903, USA. [5]Howard Hughes Medical Institute, Pasadena, California 91125, USA.

Correspondence should be addressed to D.C.R. *email: dcrees@caltech.edu*

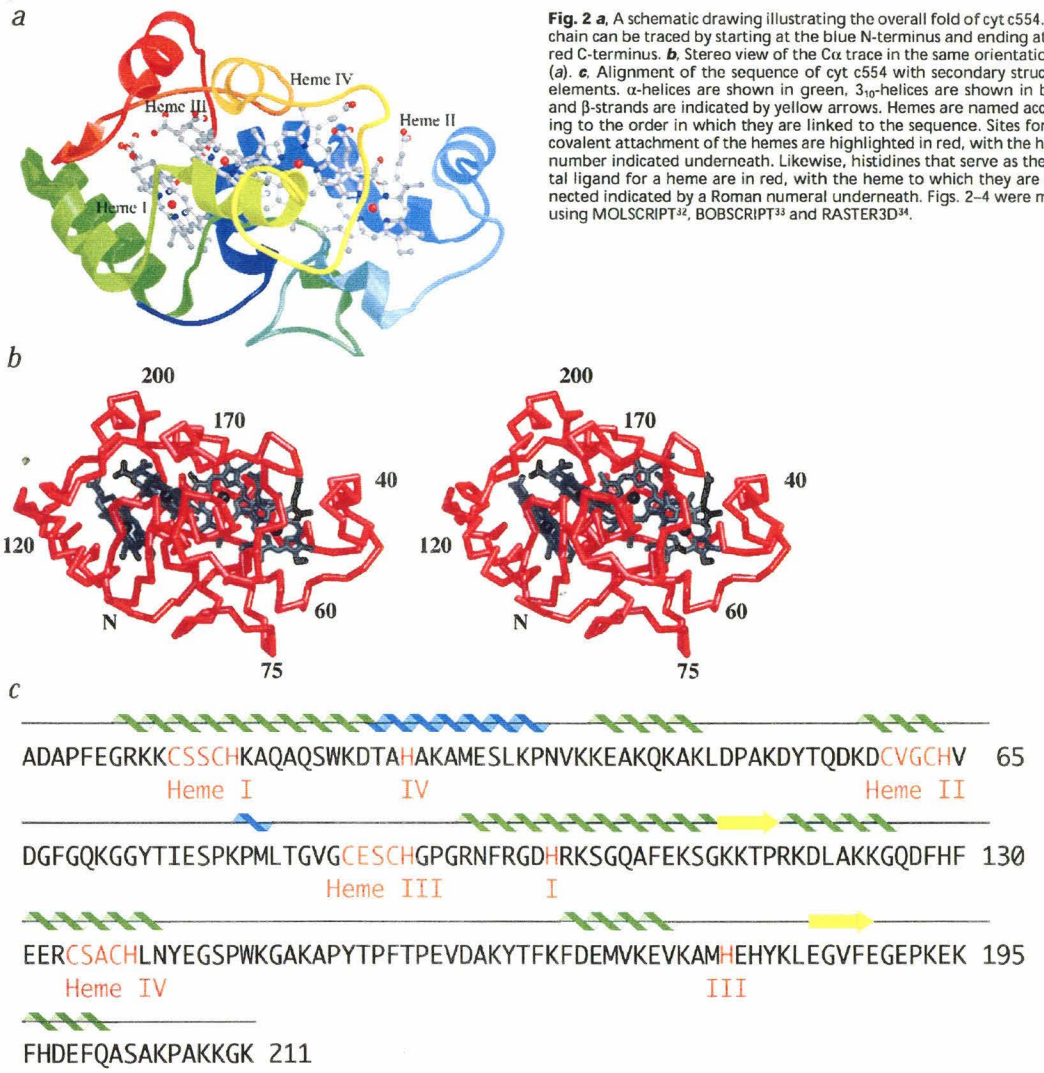

Fig. 2 ***a***, A schematic drawing illustrating the overall fold of cyt c554. The chain can be traced by starting at the blue N-terminus and ending at the red C-terminus. ***b***, Stereo view of the Cα trace in the same orientation as (*a*). ***c***, Alignment of the sequence of cyt c554 with secondary structure elements. α-helices are shown in green, 3_{10}-helices are shown in blue, and β-strands are indicated by yellow arrows. Hemes are named according to the order in which they are linked to the sequence. Sites for the covalent attachment of the hemes are highlighted in red, with the heme number indicated underneath. Likewise, histidines that serve as the distal ligand for a heme are in red, with the heme to which they are connected indicated by a Roman numeral underneath. Figs. 2–4 were made using MOLSCRIPT[32], BOBSCRIPT[33] and RASTER3D[34].

Crystallographic studies of cyt c554 were undertaken in order to provide a structural basis for the participation of this protein in the electron transfer reactions associated with ammonia oxidation. The arrangement of the heme groups and the interactions with the surrounding polypeptide chain will further provide a structural framework for a more detailed analysis of the spectroscopic and electron transfer properties of the protein.

Overall fold

The structure of cyt c554 crystallized at pH 10.1 has been solved to 2.6 Å resolution by the method of multiple isomorphous replacement. Data collection and refinement statistics are listed in Table 1. The secondary structure of cyt c554 consists primarily of α-helices, with two stretches of 3_{10}-helix and two short, parallel β-strands (Fig. 2*a*,*b*). A search of the Brookhaven Protein Data bank using the EMBL Dali server[6] did not reveal significant similarity to any previously determined protein folds; however, as detailed below, striking similarities are evident in the heme arrangement and the fold of the polypeptide chain surrounding the hemes between cyt c554 and HAO.

Heme configuration

All four hemes in cyt c554 are attached to the protein through thioether linkages to the *c*-heme binding motif, -C-x-y-C-H-. As shown in Fig. 2*c*, where the sequence of cyt c554 has been aligned with its secondary structure elements, the hemes have been numbered in the order that they are covalently connected to the polypeptide chain. The overall heme arrangement, with the inter-heme iron distances indicated, is shown in Fig. 3*a*. The four hemes are arranged as two di-heme pairs. Within each pair, the heme planes are roughly parallel with each other.

1998 Nature America Inc. • http://structbio.nature.com

1998 Nature America Inc. • http://structbio.nature.com

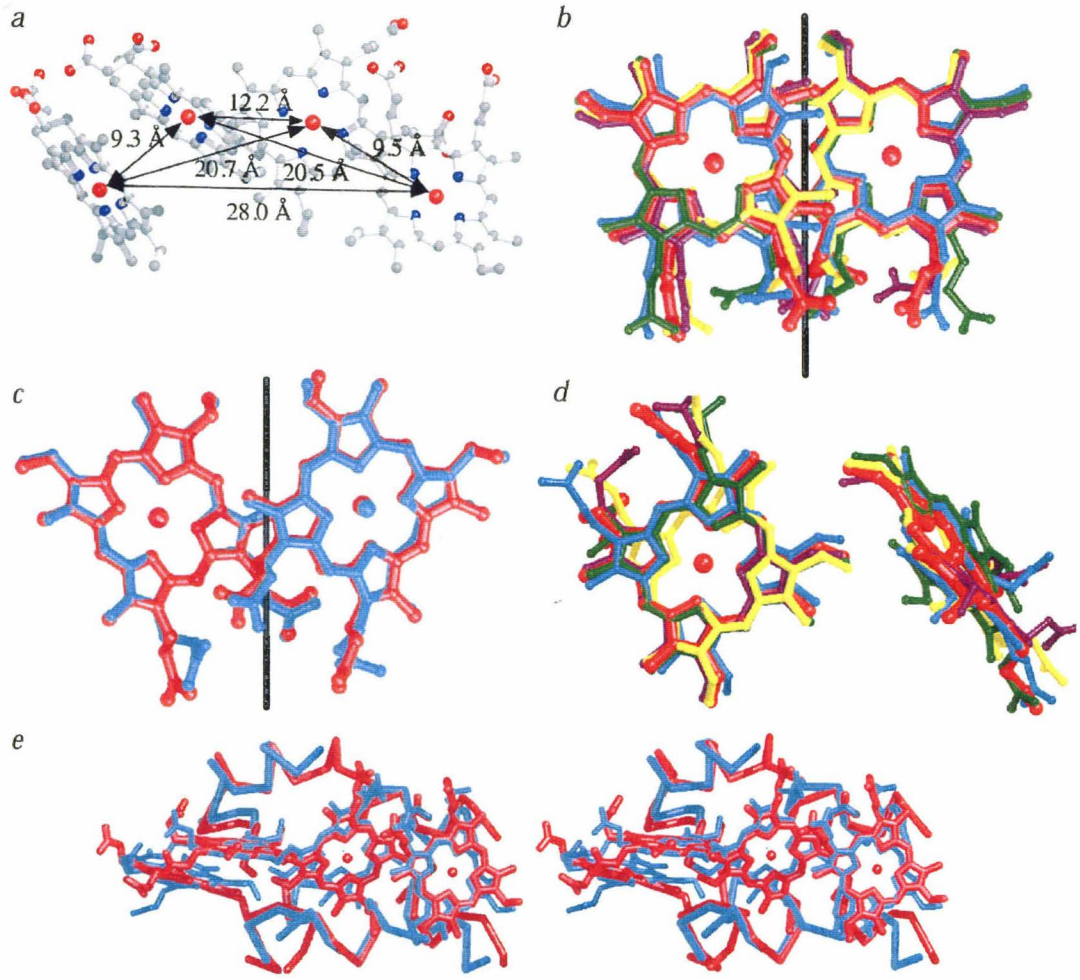

1998 Nature America Inc. • http://structbio.nature.com

Fig. 3 Heme configuration and superposition of heme stacking motifs. ***a***, Inter-heme iron distances and overall heme configuration. Hemes are shown in the same view as in Fig. 2*a*. ***b***, Overlay of hemes I and III from cyt c554 (red) with hemes 1 and 2 from HAO (teal), hemes 3 and 5 from HAO (magenta), hemes 6 and 7 from HAO (green) and hemes 1 and 2 from the split Soret cytochrome (yellow). The pseudo two-fold axis has been calculated for the hemes of cyt c554 and is shown as a black line. ***c***, Overlay of hemes II and IV from cyt c554 (red) with P460 and 6 of HAO (teal). The 5-coordinate hemes II (cyt c554) and P460 (HAO) are on the right. The pseudo two-fold axis calculated for hemes II and IV of cyt c554 is indicated as a black line. ***d***, Overlay of the two central hemes, hemes III and IV, from cyt c554 with hemes 5 and 6 from HAO (teal), hemes 7 and 8 from HAO (green), hemes 69 and 70 from cyt c551.5 (magenta) and hemes 201 and 203 from cyt c_3 (yellow). ***e***, Stereoview of the overlay of all hemes and surrounding structural elements from cyt c554 (red) with hemes 3–6 of HAO (teal).

Heme I is located at one end of the molecule and heme II is at the opposite end. Hemes III and IV are located towards the middle of the molecule, with heme III adjacent to heme I and heme IV adjacent to heme II. Table 2 summarizes the interplanar geometry between the hemes. The heme organization of cyt c554 differs substantially from that observed in either the tetra-heme cytochrome c_3[7] or the tetra-heme cytochrome associated with the photosynthetic reaction center[8].

Two distinct types of di-heme packing arrangements, parallel and perpendicular, occur in cyt c554 with the hemes in van der Waals contact. Significantly, both types of packing arrangements are present in other multi-heme cytochromes[7,9–11], and hence likely represent common motifs that will continue to emerge as more structures of multi-heme cytochromes become available. These heme-packing motifs may reflect favorable heme–heme interactions that facilitate electron transfer processes between hemes. At present, all multi-heme proteins exhibiting these types of packing arrangements have been isolated from organisms that either oxidize or reduce nitrogen or sulfur containing compounds as their primary energy source; this correlation may reflect the multi-electron redox processes associated with the energy metabolism of these organisms.

1998 Nature America Inc. • http://structbio.nature.com

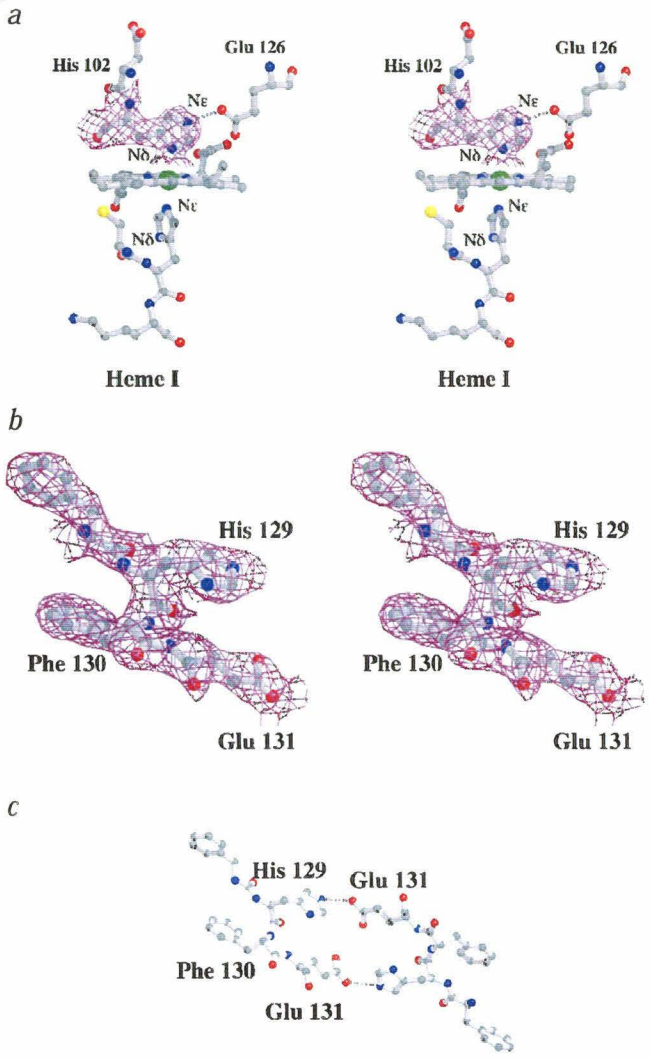

Fig. 4 Unusual aspects of the structure of cyt c554. ***a***, Stereoview of heme I. Note the iron coordination by the Nδ atom of His 102. The model is superimposed onto a σ_A weighted $2|F_o| - |F_c|$ style omit map around His 102 calculated using the program REFMAC[24] after the truncation of His 102 to an Ala. ***b,c***. The His 129–Phe 130 *cis*-peptide bond. (*b*) The final model in the region of Phe 130 superimposed onto a σ_A weighted $2|F_o| - |F_c|$ omit style map calculated using the program REFMAC after the deletion of His 129 and Phe 130 from the model. (*c*) Crystal contacts between His 129 and Glu 131 show that crystal contacts could influence the formation of the *cis*-peptide bond.

The first of these di-heme packing arrangements involves parallel but offset packing of the heme groups. Two variants of the parallel packing arrangement occur in cyt c554 (Fig. 3*b,c*), with counterparts present in other multi-heme proteins. In both cases, heme planes are separated by a distance of closest approach of 3.5–3.8 Å between ring atoms, while the distance between irons in the heme pair is ~9 Å.

In the first parallel arrangement, adopted by hemes I and III of cyt c554, the two hemes are approximately related by a two-fold rotation axis that is nearly parallel to the heme planes. Pyrrole rings A and B of each heme straddle the two-fold axis, with the heme edges alternatively parallel and perpendicular to this axis (Fig. 3*b*). The two pairs of hemes of the dimeric split Soret cytochrome[11], and three heme pairs in HAO[10] (hemes 1 and 2; hemes 3 and 5; and hemes 6 and 7) all exhibit this packing arrangement. Each of these heme pairs superimposes with hemes I and III of cyt c554 with a root-mean-square (r.m.s.) deviation of 0.5–0.7 Å, and the inter-heme iron distances vary between 9.0–9.8 Å. The methyl carbon on pyrrole ring C is in direct van der Waals contact with the histidine coordinating the adjacent heme, making closer packing in this manner impossible.

In the second parallel stacking arrangement, adopted by hemes II and IV of cyt c554, the hemes are again approximately related by a two-fold rotation axis that is nearly parallel to the heme planes. Relative to the first parallel arrangement, pyrrole rings B and D are adjacent to the two-fold axis, and each heme is then further rotated by ~30° about the normal to its plane (Fig. 3*c*). Hemes P460 and 6 of HAO exhibit this arrangement, and may be superimposed with hemes II and IV of cyt c554 with an r.m.s. deviation of 0.51 Å. Interestingly, in both of these pairs, one of the hemes is five-coordinate (heme II of cyt c554 and heme P460 of HAO).

A third parallel stacking arrangement may be identified in the photosynthetic reaction center[8] between the two bacteriochlorophyll groups that form the special pair. This arrangement is similar to the preceding one except that pyrrole rings B and C sandwich the rotation axis. In the reaction center, there is a much more extensive overlap between the chlorophyll planes, with the magnesiums separated by 7.6 Å. This closer distance is a consequence of the acetyl group of each chlorophyll coordinating the other magnesium. In all known protein-associated hemes, including cyt c554, non-porphyrin groups serve as the fifth and sixth ligands (when present) that prevent this close of an interaction.

The second distinct type of heme packing arrangement seen in cyt c554, the perpendicular packing arrangement, is exemplified by the two central hemes, III and IV. The perpendicular packing arrangement orients the heme planes at a 110° angle to each other, with a heme iron separation of 12.2 Å. This type of heme packing has previously been seen in HAO[10], cyt c551.5[9] and cyt c_3[7] (Fig. 3*d*). These di-heme clusters each superimpose with hemes III and IV of cyt c554 with r.m.s. deviations of 0.5–0.9 Å.

Intriguingly, the four hemes of cyt c554 may be structurally aligned with hemes 3–6 of HAO (r.m.s. deviation 1.2 Å) and are connected to the protein in the same order, which is suggestive

1998 Nature America Inc. • http://structbio.nature.com

1998 Nature America Inc. • http://structbio.nature.com

of an evolutionary relationship between these two redox partners. The exact relationship is difficult to establish, however, since no significant sequence and structural similarities can be detected between cyt c554 and HAO by automated searches. A side-by-side alignment of the structures using the EMBL Dali server[6] results in a Z-score of 0.5, where a Z-score less than 2.0 is considered structurally dissimilar. However, when the hemes of cyt c554 are overlaid with hemes 3–6 of HAO, there is secondary structure agreement between the two molecules in the immediate heme core environment (Fig 3*e*). Furthermore, the polypeptide chains surrounding these hemes in cyt c554 and HAO follow the same general paths, even though they cannot always be superimposed. Although the overall sequence similarity is poor in the regions where the secondary structure overlays, side chains with similar properties overlap, leading to a similar heme core. Given the structural and sequence differences, a common evolutionary ancestry cannot be convincingly established, but it is striking that the only two examples of this tetraheme arrangement have been found in two proteins that are redox partners.

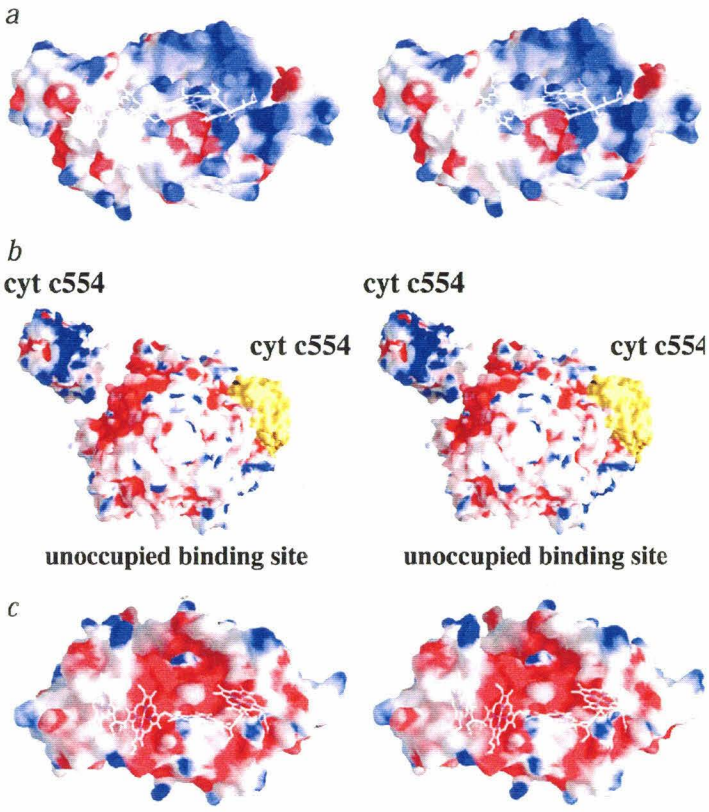

Fig. 5 ***a***, Stereoview of the GRASP[35] electrostatic surface potential representation of cyt c554 illustrating the large positive ridge (right side) proposed to represent the HAO docking site. The color scheme shows positively charged surface area as blue, negatively charged surface area as red, and uncharged surface area as white. ***b***, Stereoview of the docking model between cyt c554 and the HAO trimer. The view is down the three-fold axis of the HAO trimer. One molecule of cyt c554 (yellow) is shown docked to HAO, while a second molecule of cyt c554 is pulled away from HAO to illustrate the complementary surfaces of the two molecules, in terms of both shape and electrostatic potential. The third putative binding site for cytochrome c554 on HAO has been left unoccupied at the bottom of the figure. ***c***, Further rotation of cyt c554 from the view in (*a*) shows a negative cavity on the reverse side of the molecule. The function of this negative cavity is not known.

Unusual heme properties

The distal histidine ligand of heme I, His 102, is coordinated to the iron through Nδ rather than through Nε (Fig. 4*a*). A survey of heme iron coordination using PROMISE[12] shows that none of the currently available heme-protein structures has a heme iron coordinated with the Nδ of a histidine. It has been proposed that heme iron coordination by the histidine Nδ is sterically unfavorable[13]; the structure of cyt c554 reveals that this need not be the case. The side chain torsion angles for His 102 have favorable values. However, there appear to be limited backbone conformations that will allow heme iron coordination by the histidine Nδ. As a result, it does not seem that a Nδ coordination would be achievable in a -C-x-y-C-H- heme binding motif where the backbone is conformationally constrained. This is reflected in the great preference for Nε heme iron coordination that is seen. In addition to the Fe coordination, the orientation of this residue is stabilized by a hydrogen bond between Nε and the side chain of Glu 126. Glu 126 is further hydrogen bonded to a water (W13) that is in turn hydrogen bonded to the Nδ of His 92, which acts as the proximal ligand to heme III. This hydrogen bonding network between the two hemes may contribute to the pH dependent interaction between hemes that has been observed spectroscopically.

In contrast to the other three hemes, heme II is five-coordinate and thus likely the +47 mV high-spin heme[14]. No amino acid side chains or solvent molecules are close enough to coordinate the heme iron. The side chains of Thr 154, Pro 155, and Phe 156 pack against the porphyrin ring, shielding the sixth coordination site. It has been postulated that the five-coordinate heme would have an open site capable of binding to a ligand, possibly NO, and therefore may participate directly in the reaction oxidizing ammonia to nitrite as well as being an electron carrier[1]. In the comparison between cyt c554 and HAO discussed previously, heme II corresponds to heme P460 which forms the active site for HAO and is also five-coordinate. While this suggests that heme II may have a catalytic function, the crystal structure of cyt c554 indicates that this is unlikely in the absence of conformational rearrangements involving residues that limit access to this heme.

In the vicinity of heme III, a *cis*-peptide bond occurs between His 129 and Phe 130. This *cis*-peptide bond is located in a loop at the end of one of the two β-strands, with Phe 130 beginning the next α-helix (Fig. 4*b*). The aromatic side chain of Phe 130

1998 Nature America Inc. • http://structbio.nature.com

Table1 Summary of crystallographic statistics

Data sets	Nat1	Nat2	$HoCl_3$	Ir^{3+}	TMLA			
High resolution (Å)	2.6	3.0	3.7	2.8	3.3			
Completeness (%)	92.7 (92.1)	97.8 (97.2)	97.0 (100.0)	95.6 (88.3)	94.3 (95.9)			
Reflections	51,408	33,016	12,161	26,175	21,005			
Unique reflections	11,956	8,303	4,497	9,925	6,175			
I/σ	10.3 (3.4)[1]	10.6 (3.7)	5.03 (3.1)	9.6 (2.5)	10.4 (5.1)			
R_{sym}[2] (%)	9.7 (29.1)	14.7 (32.7)	18.4 (30.9)	10.6 (23.0)	11.4 (24.3)			
Phasing Statistics	Phasing power[3] for each resolution bin (Å)							
	No. of sites	R_{cullis}[4]	9.99	6.57	5.23	4.47	3.95	3.60	Overall (3.6 Å)
Native Anomalous	4	0.91	1.99	1.72	1.44	1.14	1.10	0.916	1.45
$HoCl_3$	3	0.74	2.95	2.39	1.89	1.52	1.31	1.14	2.04
$HoCl_3$ (anomalous)	3	0.85	1.39	1.19	0.88	0.65	0.62	0.58	0.99
Ir^{3+}	10	0.61	3.75	3.78	3.06	2.27	2.04	1.94	2.93
Ir^{3+} (anomalous)	10	0.82	2.57	2.31	2.07	1.74	1.43	1.18	1.88
TMLA	7	0.79	2.64	2.63	2.10	1.45	1.34	1.23	1.94
TMLA (anomalous)	7	0.75	2.27	2.04	1.63	1.27	1.14	0.97	1.62
Figure of merit			0.84	0.80	0.73	0.65	0.61	0.53	0.68
Refinement statistics									
Resolution range		20–2.6 Å							
R_{cryst}[5]		20.8%							
R_{free}[6]		25.4%							
R.m.s. deviation bond lengths		0.015 Å							
R.m.s. deviation bond angles		1.89°							

[1]Numbers in parentheses indicate values for the highest resolution bin.
[2]$R_{sym} = \Sigma[I_i - <I>]/\Sigma[<I>]$ where i is ith measurement and <I> is the weighted mean of I.
[3]Phasing power = The mean value of the heavy atom structure factor divided by the lack of closure error.
[4]$R_{cullis} = \Sigma||F_{PH}| - |F_P|| - |F_H|| / \Sigma|F_{PH}| - |F_H||$ where F_P and F_{PH} are the native and derivative structure factor amplitudes.
[5]$R_{cryst} = \Sigma||F_{obs}| - |F_{calc}|| / \Sigma|F_{obs}|$
[6]R_{free} is the same as R_{cryst} for 10% of the data omitted from refinement totaling 1,167 reflections.

lies within 4 Å of the porphyrin ring of heme III. There is the possibility that the *cis* conformation of the peptide bond is preferentially stabilized by a nearby crystal contact. Crystal contacts have previously been implicated in stabilization of a functionally relevant *cis*-peptide bond in the structure of flavodoxin, where Asn 137 from a symmetry-related molecule is directly hydrogen bonded to the backbone[15]. In cyt c554, the two residues adjacent to the *cis*-peptide bond, His 129 and Glu 131, interact around a crystallographic two-fold axis, which may stabilize the *cis* conformation (Fig. 4*c*).

A fundamental property of electron transfer proteins such as cyt c554 is the electrochemical behavior of the associated cofactors. This is typically characterized in terms of the reduction potentials that measure the thermodynamic tendency for these groups to accept an electron. The factors that influence the reduction potentials of electron transfer proteins have been extensively studied (reviewed in refs 16,17), and an important objective is to understand the overall redox behavior of the component cofactors. In the case of cyt c554, it is likely that the five coordinate heme represents the high spin heme that titrates at +47 mV[14]. Given the sensitivity of the reduction potentials to various structural and environmental factors, including interaction between the hemes (cooperativity effects), pH and oxidation state linked structural changes, however, a specific assignment between the remaining low-spin hemes and the three six-coordinate hemes does not seem warranted, in the absence of more detailed information concerning these effects.

Binding of cytochrome c554 to HAO and cytochrome c552

Based on the pI's of HAO (3.4)[18], cyt c554 (10.7) and cyt c552 (3.7)[2], it is plausible that electrostatic effects contribute to the energetics of protein–protein interactions. Surface potential representations were generated to search for reasonable interaction sites. There is a large ridge of positively charged surface area above heme I of cyt c554, which could be involved in binding to HAO (Fig. 5*a*). This positive ridge is 30 Å wide, which is almost exactly the size of the negative cavity between the monomers in the HAO trimer, where it was proposed that cyt c554 may bind[10]. Although speculative, docking between cyt c554 and HAO at this site appears qualitatively reasonable (Fig. 5*b*). In this model, the solvent exposed edge of heme 1 of HAO is adjacent to the solvent exposed edge of heme I of cyt c554, with an iron–iron distance between the two hemes of 20 Å, and a closest distance between heme rings of 8 Å. Although electrostatic effects have been proposed to influence the binding between cyt c552 and cyt c554, there is no clear binding region on cyt c552 that could take advantage of their respective electrostatic charges. Despite the high pI of cyt c554, there is a negatively charged cavity on the opposite side of the molecule from the positive ridge (Fig. 5*c*). The function of this negative cavity is unknown.

The 2.6 Å resolution crystal structure of cyt c554 has revealed striking structural similarities in the structure of the tetraheme core to that observed in its redox partner HAO. Furthermore, this tetra-heme arrangement is composed of diheme interactions that have been identified in other multiheme proteins that participate in electron transfer reactions. From the structures of the individual cyt c554 and HAO molecules, initial proposals into the electron transfer processes between these components can be formulated; more substantial progress will undoubtedly require determination of the HAO–cyt c554 complex. This structure may also provide further

1998 Nature America Inc. • http://structbio.nature.com

1998 Nature America Inc. • http://structbio.nature.com

insight into the question of why so many hemes are required for the oxidation of hydroxylamine.

Methods

Crystallization. Cyt c554 was produced and purified as described[4]. Crystals of oxidized cyt c554 were obtained at 22 °C by the vapor diffusion method using sitting drops with 5 µl of 40 mg ml^{-1} protein plus 5 µl of the reservoir solution (62.5% w/vol potassium phosphate pH 10.1, prepared by titrating a solution of 92.5% w/vol K_2HPO_4 to pH 10.1 with KOH, then diluting). In a solution of 35% w/vol potassium phosphate pH 10.1, oxidized native protein shows an EPR spectrum identical to that seen at physiological pH, with a g-value of 3.3[1] (data not shown). Crystals belonging to the tetragonal space group $P4_322$ with a = b = 68.20 Å and c = 168.83 Å grew within 2 weeks to a maximal size of 0.5 mm × 0.5 mm × 1.5 mm. Although the volume of the unit cell suggested two molecules per asymmetric unit, the crystals had one monomer per asymmetric unit, with 68% solvent content (V_m = 3.8). Crystals were cryo-cooled in the mother liquor using no additional cryo protectant.

Preparation of derivatives. The Ho^{3+} derivative was prepared by soaking mother liquor containing 5 mM $HoCl_3$ for 5 h. Interestingly, Ho^{3+} formed a derivative even though the crystallization conditions were high in phosphate, as phosphate has been shown to compete with proteins for the binding of lanthanides[19]. Although three phosphates are included in the final model, none of the Ho^{3+} ions is bound to any of these phosphates. The trimethyl lead acetate (TMLA) derivative was prepared by soaking crystals in mother liquor containing 30 mM TMLA for three weeks[20]. Because of the extended length of time of the derivative soak, a small amount of uncrystallized protein was added to the soak. The Ir^{3+} derivative was prepared by soaking in mother liquor saturated with cis-dinitro bis(ethylene-diamine)Ir(III) chloride for 18 h. To minimize non-isomorphism between native data set 2 and all the derivative data sets, native cyt c554 crystals were soaked in protein-free artificial mother liquor for 24 h prior to data collection.

Data collection. Native data set 1 was collected at -180 °C on beam line 7-1 at the Stanford Synchrotron Radiation Laboratories using a wavelength of 1.08 Å on a 180 mm MAR research image plate detector. All other data sets were collected on an RAXIS II image plate using a Rigaku rotating anode generating Cu Kα radiation. Curiously, R_{sym} values for data sets collected using Cu Kα radiation were particularly high compared to data sets collected using synchrotron radiation (Table 1). Often, R_{sym} was over 10% even in the lowest resolution bins, where I/σ was greater than 15. The high values of R_{sym} were not significantly improved by using stringent rejection criteria when processing data. To assess whether the high values of R_{sym} were a result of photoreduction by the X-rays during the course of data collection[21], single crystal spectra were measured on a microspectrophotometer. After 20 h exposure to Cu Kα radiation at room temperature, initially oxidized crystals exhibited a spectrum with characteristics of reduced protein, indicating photoreduction was potentially occurring on all data sets taken using Cu Kα radiation (data not shown). It is unclear whether the photoreduction is a result of the longer wavelength of Cu Kα radiation, the longer exposure time necessary with the less intense X-rays, or a combination of both. Although the single crystal spectra were taken on a crystal exposed to radiation at room temperature, similar photoreduction phenomena occur at cryogenic temperatures[22]. Because of this consistent discrepancy in symmetry related reflections, I/σ rather than R_{sym} was used as the primary indicator of data quality, and was therefore used as the primary statistic to determine the high resolution limit, for data sets taken using Cu Kα radiation.

Data processing and phasing. Data were processed using DENZO and Scalepack[23], and the CCP4 suite of programs[24]. The difference Patterson map of the Ho^{3+} derivative was interpreted using SHELX[25]. Sites for the other two heavy atom derivatives were determined using difference Fourier maps phased with the Ho^{3+} derivative. Heavy atom positions were initially refined using MLPHARE[24] and the refined positions and occupancies were further refined using SHARP[26] to 3.6 Å resolution. The phases from SHARP were improved using solvent flattening with DM[24] to 3.5 Å resolution. Phasing statistics are given in Table 1. The positions of the hemes in the initial experimental maps were striking and each heme iron had experimental density greater than 5σ associated with it. Using the center of the 5σ density as the location of each of the heme irons, the anomalous scattering contribution of the irons was added to the phase calculation.

Table 2 Interheme angles and distances

Heme pair	Angle[1]	Pair?	Interheme Fe^{3+} distance (Å)
I and II	88.4°	no	28.0
I and III	13.6°	yes	9.3
I and IV	110.8°	no	20.7
II and III	84.1°	no	20.5
II and IV	24.7°	yes	9.5
III and IV	108.3°	yes	12.2

[1]Inter-heme plane angles were calculated using the program MG86[36].

Model building and refinement. All 211 residues of cytochrome c554 were built into the maps at 3.5 Å resolution using the program O[27]. Subsequent rounds of modeling employed phase combined maps produced with SIGMAA[24] until the R_{free} dropped to 32%. Refinement continued using σ_A weighted maps calculated using the program REFMAC[24] until the final model was obtained. Refinement was initially carried out using REFMAC[24], and was later continued in X-PLOR[28] using maximum likelihood simulated annealing. The final model contains 1,908 atoms including four hemes, 66 water molecules, and three phosphates. The crystallographic R-factor is 20.8% and the R_{free} is 25.4%. The final model has r.m.s. deviations for bond lengths and angles of 0.015 Å and 1.89° respectively, with 84.2% of the residues in the most favored regions of the Ramachandran plot, 15.3% in the additionally allowed regions, and 0.6% of the residues (Lys 209) in the generously allowed regions and no residues in the disallowed regions as calculated using the program PROCHECK[29].

R.m.s. deviations of heme overlays were calculated using the program LSQKAB[24], and the two-fold axes drawn in Fig. 3 were calculated using the rotation matrix determined in LSQKAB[24]. Coordinates for HAO[10], cyt c551.5[9], the photosynthetic reaction center[8] and cyt c_3[7] were obtained from PDB entries 1FGJ, 1NEW, 1PRC and 3CYR respectively.

Coordinates. Coordinates have been deposited in the Protein Data Bank (accession number 1BVB).

Acknowledgments

We thank J. Hu, L. Joshua-Tor, M. Stowell, D. Cascio, M. Soltis, H. Schindelin, C. Kisker and C. Kielkopf for experimental assistance; C. Drennan and H. Axelrod for critical reading and helpful discussions; K. Matthews and B. Crane for the microspectrophotometery; M. Carrondo for the split Soret cytochrome coordinates; and R. Timkovich for the cytochrome c552 coordinates. This work was supported by an NSF grant to A.B.H and an NIH grant to D.C.R. T.M.I. is supported by an NIH fellowship. The rotation camera facility at SSRL is supported by the NIH and Department of Energy.

Received 26 June, 1998; accepted 14 September, 1998.

1998 Nature America Inc. • http://structbio.nature.com

1998 Nature America Inc. • http://structbio.nature.com

1. Andersson, K., Lipscomb, J., Valentine, M., Münck, E. & Hooper, A. Tetraheme cytochrome c-554 from *Nitrosomonas europaea:* heme-heme interactions and ligand binding. *J. Biol. Chem.* **261**, 1126–1138 (1986).
2. Yamanaka, T. & Shinra, M. Cytochrome c-552 and cytochrome c-554 derived from *Nitrosomonas europaea*: purification, properties, and their function in hydroxylamine oxidation. *J. Biochem.* **75**, 1265–1273 (1974).
3. Bergmann, D., Arciero, D. & Hooper, A. Organization of the *hao* gene cluster of *Nitrosomonas europaea*: genes for two tetraheme c cytochromes. *J. Bacteriol.* **176**, 3148–3153 (1994).
4. Arciero, D., Collins, M., Haladjian, J., Bianco, P. & Hooper, A. Resolution of the four hemes of cytochrome c554 from *Nitrosomonas europaea* by redox potentiometry and optical spectroscopy. *Biochemistry* **30**, 11459–11465 (1991).
5. Arciero, D., Balny, C. & Hooper, A. Spectroscopic and rapid kinetic studies of reduction of cytochrome c554 by hydroxylamine oxidoreductase from *Nitrosomonas europaea*. *Biochemistry* **30**, 11466–11472 (1991).
6. Holm, L. & Sander, C. Protein structure comparison by alignment of distance matrices. *J. Mol. Biol.* **233**, 123–138 (1993).
7. Matias, P., Frazao, C., Morais, J., Coll, M. & Carrondo, M. Structure analysis of cytochrome c_3 from *Desulfovibrio vulgaris* Hildenborough at 1.9 Å resolution. *J Mol. Biol.* **234**, 680–699 (1993).
8. Deisenhofer, J., Epp, O., Miki, K., Huber, R. & Michel, H. Structure of the protein subunits in the photosynthetic reaction center of *Rhodopseudomonas viridis* at 3 Å resolution. *Nature* **318**, 618–624 (1985).
9. Coutinho, I.B., Turner, D.L., Liu, M.Y., LeGall, J. & Xavier, A.V. Structure of the three-haem core of cytochrome $c_{551.5}$ determined by ^{1}H NMR. *J. Biol. Inorg. Chem.* **1**, 305–311 (1996).
10. Igarashi, N., Moriyama, H., Fujiwara, T., Fukumori, Y. & Tanaka, N. The 2.8 Å structure of hydroxlyamine oxidoreductase from a nitrifying chemoautotrophic bacterium, *Nitrosomonas europea*. *Nature Struct. Biol.* **4**, 276–284 (1997).
11. Matias, P. *et al.* A preliminary analysis of the three-dimensional structure of dimeric di-haem split-Soret cytochrome c from *Desulfovibrio desulfuricans* ATCC 27774 at 2.5 Å resolution using the MAD phasing method: a novel cytochrome fold with a stacked-haem arrangement. *J. Biol. Inorg. Chem.* **2**, 507–514 (1997).
12. Degtyarenko, K.N., North, A.C.T., Perkins, D.N. & Findlay, J.B.C. PROMISE: a database of information on prosthetic centres and metal ions in protein active sites. *Nucleic Acids Res.* **26**, 376–381 (1998).
13. Moore, G. & Pettigrew, G. *Cytochromes c—evolutionary, structural and physiochemical aspects* (Springer-Verlag, Berlin; 1990).
14. Loew, G.H. In *Iron porphyrins* (eds Lever, A.P.B. & Gray, H.B.) (Addison-Wesley Publishing Co., Reading; 1983).
15. Ludwig, M. *et al.* Control of oxidation-reduction potentials in flavodoxin from *Clostridium beijerinckii*: the role of conformational changes. *Biochemistry* **36**, 1259–1280 (1997).
16. Rees, D.C. & Farrelly, D. Biological electron transfer. *The enzymes* **19**, 37–97 (1990).
17. Stephens, P.J., Jollie, D.R. & Warshel, A. Protein control of redox potential of iron-sulfur proteins. *Chem. Rev.* **96**, 2491–2513 (1996).
18. Hooper, A., Maxwell, P. & Terry, K. Hydroxylamine oxidoreductase from *Nitrosomonas:* absorption spectra and content of heme and metal. *Biochemistry* **17**, 2984–2989 (1978).
19. Petsko, G. Preparation of isomorphous heavy-atom derivatives. *Meth. Enz.* **114**, 147–157 (1985).
20. Holden, H.M. & Rayment, I. Trimethyl lead acetate—a first choice heavy atom derivative for protein crystallography. *Arch. Biochem.* **291**, 187–194 (1991).
21. Nave, C. Radiation damage in protein crystallography. *Radiat. Phys. Chem.* **45**, 483–490 (1995).
22. Gonzales, A. & Nave, C. Radiation damage in protein crystals at low temperature. *Acta Crystallgr. D* **50**, 874–877 (1994).
23. Otwinowski, Z. In *CCP4 study weekend data collection and processing* (eds Sawyer, L., Isaacs, N. & Bailey, S.) 56–62 (SERC Daresbury Laboratory, UK: 1993).
24. Bailey, S. The CCP4 suite—programs for protein crystallography. *Acta Crystallogr. D* **50**, 760–763 (1994).
25. Sheldrick, G.M. Phase annealing in SHELX-90—direct methods for larger structures. *Acta Crystallogr. A* **46**, 467–473 (1990).
26. De La Fortelle, E. & Bricogne, G. Maximum likelihood heavy atom parameter refinement for multiple isomorphous replacement and multiwavelength anomalous diffraction methods. *Meth. Enz.* **276**, 472–494 (1997).
27. Jones, T.A., Zou, J.Y., Cowan, S.W. & Kjeldgaard, M. Improved methods for building protein models in electron density maps and the location of errors in these models. *Acta Crystallogr. A* **47**, 110–119 (1991).
28. Brünger, A.T. *X-PLOR version 3.1—A system for x-ray crystallography and NMR* (Yale University Press, New Haven and London; 1992).
29. Laskowski, R.A., Mcarthur, M.W., Moss, D.S. & Thornton, J.M. PROCHECK - a program to check the stereochemical quality of protein structures. *J. Appl. Crystallogr.* **26**, 283–291 (1993).
30. Prince, R.C. & George, G.N. The remarkable complexity of hydroxylamine oxidoreductase. *Nature Struct. Biol.* **4**, 247–250 (1997).
31. McTavish, H., Arciero, D. & Hooper, A. Interaction with membranes of cytochrome c554 from *Nitrosomonas europaea*. *Arch. Biochem. Biophys.* **324**, 53–58 (1995).
32. Kraulis, P.J. MOLSCRIPT—a program to produce both detailed and schematic plots of protein structures. *J. Appl. Crystallgr.* **24**, 946–950 (1991).
33. Esnouf, R. BOBSCRIPT—An extensively modified version of Molscript that includes greatly enhanced coloring capabilities. *J. Mol. Graph.* **15**, 133–138 (1997).
34. Merritt, E.A. & Murphy, M.E.P. Raster3D Version 2.0—a program for photorealistic molecular graphics. *Acta Crystallogr.* **D50**, 869–873 (1994).
35. Sharp, K., Fine, R. & Honig, B. Computer simulations of the diffusion of a substrate to an active site of an enzyme. *Science* **236**, 1460–1463 (1987).
36. Allen, F. & Kennard, O. 3D search and research using the Cambridge Data Base. *Chemical Design and Automation News* **8**, 1&31–37 (1993).

1998 Nature America Inc. • http://structbio.nature.com

Chapter 7

Iverson, T.M., Arciero, D.M., Hooper, A.B., Rees, D.C. (2000) High-resolution Structures of the Oxidized and Reduced States of Cytochrome c554 from *Nitrosomonas europaea*. *J. Biol. Inorg. Chem.* in preparation.

High-resolution Structures of the Oxidized and Reduced States of Cytochrome c554 from *Nitrosomonas europaea*

Tina M. Iverson, David M. Arciero, Alan B. Hooper and Douglas C. Rees

T. M. Iverson
Graduate Option in Biochemistry, MC 147-75 CH, California Institute of Technology, Pasadena, CA 91125

D. M. Arciero · A. B. Hooper
Department of Biochemistry, University of Minnesota, St. Paul, MN 55108

D. C. Rees (✉)
Division of Chemistry and Chemical Engineering and Howard Hughes Medical Institute, MC 147-75 CH, California Institute of Technology, Pasadena, CA 91125
e-mail: dcrees@caltech.edu
Tel: (626) 395-8393
Fax: (626) 744-9524

Abstract Cytochrome c554 (cyt c554) is a tetra-heme cytochrome involved in the oxidation of NH_3 by *Nitrosomonas europaea*. The x-ray crystal structures of cyt c554 in the oxidized and dithionite reduced forms have been solved by molecular replacement at 1.6 Å and 1.8 Å resolution respectively. Upon reduction, a conformational change occurs in the conformation of the polypeptide chain between residues 175 and 179, adjacent to hemes III and IV. Cyt c554 displays conserved heme-packing motifs that are continuing to emerge in other heme-containing proteins. By comparison to hydroxylamine oxidoreductase, the redox partner, and cytochrome *c* nitrite reductase, an enzyme involved in nitrite ammonification, substantial structural similarity has been observed in the heme core environment. At the resolution of these structures, the structural determinants of these heme packing are shown to extend to the buried water molecules that orient the histidine ligands to the heme iron. In the original structure determination of a tetragonal crystal form, a *cis*-peptide bond between His 129 and Phe 130 was identified that appeared to be stabilized by crystal contacts. In the rhombohedral crystal form used in the present high-resolution structure determination, this peptide bond is clearly *trans*-, but with disallowed angles of Φ and Ψ.

Key Words cytochrome · electron transfer · heme · nitrification · *Nitrosomonas europaea* · x-ray crystallography · conformational change · oxidation · reduction

Abbreviations cyt c554 cytochrome c554 · HAO hydroxylamine oxidoreductase · AMO ammonia monooxygenase · cyt c552 cytochrome c552 · cyt *c* NR cytochrome *c* nitrite reductase

Introduction

Cytochrome c554 (cyt c554) is a tetra-heme [1] cytochrome involved in ammonia oxidation by the chemoautotrophic soil bacterium *Nitrosomonas europaea* [2, 3]. This transformation of ammonia represents a key component of the process of nitrification in the biological nitrogen cycle. Oxidation of NH_3 serves as the sole energy source for *N. europaea* [4] and the physiological process occurs in two enzymatic steps followed by the energy yielding electron transfer steps. The first enzymatic step, catalyzed by the integral-membrane protein ammonia monooxygenase (AMO), converts NH_3 to hydroxylamine (NH_2OH) and water and requires the input of two electrons as well as molecular dioxygen. Following this, hydroxylamine oxidoreductase (HAO) converts NH_2OH to NO_2^- at a catalytic phlorin. This latter reaction releases four electrons that are passed pairwise to two molecules of cyt c554. Although there is controversy over the exact nature of the electron transport proteins following cyt c554 *in vivo*, the pathway can be reconstructed *in vitro* with cytochrome c552 (cyt c552) [2].

Crystallographic studies of cyt c554 [10] revealed a primarily α-helical secondary structure. The four covalently attached hemes are stacked into two types of pairs [10]. The first type of heme pair stacks with the planes of each pair of porphyrin rings nearly parallel and overlapping at the edge, and occurs in two variants. In the first variant, two

hemes exhibiting bis-histidine coordinate stack with the heme edges parallel to a pseudo two-fold axis. This type of heme stacking has been observed in the split-Söret cytochrome [11], HAO [12], cytochrome *c* nitrite reductase (cyt *c* NR) [13] and cytochrome *c* fumarate reductase (cyt *c* FR) [14-16]. In the second variant of parallel stacked hemes exhibited by cyt c554, one of the two stacked hemes has bis-histidine iron coordination, while the other is a five-coordinate iron. The planes of the hemes remain parallel, but the edges now lie at a 30° angle to the pseudo two-fold axis. This heme-stacking motif has been observed in HAO [12], cytochrome *c* nitrite reductase (cyt *c* NR) [13], where both of these proteins have catalytic activity associated with the five-coordinate heme.

The second type of heme pair is arranged with the planes of the porphyrins nearly perpendicular to one another as has previously been observed in cytochrome c_3 [17] and proteins with c_3-like repeating units [18, 19] as well as in HAO [12] and cyt *c* NR [13]. All of the proteins exhibiting these heme-stacking are involved in the metabolic pathways that require multiple electron transfer steps, suggesting that the stacked heme motifs may aid the rapid transfer of multiple electrons [10].

In view of the function of cyt c554 as a multi-electron transfer protein displaying a conserved heme arrangement, we have determined the structure in the fully oxidized

and dithionite reduced states to characterize oxidation-state dependent conformational changes. These studies serve to identify regions of cyt c554 that may be functionally important for the oxidation-reduction processes required for biological nitrification, and allow a better structural understanding of the heme packing motifs.

Materials and Methods

Crystallization and Data Collection

Cyt c554 was produced, purified [9] and crystallized [10] as previously described. Instead of the tetragonal crystals produced from early preparations, one protein preparation yielded rhombohedral crystals. These crystals were of superior quality to the tetragonal crystals with a diffraction limit up to 1.6 Å resolution. Fully oxidized crystals, grown aerobically, were reduced by adding an excess of $Na_2S_2O_4$ to the mother liquor containing the crystals. The crystals were soaked in the dithionite solution for several hours prior to cryo cooling and exhibited a color change during this time. Data sets were collected at -180° C on Stanford Synchrotron Radiation Laboratories beam line 7-1 using a wavelength of 1.08 Å and a 180 mm MAR Research image plate detector.

Data Processing and Structure Solution

Data were processed and scaled using DENZO, SCALEPACK [20], and the CCP4 suite of programs [21]. The oxidized structure was solved by molecular replacement with AMORE [22] using the structure of cyt c554 from the tetragonal crystal form (1BVB) as the search model. Since the dithionite reduced crystals were isomorphous with the oxidized crystals, the same molecular replacement solution was subjected to additional rigid body refinement against the reduced data. To ensure accurate comparison of the statistics, the same set of test reflections were selected for the R_{free} from each data set.

Model Building and Refinement

The program O [23] was used for model building of the cyt c554 structure. Refinement was carried out using REFMAC [21, 24], XPLOR [25] and SHELX [26]. Maps for model building were calculated with the CCP4 suite of programs [21] and were weighted using σa-coefficients determined in REFMAC [21, 24]. As a result of anisotropic density associated with the heme irons, the histidine ligation distances to the irons were difficult to determine using standard temperature factors when calculating maps. Thus, anisotropic temperature factors for the heme irons were refined in SHELX

[26], and σa-weighted maps from this calculation were used to determine the iron ligation distances. The resultant ligation distances were constrained in X-PLOR [25], which refined the overall protein model to significantly better geometry. Data collection and refinement statistics are summarized in Table 7.1.

Results and Discussion

Overall Fold

The crystal structures of oxidized and dithionite reduced cyt c554 have been refined to 1.6 Å and 1.8 Å resolution respectively. When cyt c554 from the original, tetragonal space group was superimposed onto oxidized cyt c554 from the rhombohedral space group described here, the rmsΔ was 0.6 Å for the Cα atoms. The structural changes that occur between the two crystal forms are located in areas of the protein either involved in crystal contacts (Fig. 7.1a - residues 142 to 153) or that have higher temperature factors and are therefore expected to be more mobile (Fig. 7.1b).

Changes in polypeptide fold upon reduction

Alignment of oxidized and dithionite reduced cyt c554 in the rhombohedral space group resulted in an rmsΔ of 0.4 Å overall, thus upon dithionite reduction, the majority of the protein remains in the same conformation. However, one interesting conformational change occurs between residues 175 and 179 (Fig. 7.1c). This loop lies above Hemes III and IV with His 179 serving as a ligand to Heme III. The conformational change displaces the backbone over 2 Å and may be triggered by a change in the peptide bond orientation between Met 178 and His 179 (Fig. 7.2). In the oxidized form of cyt c554, the peptide carbonyl is in van der Waals contact (4.7 Å) with the porphyrin of Heme III. Upon reduction, reorientation of the peptide bond places the backbone carbonyl 8.3 Å away from heme III, with an ordered water molecule replacing the peptide carbonyl. The relative rigidity of the region between residues 175 and 179 is reflected in the low temperature factors for this loop (all < 20 $Å^2$) in both the oxidized and reduced protein (Fig. 7.1b). This suggests that the observed structural changes are significant and not associated with inherent flexibility of cyt c554 in that region. The conformational change was observed in three different crystals of dithionite reduced cyt c554 (data not shown). It is possible that this conformational change is reflected in the biphasic kinetic of dithionite reduction [5].

Spectroscopic studies [1, 7] have established that three of the four hemes in cyt c554 are low-spin, while the fourth is high-spin and thus likely 5-coordinate [8]. The high-spin heme has a reduction potential of +47 mV, while the low-spin hemes titrate with midpoint potentials of +47 mV, -147 mV, and -276 mV [9]. While the five-coordinate heme II likely represents the +47 mV high-spin heme, the remainder of the reduction potentials have not yet been assigned. As the backbone conformational change is probably associated with the reduction of heme III, which has an unknown reduction potential, it is difficult to determine the physiological relevance of this movement.

A second conformational change associated with the reduction of cyt c554 is a change in the position of the propionate group of heme IV. The determinants of this conformational change are unclear. Other side chains that change position between the structures of the two oxidation states lie on the surface of the protein, and it is unclear if the change in side chain position reflects actual oxidation-state dependent changes or inherent mobility.

Role of ordered water molecules in the stacked-heme motif

Alignment of the hemes common to cyt c554, HAO [12] and cyt *c* NR [13] shows that in addition to the conserved heme arrangement, there is similarity in the conformation of the surrounding polypeptide chain. As cyt *c* NR and cyt c554 have been solved at resolutions where ordered water molecules can be unambiguously assigned, the role of conserved, buried water molecules involved in heme-stacking can be investigated. Cyt c554 and cyt *c* NR can be aligned such that hemes II through IV of cyt c554 are superimposed onto hemes 515 through 517 of cyt *c* NR. In this alignment polypeptide chains surrounding the hemes overlay. However, disappointingly few water molecules are in conserved locations. The water molecules that do appear in conserved locations in the two structures form hydrogen bond contacts to the histidine ligands of the two perpendicular stacked (central) hemes, stabilizing the orientation of the plane of the imidazole ring such that they are similar in the two structures (Fig. 7.3). As modulation of the reduction potential [27] and the electronic configuration of hemes [28] may be affected by the orientation of the imidazole ring of the histidine ligand, the structural conservation of the ligand side chain may be involved may reflect a necessary component for heme-packing motifs.

Although HAO has not been solved at a resolution where ordered water molecules can be distinguished, the planes of the imidazole rings of the histidine ligands are similar to those from cyt c554 and cyt c NR. Surprisingly, the distal ligand to heme I of cyt c554 exhibits a similar orientation to heme 3 of HAO despite that histidine 102 coordinates the heme iron with the Nδ atom, while all histidine ligands to heme irons in HAO coordinate with the Nε atom.

The similarities between the polypeptide chain surrounding the hemes as well as the extent of the heme packing motifs themselves suggest an evolutionary relationship exists between cyt c554, HAO, and cyt *c* NR. Cyt *c* NR is involved in nitrite ammonifiction, and catalyzes essentially the same reaction as occurs during nitrification by *N. europaea*, but in the physiologically reverse direction. In both cyt *c* NR and HAO, the reaction is catalyzed at a five-coordinate heme, however in cyt *c* NR, the protein ligand is a lysine, rather than a histidine. The similarities between the heme packing of cyt *c* NR and the two proteins involved in nitrification thus seem to be an example of convergent evolution. The evolutionary relationship between HAO and cyt c554 is less clear, despite the apparent lack of significant sequence identity, it seems remarkable that this motif would have evolved separately in the two redox partners.

Heme Iron Ligation

At the resolution of these structures, the heme iron ligation distances can be compared and are listed in Table 7.2. As expected [8], the six-coordinate low spin heme irons found in hemes I, III and IV have shorter histidine ligation distances than the five-coordinate high-spin iron found in heme II. Additionally, the iron of heme II lies ~ 0.3 Å out of the plane of the heme resulting in longer average Fe-N_p (pyrrole nitrogen) ligation distances than the six-coordinate low-spin counterparts.

Reduced heme iron (Fe^{2+}) would have a slightly larger radius than oxidized heme iron (Fe^{3+}) and thus is expected to have longer coordination distances to the histidine ligands. In these crystal structures, the coordination distances appear to obey a general trend of lengthening upon reduction, however, the small change in coordination distance between oxidized and reduced heme iron (Table 7.2) is smaller than the estimated coordinate error of the crystal structures presented here (Table 7.1).

His 129 - Phe 130 Peptide Bond

The overall geometry and refinement for these structures of cyt c554 is reasonable (Table 7.1) and only a few Ramachandran outliers are seen. In the oxidized crystal, Ala

207 and Lys 209 are in the generously allowed and disallowed regions of the Ramachandran plot respectively. These two residues lie at the C-terminus of the protein and are relatively disordered, thus the poor geometry is a reflection of the poor electron density in this region. Because of this disorder, the C-terminus has been omitted from the model of the reduced crystal, as there was no clear density beyond residue 208. In contrast, in both the oxidized and reduced crystals, the peptide bond of Phe 130 is in clear density and has Φ and Ψ angles in the disallowed region of the Ramachandran diagram (Fig. 7.4a).

In the tetragonal crystal form of cyt c554, the bond between His 129 and Phe 130 appeared to be in a *cis-* conformation (Fig. 7.4b) [10]. This *cis*-peptide bond was stabilized by a crystal contact involving the side chains of His 129 and Asp 131 around the crystallographic 2-fold axis, whereas the rhombohedral crystal form has no crystal contact in this area.

One possible explanation for the behavior of this peptide bond is that the *cis*-peptide bond is a crystal packing artifact, and that the peptide bond in that region is normally *trans-* but has disallowed Φ and Ψ angles. A more intriguing possibility is that this peptide bond is functionally significant. By having a high-energy disallowed *trans*-peptide bond, it would facilitate isomerization to *cis-*. This *cis-* form may have been

fortuitously stabilized in the tetragonal crystal form by crystal contacts. Crystal contacts have previously been implicated in the stabilization of functionally relevant *cis*- peptide bonds [29]. The location of Phe 130 is in a pocket above Hemes I and III near the proposed binding site for HAO. Thus, the His 129 - Phe 130 peptide bond may have implications for electron transfer between cyt c554 and HAO, or could be involved in complex formation.

Conclusions

This study shows a high-resolution view of cyt c554, a member of the biological nitrogen cycle, in two oxidation states of the protein. A conformational change accompanies four-electron dithionite reduction. The structural determinants of heme-packing motifs extend to the orientation of the imidazole rings of the histidine ligands to the heme irons. This involves the structural conservation of buried water molecules that stabilize the imidazole orientation, however the remainder of the water molecules are not conserved between these proteins. Disallowed Ramachandran angles at Phe 130 suggest functional significance of this residue, which has yet to be investigated biochemically. Further crystallographic studies will attempt to trap a two electron reduced state of cyt c554. Additionally, it would be of great benefit to determine the structure of the HAO-cyt c554 complex. A structure of this complex would illuminate specific inter-molecular interactions between the two proteins.

Acknowledgements

We thank R. Dieckmann, J. Chiu, and F. A. Tezcan for experimental assistance and J.A. Shelnutt for calculations of the distortions of the porphyrins. This work was supported by an NSF grant (#) to ABH and an NIH grant (GM45162) to DCR. TMI is supported by an NIH fellowship (GM07737). This work is based upon research conducted at the Stanford Synchrotron Radiation Laboratory (SSRL), which is funded by the Department of Energy, Office of Basic Energy Sciences.

Fig. 7.1 (next page): **a**. RMS deviations of oxidized, rhombohedral cyt c554 and cyt c554 from the tetragonal crystal form. The structure of cyt c554 in the tetragonal crystal form is colored according to the differences between the two crystal forms, with large differences in red, negligible differences in blue, and intermediate differences scaled in orange, yellow, and green. The arrow indicates a loop between residues 152 and 153 that shifts over 1 Å between the two crystal forms that is involved in a crystal contact in the tetragonal crystal form. **b**. Variation in temperature factors of cyt c554. The model of oxidized cyt c554 in the rhombohedral crystals form is colored according to variation of temperature factors. Red indicates the most mobile regions of the model and blue indicates the most stable regions, with intermediate mobility scaled in orange, yellow, and green. Reduced cyt c554 has a similar distribution of temperature factors (data not shown). **c**. Differences in oxidized and reduced rhombohedral cyt c554. The rmsΔ of the two models have been superpositioned onto the structure of reduced cyt c554 in the rhombohedral crystal form. The largest shifts in C_α coordinates (red) occur between residues 175 and 179 and maximally displace the loop 2.3 Å. Careful inspection of this loop in Fig. 1b and Fig. 1c shows the nature of the conformational change with respect to the rest of the protein. All molecular representations were made using MOLSCRIPT [30], BOBSCRIPT [31] and RASTER3D [32].

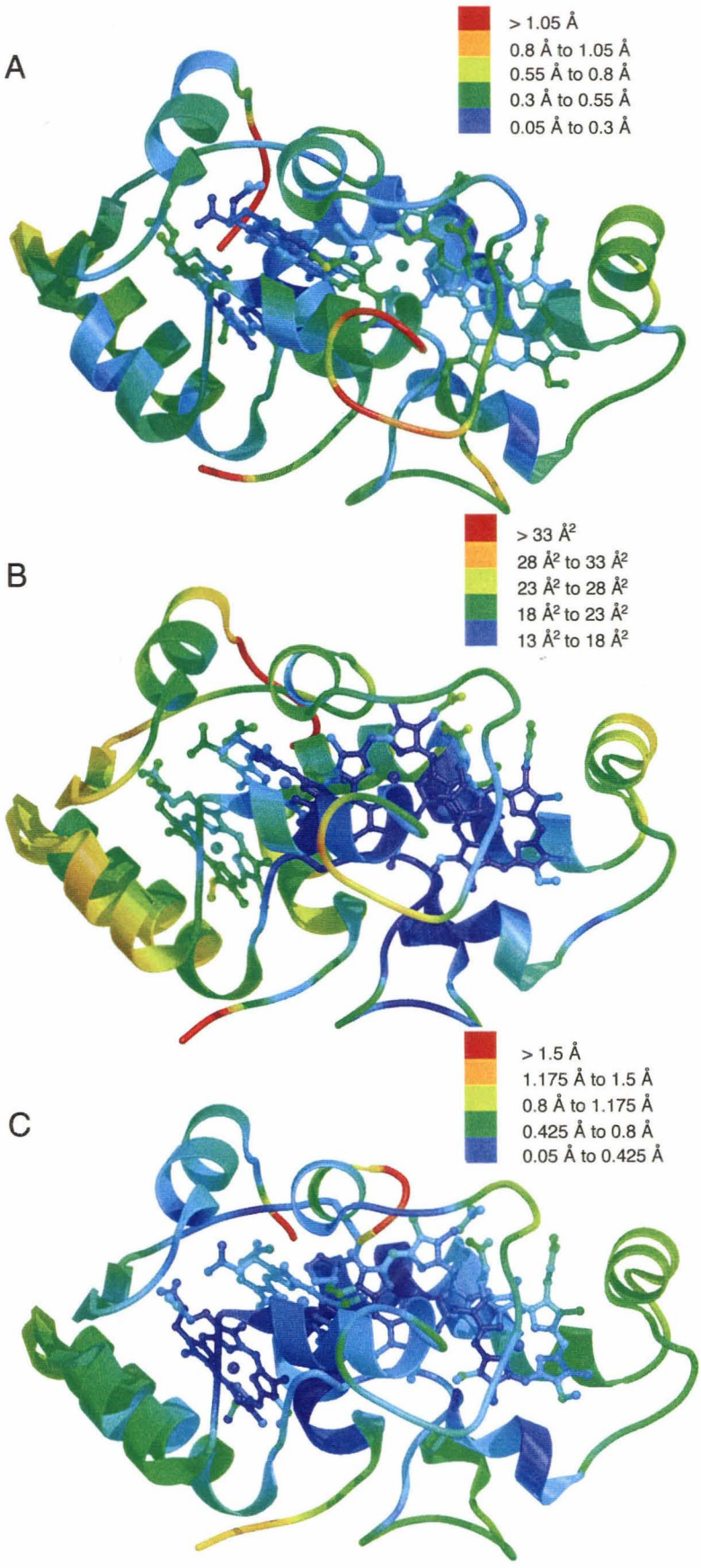
A
> 1.05 Å
0.8 Å to 1.05 Å
0.55 Å to 0.8 Å
0.3 Å to 0.55 Å
0.05 Å to 0.3 Å
B
> 33 Å²
28 Å² to 33 Å²
23 Å² to 28 Å²
18 Å² to 23 Å²
13 Å² to 18 Å²
C
> 1.5 Å
1.175 Å to 1.5 Å
0.8 Å to 1.175 Å
0.425 Å to 0.8 Å
0.05 Å to 0.425 Å

Fig. 7.2: Stereoview of the conformational change in the loop between 175 and 179. Reduced cyt c554 is shown in red, while oxidized cyt c554 is shown in blue. The side chains of His 179 and Met 178 as well as the peptide bond between those two residues are shown. This peptide bond changes conformation upon reduction.

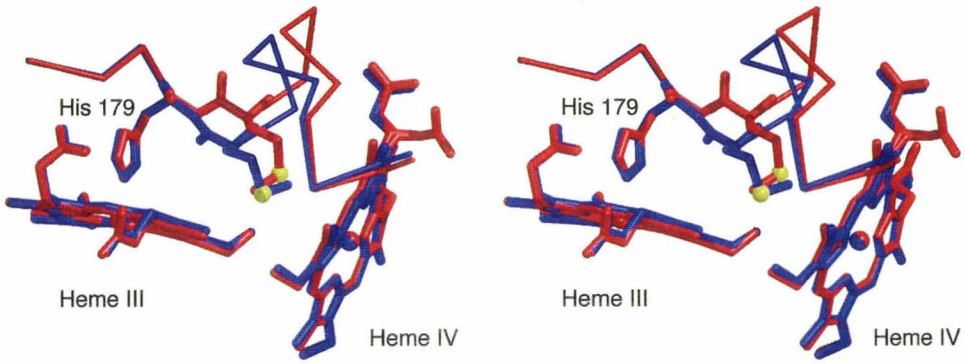

Fig. 7.3: Alignment of hemes and surrounding secondary structure of cyt c554 and cyt *c* NR. Water molecules located in conserved positions are shown. Cyt c554 is colored red and cyt *c* NR is colored green.

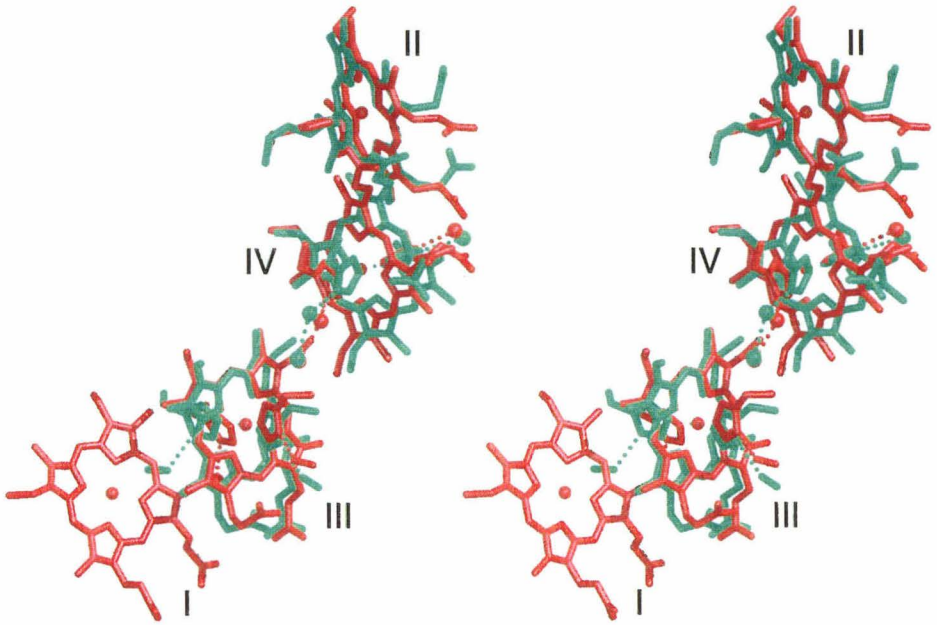

Fig. 7.4: Peptide bond at Phe 130. a. The His 129 - Phe 130 peptide bond is shown superpositioned onto σa weighted $2|F_o| - |F_c|$ density calculated after the omission of both His 129 and Phe 130. b. The His 129-Phe 130 peptide bond in the tetragonal crystal form shows a *cis*-conformation, and is influenced by crystal contacts around the crystallographic 2-fold axis of symmetry.

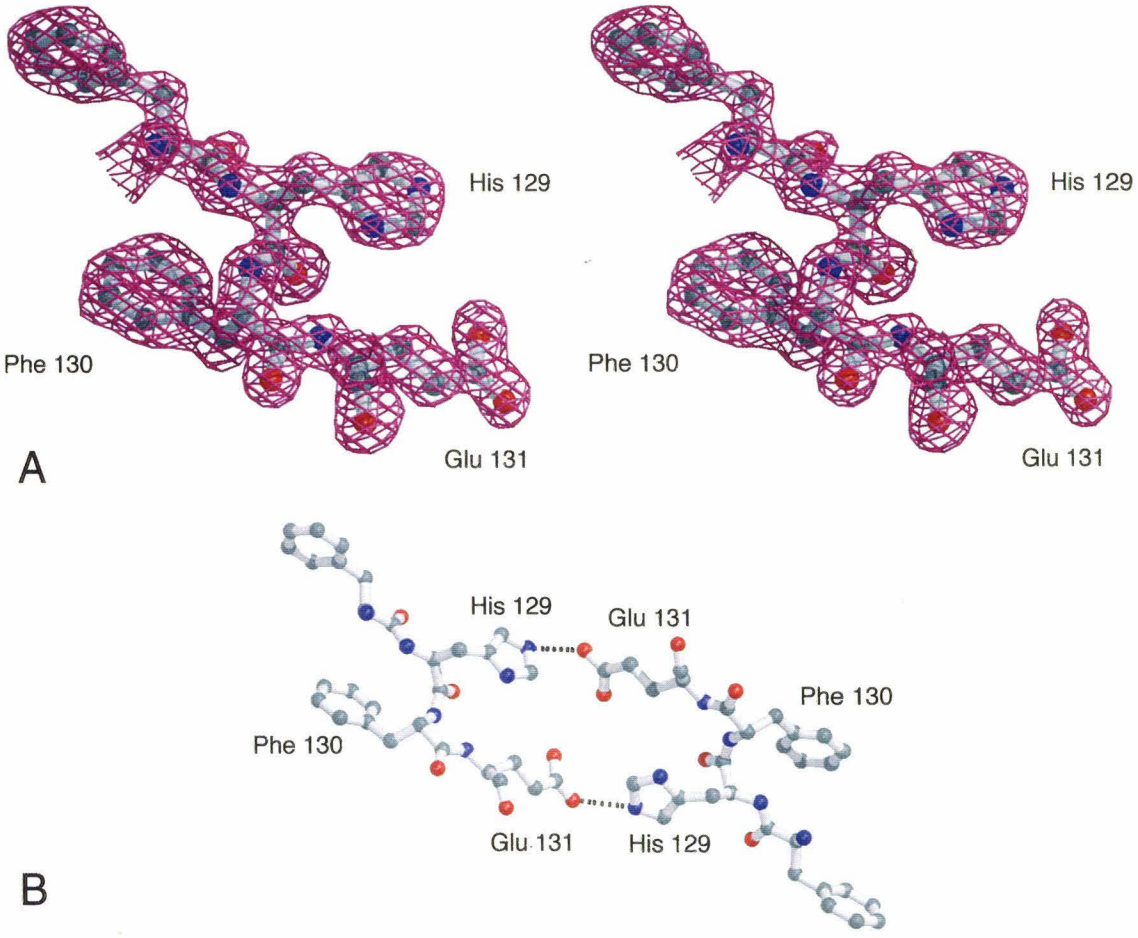

Table 7.1: Data Collection and Refinement Statistics

	Oxidized	Reduced
Unit Cell Constants		
a=b (Å)	147.89	147.24
c (Å)	33.91	33.88
Data		
Resolution (Å)	1.6	1.8
Observations	109,601	112,676
Unique Observations	35,562	24,588
Completeness (%)	97.3 (86.1)[1]	95.5 (85.9)
R_{sym}[2]	0.045 (0.174)	0.051 (0.288)
I/σ	28.0 (7.3)	28.5 (5.1)
Refinement		
R_{cryst}[3]	0.188	0.197
R_{free}[4]	0.215	0.236
Estimated Coordinate Error[5]	0.09 Å	0.13 Å
No. of free-R reflections	1808	1242
RMSΔ bond lengths	0.021 Å	0.016 Å
RMSΔ bond angles	1.99°	1.6°
Number of atoms	1988	1954
Residues	1-211	1-208
Water molecules	142	142
Other HET atoms	3 ips*	1 ips*, 1 dtn*, 1 SO_3*
Ramachandran statistics		
% Most favored	87.0	87.4
% Allowed	11.3	12.0
% Generously allowed	0.6 (Ala 207)	0.0
% Disallowed	1.1 (Phe 130, Lys 209)	0.6 (Phe 130)

[1]Numbers in parentheses indicate values for the highest resolution bin.

[2]$R_{sym} = \Sigma[I_i - \langle I \rangle]/\Sigma[\langle I \rangle]$ where i is the ith measurement and $\langle I \rangle$ is the weighted mean of I.

[3]$R_{cryst} = \Sigma||F_{obs}| - |F_{calc}||/\Sigma|F_{obs}|$

[4]R_{free} is the same as R_{cryst} for a selection of randomly omitted reflections.

[5]Estimated Coordinate Error is the Cruickshanks value determined in REFMAC.

*ips is inorganic phosphate (PO_4^{2-}) and dtn is dithionite ($S_2O_4^{2-}$). SO_3 is the oxidative breakdown product of dithionite.

Table 2: Heme Iron Ligation distances

	Heme I	Heme II	Heme III	Heme IV
Oxidized proximal	1.95 Å	2.17 Å	2.03Å	1.97 Å
Oxidized distal	2.08 Å	n/a	2.01 Å	2.03 Å
Oxidized N_p	1.98 Å	2.03 Å	1.99 Å	1.97 Å
Reduced proximal	2.00 Å	2.20 Å	2.04 Å	2.06 Å
Reduced distal	2.07 Å	n/a	2.10 Å	2.06 Å
Reduced N_p	1.98 Å	2.04 Å	1.98 Å	1.98 Å

Proximal refers to the histidine involved in the -C-x-y-C-H- heme binding motif, while distal refers to the histidine found elsewhere in the sequence. Heme II is 5-coordinate and therefore has no distal ligand. N_p refers to pyrrole nitrogen atoms and is an average of the four N_p-Fe bond lengths.

References

1. Andersson, K, Lipscomb, J, Valentine, M, Münck, E and Hooper, A (1986) J Biol Chem 261: 1126-1138

2. Yamanaka, T and Shinra, M (1974) J Biochem 75: 1265-1273

3. Suzuki, I and S-C., K (1981) Can J Biochem 59: 484-488

4. Wood, PM (1986) In: Prosser, JI (ed) Nitrification. IRL Press, Oxford, pp 39-62

5. DiSpirito, AA, Balny, C and Hooper, AB (1987) Eur J Biochem 162: 299-304

6. Tsang, DCY and Suzuki, I (1982) Can J Biochem 60: 1018-1024

7. Petersson, L and Andersson, KK (1987) Biochim Biophys Acta 915: 261-266

8. Scheidt, WR and Gouterman, M (1983) In: Lever, ABP and Gray, HB (ed) Iron Porphyrins Part One. Addison - Wesley Publishing Co, Inc., London, pp 89-139

9. Arciero, D, Collins, M, Haladjian, J, Bianco, P and Hooper, A (1991) Biochemistry 30: 11459-11465

10. Iverson, TM, Arciero, DM, Hsu, BT, Logan, MSP, Hooper, AB and Rees, DC (1998) Nat Struct Biol 5: 1005-1012

11. Matias, P, Morias, J, Coelho, A, Meijers, R, Gonzalez, A, Thompson, A, Sieker, L, LeGall, J and Carrondo, M (1997) JBIC 2: 507-514

12. Igarashi, N, Moriyama, H, Fujiwara, T, Fukumori, Y and Tanaka, N (1997) Nat Struct Biol 4: 276-284

13. Einsle, O, Messerschmidt, A, Stach, P, Bourenkov, GP, Bartunik, HD, Huber, R and Kroneck, PMH (1999) Nature 400: 476-480

14. Bamford, V, Dobbin, PS, Richardson, DJ and Hemmings, AM (1999) Nat Struct Biol 6: 1104-1109

15. Taylor, P, Pealing, SL, Reid, GA, Chapman, SK and Walkinshaw, MD (1999) Nat Struct Biol 6: 1108-1112

16. Leys, D, Tsapin, AS, Nealson, KH, Meyer, TE, Cusanovich, MA and VanBeeumen, JJ (1999) Nat Struct Biol 6: 1113-1117

17. Matias, P, Frazao, C, Morais, J, Coll, M and Carrondo, M (1993) J Mol Biol 234: 680-699

18. Matias, PM, Saraiva, LM, Soares, CM, Coelho, AV, LeGall, J and Carrondo, MA (1999) JBIC 4: 478-494

19. Coutinho, IB, Turner, DL, Liu, MY, LeGall, J and Xavier, AV (1996) J Biol Inorg Chem 1: 305-311

20. Otwinowski, Z (1993) In: Sawyer, L, Isaacs, N and Bailey, S (ed) CCP4 Study Weekend Data Collection and Processing. SERC Daresbury Laboratory, UK, pp56-62

21. Bailey, S (1994) Acta Cryst D50: 760-763

22. Navaza, J (1994) Acta Cryst A50: 157-163

23. Jones, TA, Zou, JY, Cowan, SW and Kjeldgaard, M (1991) Acta Cryst A47: 110-119

24. Murshudov, GN, Vagin, AA and Dodson, EJ (1997) Acta Crystallogr D53: 240-255

25. Brünger, AT (1992) X-PLOR version 3.1 - A system for x-ray crystallography and NMR. Yale University Press, New Haven and London

26. Sheldrick, GM (1990) Acta Cryst A46: 467-473

27. Rousseau, DG and Rousseau, DL (1992) J Struct Biol 109: 13-17

28. Shokhirev, NV and Walker, FA (1998) J Biol Inorg Chem 3: 581-594

29. Ludwig, M, Pattridge, K, Metzger, A, Dixon, M, Eren, M, Feng, Y and Swenson, R (1997) Biochemistry 36: 1259-1280

30. Kraulis, PJ (1991) J Appl Cryst 24: 946-950

31. Esnouf, RM (1997) J Mol Graph 15: 133-138

32. Merritt, EA and Murphy, MEP (1994) Acta Cryst D50: 869-873

Chapter 8

Tina M. Iverson, Michael P. Hendrich, David M. Arciero, Alan B. Hooper, Douglas C. Rees (2002) In: *The Metalloprotein handbook*, T. Poulos, ed., in preparation.

Cytochrome c554

Tina M. Iverson[1], Michael P. Hendrich[2], David M. Arciero[3], Alan B. Hooper[3], Douglas C. Rees[4]

1. Graduate Option in Biochemistry, 147-75 CH, California Institute of Technology, Pasadena, CA 91125.

2. Department of Chemistry, Carnegie Mellon University, 4400 5th Ave., 268-1061, Pittsburgh, PA 15213-2683.

3. Department of Biochemistry, Molecular Biology and Biophysics, University of Minnesota, St. Paul, MN 55108. E-mail hooper@umn.edu.

4. Division of Chemistry and Chemical Engineering and Howard Hughes Medical Institute, MC 147-75 CH, California Institute of Technology, Pasadena, CA 91125. E-mail: dcrees@caltech.edu. Tel: (626) 395-8393. Fax: (626) 744-9524.

Supported by NSF Research to ABH # MCB-9316906.

Cytochrome c554 (cyt c554) is a tetra-heme cytochrome from the chemolithotrophic bacterium, *Nitrosomonas europaea*, which derives energy for growth from oxidation of ammonia to nitrite with hydroxylamine as the free intermediate. Cyt c554 participates in this pathway as an electron acceptor of the hydroxylamine-oxidizing enzyme. The hemes of cyt c554 display conserved packing motifs involving stacked pairs with the planes of the porphyrin rings approximately parallel and stacked at a plane-to-plane distance of 3.6 Å to 3.8 Å. Currently, the stacked-heme motifs have been seen exclusively in other bacterial proteins involved in the metabolism of sulfur or nitrogen containing compounds, and may represent a structural arrangement necessary for the transfer of multiple electrons associated with these types of metabolic pathways. **(3D structure near here)**

INVOLVEMENT IN THE BIOLOGICAL NITROGEN CYCLE

(Figure 8.1 near here) The chemoautotrophic soil bacterium *Nitrosomonas europaea* generates all of its energy from the oxidation of NH_3 to NO_2^-.[1] As a result, *N. europaea* plays a key role in the biological nitrogen cycle (Figure 8.1). In addition to maintaining balanced ecosystems[2], applications of the nitrification (the oxidation of NH_3 to NO_2^-) by the organism include the removal of ammonia in sewage treatment plants[3] and rivers polluted by NH_3-containing compounds[4], e.g., fertilizer runoff or ammonia-

based industrial waste. Molecular oxygen is required for the oxidation of NH_3 to NH_2OH (Figure 8.2), consequently *N. europaea* is an obligate aerobe. (**Figure 8.2 near here**)

THE BIOCHEMISTRY OF NITRIFICATION

The pathway by which *N. europaea* oxidizes NH_3 (Figure 8.2) involves two enzymatic steps. Ammonia monooxygenase (AMO), an integral-membrane protein[5, 6], first oxidizes ammonia to hydroxylamine (NH_2OH)[7]. This oxidation requires the input of two electrons and molecular dioxygen. NH_2OH is further oxidized, to NO_2^- by hydroxylamine oxidoreductase (HAO)[1] which removes four electrons and inserts of an atom of oxygen from water. Thus, two electrons per NH_3 oxidized enter the electron transport chain leading to a cytochrome oxidase[10] or to reduce nitrite or nitric oxide when the oxygen concentration is low[11]. The physiological acceptor of electrons from HAO is cyt c554 (Figure 8.2), which contains four covalently attached heme moieties[8] having a range of midpoint potentials, but apparently accepts only two electrons in the two lower potential hemes per turnover[9]. Cyt c554 cannot pass electrons directly to the terminal electron acceptors, indicating the existence of at least one intervening electron transfer protein. The identity of the intervening electron carrier(s) *in vivo* is not known[12-14]. The soluble, monoheme cytochrome c552 (cyt c552) can be rapidly reduced in the presence of hydroxylamine and catalytic amounts of HAO and cyt c554 *in vitro*, but the role for cyt c552 as an electron donor to terminal electron acceptors has not been established[15]. In

keeping with what appears to be a key role in the central energy yielding redox interactions of this organism, the approximate cellular content of AMO, HAO, cyt c554, cytochrome aa_3 fall within a five fold range and cyt c552concentrations are significantly higher[11]. Additionally, the intermediate(s) in the electron donor pathway to AMO that begin the biological nitrification process remains unclear[16, 17]. Although cyt c554 normally localizes to the periplasm[11] as does HAO, exogenous electrostatic association of cyt c554 with the membrane has been observed[18].

SEQUENCE INFORMATION

The genome of *N. europaea* contains three gene copies of *cycA* (also called *hcy*), the gene encoding cyt c554[19, 20] each of which contain four -C-x-y-C-H heme-binding motifs. The gene copies themselves differ by only a few bases and the amino acid sequence predicted by the genes that have been sequenced to date are identical[19, 20, 21]. The pathway utilized by *N. europaea* to oxidize NH_3 represents a highly specialized process of energy harvesting, and currently no other proteins, including other tetra-heme cytochromes, exhibit significant sequence similarity to cyt c554. Thus, cyt c554 has long been considered to represent its own class[21].

The gene *amoA*, coding for one of the subunits of AMO has been sequenced in a number of ammonia-oxidizing autotrophic bacteria in the β or γ subdivision of proteobacteria. Genes of AMO from three different members of the β subdivision show a minimum of 83% identity. Additionally, *amoA* of this subdivision exhibits significant sequence similarity (~44%) to the genes encoding the particulate methane monooxygenase (pMMO) of the methanotrophs. The gene *amoA* of the nitrifier of the γ subdivision shows 51% identity to the corresponding members of the β subdivision and 83% identity to the pMMO genes.

Genes for HAO and cyt c554 have been detected by gene hybridization in *Paracoccus denitrificans*[23] and *Nitrosospira* spp[22], another autotrophic ammonia oxidizing bacteria of the β subdivision, suggesting these organisms may use a similar pathway for NH_3 oxidation as *Nitrosomonas*. As more sequence information becomes available, it seems likely that other autotrophic ammonia oxidizers of the β and γ subdivisions will be shown to contain homologs of both cyt c554 and HAO.

PROTEIN PRODUCTION AND PURIFICATION

The first purification protocol[15] for cyt c554 employed the extreme solubility and stability of the protein. When a cell extract of *N. europaea* is brought to 80% saturation with $(NH_4)_2SO_4$, only two proteins remain soluble: cyt c554 and HAO. As the saturation

increases from 80% to 90%, HAO precipitates, leaving cyt c554 in solution and relatively pure. To increase purity, additional chromatography can be performed[24]. This series involves an octyl-Sepharose column followed by dialysis to remove the $(NH_4)_2SO_4$ followed by an Amberlite CG-50 column and gel filtration using Sephadex G-100.

THREE-DIMENSIONAL STRUCTURE DETERMINATION

Crystallization

Cyt c554 has been crystallized in three distinct crystal forms. High concentrations of phosphate at pH 10.1 resulted in the growth of two of these crystal forms: one in the tetragonal space group $P4_322$[25], and the other in the rhombohedral space group R3[26]. The preliminary structure was determined by the method of multiple isomorphous replacement and based on the tetragonal crystal form at 2.6 Å resolution[25]. The rhombohedral crystal form has subsequently been solved by molecular replacement and has been refined to 1.6 Å and 1.8Å resolution in the oxidized and dithionite reduced states, respectively[26]. A third distinct crystal form diffracting to 2.3 Å resolution grew from ammonium sulfate precipitant in the monoclinic space group $P2_1$[27]. A structural analysis of this crystal form has not yet been reported.

Description of the polypeptide fold

Cyt c554 is oblong in shape with dimensions 60 ×30 × 30 Å. The polypeptide chain primarily consists of helices, most of which adopt α-helical conformations, but additionally the fold contains two stretches of 3_{10} helix, and two short, parallel β-strands (see 8.3D representation). Consistent with the specialized nature of cyt c554, the fold of the polypeptide chain initially appeared to be unlike any previously determined folds, however, remarkable similarities exist between the heme arrangement of cyt c554, HAO, and cytochrome *c* NR (cyt *c* NR). These similarities extend to the polypeptide chain surrounding the hemes, despite the lack of any detectable sequence identity between these proteins.

Heme iron coordination and heme configuration

The polypeptide chain of cyt c554 compactly binds the four hemes such that the porphyrins are positioned within van der Waals contact of one another and the interheme iron distances are relatively short (Figure 8.3). **(Figure 8.3 near here)** Each of the four heme moieties of cyt c554 has the heme iron coordinated by histidine side chains. The heme iron of hemes III and IV are coordinated with standard bis-histidine coordination, whereas the heme iron ligation seen in hemes I and II appears more unusual. Although two histidines coordinate the iron of heme I, this appears to be the first example of a heme iron coordinated by the Nδ atom of a histidine side chain (Figure 8.4) while heme II

is a true 5-coordinate heme, with no known role other than electron transfer. Cyt c554 is not known to bind small molecules physiologically; it neither is associated with enzymatic activity nor is it regulated allosterically by small molecules such as hydroxylamine. Recent unpublished data indicates that several small molecules (NO, CN-, F-) that typically bind to 5-coordinate hemes do not bind to the open position of heme II. The crystal structure of cyt c554 shows that the side chains of Thr 154, Pro 155 and Phe 156 shield the open ligation site on the iron of heme II. The inaccessibility of this heme site affords a heme reduction potential that is not significantly affected by direct solvent interactions. **(Figure 8.4 near here)**

High-resolution structural information for cyt c554[26] has allowed measurement of the bond lengths of the histidine ligands to the heme iron, which are listed in Table 1. The bond lengths vary depending on the oxidation-state of the protein, as expected.

The most interesting aspect of the hemes is their packing arrangement in the protein. The four hemes of cyt c554 stack into distinct types of pairs (Figure 8.5). The first type of pair appears stacked with the porphyrin planes approximately parallel to one another and has two slight variants, depending of the coordination of the heme iron. The second type of pair shows two hemes in van der Waals contact with the heme planes approximately perpendicular.

The first variant of the stacked heme pair occurs when two hemes of bis-histidine iron coordination are related by a two-fold axis passing between the hemes, and separated by a plane-to-plane distance of ~3.6 Å to ~3.8 Å (Figure 8.5A). The heme orientation of one site is inverted relative to the other site. Other proteins exhibiting this type of stacked heme pairs include the split-Soret cytochrome[28], cyt *c* NR[29], cytochrome *c* fumarate reductase (cyt *c* FR) [30-32] and HAO[33], the redox partner of cyt c554.

A second variant of the stacked heme pair occurs when a six-coordinate bis-histidine heme stacks onto a five-coordinate heme with a ~30° angle between the heme edge and the two-fold axis (Figure 8.5B). This stacking arrangement has been observed in HAO[33] and cyt *c* NR[29], however in each of these cases, catalytic activity is associated with the five-coordinate heme[29, 34], and in cyt *c* NR, the fifth ligand is a lysine, albeit with a bent conformation reminiscent of a histidine ring (Figure 8.6). **(Figure 8.5 near here)**

In contrast to the stacked pairs exhibited by hemes I and III and hemes II and IV of cyt c554, the central hemes (hemes III and IV) of cyt c554 are packed in with the heme planes at an angle of 110° to one another (Figure 8.5C). This approximately perpendicular arrangement has packing angles similar to those exhibited by cyt c_3[35] and cyt c_3 like proteins[36-39], as well as HAO[33], and cyt *c* NR[29]. Both types of the heme

packing observed in cyt c554 appear to be emerging motifs in multi-heme proteins involved in metabolic processes requiring the rapid transfer of multiple electrons.

The heme arrangements in cyt c554, HAO and cyt *c* NR exhibit more extensive similarities beyond the pairs of hemes[25, 29]. In these cases, the heme packing motifs extends to three or four aligned hemes, with the five-coordinate heme overlaying. An intriguing aspect of the heme arrangement in cyt c554, HAO and cyt *c* NR is that the polypeptide chain immediately adjacent to the heme environment exhibits structural similarity[25], despite the lack of sequence identity (Figure 8.6). Although the polypeptide chain is similar for these three proteins, the conservation of buried water molecules between cyt c554 and cyt *c* NR appears limited to those that orient the histidine ligands to the heme irons[26]. Water molecules cannot clearly be identified in the structure of HAO, however, the imidazole rings of the histidine ligands to the heme iron have the same relative orientation as those seen in cyt c554 and cyt *c* NR. The relative orientations of histidine ligands to heme irons has been suggested to alter the electronic configuration of the porphyrin[40], and thus may be functionally relevant in the formation of the stacked-heme pairs. **(Figure 8.6 near here)**

The heme alignment and corresponding secondary structure similarity between cyt c554, HAO, and cyt *c* NR strongly suggest a possible evolutionary relationship

between these three proteins. While cyt c554 and HAO are involved in the nitrification process, oxidizing NH_3 to NO_2^-, cyt *c* NR acts in the reverse process of nitrite ammonification, reducing NO_2^- to NH_3 at a catalytic heme. Cyt *c* NR is additionally capable of catalyzing the reduction of sulfite to hydrogen sulfide. The remarkable similarity in the heme packing motifs of these three proteins combined with the similar active site architecture between HAO and cyt *c* NR support evolutionary relatedness between these proteins that act in catalyzing a similar reaction in physiologically opposite directions. Although cyt c554 and HAO have virtually no sequence identity in the structurally similar heme core environment, it is striking that cyt c554 contains a motif that is a subset of the structure of HAO. Similar internal structure of these proteins acting in the same pathway suggests a common evolutionary ancestor, however the lack of sequence identity precludes a definitive determination of the evolutionary relationship between the redox partners.

Since the reactants for HAO and cyt *c* NR are so similar and the geochemical milieu supporting their evolution had these reactants in common, it is possible that HAO, cyt c554, and cyt *c* NR share a common ancestry. The divergence between these proteins may have occurred long enough ago that the sequence similarity has all but disappeared, but a significant similarity of secondary structure has been retained.

The Phe130-His131 peptide bond

One interesting feature discovered in the structure determination of the tetragonal crystal form of cyt c554 was the presence of a non-proline *cis*-peptide bond between Phe 130 and His 131. This *cis*-peptide bond appeared to be stabilized by crystal contacts (Figure 8.7A) that were not present in he rhombohedral crystal form. In the absence of the stabilizing crystal contacts, the peptide bond appeared to be *trans*-, but with disallowed angles of Φ and Ψ (Figure 8.7B). *Cis*-peptide bonds can be functionally relevant[41, 42], and the transient *cis*-peptide bonds stabilized by crystal contacts in flavodoxin have been suggested to be necessary for catalytic activity, however a functional role for the *cis*-peptide bond in cyt c554 has not yet been conclusively determined. **(Figure 8.7 near here)**

SPECTROSCOPIC PROPERTIES

The relatively unusual spectral properties of cyt c554 may reflect the interactions between the stacked heme arrangements. Other proteins with similar heme packing arrangements also exhibit complex spectral properties, suggesting the hemes are coupled in some manner, but the detailed spectra of each protein is distinct. Although the split-Soret cytochrome *c*[43] has not been thoroughly investigated spectroscopically, it exhibits unusual optical properties. In the remainder of the proteins known to have stacked

hemes, i.e. cyt c554[8], HAO[44], and cyt c NR[45, 46], the EPR or Mössbauer spectra suggest the hemes are coupled in some manner.

Optical spectroscopy

Cyt c554 was named for the 554 nm absorbence of the α-band[15] seen upon reduction at physiological pH, however the spectral property used for the protein's nomenclature is pH dependent, and can vary between 551 nm and 556 nm[8]. Additionally, both the Soret maximum and spectral features associated with the spin-state of the heme irons are pH dependent. This includes a shoulder to the Soret maximum at 360 nm, which indicates the presence of low-spin heme iron, and the presence of the charge transfer band at 645 nm associated with the presence of high-spin heme iron.

EPR spectroscopy

The EPR spectra of cyt c554[8, 47] differ fundamentally from the spectra of classic heme-containing proteins[48]. Like the visible spectra, they are highly pH dependent and are additionally sensitive to ionic strength[8]. g-values of 2.85, 2.2, 1.55 and 2.67, 2.2, 1.76 at pH 10.5 indicate the presence of two distinct low-spin species. In contrast, the spectra show peaks near g=6 and g=2 at low pH, indicating predominantly high-spin heme. A dominant g-value of 3.3 at neutral pH cannot be ascribed to any known spin state of heme iron or to any mixture of spin states for four heme irons. As there are no other EPR

active species in the protein, it has been suggested that g=3.3 results from some unknown combination of heme-heme interactions. Heme coupling could be affected by the tight heme packing motifs seen in the crystal structure.

The packing of the four hemes in cyt c554[25] is similar to the packing of hemes 3-6 in HAO[33] and the EPR spectra from both proteins generally reflect the presence of heme-heme interactions. The EPR spectra of HAO are consistent with pair-wise interactions between the heme pairs 3 and 5, and pairs 4 and 6[44, 49]. The strength of the interactions is indicative of an exchange coupling between the iron sites. Surprisingly however, no bond pathway is observed in the crystal structure that would be consistent with the strength of the exchange interaction. Consequently, it appears that the exchange coupling is derived from an electronic overlap between the π-orbitals of the porphyrins. The EPR spectra of cyt c554 are also consistent with a similar exchange pathway between all four of the hemes. The main differences between the cyt c554 and HAO EPR spectra may be due to the accessibility of solvent to the 5-coordinate heme site in HAO.

Mössbauer spectroscopy

Mössbauer spectroscopy of cyt c554 reveals the presence of both high-spin and low-spin heme iron. At physiological pH, 75% of the hemes are low-spin while 25% of the hemes are high spin[8], suggesting the presence of three six-coordinate hemes and one five-

coordinate heme. This is consistent with the optical and EPR spectra described above as well as Resonance Raman spectroscopy[50] that showed the presence of both low-spin and high-spin heme. The Mössbauer spectra do not contain hyperfine interactions[8] suggesting the hemes are magnetically coupled, and further supporting coupling as the rationale for the appearance of the atypical EPR spectra. This coupling of the heme irons may occur in pairs, consistent with contact shifted NMR spectra[51] and the stacking of heme pairs observed in the crystal structure[25]. The Mössbauer spectrum of the high-spin iron of oxidized cyt c554 (δ=0.40 mm/s, ΔEq=1.10 mm/s) originates from a species that is not observed in the Mössbauer spectra of oxidized HAO. Furthermore, the high-spin site of reduced cyt c554 (δ=0.94 mm/s, ΔEq=2.43 mm/s) has substantially different iron parameters than that of reduced HAO (δ=0.96 mm/s, ΔEq=4.21 mm/s)[52]. These differences indicate that while the heme pair containing the 5-coordinate heme in both proteins stacks similarly, the electronic structure of the 5-coordinate hemes is significantly different. HAO contains a covalently linked tyrosine to the 5-coordinate active site heme, but how this would affect the electronic configuration is uncertain.

FUNCTIONAL ASPECTS

Oxidation and Reduction of Cyt c554

The reduction potentials of the four hemes of cyt c554 at pH 7.0 have been determined by a combination of voltammetry and spectroscopy, using an optically transparent thin layer electrode[24]. The high-spin heme has a reduction potential of +47 mV, while the low-spin hemes titrate with midpoint potentials of +47 mV, -147 mV, and -276 mV. Five-coordination results in a high-spin heme iron[53], thus heme II can be assigned a reduction potential of +47 mV; however, the remainder of the reduction potentials have not yet been assigned.

Electron transfer kinetics

As cyt c554 physiologically acts as a two-electron acceptor[9], the rates of electron transfer of two electrons are of interest. Stopped-flow kinetic studies of electron transfer at physiological pH revealed that one electron is passed from HAO to cyt c554 with a rate constant of 250-300 s^{-1}, while a second electron is passed ten times more slowly with a rate constant of 25-30 s^{-1}.[54]

Kinetics of dithionite reduction of cyt c554 appear biphasic and result in non-physiological four-electron reduction of the protein. The first phase mimics the

physiological reduction rates, and involves the reduction of two hemes. In contrast, the second phase, involving the reduction of the remaining two hemes, proceeds over 300 times more slowly[17]. The multi-phasic reduction kinetics is consistent with negative cooperativity between the hemes, or a conformation change occurring during reduction and may reflect a large backbone movement observed between the oxidized and reduced states of cyt c554[26]. The conformational change occurs in a stable loop (residues 175 - 179) between heme III and heme IV and displaces the loop over 2 Å (Figure 8.8). Residue 179 serves as the histidine ligand to heme III, and the conformational change may be triggered by a change in peptide orientation between Met 178 and His 179. In the oxidized crystal form, the carbonyl group of this peptide bond appears to be in van der Waals contact with the porphyrin of heme III. Upon the reduction of heme III, this carbonyl group flips away from the porphyrin. As the reduction potential for heme III has not been assigned, it is difficult to interpret the relevance of the shift in backbone position upon the change in oxidation state.

Interaction of cyt c554 with other members of the nitrification pathway

(Figure 8.9 near here) Based on the pI values for HAO (3.4)[55], cyt c554 (10.7)[15] and cyt c552 (3.7)[15], electrostatic effects probably contribute to intermolecular interactions between the soluble components of the nitrification pathway. Electrostatic surface representations of HAO[33] and cyt c554[25] show that HAO and cyt c554 contain

apparently complementary surfaces that are negatively and positively charged, respectively, indicating a suitable binding mode for these two molecules (Figure 8.9). Although the solution structure of cyt c552 has been solved[56], a clear binding mode for cyt c552 and cyt c554 remains to be established.

8.3D representation Two views of the fold of cyt c554 are shown with a 90° rotation between them. The N-terminus is colored in black, and the protein can be traced by following the color gradient to the C-terminus (red).

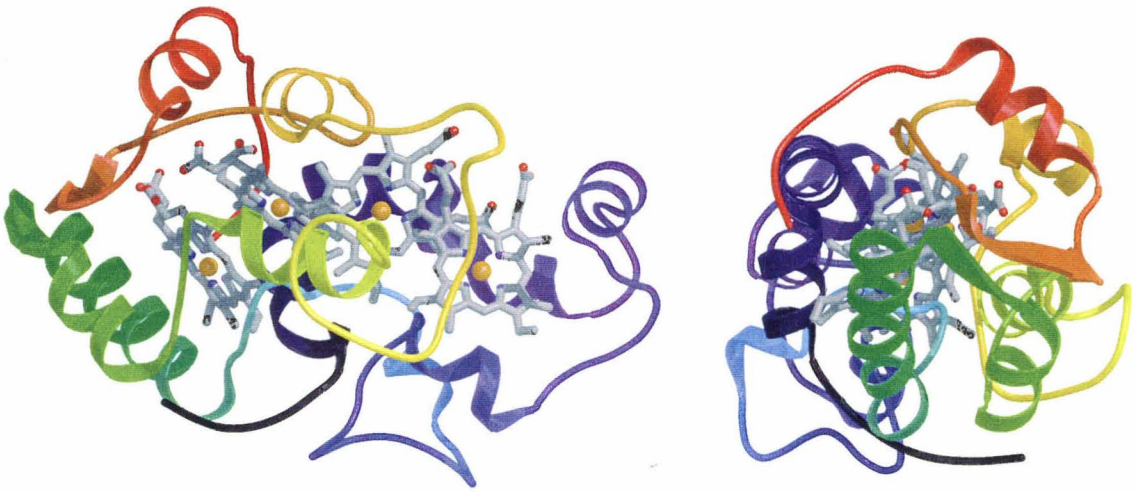

Figure 8.1 The biological nitrogen cycle.

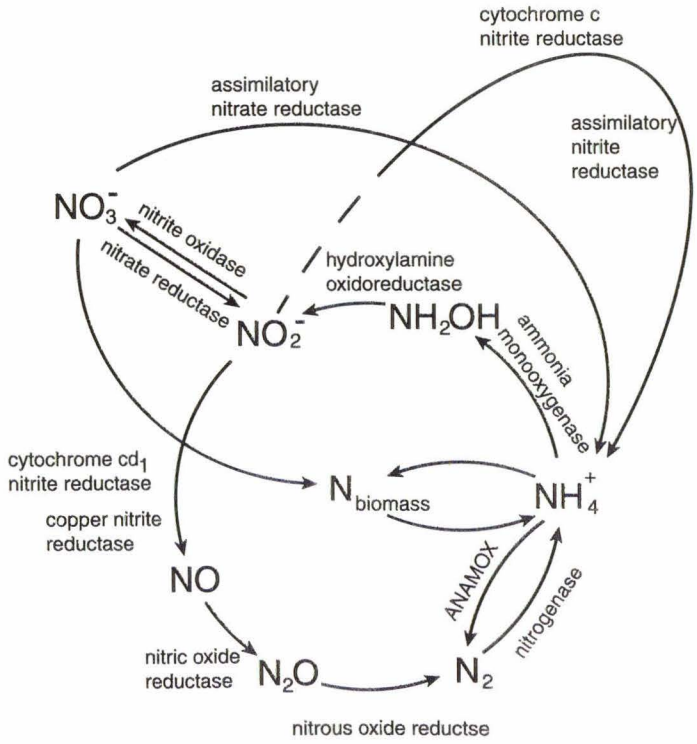

Figure 8.2 Biological nitrification catalyzed by *Nitrosomonas europaea.* The role of cyt c552 is uncertain in this pathway.

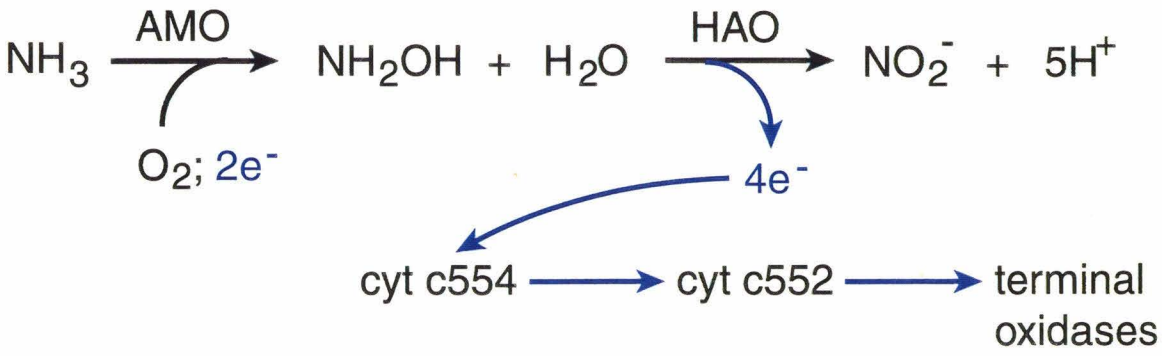

Figure 8.3 Heme organization and interheme iron distances.

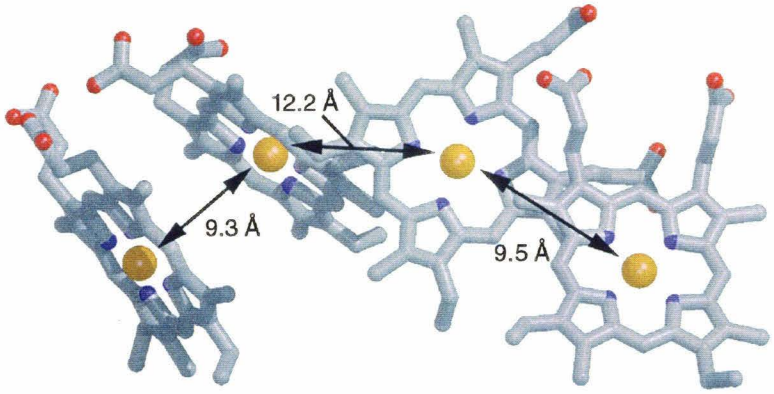

Figure 8.4 The unusual histidine Nδ ligation of heme I of cytochrome c554. The model is superimposed onto an $|F_o|$ - $|F_c|$ omit map at 1.6 Å resolution calculated after the removal of His 102. The histidine is stabilized in this orientation by a hydrogen-bond from the Nε atom to Gln 126.

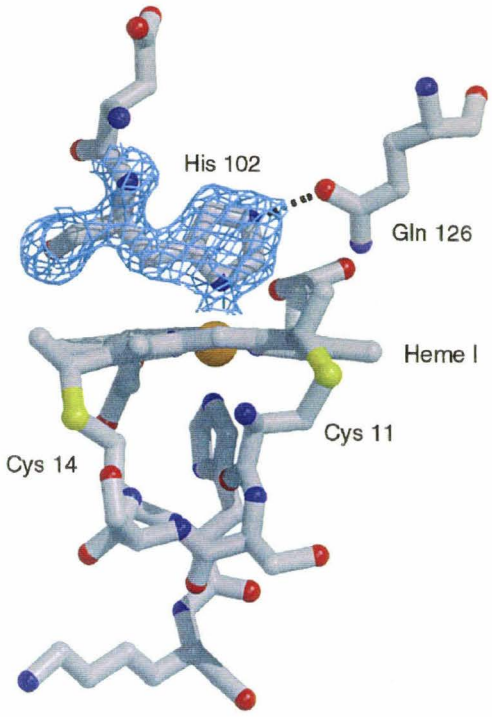

Figure 8.5 Two variants of parallel stacked heme pairs. On the left are 0° and 90° views of the stacked heme pairs, where both hemes are six-coordinate with bis-histidine heme-iron ligation. On the right are 0° and 90° views of the stacked heme pairs when one hemes has six-coordinate bis-histidine ligation and the other has five-coordinate ligation.

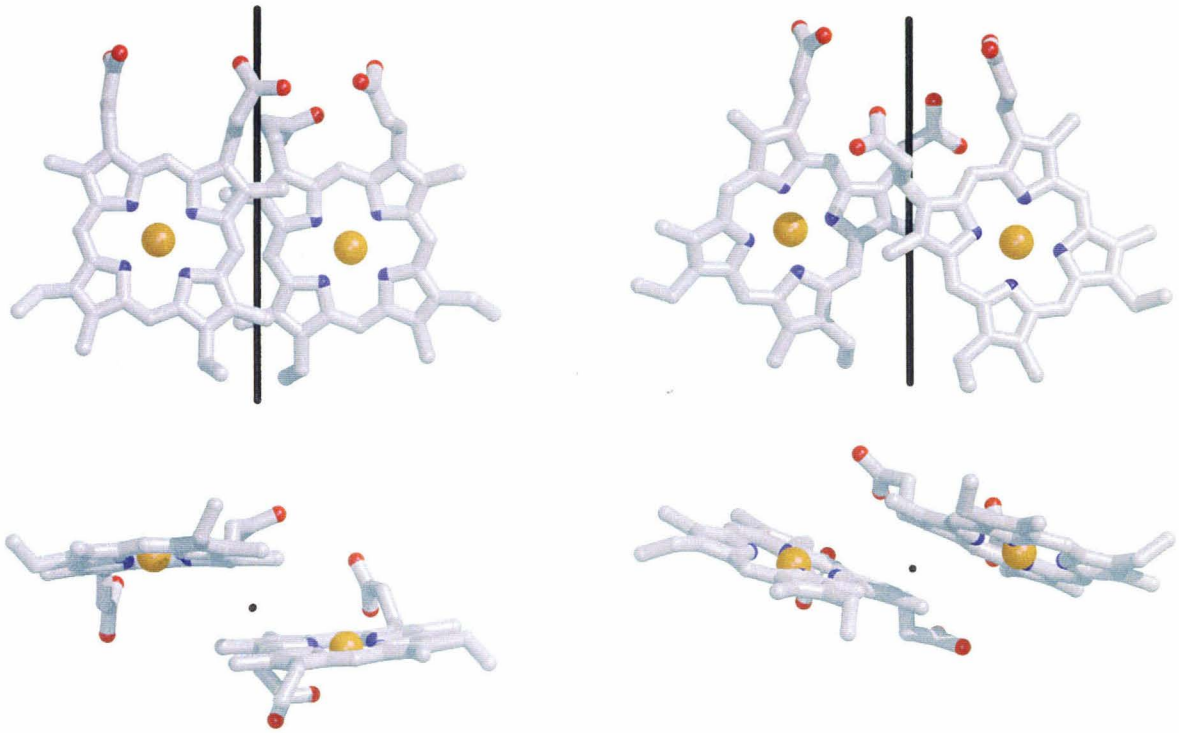

Figure 8.6 Stereoview of the alignment of the heme cores of HAO (blue), cyt c554 (red), and cyt *c* NR (green).

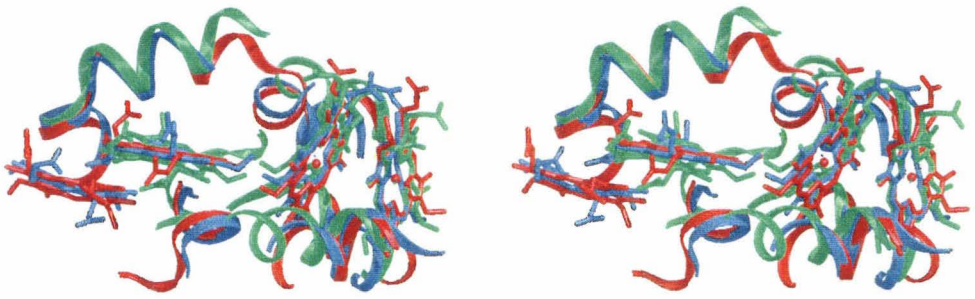

Figure 8.7 The His 129-Phe130 peptide bond appears *cis*- in the 1.6 Å resolution crystal structure determination with the rhombohedral crystal form (top) and *trans*- in the 2.6 Å resolution tetragonal crystal form (bottom).

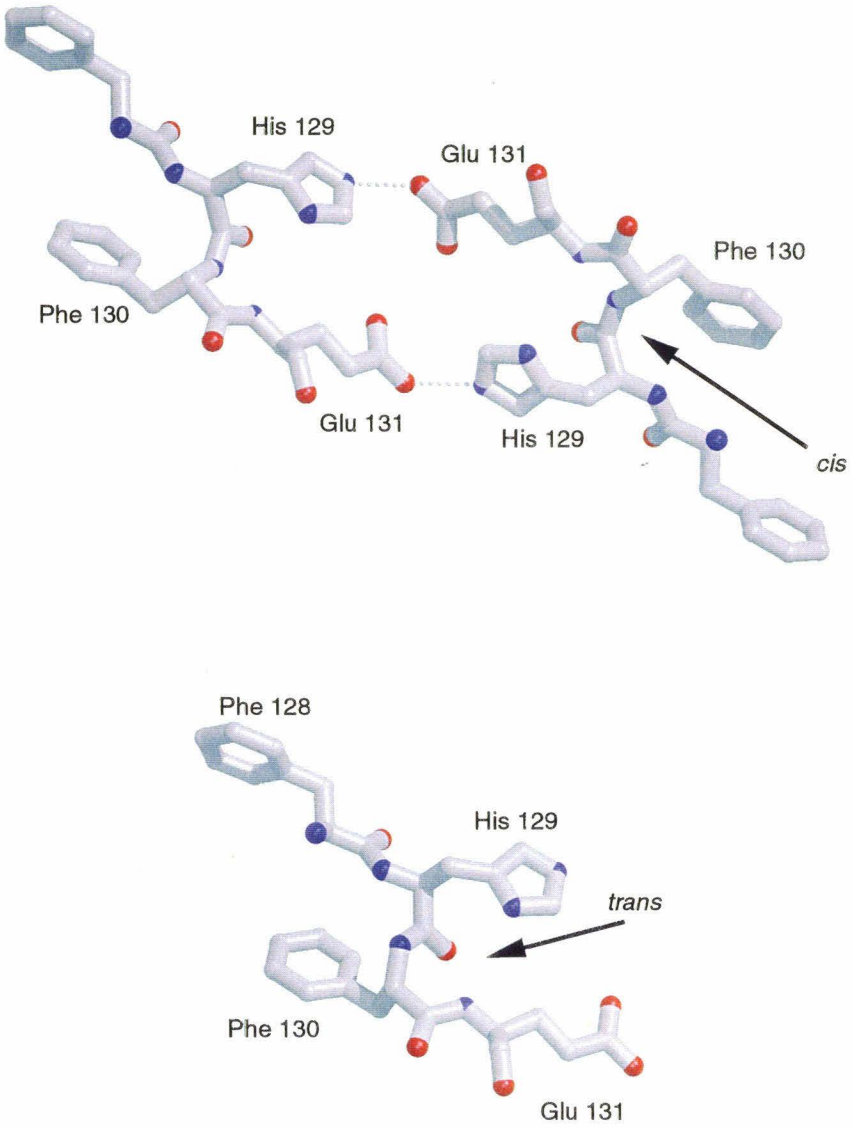

Figure 8.8 A conformational change occurs near heme III and heme IV upon reduction. In the oxidized state (black), the Met 178-his 179 peptide bond is within 5 Å of the heme porphyrin. Upon reduction (white) the peptide bond flips away, causing a >2 Å displacement of the loop between residues 173 and 179.

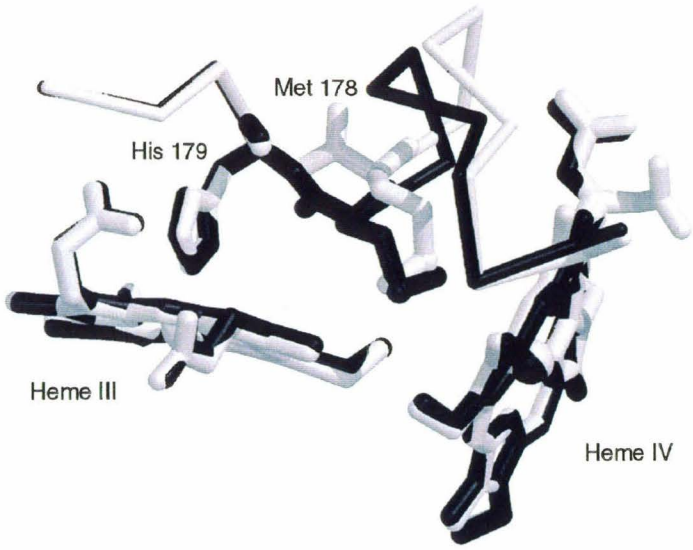

Figure 8.9 Stereoview of a GRASP electrostatic surface potential representation of HAO (center) and cyt c554. The complementary negatively and positively charged surfaces respectively indicate a likely binding mode (yellow).

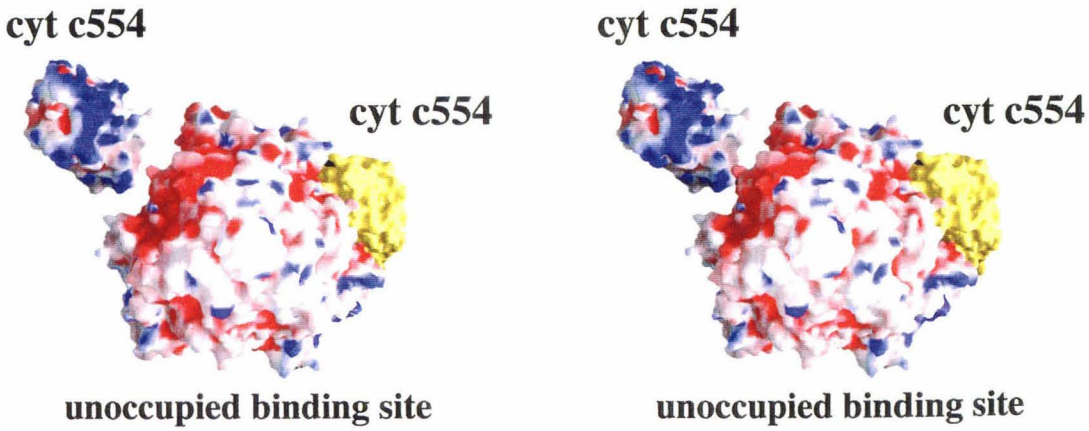

REFERENCES

1. P. M. Wood, in J. I. Prosser (ed), Nitrification, IRL Press, Oxford, pp 39-62 (1986)

2. R. A. Herbert, *FEMS Microbiol. Rev.,* **23**, 563 - 590 (1999).

3. H. A. Painter, in J. I. Prosser (ed), Nitrification, IRL Press, Oxford, pp 185-211 (1986)

4. J. E. Alleman and K. Preston, in A. Swann (ed.), *Proceedings of the Second Annual Conference of Commercial Aquaculture*, Bloomington, IL (1991). Also available on the World Wide Web: **http://ce.ecn.purdue.edu/~alleman/w3-articles/nitrifier-physiology/nitrifier-behavior.html**

5. J. A. Zahn and A. A. Dispirito, *J. Bacteriol.,* **178**, 1018-1029 (1996).

6. J. A. Zahn, D. M. Arciero, A. B. Hooper and A. A. DiSpirito, *FEBS Lett.,* **397**, 35-38 (1996).

7. J. H. Shears and P. M. Wood, *Biochem. J.,* **226**, 499-507 (1985).

8. K. Andersson, J. Lipscomb, M. Valentine, E. Münck and A. Hooper, *J. Biol. Chem.,* **261**, 1126-1138 (1986).

9. D. M. Arciero, C. Balny and A. B. Hooper, *J. Inorg. Biochem.,* **36**, 217-217 (1989).

10. T. Yamazaki, Y. Fukumori and T. Yamanaka, *J. Biochem.,* **103**, 499-503 (1988).

11. A. A. DiSpirito, L. R. Taaffe, J. D. Lipscomb and A. B. Hooper, *Biochim. Biophys. Acta,* **827**, 320-326 (1985).

12. R. C. Prince and G. N. George, *Nat. Str. Biol.,* **4**, 247-250 (1997).

13. D. J. Richardson and N. J. Watmough, *Curr. Op. Chem. Biol.,* **3**, 207-219 (1999).

14. T. Yamanaka, *Plant Cell Physiol.*, **37**, 569-574 (1996).

15. T. Yamanaka and M. Shinra, *J. Biochem.*, **75**, 1265-1273 (1974).

16. D. C. Y. Tsang and I. Suzuki, *Can. J. Biochem.*, **60**, 1018-1024 (1982).

17. A. A. DiSpirito, C. Balny and A. B. Hooper, *Eur. J. Biochem,* **162**, 299-304 (1987).

18. H. McTavish, D. M. Arciero and A. B. Hooper, *Arch Biochem Biophys,* **324**, 53-58 (1995).

19. N. G. Hommes, L. A. Sayavedra-Soto and D. J. Arp, *Gene,* **146**, 87-89 (1994).

20. H. McTavish, F. LaQuier, D. M. Arciero, M. S. P. Logan, G. Mundfrom, J. A. Fuchs and A. B. Hooper, *J. Bacteriol.*, **175**, 2445-2447 (1993).

21. D. Bergmann, D. Arciero and A. Hooper, *J. Bact.*, **176**, 3148-3153 (1994).

22. M. A. Bruns, J. M. Fries, J. M. Tiedje and E. A. Paul, *Microb. Ecol.*, **36**, 293-302 (1998).

23. L. C. Crossman, J. W. B. Moir, J. J. Enticknap, D. J. Richardson and S. Spiro, *Microbiology,* **143**, 3775-3783 (1997).

24. D. M. Arciero, M. Collins, J. Haladjian, P. Bianco and A. B. Hooper, *Biochemistry,* **30**, 11459-11465 (1991).

25. T. M. Iverson, D. M. Arciero, B. T. Hsu, M. S. P. Logan, A. B. Hooper and D. C. Rees, *Nat. Struct. Biol.*, **5**, 1005-1012 (1998).

26. T. M. Iverson, D. M. Arciero, A. B. Hooper and D. C. Rees, (in preparation).

27. C. Nagata, N. Igarashi, H. Moriyama, T. Fujiwara, Y. Fukumori and N. Tanaka, *J. Biochem (Tokyo),* **117**, 931-932 (1995).

28. P. Matias, J. Morias, A. Coelho, R. Meijers, A. Gonzalez, A. Thompson, L. Sieker, J. LeGall and M. Carrondo, *J. Biol. Inorg. Chem.,* **2**, 507-514 (1997).

29. O. Einsle, A. Messerschmidt, P. Stach, G. P. Bourenkov, H. D. Bartunik, R. Huber and P. M. H. Kroneck, *Nature,* **400**, 476-480 (1999).

30. V. Bamford, P. S. Dobbin, D. J. Richardson and A. M. Hemmings, *Nat. Struct. Biol.,* **6**, 1104-1109 (1999).

31. D. Leys, A. S. Tsapin, K. H. Nealson, T. E. Meyer, M. A. Cusanovich and J. J. VanBeeumen, *Nat. Struct. Biol.,* **6**, 1113-1117 (1999).

32. P. Taylor, S. L. Pealing, G. A. Reid, S. K. Chapman and M. D. Walkinshaw, *Nat. Struct. Biol.,* **6**, 1108-1112 (1999).

33. N. Igarashi, H. Moriyama, T. Fujiwara, Y. Fukumori and N. Tanaka, *Nat. Struct. Biol.,* **4**, 276-284 (1997).

34. A. B. Hooper and K. R. Terry, *Biochemistry,* **16**, 455-459 (1977).

35. P. M. Matias, C. Frazao, J. Morais, M. Coll and M. A. Carrondo, *J Mol Biol,* **234**, 680-699 (1993).

36. I. B. Coutinho, D. L. Turner, M. Y. Liu, J. LeGall and A. V. Xavier, *J. Biol. Inorg. Chem.,* **1**, 305-311 (1996).

37. L. Banci, I. Bertini, M. Bruschi, P. Sompornpisut and P. Turano, *Proc. Natl. Acad. Sci. USA,* **93**, 14396-14400 (1996).

38. M. Czjzek, F. Guerleqiun, M. Bruschi and R. Haser, *Structure,* **4**, 395-404 (1996).

39. P. M. Matias, L. M. Saraiva, C. M. Soares, A. V. Coelho, J. LeGall and M. A. Carrondo, *J. Biol. Inorg. Chem.,* **4**, 478-494 (1999).

40. N. V. Shokhirev and F. A. Walker, *J. Biol. Inorg. Chem.,* **3**, 581-594 (1998).

41. M. L. Ludwig, K. A. Pattridge, A. L. Metzger, M. M. Dixon, M. Eren, Y. Feng and R. P. Swenson, *Biochemistry,* **36**, 1259-1280 (1997).

42. A. Jabs, M. S. Weiss and H. R, *J. Mol. Biol.,* **286**, 291-304 (1999).

43. M.-C. Liu, C. Costa, I. B. Coutinho, J. J. G. Moura, I. Moura, A. V. Xavier and J. LeGall, *J. Bacteriol.,* **170**, 5545-5551 (1988).

44. M. Hendrich, M. S. P. Logan, K. Andersson, D. M. Arciero, J. Lipscomb and A. B. Hooper, *J. Am. Chem. Soc.,* **116**, 11961-11968 (1994).

45. W. Schumacher and P. M. H. Kroneck, *Arch.Microbiol.,* **156**, 70-74 (1991).

46. W. Schumacher, U. Hole and P. M. H. Kroneck, *Biochem. Biophys. Res. Commun.,* **205**, 911-916 (1994).

47. K. K. Andersson, J. D. Lipscomb and A. B. Hooper, *Inorg. Chim. Acta,* **79**, 181-182 (1983).

48. G. Palmer, in A. B. P. Lever and H. B. Gray (ed), Iron Porphyrins part Two, Addison-Wesley Publishing Company, London, pp 43-85 (1983).

49. D. M. Arciero, A. Golombek, M. P. Hendrich and A. B. Hooper, *Biochemistry,* **37**, 523-529 (1998).

50. K. K. Andersson, G. T. Babcock and A. B. Hooper, *FEBS Letters,* **170**, 331-334 (1984).

51. K. K. Andersson, J. D. Lipscomb and A. B. Hooper, *Inorg. Chim. Acta,* **79**, 181-182 (1983).

52. K. K. Andersson, T. A. Kent, J. D. Lipscomb, A. B. Hooper and E. Münck, *J. Biol. Chem.,* **259**, 6833-6840 (1984).

53. W. R. Scheidt and M. Gouterman, in A. B. P. Lever and H. B. Gray (ed), Iron Porphyrins Part One, Addison - Wesley Publishing Co, Inc., London, pp 89-139 (1983)

54. D. Arciero, C. Balny and A. Hooper, *Biochemistry,* **30**, 11466-11472 (1991).

55. A. B. Hooper, P. Maxwell and K. Terry, *Biochemistry,* **17**, 2984-2989 (1978).

56. R. Timkovich, D. Bergmann, D. M. Arciero and A. B. Hooper, *Biophys. J.,* **75**, 1964-1972 (1998).

Appendices: Carbonic Anhydrases

A-1. Archaeal methanogenesis and the γ-class carbonic anhydrase from *Methanosarcina thermophila*

Methane producing microbes release about 400 million metric tons of methane into the atmosphere each year, thus significantly contributing to the global greenhouse effect. Microbial methane production requires strictly anaerobic environments *(1)*, which can include the interior of animals (such as the rumen of cattle), watery landscapes (natural wetlands, bogs, or rice paddies), or human-made sites (landfills or sewage digestors). In any of these locations, the biological production of methane requires a food chain of at least three interacting metabolic groups of obligate anaerobes (Fig. A-1.1) *(2)*.

One type of anaerobe, the methanogenic archaeon, derives all its energy from the methanogenesis of a very restricted number of substrates: acetate; carbon dioxide; hydrogen; formate; methanol; and methylamines *(3)*. Depending upon the substrate available, methanogenic archaea use separate pathways *(4)* in which methane is produced from the methyl group of acetate (reaction 1), the reduction of carbon

dioxide (reactions 2a and 2b), or the reduction of methanol or methylamines (reaction 3). The pathways of methane formation described by each equation involve a number of enzymes and coenzymes that are found exclusively in archael methanogenic pathways *(5)*. The existence of these unique enzymes has led to the proposal of the three-domain phylogeny: archaea; bacteria; and eukarya *(6)*.

$CH_3COO^- + H^+ \rightarrow CH_4 + CO_2$ (1)

$CO_2 + 4H_2 \rightarrow CH_4 + 2H_2O$ (2a)

$4H_2CO_2 \rightarrow 3CO_2 + CH_4 + 2H_2O$ (2b)

$4(R\text{-}CH_3) + 2H_2O \rightarrow 4RH + 3CH_4 + CO_2$ (3)

The methanogenic archaeon *Methanosarcina thermophila* can derive all of its energy from the conversion of acetate to methane (reaction 1, Fig. A-1.2) in conditions where other substrates are not available. In the first step of the fermentation of acetate, acetate kinase (Ack) phosphorylates the carboxyl group of acetate *(7, 8)*, consuming one molecule of ATP (Fig. A.1.3 step 1). Following this, the substrate is activated by phosphotransacetylase (Pta) *(9)* yielding acetyl-CoA as the product (Fig. A-1.3 step 2). The key enzyme in the aceticlastic pathway is the five-subunit carbon monoxide dehydrogenase (Cdh). Cdh cleaves the C-C and C-S bonds in the acetyl moiety of acetyl-CoA *(10, 11)*, oxidizes the carbonyl group to CO_2, and transfers the methyl group to tetrahydrosarcinapterin *(12)* (H_4SPT; Fig.

A.1.3 step 3). Electrons derived from the carboxyl group of acetate are passed from Cdh to a transmembrane cytochrome *b* (cyt *b*) complex by ferredoxin (FdxA) *(13)* (Fig. A-1.3 step 4). It has been suggested that the integral-membrane cyt *b* complex may aid in the formation of a transmembrane proton gradient used to drive ATP synthesis *(14)*. The CH_3-H_4SPT molecule is activated by a membrane-bound methyltransferase (Tase) to form CH_3-S-CoM (Fig. A-1.3 step 5). This reaction may be coupled to the transport of a sodium ion across the membrane of *M. thermophila*, which could help drive ATP synthesis *(15)*. The activated CH_3-S-CoM can now be acted on by methyl-CoM reductase (Mer; Fig. A-1.3 step 6), an enzyme common to all methanogenic pathways (reactions 1 - 3) and the final chemical reaction occurring during methanogenesis *(16)*. Electrons are supplied to this last reaction by heterodisulfide reductase (Hdr) *(17)* and coenzyme B (Fig. A-1.3 step 7).

During the fermentation of acetate by *M. thermophila*, the activity of a secreted carbonic anhydrase (Cam) increases, suggesting involvement of this enzyme in acetate catabolism *(18)*. It is proposed that CO_2, a byproduct of the reaction catalyzed by Cdh, is converted to HCO_3^- by Cam outside of the cell to facilitate either the uptake of acetate or the removal of CO_2 from the cytoplasm (Fig. A-1.3 step 8).

The structure of Cam has previously been solved at 2.8 Å resolution *(19)* revealing an unusual left-handed β-helix fold, and showing the evolutionary convergence of the ligation of the active site zinc between Cam and mammalian carbonic anhydrases. Using a new crystal form, the structure of Cam has been solved in nine states of the enzyme at resolutions between 1.46 Å and 1.95 Å by molecular replacement *(20;* Iverson et al. in press*)*. The high-resolution structure of Cam, combined with previous kinetic studies *(18, 21, 22, 23)*, has revealed mechanistic insights in the function of this enzyme.

Fig. A-1.1: Microbial Food Chain. Three of the four types of microbes shown are required for the complete decomposition of complex biomass to methane and carbon dioxide.

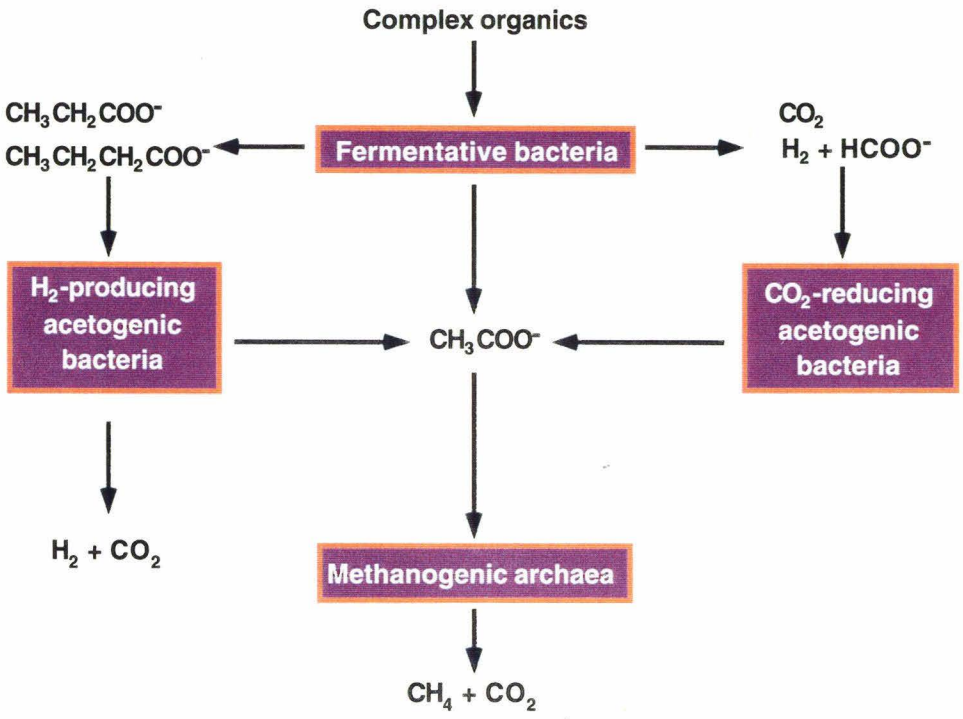

Fig. A-1.2 Pathway for the conversion of acetate to methane by methanoarchaea. Chemically modified acetate intermediates are indicated with necessary cofactors, intermediate products, and reactants indicated. Enzymes used in this pathway are shown in Fig. A.1.3.

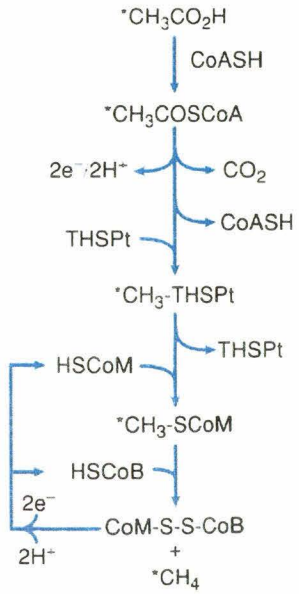

Fig. A-1.3: Methanogenic fermentation of acetate by *M. thermophila.* Steps described in the text are indicated by number. Electron transfer steps are indicated with a black arrows, while chemical pathways are indicated with colored arrows.

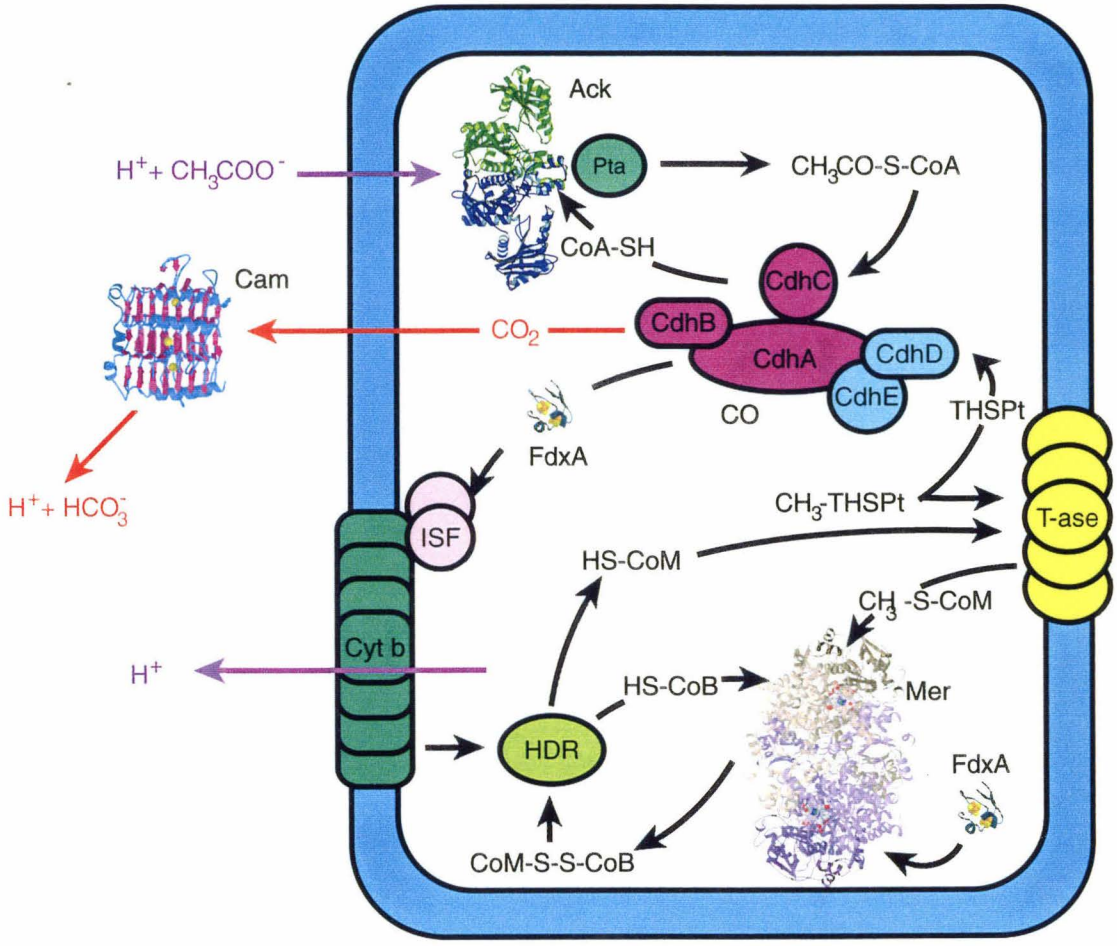

REFERENCES

1. Whitman, W., Coleman, D., and Wiebe, W. (1998) *Proc. Natl. Acad. Sci. USA 95*, 6578-6583.

2. Zinder, S. (1993) in *Methanogenesis* (Ferry, J., Ed.) pp 128-206, Chapman and Hall, New York.

3. Ferry, J. (1997) *BioFactors 6*, 25-35.

4. Blaut, M. (1994) *Antoine van Leeuwenhoek 66*, 187-208.

5. DiMarco, A., Bobik, T., and Wolfe, R. (1990) *Annu. Rev. Biochem. 59*, 355-394.

6. Woese, C., Kandler, O., and Wheelis, M. (1990) *Proc. Natl. Acad. Sci. USA 87*, 4576-4579.

7. Aceti, D., and Ferry, J. (1988) *J. Biol. Chem. 263*, 15444-15488.

8. Fisher, R., and RK, T. (1988) *FEBS Lett. 228*, 249-253.

9. Lundie, L., and Ferry, J. (1989) *J. Biol. Chem. 264*, 18392-18396.

10. Abbanat, D., and Ferry, J. (1991) *Proc. Nat. Acad. Sci. USA 88*, 3272-3276.

11. Raybuck, S., Ramer, S., Abbanat, D., Peters, J., Orme-Johnson, W., Ferry, J., and Walsh, C. (1991) *J. Bacteriol. 173*, 929-932.

12. Grahame, D. (1991) *J. Biol. Chem. 266*, 22227-22233.

13. Fisher, R., and Thauer, R. (1990) *FEBS Lett. 269*, 368-372.

14. Mountfort, D. (1978) *Biochem. Biophys. Res. Commun. 85*, 1346-1350.

15. Al-Mahrouq, H., Carper, S., and Lancaster, J. J. (1986) *FEBS Lett. 207*, 262-265.

16. Jablonski, P., and Ferry, J. (1991) *J. Bacteriol. 173*, 2481-2487.

17. Hedderich, R., Berkessel, A., and Thauer, R. (1990) *Eur. J. Biochem. 193*, 255-261.

18. Alber, B. E., and Ferry, J. G. (1994) *Proc. Natl. Acad. Sci. USA 91*, 6909-6913.

19. Kisker, C., Schindelin, H., Alber, B. E., Ferry, J. G., and Rees, D. (1996) *EMBO J. 15*, 2323-2330.

20. Iverson, T., Alber, B., Kisker, C., Ferry, J., and Rees, D. (submitted) *Biochemistry*.

21. Alber, B. E., and Ferry, J. G. (1996) *J. Bacteriol. 178*, 3270-3274.

22. Alber, B. E., Colangelo, C. M., Dong, J., Stålhandske, C. M. V., Baird, T. T., Tu, C., Fierke, C. A., Silverman, D. N., Scott, R. A., and Ferry, J. G. (1999) *Biochemistry 38*, 13119-13128.

23. Tripp, B. C. and Ferry, J.G. (submitted) *Biochemistry*.

Appendix A-2

Iverson, T.M., Alber, B.E., Kisker, C., Ferry, J.G., Rees, D.C. (2000) A closer look at the active site of γ-class carbonic anhydrases: high-resolution crystallographic studies of the carbonic anhydrase from *Methanosarcina thermophila.* *Biochemistry.* In revision.

A Closer Look at the Active Site of γ-Class Carbonic Anhydrases: High-resolution Crystallographic Studies of the Carbonic Anhydrase from *Methanosarcina thermophila*[†,§§]

Tina M. Iverson[‡], Birgit E. Alber[§,@], Caroline Kisker[‖,#], James G. Ferry[§], and Douglas C. Rees[‖,⊥*]

‡ Graduate Option in Biochemistry, 147-75CH, California Institute of Technology, Pasadena, CA, 91125

§ Department of Biochemistry and Molecular Biology, Pennsylvania State University, University Park, PA 16802

@ Present address: Institut für Biologie II, Mikrobiologie, Albert-Ludwigs-Universität Freiburg, Schänzlestr. 1, D-79104 Freiburg, Germany

‖ Division of Chemistry and Chemical Engineering, California Institute of Technology, Pasadena, CA 91125

Present address: State University of New York At Stony Brook, Department of Pharmacological Sciences, Stony Brook, NY 11794-8651

⊥ Howard Hughes Medical Institute, Division of Chemistry and Chemical Engineering, 147-75CH, California Institute of Technology, Pasadena, CA 91125

*To whom correspondence should be addressed at dcrees@caltech.edu. Phone (626) 395-8393 FAX (626) 744-9524

† This work was supported by a grant from the National Institutes of Health to J.G.F. (GM44661). T.M.I. is supported by a NIH training grant (GM07737).

§§ Coordinates for all structures described here have been deposited with the PDB and have been released. PDB accession numbers are listed in Table A-2.1.

RUNNING TITLE: Crystallographic studies of γ-carbonic anhydrase

Abbreviations: Cam, *Methanosarcina thermophila* carbonic anhydrase; Zn-Cam, Cam that has been heterologously produced in *Eschericia coli*, metal-depleted and reconstituted with zinc; Co-Cam, Cam that has been heterologously produced in *E. coli*, metal-depleted and reconstituted with cobalt; HCAII, human carbonic anhydrase isozyme II; E, enzyme; Bct, bicarbonate; PEG, polyethylene glycol; EXAFS, extended x-ray absorption fine structure; PDB, Protein Data Bank.

ABSTRACT: The prototype of the γ-class of carbonic anhydrase has been characterized from the methanogenic archaeon *Methanosarcina thermophila*. Previously reported kinetic studies of the γ-class carbonic anhydrase are consistent with this enzyme having a similar reaction mechanism as the mammalian α-class of carbonic anhydrase. However, the overall folds of these two enzymes are dissimilar and, apart from the zinc-coordinating histidines, the active site residues bear little resemblance. The crystal structures of zinc-containing and cobalt-substituted γ-class carbonic anhydrase from *M. thermophila* are reported here between 1.46 Å and 1.95 Å resolution in the unbound form and co-crystallized with either SO_4^{2-} or HCO_3^-. Relative to the tetrahedral coordination geometry seen at the active site in the α-class of carbonic anhydrases, the active site of the γ-class enzyme contains additional metal-bound water ligands, so the overall coordination geometry is trigonal bipyramidal for the zinc-containing enzyme and octahedral for the cobalt-substituted enzyme. Ligands bound to the active site all make contacts with the side chain of Glu 62 in manners that suggest the side chain is likely protonated. In the uncomplexed zinc-containing enzyme, the side chains of Glu 62 and Glu 84 appear to share a proton; additionally Glu 84 exhibits multiple conformations. This suggests that Glu 84 may act as a proton shuttle, which is an important aspect of the reaction mechanism of α-class carbonic anhydrases. A hydrophobic pocket on the surface of the enzyme may participate in the trapping of CO_2 at the active site. Based on

the coordination geometry at the active site, ligand binding modes, the behavior of the side chains of Glu 62 and Glu 84, and analogies to the well-characterized α-class of carbonic anhydrase, a more-defined reaction mechanism is proposed for the γ-class of carbonic anhydrase.

Carbonic anhydrases are zinc-containing enzymes that were first noted for their physiological role in interconverting CO_2 and HCO_3^- *(1)*. Based on sequence similarities, there are three distinct classes of carbonic anhydrases: α, β, and γ. The α-class is generally thought of as mammalian, and includes at least fourteen mammalian isozymes, along with two isozymes from *Chlamydomonas reinhardtii*, and two prokaryotic isozymes *(2, 3)*. The β-class is primarily found in phototrophic organisms, including plants. The prototype for the γ-class of carbonic anhydrase has been discovered in the methanoarchaeon *Methanosarcina thermophila* (Cam^1) *(4)*. Crystal structures have been reported for Cam *(5)* and several isozymes of the α-class of carbonic anhydrase *(6-11)*, but there is currently no crystallographic information available for any representative of the β-class of carbonic anhydrase.

In *M. thermophila*, Cam activity increases when the substrate for growth is switched from methanol to acetate *(12)*, suggesting involvement of this enzyme in acetate catabolism. *M. thermophila* obtains energy for growth by cleaving the C-C bond of acetate and reducing the methyl group to CH_4 with electrons derived from the oxidation of the carbonyl group to CO_2. It is proposed that CO_2 is converted to HCO_3^- by Cam outside the cell to facilitate either the uptake of acetate or the removal of CO_2 from the cytoplasm. Cam catalyzes the interconversion of CO_2 and HCO_3^- with turnover numbers

as high as 6×10^4 sec^{-1} *(13)*, which approaches the turnover number of 10^6 sec^{-1} observed for α-carbonic anhydrases *(14)*.

Kinetic studies *(13)* suggest that the hydration of CO_2 by Cam may occur by a mechanism similar to that proposed for human carbonic anhydrase II (HCAII) *(14-17)*. HCAII, the best studied carbonic anhydrase and the isozyme with highest activity *(18)*, belongs to the α-class of carbonic anhydrases and utilizes a "zinc-hydroxide" mechanism for catalysis. The overall enzyme-catalyzed reaction occurs in two distinct half-reactions. The first half-reaction is the interconversion of CO_2 and HCO_3^- (eqs 1a and 1b, where E signifies the enzyme) and involves nucleophilic attack of the zinc hydroxyl ion on CO_2. This is followed by exchange of zinc bound HCO_3^- with water. The second half reaction corresponds to the rate-determining intramolecular and intermolecular proton transfer steps (eqs 2a and 2b), which regenerates the zinc-hydroxide at the active site.

$$E\text{-}Zn^{2+}\text{-}OH^- + CO_2 \leftrightarrow E\text{-}Zn^{2+}\text{-}HCO_3^- \qquad (1a)$$

$$E\text{-}Zn^{2+}\text{-}HCO_3^- + H_2O \leftrightarrow E\text{-}Zn^{2+}\text{-}H_2O + HCO_3^- \qquad (1b)$$

$$E\text{-}Zn^{2+}\text{-}H_2O \leftrightarrow {}^+H\text{-}E\text{-}Zn^{2+}\text{-}OH^- \qquad (2a)$$

$${}^+H\text{-}E\text{-}Zn^{2+}\text{-}OH^- + B \leftrightarrow E\text{-}Zn^{2+}\text{-}OH^- + BH^+ \qquad (2b)$$

The proton indicated in eqs 2a and 2b represents protonation of His 64 of HCAII, which shuttles protons between the active site zinc and the buffer molecules (B) in the solvent *(19, 20)*. Intramolecular proton transfer (eq 2a) is rate-limiting at saturating buffer concentrations. At low buffer concentrations, intermolecular transfer (eq 2b) is rate limiting.

In addition to the similar kinetic properties, Cam and HCAII exhibit structural similarities in coordination of the zinc ion. The crystal structure of HCAII *(8)* reveals an active site containing a zinc ion tetrahedrally coordinated to three histidines and a highly conserved water molecule. The structure of Cam has been previously solved at 2.8 Å resolution *(5)*. Although the overall folds of Cam and HCAII are unrelated, the histidines coordinating the Zn^{2+} ion of Cam superimpose on the corresponding histidines of HCAII. Neighboring residues in the active site of Cam differ completely from those in HCAII, however, and it is not obvious how the residues surrounding the metal site in Cam function, by analogy to catalytically essential residues in HCAII.

One key residue for the catalytic mechanism in HCAII is Thr 199, which has no obvious structurally analogous residue in Cam *(5)*. Thr 199 plays two known mechanistic roles. The first is in selecting protonated molecules to bind to the active site zinc. Because of this role, Thr 199 is often referred to as the "gatekeeper" residue. To

achieve this selection, the side chain hydroxyl is hydrogen-bonded to the side chain carboxyl of Glu 106, so that the Thr 199 OH must be a hydrogen-bond donor in that interaction. Consequently, Thr 199 acts as a hydrogen-bond acceptor in any other hydrogen bond interactions. Thr 199 OH is directly hydrogen bonded to the Zn-bound water molecule and therefore selects only protonated molecules to bind in that position *(21)*. As a result of this directional hydrogen-bond, a lone pair of the Zn-bound OH is optimally oriented for attack on CO_2 *(22)*. Thr 199 may play other roles in the interconversion of HCO_3^- and CO_2. Crystallographic studies of HCAII with the inhibitors CN^- and CNO^- have shown that, rather than binding to the active site metal as anticipated, both CN^- and CNO^- bind to the backbone amide nitrogen of Thr 199 *(23)*. The results from this study suggest that the backbone amide nitrogen of Thr 199 is also involved in catalysis, possibly to both orient and/or polarize the CO_2, preparing it for attack by the Zn-bound OH.

There are also differences in the kinetic behavior of HCAII and Cam. In HCAII, a higher coordination number of the metal ion is postulated to decrease the turnover rate. Indeed, only cobalt substituted HCAII retains any activity, with 50% of the activity of the native enzyme *(24)*. Crystal structures of HCAII metal-substituted with Co, Cu, Ni or Mn, show an increased number of metal coordinating ligands and longer average coordination distances *(25)*, consistent with the theory that the coordination number is a

primary factor influencing the turnover rate in HCAII. In contrast to mammalian carbonic anhydrases, substitution of the zinc ion by cobalt doubles Cam activity *(13)*, even though EXAFS analysis indicates a higher coordination number for cobalt-substituted Cam (Co-Cam) relative to zinc-containing Cam (Zn-Cam). Consequently, while the mechanisms of the α- and γ-classes of carbonic anhydrase enzymes may be similar, they are unlikely to be identical. Further understanding of the similarities and differences of α- and γ-class carbonic anhydrases will identify chemical constraints within which the different classes evolved, and will provide further insight to the fundamental features of the catalytic mechanism of carbonic anhydrases.

The crystal structures of uncomplexed Co-Cam, as well as Co-Cam co-crystallized with HCO_3^- and SO_4^{2-} were determined at high resolution to investigate whether the change in activity for Co-Cam is an effect of active site coordination, and to learn more about the mechanism of Cam. For accurate comparison to Zn-Cam, high-resolution structures of Zn-Cam, as well as Zn-Cam co-crystallized with HCO_3^- and SO_4^{2-} have also been determined. These high-resolution structures allow a first look at the solvent structure of the enzyme. As solvent molecules are used as a catalytic group in the reaction, only high-resolution structures can give a complete picture of the active site. These structures allow assignment of several catalytically important residues and solvent molecules in the active site of Cam.

EXPERIMENTAL PROCEDEURES

Crystallization. "Cam" refers to native carbonic anhydrase isolated from *Methanosarcina thermophila (12).* "Zn-Cam" and "Co-Cam" designate enzymes in which the indicated metal was incorporated into the active site of as-purified enzyme produced in *E. coli*, by preparation of the apoenzyme using the denaturant guanidine-HCl and the metal chelator dipicolinate followed by reconstitution in the presence of $ZnSO_4$ or $CoCl_2$ *(13).* For all crystallizations described, the stock protein concentration is 10 mg/mL buffered in 5 mM phosphate pH 7.0. Cubic crystals of Zn-Cam were obtained in hanging drops using 3% PEG 8000 and 0.1 M $(NH_4)_2SO_4$ at 22 °C. Cubic crystals of Co-Cam were obtained in hanging drops containing 5% PEG 8000 and 0.5 M $(NH_4)_2SO_4$. The final pH of an artificial crystallization solution was measured as pH 6.2. The pH of the crystallization reaction including Co-Cam was measured using a microelectrode as pH 5.8. The crystals appeared within 3 days and grew to a maximal size of 0.5 mm × 0.5 mm × 0.5 mm. Cubic crystals belonged to the space group $P2_13$ with unit cell dimensions between a=82.3 Å and a=82.7 Å and one monomer per asymmetric unit. For cryo-cooling, all crystals described in this paper were soaked in a solution containing all of the crystallization components plus 25% glycerol.

Co-crystals of Cam with bicarbonate were obtained in hanging drops containing 7.5% PEG 8000, 0.8 M $(NH_4)_2SO_4$, and 20 mM $NaHCO_3$. The crystals were isomorphous with the substrate free crystals. Zn-Cam crystals only formed using PEG 8000 from Hampton, and formation of all bicarbonate co-crystals was dependent on the lot of PEG 8000. This is presumably due to the batch-to-batch variability of chemical impurities in PEG 8000 *(26)*.

When the uncomplexed crystals were left in the crystallization conditions longer than one day after crystal formation, a large, unanticipated feature appeared in the electron density maps adjacent to the metal ion. In view of the size and tetrahedral shape of this density, and the fact that $(NH_4)_2SO_4$ was present in the crystallization conditions, this density was modeled as SO_4^{2-}.

Data collection. Data for Zn-Cam complexed with SO_4^{2-}, as well as a low resolution pass for Zn-Cam were collected at 113 K using CuKα radiation from an RU 200 rotating anode at a wavelength of 1.54 Å on an Raxis IIc image plate. All other data sets were collected at 93 K at the Stanford Synchrotron Radiation Laboratory beam line 7-1 (λ=1.08 Å) using a MAR Research image plate detector. All data were processed using DENZO and scaled with SCALEPACK *(27)*. The resolutions of the data sets merged from 1.46 Å to 1.95 Å (Table A-2.1).

The structure of Co-Cam was solved by molecular replacement in AMORE *(28)* using the Cam monomer *(5)* as a search model. The other cubic crystals of Cam were isomorphous with cubic Co-Cam. Therefore, the refined monomer of Co-Cam from the cubic space group was used as a starting model in those cases.

Model Building and Refinement. All Cam models were built using the program O *(29)*. Refinement was carried out using REFMAC *(30, 31)* and X-PLOR *(32)*. Uncomplexed structures were first refined with bond lengths of the metal coordinating ligands restrained to the distances determined by EXAFS *(13)*. After the R_{cryst} dropped below 19%, the refinement proceeded unrestrained. The R_{free} was composed of 1093 randomly selected reflections from the native Co-Cam data set (6%). The reflections for R_{free} for the remaining data sets are identical to those from the Co-Cam data set with additional randomly selected reflections selected for data sets of higher resolution. PDB accession codes and statistics are given in Table A-2.1.

RESULTS

Overall fold of the enzyme. The overall fold of Zn-Cam is a left-handed β-helix (Fig. A-2.1) as previously reported *(5)*. Superposition of residues 9-213 of the monomers of Zn-Cam and Co-Cam resulted in an rms deviation of 0.22 Å overall and 0.14 Å for the

residues in the β-helix, indicating no significant overall structural change occurs upon metal substitution. When a trimer of Zn-Cam from the previously reported tetragonal space group ($P4_32_12$) *(5)* was superimposed onto a trimer of Co-Cam, the rmsΔ was 0.37 Å for the C_α-atoms of residues 6-212, and 0.23 Å for the C_α-atoms of residues of the β-helix. Thus, with the exception of the N-termini described below, no significant structural changes occur in the trimer with the change in space group.

The structure of Zn-Cam in the tetragonal space group *(5)* shows two trimers related by a two-fold axis with an interaction between the N-termini (residues 0-6) creating a six-stranded β-barrel. In the cubic space group $P2_13$, there is no two-fold axis relating the trimers, indicating that Cam forms a trimer and not a hexamer in the crystal. In the model of Zn-Cam in complex with HCO_3^-, the N-termini are lying across the top of the trimer in an extended conformation. However, in the remainder of the models, the N-termini are disordered.

The active site. As previously described *(5)*, the active site contains a zinc ion coordinated to the protein by three histidine side chains. In the structures described here, the active site coordination geometry differs depending on the divalent cation at the metal center and the presence or absence of additional ligands. The coordination geometry relative to the metal center is summarized in Table A-2.2.

1. Active site of uncomplexed Zn-Cam. In the active site of uncomplexed Zn-Cam, the Zn^{2+} has three protein and two solvent ligands arranged in trigonal bipyramidal geometry (Fig. A-2.2A, Table A-2.3). As was determined previously for Cam *(5)*, the zinc is coordinated between two monomers with His 81 and His 122 contributed by one monomer, and His 117 contributed from an adjacent monomer. In the previously described structure, only one Zn-bound water molecule was identified, due to difficulties in conclusively assigning water molecules at 2.8 Å resolution. The water molecule assigned in the 2.8 Å resolution structure corresponds to Wat 2 in the high-resolution structure of Zn-Cam.

In the current high-resolution study, an additional solvent molecule coordinating the zinc ion could be identified in the electron density maps. The coordination geometry for the Zn^{2+} is summarized in Table A-2.3. Penta-coordination is consistent with the EXAFS data, which shows a Zn^{2+} coordination sphere of $Zn(N,O)_{2-3}$ $(imidazole)_3$ *(13)*. The average bond distance of 2.14 Å is within experimental error of the distance determined by EXAFS of 2.06 Å, where the errors in EXAFS determination are approximately 0.02 Å and the coordinate error for the crystal structures are listed in Table A-2.1.

An interesting aspect of these structures is the multiple conformations for the side chain of Glu 84. In Zn-Cam, two discrete conformations of Glu 84 are present, one of which points toward the active site and lies within hydrogen-bonding distance of the side chain of Glu 62. In the other structures described in this paper, a third conformation for the side chain of Glu 84 was observed (Fig. A-2.3A). Since the side chains of Glu 84 and Glu 62 lie within hydrogen-bonding distance, it is likely that a proton lies between these two side chains. This indicates that the protein environment has elevated the pKa value for one or both of these side chains above that observed in solution. The observation further suggests that protons may be shuttled out of the active site via a mechanism involving both Glu 62 and Glu 84. Glu 84 may be analogous to the proton shuttle residue His 64 of HCAII (Fig. A-3.3B), which also exhibits two discreet conformations in the crystal structure *(33)*. Replacement of Glu 84 with alanine in Cam decreases protein activity to 1% of wild type levels, and is restored to 53% of wild type activity by the addition of imidazole *(34)*. Imidazole has been shown to act as an alternative proton shuttle in HCAII *(20)*, lending biochemical support to the crystallographic observation that Glu 84 may act as a proton shuttle in Cam.

2. Active Site of Uncomplexed Co-Cam. The active site of Co-Cam shows the cobalt to be hexa-coordinate in a distorted octahedral arrangement, with ligands provided by the three histidine side chains and three water molecules (Fig. A-2.2B, Table A-2.4).

Hexa-coordination is consistent with the EXAFS data that suggests $Co(N,O)_{2-3}$ $(imidazole)_{2-3}$ coordination *(13)*. Only one of the three water molecules (Wat 1) coordinating the cobalt corresponds to a water molecule (Wat 1) coordinating the zinc in Zn-Cam (Table A-2.2). Thus, Wat 2 of Zn-Cam and Wat 2 and Wat 3 of Co-Cam are unique to each structure, respectively. In contrast, almost 70% of the water molecules not located in the active site have equivalent locations in these two uncomplexed structures.

The average Co^{2+}-ligand bond length of 2.32 Å observed for Co-Cam is similar to the average ligation distance of 2.2 Å observed for other six-coordinate Co^{2+} in protein structures *(35-39)*. The average Co-ligand bond length determined by EXAFS analysis of Co-Cam is 2.09 Å *(13)* and the disagreement in bond lengths is just outside of the experimental error of both techniques. This disagreement may arise from pH differences between the crystallization conditions (pH 5.8) and EXAFS conditions (pH 7.0). In HCAII, lowered pH lengthens metal-ligand bond lengths *(8, 25, 40)*, so that a comparison of ligation bond lengths may not be accurate when the pH of the buffer differs.

3. Active Site of Zn-Cam Co-crystallized with Bicarbonate. Crystallographically, carbonic acid (H_2CO_3) and bicarbonate (HCO_3^-) are indistinguishable at the resolution of these structures. Although HCO_3^- was added the crystallization conditions, the species

bound to the active site might be H_2CO_3 rather than HCO_3^-. First, the pH of the crystallization conditions is very near the p*Ka* of bicarbonate, so that protonation may have occurred in solution. Second, the p*Ka* of bicarbonate could be elevated when bound to the protein, as appears to be the case for the neighboring Glu 62 and Glu 84 side chains. Third, HCO_3^- has a very low affinity for the enzyme, similar to that of HCAII. In HCAII, it has not been possible so far to co-crystallize native enzyme with the substrate due to the weak binding. H_2CO_3 might have more stable contacts than HCO_3^-, which could facilitate trapping of this species in the crystal.

The hydrogen-bonding contacts of the species observed at the active site cannot unambiguously identify the nature of the ligand. The ligand has three oxygens within hydrogen-bonding distance (< 3.2 Å) of the side chain of Glu 62. It is not possible, however, to establish the location and nature of the bound protons, since the potential hydrogen-bonds are not optimally oriented. Furthermore, it is possible that the interaction between the side chain of Glu 62 and the active site ligand is primarily electrostatic, where the partial positive charge of one hydrogen stabilizes multiple oxygen-oxygen contacts. For the purposes of describing the interaction, the species will be referred to as bicarbonate (HCO_3^-), despite its ambiguous identity.

Bicarbonate binds in a bidentate fashion to the Zn^{2+} replacing both Wat 1 and Wat 2 (Fig. A-2.2C, Table A-2.5). The HCO_3^- is stabilized by the coordination of one oxygen (O3) directly to the active site zinc and by a hydrogen bond contact of this same oxygen (O3) to the side chain of Glu 62. A second bicarbonate oxygen (O1) makes a long contact to the Zn^{2+}. The third oxygen (O2) is within hydrogen-bonding distance to both carboxylate oxygens of the Glu 62 side chain.

4. *Active site of Co-Cam Co-Crystallized with Bicarbonate.* HCO_3^- binds in a monodentate fashion to the cobalt, replacing one of the coordinating water molecules (Wat 3 from Co-Cam) as well as a second water molecule (Wat 4 from Co-Cam) that is part of a water molecule network in the active site (Fig. A-2.2D, Table A-2.6). The water molecule replaced in the Co-Cam-HCO_3^- complex is not present in Zn-Cam, so that the HCO_3^- binding differs between Zn-Cam and Co-Cam. Multiple binding modes of HCO_3^- suggest that the active site cavity can accommodate a continuum of binding modes for the substrate, as is proposed for HCAII *(41, 42)*. The ligand is partially stabilized in this binding mode by a hydrogen-bond contact to the side chain of Glu 62.

5. Active Site of Zn-Cam in Complex with Sulfate. Sulfate has been shown not to inhibit Cam activity at concentrations up to 0.3 M at pH 5.9 *(34)*. Therefore it was surprising to find that in Cam, sulfate can bind directly to the Zn^{2+} in a manner suggestive of an inhibitor. The binding replaces both zinc-coordinating waters and thus retains the distorted trigonal bipyramidal coordination (Fig. A-2.2E, Table A-2.7). One oxygen (O1) is within hydrogen-bonding distance of the side chain of Glu 62. This suggests that a proton is shared between the side chain of Glu 62 and the active site ligand, and further supports an elevation of the pKa value for the Glu 62 side chain.

6. Active Site of Co-Cam Complexed with Sulfate. In the complex of Co-Cam and SO_4^{2-}, the SO_4^{2-} binds to the cobalt in a bidentate fashion, replacing Wat 1 and Wat 3, but retaining Wat 2 (Fig. A-2.2F, Table A-2.8). Although the SO_4^{2-} contacts the side chain of Glu 62 as in the Zn-Cam-SO_4^- complex, in the Co-Cam-SO_4^{2-} structure, there are two contacts within hydrogen-bonding distance, rather than one. It is possible that these two contacts are sharing a single proton, most-likely donated by a protonated Glu 62.

DISCUSSION

Reaction mechanism implications. As discussed above, kinetic analyses indicate that Cam and HCAII each catalyze the interconversion of CO_2 and HCO_3^- through a zinc-hydroxide mechanism *(13)*. Comparison of the active site structures of Cam and HCAII highlight side chains that may function analogously in these two enzymes. As HCAII has been extensively studied, this comparison helps construct a preliminary structure-based mechanism for Cam. Differences in the active sites are also of interest as they highlight aspects of the reaction mechanism that have evolved to proceed using different components, yet are still compatible with high rates in both cases.

In the first half-reaction (eqs. 1a and 1b), a metal-bound hydroxyl group directly attacks CO_2. In HCAII, it is proposed that CO_2 binds in a hydrophobic pocket of the active site lined with the side chains of Val121, Val143, Leu198, and Trp209 *(43)*. The active site of Cam is located at the base of a cleft between the two monomers. An electrostatic surface potential representation (Fig. A-2.4) shows the HCO_3^- from the Zn-Cam-HCO_3^- complex appears solvent accessible. Below the active site cavity of Cam, there appears to be a relatively apolar surface (Fig. A-2.4). This surface, composed of the side chains of Leu 83, Phe 132b (where b denotes that the residue belongs to the adjacent monomer), Met 135b, Phe 138, Phe 140, Ile 157, and Val 172, may be analogous to the hydrophobic pocket in HCAII, thus serving as a binding site for CO_2 in the active site.

In HCAII, following the trapping of CO_2 by the hydrophobic pocket, CO_2 may interact with the amide nitrogen of Thr 199 *(23, 44)*, replacing the deep water molecule *(8)*. In the Co-Cam-HCO_3^- structure, Gln 75b Nε and Asn 202b Nδ serve as hydrogen-bond donors for the O2 and O3 of the metal-bound HCO_3^- (Fig. A-3.3A). However, they do not contact the HCO_3^- in the Zn-Cam-HCO_3^- structure. These two residues are possible candidates for orienting CO_2 for attack or stabilizing a transition state. Since the active site solvent structure is very different between Zn-Cam and Co-Cam, candidates for a deep water molecule are less clear. Although water molecules are missing from each structure upon binding of HCO_3^-, (Wat 4 from Co-Cam and Wat 24 from Zn-Cam) these water molecules are not analogous.

In HCAII, the first half-reaction culminates in the formation of a bond between the metal-bound OH and the CO_2 to form metal-bound HCO_3^-, followed by an exchange of the HCO_3^- with water (eq. 1b). During this transition state, the side chain of Thr 199 helps orient the product. Although an exact analogue of Thr 199 does not exist in Cam, Glu 62 does act to stabilize the binding of ligands to the active site, and thus could partially fulfill a gatekeeper function. Studies of HCAII have previously suggested that bicarbonate may isomerize to form a leaving group *(45)*. Multiple binding modes for HCO_3^- in the active site of Cam suggest there may be a continuum of binding modes

available to the substrate, and perhaps that isomerization could occur before product release.

Active site coordination has been postulated to be a primary factor in determining the first committed step of catalysis by HCAII (eqs 1a and 1b) *(8, 46)*. The most obvious structural similarity between the α- and γ-classes of carbonic anhydrase is the conserved metal coordination by three histidines. Two of the histidines use the Nε nitrogen for metal coordination, while the third uses the Nδ nitrogen (Fig. A-2.3A and A-2.3B). However, as discussed above, solvent-ligation of the metal center of Cam differs from HCAII with respect to the water ligands. Both native Zn-containing HCAII and Co-substituted HCAII have distorted tetrahedral geometries, while Zn-Cam is trigonal bipyramidal and Co-Cam is octahedral. The active site coordination and geometry in Zn-Cam most closely resembles that of Ni-substituted HCAII, while the geometry of Co-Cam most closely resembles that of Mn-substituted HCAII *(25)*. Both Ni- and Mn-substituted HCAII are essentially inactive enzymes. It is a fascinating mystery why the Cam catalyzed reaction proceeds at a high rate with an increased number of active site ligands relative to HCAII, and dramatically illustrates the complexity of protein-solvent-metal interactions and their implications for reaction mechanisms.

In HCAII, the second half-reaction (eqs. 2a and 2b) contains the proton transfer step, which shuttles a proton from the metal-bound water molecule into the solvent, regenerating the metal-hydroxide active site. Residues that potentially act analogously in HCAII and Cam are more clear for this half-reaction. The proton shuttle His 64 of HCAII has two discrete conformations in the crystal structure *(33)*. In this ensemble of structures, Glu 84 has three discrete conformations, and in one of those conformations, a proton apparently is shared between the side chains of Glu 62 and Glu 84 (Fig. A-2.3). Glu 62 and Glu 84 are located at the base of the active site in a negatively charged tunnel (Fig. A-2.4) which may aid in the protein-solvent transfer of protons. The direct contact between Glu 84 and Glu 62, combined with the likely protonation of Glu 62 when a ligand is bound to the active site, suggest that the proton shuttle involves both side chains. However, a proton could alternatively be shuttled from the active site to Glu 84 through an intervening water molecule (Wat 67 in Zn-Cam) that provides a hydrogen-bond bridge between the active site ligands and the side chain of Glu 84.

Based on the finding in this study, as well as previous biochemical evidence, a preliminary reaction mechanism is proposed (Fig. A-2.5) which provides a foundation for future studies. This mechanism is missing aspects that are involved in the first half-reaction as they cannot be determined conclusively with the findings to date. In the proposed mechanism, CO_2 binds adjacent to the zinc-bound hydroxyl (representations A

and B), the position of which is unknown. The hydroxyl attacks CO_2 leading to a transition state in which the protonated oxygen of the bicarbonate is coordinated to the metal, possibly stabilized by either Gln 75 or Asn 202. These steps are primarily based on analogy to the well-characterized HCAII and a kinetic analysis of Cam suggesting a zinc-hydroxide mechanism. The subsequent steps are based on structures revealed by this study. In the next step, the bicarbonate may isomerize (representations C and D) before replacement by a water molecule (representation E). In the final steps, Glu 62 shuttles a proton from one of the metal-bound water molecules, transferring it to Glu 84 and regenerating the active zinc-bound hydroxyl (representations F and G).

Summary and Conclusions. This study, presenting a high-resolution structure for Zn-Cam and the first structure of the Co-substituted Cam, has advanced our structural and functional understanding of the prototype of the novel γ-class of carbonic anhydrase. The results identify five and six coordination of the metals in Zn-Cam and Co-Cam, a distinct departure from the active site coordination of the α-class of carbonic anhydrases. The high-resolution structures also identify active site water molecules involved both in metal ligation and the hydrogen-bonding network with adjacent residues that are likely to be catalytically important. The structures presented here have identified multiple positions for Glu 84 consistent with a role for this residue in proton transfer from the zinc-bound water molecule to bulk solvent.

The results presented here also raise questions concerning the mechanism of Cam. For example, many of the active site residues (Glu 62, Glu 84, Asn 202) are poorly conserved between Cam and homologs sharing significant sequence similarity with Cam, which is surprising since these appear to be critical for the catalytic mechanism of Cam. However, to date none of these homologous proteins have yet been shown to actually exhibit carbonic anhydrase activity. Additionally, there are several residues near the active site that are well conserved in homologs (Arg 59, Asp 61, Gln 75) where it is unclear how they function in the catalytic mechanism. The results identify residues that potentially function in proton transport; however, residues with the potential to function in CO_2 hydration have yet to be identified. Crystallographic analysis of inhibitor complexes may suggest the location of the CO_2 binding site. Site-directed mutagenesis is expected to identify residues essential for the first half-reaction and the so-called "gatekeeper" function; indeed, this study has suggested Gln 75 and Asn 202 as potential targets for site-specific replacement.

ACKNOWLEDGEMENTS

We are grateful to C. Fierke, D. Silverman and R. Cheng for critical reading and helpful discussions, B. Tripp for unpublished results and H. Schindelin for experimental assistance. This work is based upon research conducted at the Stanford Synchrotron Radiation Laboratory (SSRL), which is funded by the Department of Energy, Office of Basic Energy Sciences.

Fig. A-2.1: Stereoview illustrating the Cam trimer. The overall fold is a left-handed β-helix, consisting of three untwisted, parallel β-sheets connected by left-handed crossovers. Figures 1, 2, and 3 were made using MOLSCRIPT *(47)*, BOBSCRIPT *(48)* and RASTER3D *(49)*.

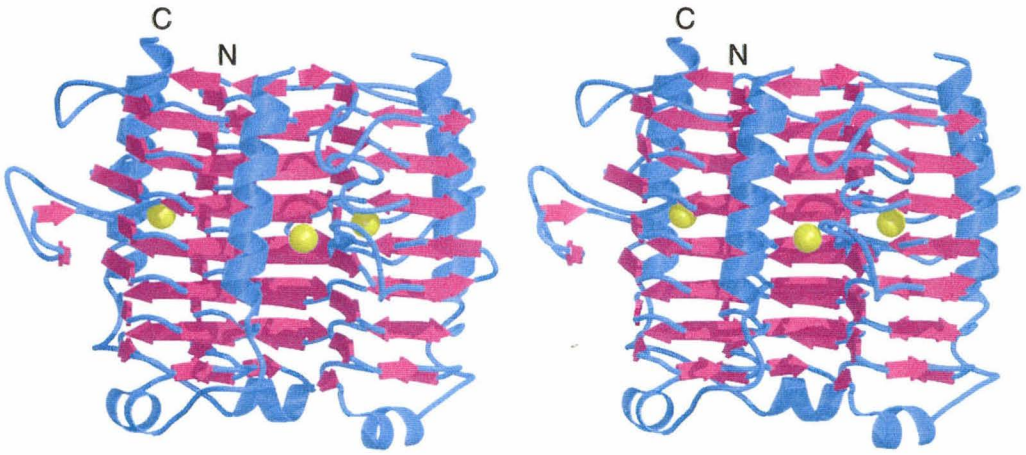

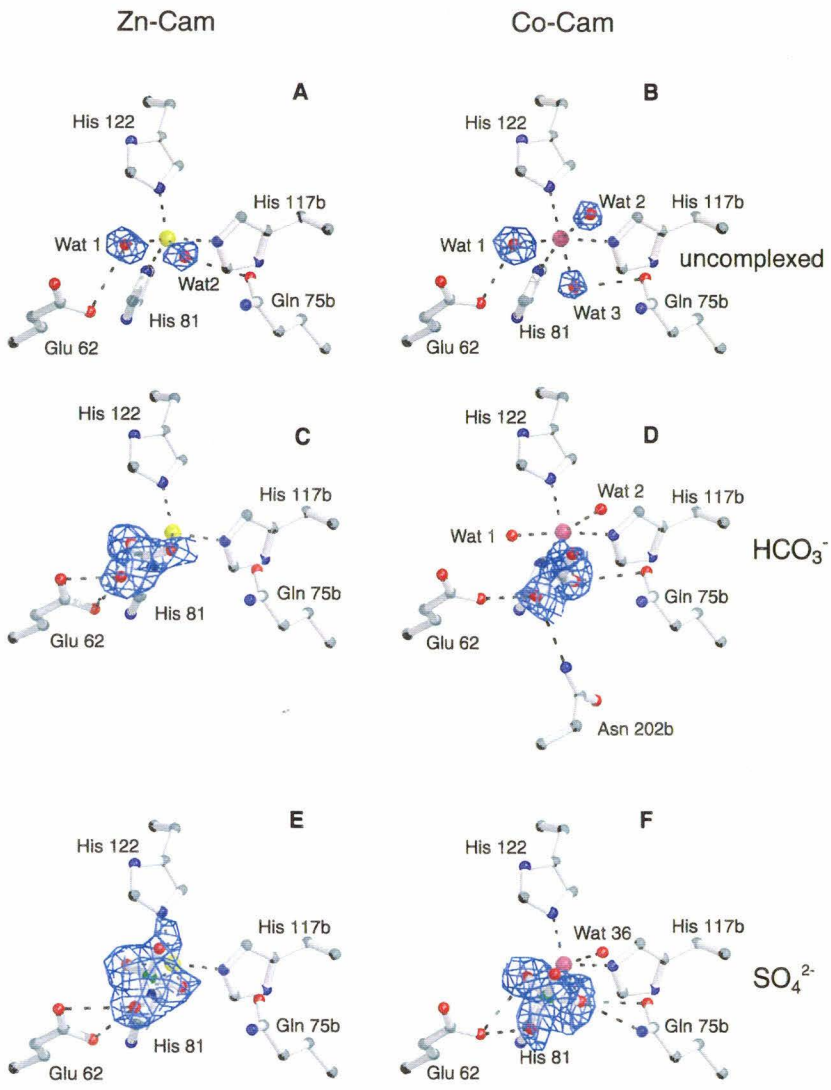

Fig. A-2.2: Active site coordination. Models are superimposed onto $|F_o|-|F_c|$ omit maps calculated after the removal of the relevant active site ligands and contoured at 4σ. **A.** Coordination of Zn-Cam exhibits distorted trigonal bipyramidal geometry. **B.** Coordination of Co-Cam shows distorted octahedral geometry. **C.** Coordination of Zn-Cam bound to bicarbonate. **D.** The model of Co-Cam bound to HCO_3^-. **E.** The model of Zn-Cam bound to SO_4^{2-}. **F.** The model of Co-Cam bound to SO_4^{2-}.

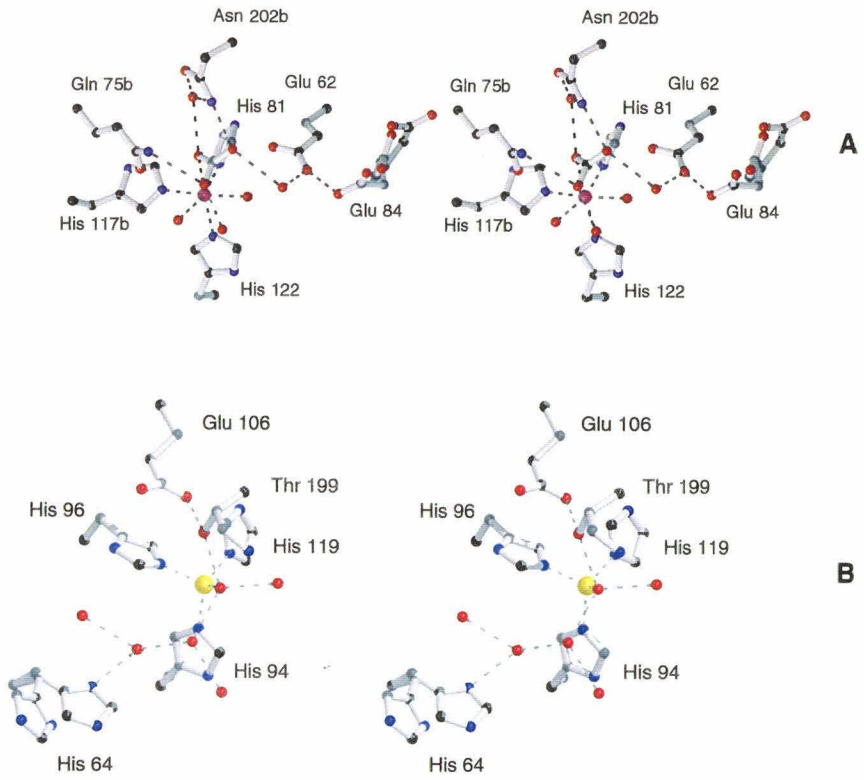

Fig. A-2.3: A. Stereoview of some catalytically important residues. The active site of Co-Cam in complex with HCO_3^- is shown with residues that may be functionally important. The hydrogen bonds between HCO_3^- and the candidates for a Thr 199 analog (Gln 75b and Asn 202b) are shown. Glu 84 is shown in three conformations, two of which are alternative conformations in the Zn-Cam structure, while the third conformation is present in the remaining structures. **B.** Stereoview of the active site of HCAII. The view is shown with the metal-ligating histidines in the same relative orientation as in 3A, i.e., His 119 of HCAII, which coordinates using the Nδ atom, is shown in the same relative location as His 81 of Cam, which also ligates the metal using the Nδ atom. His 64, which is thought to act as the proton shuttle is shown in both conformations.

Fig. A-2.4: Stereoview of electrostatic surface potential representation calculated using the program GRASP *(50)* at an ionic strength of 100 mM and contoured at $\pm 12 k_B T$ (k_B is the Boltzmann constant and T is the absolute temperature). The N-terminus of the protein is at the top of the representation. The surface was made from the Zn-Cam-HCO_3^- trimer with the bicarbonate omitted and shows that the active site cavity is weakly negatively charged. The HCO_3^- is shown as a stick representation. Directly below the active site cavity (lower right) is a funnel-shaped hydrophobic pocket, which may serve to trap CO_2 into the active site. The negatively charged tunnel above the active site contains Glu 62 and Glu 84, and is believed to be the proton shuttle pathway. The view is the same as in Fig. 1.

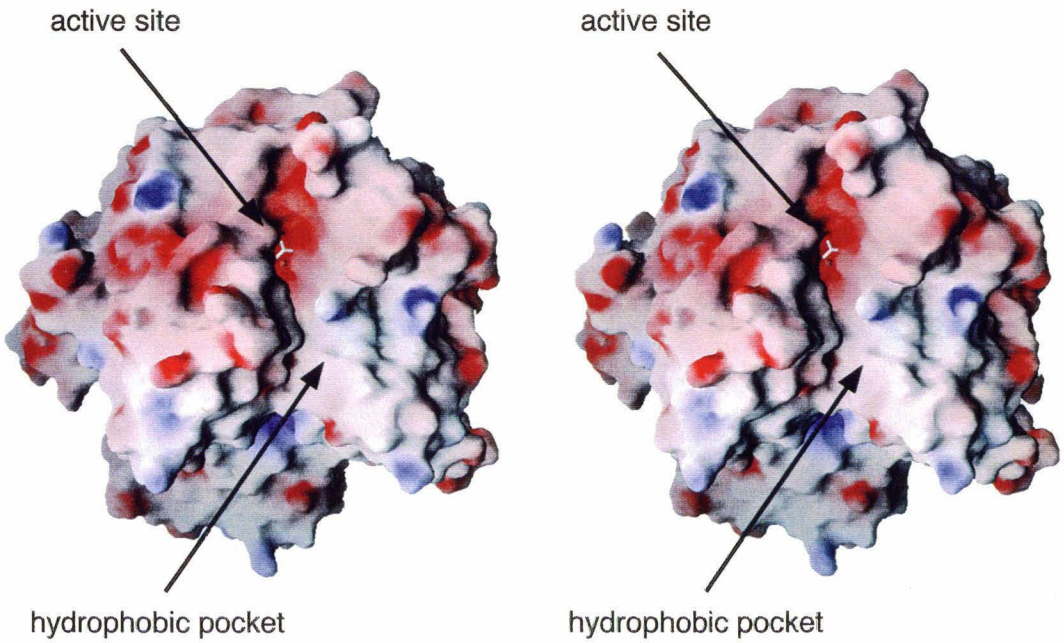

Fig. A-2.5 (next page): Proposed reaction mechanism for Cam. The reaction mechanism is drawn using Zn-Cam as the template. Co-Cam should have a similar reaction mechanism with an additional water molecule as an active site ligand. **A**. Zn^{2+} is coordinated to one water molecule and one hydroxide ion at the beginning of the first half-reaction (eqs. 1a and 1b). **B**. Carbon dioxide enters the active site along the hydrophobic pocket. **C**. Carbon dioxide is attacked by the hydroxide bound to the zinc. **D**. The bicarbonate may have several stable binding modes. This bidentate binding mode, which requires loss of a metal ligand water molecule, is similar to that seen in the structure of Zn-Cam in complex with HCO_3^-. **E**. The first half-reaction ends with exchange of bicarbonate and a water molecule from the solvent. This state is crystallographically indistinguishable from that in (**A**), and may be represented by the structures of Zn-Cam or Co-Cam. **F**. The second half-reaction (eqs. 2a and 2b) begins with the deprotonation of one zinc-bound water molecule, with the proton transferred to Glu 62. During this process, the side chain of Glu 84 swings in so that it may accept the proton. This step is represented by the structure of water-liganded Zn-Cam with the Glu 84 side chain in conformation 1. **G**. The proton is passed from Glu 62 to Glu 84. This state is represented by the structure of Zn-Cam with the Glu 84 side chain in conformation 2. With the transfer of proton to the solvent, the second half-reaction is complete and state (**A**) is regenerated.

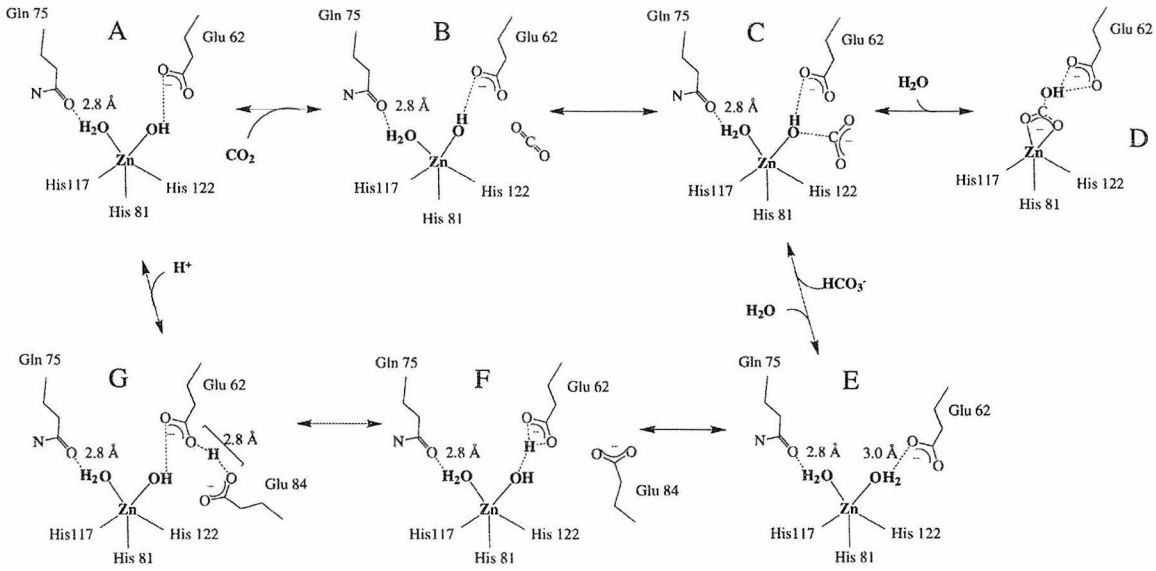
Gln 75
A
Glu 62
2.8 Å
H2O
OH
Zn
His117
His 122
His 81
CO2
B
H
Glu 62
C
H2O
D
OH
H+
HCO3-
G
2.8 Å
Glu 84
F
E
3.0 Å
OH2

Table 1: Data Collection and Refinement Statistics

	Zn-Cam	Zn-Cam+HCO_3^-	Zn-Cam+SO_4^{2-}	Co-Cam	Co-Cam+HCO_3^-	Co-Cam+SO_4^{2-}
Unit Cell (a=b=c)	82.64 Å	82.51 Å	82.68 Å	82.34 Å	82.58 Å	82.61 Å
Resolution	20 - 1.72 Å	20 - 1.85 Å	20 - 1.95 Å	20 - 1.76 Å	20 - 1.46 Å	20 - 1.55 Å
Observations	128,420	55,426	51,109	95,188	128,698	91,423
Unique Reflections	19,889	15,750	13,667	18,449	32,731	25,247
Free R reflections	1,134	937	760	1,093	1,697	1,028
Completeness (%)	98.0 (97.6)	96.9 (82.3)	97.5 (95.0)	98.7 (98.7)	99.4 (99.1)	91.6 (90.3)
R_{sym}	0.097 (0.240)	0.050 (0.238)	0.081 (0.284)	0.054 (0.283)	0.055 (0.297)	0.071 (0.276)
I/σ	19 (4.9)	16 (4.3)	14 (4.1)	21 (4.2)	20 (3.2)	15 (3.5)
R_{cryst}	0.189	0.183	0.189	0.181	0.185	0.205
R_{free}	0.227	0.236	0.236	0.217	0.206	0.229
RMSΔ Bond Lengths	0.021 Å	0.021 Å	0.019 Å	0.011 Å	0.012 Å	0.014 Å
RMSΔ Bond angles	1.7°	1.8°	1.9°	1.6°	1.6°	1.7°
Coordinate Error	0.12 Å	0.15 Å	0.18 Å	0.12 Å	0.07 Å	0.09 Å
Residues	8-213	0-213	6-213	6-213	5-213	8-213
Number of atoms	1617	1674	1601	1641	1681	1629
Water molecules	75	64	40	79	118	88
Ramachandran statistics						
% Most favored	90.8	83.4	89.8	89.1	89.8	88.4
% Allowed	9.2	15.5	9.7	9.7	10.2	11.6
% Generous	0	1.1	0.6	0.6	0	0
% Disallowed	0	0	0	0.6 (1)	0	0.6 (1)
PDB Accession	1qrg.pdb	1qrl.pdb	1qrm.pdb	1qq0.pdb	1qre.pdb	1qrf.pdb

Numbers in parenthesis indicate values for the highest resolution bin. $R_{sym}=\Sigma_i|I_i-\langle I\rangle|/\Sigma I_i$ where i is the ith measurement and $\langle I\rangle$ is the weighted mean of I. $R_{cryst}= \Sigma||F_{obs}| - |F_{calc}||/\Sigma|F_{obs}|$, R_{free} is the same as R_{cryst} for data omitted from the refinement. Coordinate error is the Cruickshanks value *(50)* determined in REFMAC *(31)* and based on the R_{free} value.

Table 2: Summary of Metal Ligation in Cam

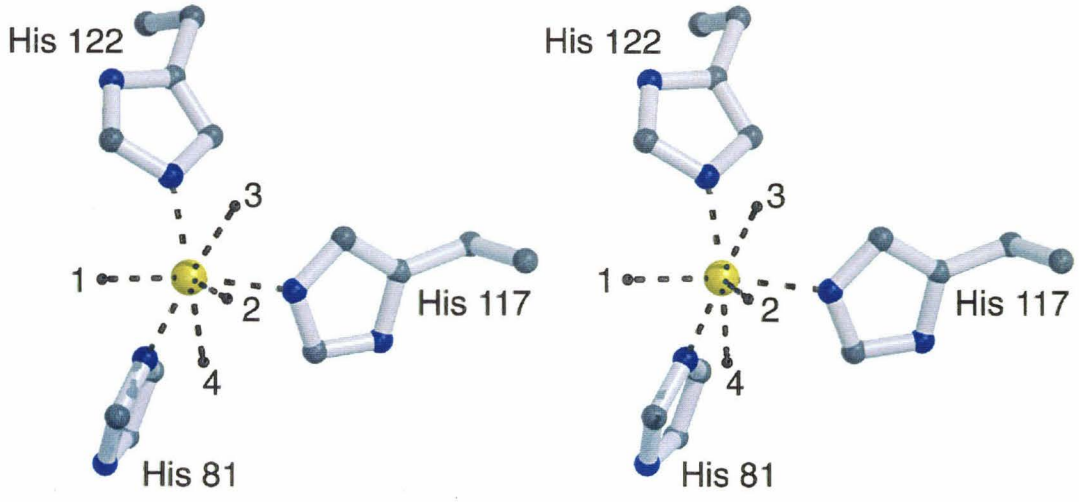

	Ligation position			
	1	2	3	4
Zn-Cam uncomplexed	Wat 1	Wat 2	×	×
Co-Cam uncomplexed	Wat 1	×	Wat 2	Wat 3
Zn-Cam- HCO_3^-	HCO_3^- O3	HCO_3^- O1*	×	×
Co-Cam- HCO_3^-	Wat 1	×	Wat 2	HCO_3O1
Zn-Cam-SO_4^{2-}	SO_4^{2-} O4	SO_4^{2-} O3	×	×
Co-Cam-SO_4^{2-}	SO_4^{2-} O4	SO_4^{2-} O3	×	Wat 36*

* denotes a significant shift in the ligation position relative to the uncomplexed form. In the Zn-Cam-HCO_3^- complex, the HCO_3^- O1 is displaced 1.5 Å relative to the location of the water molecule in Zn-Cam. In the Co-Cam-SO_4^{2-} complex, water 36 is displaced 0.9 Å from the location of Wat 3 in uncomplexed Co-Cam. Of note is that Co-Cam and Zn-Cam always fill ligation position 1, while ligation position 2 tends to be occupied in Zn-Cam (resulting in trigonal bipyramidal coordination geometry) and ligation positions 3 and 4 tend to be occupied in Co-Cam (resulting in octahedral geometry). The exception is the Co-Cam-SO_4^{2-} complex, which fills ligation positions 1, 2, and 4, resulting in more distorted coordination geometry.

Table 3: Active site geometry of Zn-Cam

Atom	Distance to Zinc	Angle			
		x-Zn-W2	x-Zn-81	x-Zn-117	x-Zn-122
W1	2.14 Å	71.9	92.8	161.4	93.1
W2	2.13 Å		121.4	90.1	119.1
His81	2.15 Å			118.0	92.3
His117	2.23 Å				100.3
His122	2.06 Å				
Average	2.14 Å				

Table 4: Active Site Geometry of Co-Cam

Atom	Distance to Cobalt	Angle				
		x-Co-W2	x-Co-W3	x-Co-81	x-Co-117	x-Co-122
W1	2.31 Å	90.9	81.2	89.4	169.0	91.0
W2	2.50 Å		82.4	169.6	84.7	82.5
W3	2.42 Å			87.4	88.2	162.8
His81	2.29 Å				93.2	107.9
His117	2.19 Å					98.4
His122	2.25 Å					
Average	2.32 Å					

Table 5: Active site geometry of Zn-Cam + HCO_3^-

Atom	Distance to Zinc	Angle			
		x-Zn-Bct O1	x-Zn-81	x-Zn-117	x-Zn-122
Bct O3	2.27 Å	45.9	92.8	152.0	94.9
Bct O1	3.24 Å		121.2	110.1	106.2
His 81	2.18 Å			90.3	119.2
His 117	2.30 Å				107.8
His 122	2.05 Å				
Average	2.41 Å (2.2 Å without Bct O1)				

Bct denotes the HCO_3^-.

Table 6: Active Site Geometry of Co-Cam Complexed with HCO_3^-

Atom	Distance to Cobalt	Angle				
		x-Co-W2	x-Co-Bct	x-Co-81	x-Co-117	x-Co-122
W1	2.25 Å	98.0	78.3	89.3	172.5	88.0
W2	2.31 Å		78.9	162.5	81.8	87.4
BctO1	2.35 Å			87.1	94.3	159.0
His81	2.22 Å				89.0	108.9
His117	2.30 Å					99.4
His122	2.19 Å					
Average	2.27 Å					

Bct denotes the HCO_3^-.

Table 7: Active Site Geometry of Zn-Cam Complexed with SO_4^{2-}

Atom	Distance to Zinc	Angle			
		x-Zn-O3	x-Zn-81	x-Zn-117	x-Zn-122
SO_4 O4	2.40 Å	62.7	98.3	163.3	85.9
SO_4 O3	2.17 Å		117.1	100.7	122.9
His81	2.17 Å			90.1	113.4
His117	2.30 Å				104.1
His122	2.11 Å				
Average	2.23 Å				

Table 8: Active Site Geometry of Co-Cam Complexed with SO_4^{2-}

Atom	Distance to Cobalt	Angle				
		x-Co-O3	x-Co-O4	x-Co-81	x-Co-117	x-Co-122
W1	2.29 Å	55.5	91.7	153.0	76.5	92.4
SO_4 O3	2.32 Å		64.2	103.8	94.2	141.4
SO_4 O4	2.09 Å			93.6	158.3	100.2
His81	2.14 Å				89.3	112.7
His117	2.31 Å					98.4
His122	2.13 Å					
Average	2.21 Å					

REFERENCES

1. Meldrum, H., and Roughton, F. (1933) *J. Physiol. 80*, 113-42.

2. Hewett-Emmett, D., and Tashian, R. (1996) *Mol. Phylogenet. Evol. 5*, 50-77.

3. Soltes-Rak, E., Mulligan, M. E., and Coleman, J. R. (1997) *J. Bacteriol. 179*, 769-774.

4. Alber, B. E., and Ferry, J. G. (1994) *Proc. Natl. Acad. Sci. USA 91*, 6909-6913.

5. Kisker, C., Schindelin, H., Alber, B. E., Ferry, J. G., and Rees, D. (1996) *EMBO J. 15*, 2323-2330.

6. Kannan, K. K., Notstrand, B., Fridborg, K., Lövgren, S., Ohlsson, A., and Petef, M. (1974) *Proc. Natl. Acad. Sci. USA 72*, 51-55.

7. Kannan, K., Ramanadham, M., and Jones, T. (1984) *Ann. NY Acad. Sci. 429*, 49-60.

8. Håkansson, K., Carlsson, M., Svensson, L. A., and Liljas, A. (1992) *J. Mol. Biol. 227*, 1192-1204.

9. Eriksson, A. E., and Liljas, A. (1993) *Proteins 16*, 29-42.

10. Boriack-Sjodin, P. A., Heck, R. W., Laipis, P. J., Silverman, D. N., and Christianson, D. W. (1995) *Proc. Natl. Acad. Sci. USA 92*, 10949-10953.

11. Stams, T., Nair, S. K., Okuyama, T., Waheed, A., Sly, W. S., and Christianson, D. W. (1996) *Proc. Natl. Acad. Sci USA 93*, 13589-13594.

12. Alber, B. E., and Ferry, J. G. (1996) *J. Bacteriol. 178*, 3270-3274.

13. Alber, B. E., Colangelo, C. M., Dong, J., Stålhandske, C. M. V., Baird, T. T., Tu, C., Fierke, C. A., Silverman, D. N., Scott, R. A., and Ferry, J. G. (1999) *Biochemistry 38*, 13119-13128.

14. Silverman, D. N., and Lindskog, S. (1988) *Acc. Chem. Res. 21*, 30-36.

15. Khalifah, R. G. (1971) *J. Biol. Chem. 246*, 2561-2573.

16. Steiner, H., Jonsson, B. H., and Lindskog, S. (1975) *Eur. J. Biochem. 59*, 253-259.

17. Christianson, D. W., and Fierke, C. A. (1996) *Acc. Chem. Res. 29*, 331-339.

18. Sly, W. S., and Hu, P. Y. (1995) *Annu. Rev. Biochem. 64,* 375-401.

19. Taoka, S., Tu, C. K., Kistler, K. A., and Silverman, D. N. (1994) *J. Biol. Chem. 269*, 17988-17992.

20. Tu, C. K., Silverman, D. N., Forsman, C., Jonsson, B. H., and Lindskog, S. (1989) *Biochemistry 28*, 7913-7918.

21. Xue, Y., Liljas, A., Jonsson, B.-H., and Lindskog, S. (1993) *PROTEINS: Struct. Funct. Genet. 17*, 93-106.

22. Merz, K. M. (1990) *J. Mol. Biol. 214*, 799-802.

23. Lindahl, M., Svensson, L. A., and Liljas, A. (1993) *Proteins 15*, 177-182.

24. Hunt, J., Rhee, M., and Storm, C. (1977) *Anal. Biochem. 79*, 614-617.

25. Håkansson, K., Wehnert, A., and Liljas, A. (1994) *Acta Cryst. D50*, 93-100.

26. Jurnak, F. (1986) *J. Cryst. Growth 76*, 577-82.

27. Otwinowski, Z. (1993) in *CCP4 Study Weekend Data Collection and Processing* (Sawyer, L., Isaacs, N., and Bailey, S., Eds.) pp 56-62, SERC Daresbury Laboratory, UK.

28. Navaza, J. (1994) *Acta Cryst. A50*, 157-163.

29. Jones, T. A., Zou, J. Y., Cowan, S. W., and Kjeldgaard, M. (1991) *Acta Cryst. A47*, 110-119.

30. Bailey, S. (1994) *Acta Cryst. D50*, 760-763.

31. Murshudov, G. N., Vagin, A. A., and Dodson, E. J. (1997) *Acta Crystallogr. D53*, 240-255.

32. Brünger, A. T. (1992) *X-PLOR version 3.1 - A system for X-ray crystallography and NMR*, Yale University Press, New Haven and London.

33. Nair, S. K., and Christianson, D. W. (1991) *J. Am. Chem. Soc. 113*, 406-411.

34. Tripp, B., and Ferry, J. (submitted) *Biochemistry*.

35. Jenkins, J., Janin, J., Rey, F., Chiadmi, M., vanTilbeurgh, H., Lasters, I., DeMaeyer, M., VanBelle, D., Wodak, S. J., Lauwereys, M., Stanssens, P., Mrabet, N. T., Snauwaert, J., Matthysens, G., and Lambeir, A. (1992) *Biochemistry 31*, 5449-5458.

36. Lloyd, L. F., Gallay, O. S., Akins, J., and Zeikus, J. G. (1994) *J. Mol. Biol. 240*, 504-506.

37. Holland, D. R., Hausrath, A. C., Juers, D., and Matthews, B. W. (1995) *Protein Sci. 4*, 1955-1965.

38. Loll, P. J., Quirk, S., Lattman, E. E., and Garavito, R. M. (1995) *Biochemistry 34*, 4216-4324.

39. Mancia, F., Keep, N. H., Nakagawa, A., Leadlay, P. F., McSweeney, S., Rasmussen, B., Bösecke, P., Diat, O., and Evans, P. R. (1996) *Structure 4*, 339-350.

40. Jönsson, B. M., Håkansson, K., and Liljas, A. (1993) *FEBS Letters 322*, 186-190.

41. Lindskog, S., and Liljas, A. (1993) *Curr. Op. Struct. Biol. 3*, 915-920.

42. Merz, K. M., and Banci, L. (1997) *J. Am. Chem. Soc. 119*, 863-871.

43. Lindskog, S. (1997) *Pharmacol. Thera. 74*, 1-20.

44. Liljas, A., Håkansson, K., Jonsson, B. H., and Xue, Y. (1994) *Eur. J. Biochem. 219*, 1-10.

45. Liang, J. Y., and Lipscomb, W. N. (1987) *Biochemistry 26*, 5293-5301.

46. Garmer, D., and Krauss, M. (1992) *J. Am. Chem Soc. 114*, 6487-6493.

47. Bacon, D., and Anderson, W. F. (1988) *J. Mol. Graph. 6*, 219-220.

48. Esnouf, R. (1997) *J. Mol. Graph. 15*, 133-138.

49. Merritt, E. A., and Murphy, M. E. P. (1994) *Acta Cryst. D50*, 869-873.

50. Sharp, K., Fine, R., and Honig, B. (1987) *Science 236*, 1460-1463.

51. Cruickshank, D. W. J. (1999) *Acta Cryst. D55*, 583-601.

A- 3. Crystallographic studies of the γ-class carbonic anhydrase from *Methanosarcina thermoplila* in complex with inhibitors†

Tina M. Iverson‡, Anthony Gianetti‡, Jessica Wuu§, Birgit E. Alber@,||, J. Greg Ferry@, and Douglas C. Rees§

‡ Graduate Option in Biochemistry, 147-75, California Institute of Technology, Pasadena, CA 91125.

§ MC 147-75 CH, Howard Hughes Medical Institute and Division of Chemistry, California Institute of Technology, Pasadena, CA 91125

@ Department of Biochemistry and Molecular Biology, Eberly College of Science, The Pennsylvania State University, University Park, PA 16802-4500

|| Present address: Institut für Biologie II, Mikrobiologie, Albert-Ludwigs-Universität Freiburg, Schänzlestr. 1, D-79104 Freiburg, Germany

† This work was supported by a grant from the National Institutes of Health to J.G.F. (GM44661).

RUNNING TITLE: Inhibitor complexes of γ-carbonic anhydrase

Abbreviations: CAM, *Methanosarcina thermophila* carbonic anhydrase; Zn-Cam, Cam that has been heterologously produced in *Escherichia coli*, metal-depleted and reconstituted with zinc; Co-Cam, Cam that has been heterologously produced in *Escherichia coli*, metal-depleted and reconstituted with cobalt; HCAII, human carbonic anhydrase II; EXAFS, extended x-ray absorption fine structure.

ABSTRACT: Carbonic anhydrases catalyze the interconversion of CO_2 and HCO_3^- by a mechanism involving two half-reactions: conversion of the substrate to product followed by the regeneration of the active form of the enzyme by a proton shuttle mechanism. Kinetic analyses and high-resolution crystal structures of the γ-class carbonic anhydrase have suggested the proton shuttle mechanism for that enzyme. To explore the CO_2 hydration step of the reaction, the three-dimensional crystal structures of Co-substituted γ-class carbonic anhydrase in complex with the inhibitors acetazolamide and cyanide have been solved at 1.68 Å and 1.75 Å resolution respectively and are compared to similar enzyme-inhibitor complexes of α-class carbonic anhydrases. The ring of the acetazolamide binds over the metal, removing all metal-bound water molecule ligands. In contrast, acetazolamide has been shown to bind to human carbonic anhydrase II (HCAII), an α-class carbonic anhydrase through contacts of the sulphonamide group. Similarly, cyanide appears to bind directly to the active site metal, a distinct departure from the binding to the HCAII. Although diffraction data has been collected from crystals of Cam that have been exposed to the substrate CO_2, there does not appear to be density for the substrate in the maps at the current state of refinement.

Carbonic anhydrases (CAs) are zinc-containing enzymes noted for their ability to interconvert CO_2 and HCO_3^- with a k_{cat} approaching 10^6 per second *(1)*. Sequence and structural analyses have indicated the existence of three distinct classes of CA: α- β- and γ- *(2-5)*.

The α-class of CA can be exemplified by Human Carbonic Anhydrase II (HCAII) which is the best-studied isozyme of this class and has the highest activity. Turnover of the reaction is accomplished by a "zinc-hydroxide" mechanism. In HCAII, the overall enzyme-catalyzed reaction occurs in two distinct half-reactions. The first half-reaction involves the interconversion of CO_2 and HCO_3^- (eqs 1a and 1b, where E signifies the enzyme) and involves nucleophilic attack of the zinc hydroxyl ion on CO_2. This is followed by exchange of zinc-bound HCO_3^- with water. The second half reaction corresponds to the rate-determining intramolecular and intermolecular proton transfer steps (eqs 2a and 2b), which regenerates the zinc-hydroxide at the active site.

$$E\text{-}Zn^{2+}\text{-}OH^- + CO_2 \leftrightarrow E\text{-}Zn^{2+}\text{-}HCO_3^- \qquad (1a)$$

$$E\text{-}Zn^{2+}\text{-}HCO_3^- + H_2O \leftrightarrow E\text{-}Zn^{2+}\text{-}H_2O + HCO_3^- \qquad (1b)$$

$$E\text{-}Zn^{2+}\text{-}H_2O \leftrightarrow {}^+H\text{-}E\text{-}Zn^{2+}\text{-}OH^- \qquad (2a)$$

$${}^+H\text{-}E\text{-}Zn^{2+}\text{-}OH^- + B \leftrightarrow E\text{-}Zn^{2+}\text{-}OH^- + BH^+ \qquad (2b)$$

The prototype of the γ-class of carbonic anhydrase is the carbonic anhydrase from *Methanosarcina thermophila* (Cam). Kinetic studies suggest that the hydration of CO_2 by Cam may occur by a mechanism similar to that proposed for human carbonic anhydrase II (HCAII) *(6, 7)*. Indeed, crystallographic *(8)* and biochemical *(9)* studies have suggested that the proton shuttle mechanism catalyzed by Cam in the second half-reaction (eqs. 2a and 2b) is quite similar in nature to the proton shuttle mechanism catalyzed by HCAII.

However, the biochemical behavior of the two enzymes is not identical. One distinct difference involves the coordination number of the active site metal. HCAII contains a four-coordinate zinc ion in distorted tetrahedral geometry, while Cam shows a five-coordinate zinc ion in trigonal bipyramidal geometry. In HCAII, substitution of the active site zinc to almost any other metal ion knocks out enzyme activity. Indeed only cobalt-substituted HCAII retains any activity, with a rate of ~50% of the native enzyme *(10)*. Crystal structures of metal-substituted HCAII show that the presence of Co, Cu, Ni, or Mn have an increased number of active site ligands *(11)*, leading to the postulation that a higher coordination number of the metal ion decreases the turnover rate. In contrast to HCAII, substitution of the zinc ion by cobalt doubles Cam activity *(7)*, even though

EXAFS analysis indicates a higher coordination number for cobalt-substituted Cam (Co-Cam) relative to Zn-containing Cam (Zn-Cam). Currently, there is not any structural or biochemical information that reliably suggests the mechanism of CO_2 hydration (eqs. 1a and 1b).

One of the great advances in understanding the substrate-product interconversion catalyzed by HCAII came through the crystallographic study of enzyme-inhibitor complexes. Most of the inhibitors, including sulphonamide type inhibitors *(11-15)*, bisulfite, and formate *(3)*, are bound directly to the active site zinc, thus explaining their inhibitory mechanism. However, cyanide and cyanate bound instead to the backbone amide nitrogen of Thr 199 *(16)*, suggesting a functional role for this amide nitrogen. It has been proposed that cyanide and cyanate act as substrate analogs in HCAII. The current proposed reaction mechanism includes Thr199 backbone amide nitrogen acting to polarize the substrate CO_2, preparing it for attack by the active site Zn-OH. Additionally, complexes of HCAII and the non-protonated anion inhibitors bromide and azide *(17)* show that these inhibitors replace the "deep" water molecule that is required for catalysis by HCAII. These inhibitor studies have suggested catalytically important structural features that are independent of the chemical properties of the protein side chains, thus

site directed mutagenesis could not have been used to identify the functional aspects in these cases.

In order to learn more regarding the CO_2 hydration step in Cam, two enzyme-inhibitor complexes have been crystallized. The binding of the inhibitors show a distinct departure from their interaction with HCAII, suggesting that the mechanism of CO_2 hydration may differ between Cam and HCAII, despite the utilization of a similar proton shuttle mechanism by both enzymes. Additionally, Co-substituted crystals of Cam have been exposed to a CO_2 atmosphere prior to cryo-cooling in hopes of trapping an enzyme-substrate complex.

EXPERIMENTAL PROCEDEURES

Crystallization. "Cam" refers to native carbonic anhydrase isolated from *Methanosarcina thermophila (6)*. "Co-Cam" designate enzymes in which the indicated metal was incorporated into the active site of as-purified enzyme produced in *E. coli*, by preparation of the apoenzyme using the denaturant guanidine-HCl and the metal chelator dipicolinate followed by reconstitution in the presence of $CoCl_2$ as previously described *(7)*. For crystallizations, the stock protein concentration was 10 mg/mL buffered in 5

mM phosphate pH 7.0. Crystallization was performed in conditions previously described with the addition of 4 mM acetazolamide or 3 mM cyanide to the protein prior to crystallization. The crystals appeared within 3 days and grew to a maximal size of 0.5 mm × 0.5 mm ×0.5 mm. Cubic crystals belonged to the space group $P2_13$ with unit cell dimensions between a=82.3 Å and a=82.9 Å and one monomer per asymmetric unit. Prior to cryo-cooling, crystals were soaked in a solution containing all of the crystallization components plus 25% glycerol. CO_2 containing crystals were prepared by growing Co-Cam crystals as previously with no inhibitor present, and using a gas pressurizing device *(18, 19)* to subject the crystal to 0.5 MPa of CO_2 for 30 seconds prior to cryo-cooling. Longer exposures to the gas or higher pressures resulted in and poor diffraction, possibly as a result of internal pH change in the crystal during reaction turnover. Data for the inhibitor complexes were collected on an R-axis IIc image plate detector using x-rays at a wavelength of 1.54 Å generated by a RU-200 rotating anode. Data for the CO_2 treated crystals were collected at SSRL beamline 9-1 at a wavelength of 0.98 Å on a MAR 345 image plate detector.

Data collection. Data for Co-Cam complexed with inhibitors were collected at 113 K using CuKα radiation from an RU 200 rotating anode at a wavelength of 1.54 Å on an Raxis IIc image plate. Data for the CO_2 treated crystals were collected at 93 K at the

Stanford Synchrotron Radiation Laboratory beamline 9-1 at a wavelength of 0.98 Å using a MAR Research image plate detector. All data were processed using DENZO and scaled with SCALEPACK *(20)*.

The crystals of the inhibitor complexes were isomorphous with the cubic crystals described previously; therefore, the refined model of Co-Cam *(8)* with all water molecules removed was used as a starting model in each case.

Model Building and Refinement. All Cam models were built using the program O *(21)*. Refinement was carried out using REFMAC *(22, 23)* and X-PLOR *(24)*. The reflections for R_{free} for the data sets are identical to those from the Co-Cam data set described elsewhere *(8)* with additional randomly selected reflections selected for data sets of higher resolution. Data collection and refinement statistics are given in Table A-3.1.

RESULTS

Co-Cam crystallized with inhibitors or exposed to the substrate CO_2 diffracted between 1.68 Å and 1.76 Å resolution, depending on the crystal. Data collection and

current refinement statistics are listed in Table A-3.1. Each of these structures is still in the process of refinement.

In both the Co-Cam inhibitor complexes, the inhibitor appears to be bound directly to the active site. Density for each inhibitor at the active site is shown in Fig. A-3.1. The position of the inhibitor at the active site was particularly disappointing in the case of the Co-Cam-CN complex, since crystal structures of HCAII with this inhibitor highlighted residues involved in CO_2 binding.

Co-Cam was also subjected to pressurization with the substrate CO_2. This represents the first known attempt to crystallize a gaseous substrate with an enzyme. However, the active site of this enzyme appears similar to the native state and does not appear to contain density that could be interpreted as a CO_2 molecule. Neither can density suggestive of bound CO_2 be found in other areas of the maps. It is possible that the binding affinity for the substrate is weak enough that the CO_2 could not be trapped at the active site. One additional explanation is that the crystals were not exposed to the substrate long enough to have a high occupancy of the CO_2 binding site.

DISCUSSION

Although the structures are not yet fully refined, preliminary analysis suggests that Cam binds to inhibitors in a different manner than was seen for HCAII. This suggests differences may exist in the mechanism CO_2 hydration between the α-class and γ-class carbonic anhydrases, however, neither a mechanism for CO_2 hydration, nor a site for CO_2 binding by Cam can yet be proposed.

CONCLUSIONS

The structures of Co-Cam in complex with known carbonic anhydrase inhibitors suggest that the CO_2 hydration half-reaction proceeds by a different mechanism than seen for α-class carbonic anhydrases, despite similar kinetic characteristics. Further work will focus on different inhibitor-complexes that may elucidate functional residues and water molecules, as well as exposing inhibitor-inactivated Cam crystals to CO_2, potentially exposing a CO_2-bound intermediate state of the enzyme.

ACKNOWLEDGEMENTS

This work is based upon research conducted at the Stanford Synchrotron Radiation Laboratory (SSRL), which is funded by the Department of Energy, Office of Basic Energy Sciences.

Figure A-3.1 Binding of inhibitors to the active site of Cam. Contours in blue represent $|2F_o| - |F_c|$ denzity while contours in green show $|F_o| - |F_c|$ difference density. A. Acetazolamide co-crystals. B. CN^- co-crystals. C. CO_2 exposed crystals. Acetazolamide has been placed into this density for that structure, while the other two structures, have only active site water ligands added.

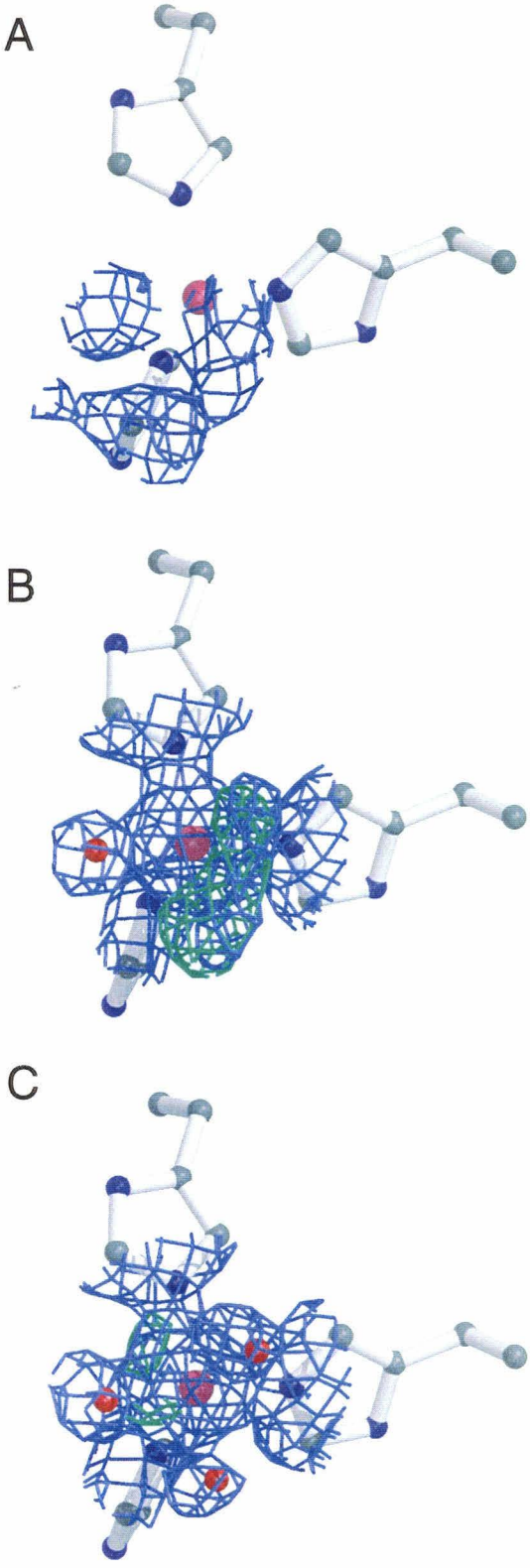

Table A-3.1: Data collection and refinement statistics

	Co-Cam + AZM	Co-Cam + CN	Co-Cam+ CO_2
Unit cell (Å)	82.9	82.6	82.3
Resolution	1.68 Å	1.75 Å	1.76Å
Total reflections	101064	60987	46086
Unique reflections	20694	18546	18407
Completeness (%)	94.4 (82.9)	96.1 (86.3)	98.2 (98.2)
$\mathbf{R_{sym}}$	0.059 (0.158)	0.064 (0.217)	0.067 (0.253)
Residues	8-213	8-213	9-213
Number of atoms	1611	1558	
Water Molecules	56	17	67
Inhibitor added	no	no	no
$\mathbf{R_{cryst}}$	0.202	0.221	0.190
$\mathbf{R_{free}}$	0.236	0.260	0.227

REFERENCES

1. Meldrum, H., and Roughton, F. (1933) *J. Physiol. 80*, 113-42.

2. Hewett-Emmett, D., and Tashian, R. (1996) *Mol. Phylogenet. Evol. 5*, 50-77.

3. Håkansson, K., Carlsson, M., Svensson, L. A., and Liljas, A. (1992) *J. Mol. Biol. 227*, 1192-1204.

4. Kisker, C., Schindelin, H., Alber, B. E., Ferry, J. G., and Rees, D. (1996) *EMBO J. 15*, 2323-2330.

5. Mitsuhasi, S., Mizushima, T., Yamashita, E., Yamamoto, M., Kumasaka, T., Moriyana, H., Ueki, T., Miyachi, S., and Tsukihara, T. (2000) *J. Biol. Chem. 275*, 5521-5526.

6. Alber, B. E., and Ferry, J. G. (1996) *J. Bacteriol. 178*, 3270-3274.

7. Alber, B. E., Colangelo, C. M., Dong, J., Stålhandske, C. M. V., Baird, T. T., Tu, C., Fierke, C. A., Silverman, D. N., Scott, R. A., and Ferry, J. G. (1999) *Biochemistry 38*, 13119-13128.

8. Iverson, T., Alber, B., Kisker, C., Ferry, J., and Rees, D. (submitted) *Biochemistry*.

9. Tripp, B., and Ferry, J. (submitted) *Biochemistry*.

10. Hunt, J., Rhee, M., and Storm, C. (1977) *Anal. Biochem. 79*, 614-617.

11. Håkansson, K., and Liljas, A. (1994) *FEBS Lett. 350*, 319-322.

12. Baldwin, J., Ponticello, G., Anderson, P., Christy, M., Murcko, M., Randall, W., Schwam, H., Sugrue, M., Springer, J., Gautheron, P., Grove, J., Mallorga, P., Viader, M.-P., McKeever, B., and Navia, M. (1989) *J. Med. Chem. 32*, 2510-?

13. Vidgren, J., Liljas, A., and Walker, N. (1990) *Int. J. Biol. Macromol. 12*, 342-?

14. Eriksson, A. E., and Liljas, A. (1993) *Proteins 16*, 29-42.

15. Vidgren, J., Svensson, A., and Liljas, A. (1993) *Int. J. Biol. Macromol. 15*, 97-100.

16. Lindahl, M., Svensson, L. A., and Liljas, A. (1993) *Proteins 15*, 177-182.

17. Jönsson, B. M., Håkansson, K., and Liljas, A. (1993) *FEBS Letters 322*, 186-190.

18. Stowell, M. H. B., Soltis, S. M., Kisker, C., Peters, J. W., Schindelin, H., Rees, D. C., Cascio, D., Beamer, L., Hart, P. J., Wierner, M. C., and Whitby, F. G. (1996) *J. Appl. Cryst. 29*, 608-613.

19. Soltis, S. M., Stowell, M. H. B., Wiener, M. C., Phillips, G. N., and Rees, D. C. (1997) *J. Appl. Cryst. 30*, 190-194.

20. Otwinowski, Z. (1993) in *CCP4 Study Weekend Data Collection and Processing* (Sawyer, L., Isaacs, N., and Bailey, S., Eds.) pp 56-62, SERC Daresbury Laboratory, UK.

21. Jones, T. A., Zou, J. Y., Cowan, S. W., and Kjeldgaard, M. (1991) *Acta Cryst. A47*, 110-119.

22. Bailey, S. (1994) *Acta Cryst. D50*, 760-763.

23. Murshudov, G. N., Vagin, A. A., and Dodson, E. J. (1997) *Acta Crystallogr. D53*, 240-255.

24. Brünger, A. T. (1992) *X-PLOR version 3.1 - A system for X-ray crystallography and NMR*, Yale University Press, New Haven and London.

A-4. Crystallization and preliminary x-ray analysis of a β-class carbonic anhydrase from *Methanobacterium thermoautotrophicum* ΔH†

Pavel Strop‡, Kerry S. Smith§, Tina M. Iverson‡, Jessica Wuu@, J. Greg Ferry§, Douglas C. Rees@

‡ Graduate Option in Biochemistry, 147-75, California Institute of Technology, Pasadena, CA 91125.

§ Department of Biochemistry and Molecular Biology, Eberly College of Science, The Pennsylvania State University, University Park, PA 16802-4500

@ MC 147-75 CH, Howard Hughes Medical Institute and Division of Chemistry, California Institute of Technology, Pasadena, CA 91125

† This work was supported by a grant from the National Institutes of Health to J.G.F. (GM44661). P.S. is supported by a fellowship from the National Science Foundation.

RUNNING TITLE: Crystallization of β-carbonic anhydrase

ABSTRACT Carbonic anhydrases are-zinc containing enzymes that catalyze the interconversion of CO_2 and HCO_3^-. Carbonic anhydrases are found ubiquitously throughout nature and currently three distinct classes are recognized: α- β- and γ-. The β-class carbonic anhydrases are present in higher plants, algae, and prokaryotes and are involved in inorganic carbon utilization as well as the Calvin-Benson cycle. Crystals of the β-class carbonic anhydrase from *Methanobacterium thermoautotrophicum* ΔH belonging to the primitive orthorhombic space group $P2_12_12_1$ and having unit cell constants of a=54.6 Å b=113.8 Å c=156.8 Å have been obtained using ethanol and methyl-pentanediol as precipitants. A complete data set to 2.7 Å resolution has been collected using CuKa radiation. A Matthew's calculation is consistent with the presence of four molecules in the asymmetric unit, while a rotation function of these data suggest 222 point group symmetry.

Abbreviations: CA, carbonic anhydrase; Cam, γ-class CA from *Methanisarcina thermophila*; Cab, β-class CA from *Methanobacterium thermoautotrophicum* ΔH; MPD, methyl pentane diol.

Carbonic anhydrases (CAs) are zinc-containing enzymes found in all phyla *(1)* that were first noted for their physiological role in interconverting CO_2 and HCO_3^- *(2)*. Based on sequence and structure analyses, three classes of carbonic anhydrases are currently recognized: α-, β-, and γ-. The α-class includes seven mammalian isozymes and two isozymes from *Chlamydomonas reinhardtii (3, 4)*, and has been characterized both biochemically and structurally. Analyses of the crystal structures *(5-9)* and biochemical evidence have suggested a detailed reaction mechanism for this enzyme.

The structure of Cam, the prototype of the γ-class of CAs has been solved *(10)*, and unlike the eukaryotic counterparts was found to be a trimer and have a unique left handed β-helix overall fold. Recent kinetic analyses *(11, 12)*, combined with high-resolution crystal structures *(13)*, suggest that Cam utilizes a reaction mechanism similar to that of the α-class CAs.

β-CAs are present in higher plants, algae, and prokaryotes. Sequence and EXAFS *(14, 15)* analyses of β-class CAs suggest that the ligands to the active site zinc include two cysteine thiols and one histidine, as well as a fourth N/O ligand that was presumed to be a catalytically active water molecule. β-class CAs typically catalyze CO_2 hydration with k_{cat} values between 10^5 and 10^6 s^{-1}, similar to the rates observed for both the α- and γ-

classes of carbonic anhydrase. The first known β-CA in the archaea was purified from the methanogenic archaeon *Methanobacterium thermoautotrophicum* ΔH *(16)* and exhibits 34% sequence identity to the β-class carbonic anhydrase from *Escherichia coli.* The calculated molecular weight of this enzyme, designated Cab, is 20 kD. Based upon native gel-filtration experiments suggesting a total molecular weight of ~90 kD it is likely that Cab exists as a tetramer. The enzyme has CO_2 hydration activity with a k_{cat} of1.7 X 10^4, similar to the values seen for the other classes of carbonic anhydrases.

Recent crystallographic studies of the β-CA from the red algae *Porphyridium purpureum (17)* have proved fruitful. The gene encoding the *P. purpureum* β-CA has undergone fusion so that it contains two nearly identical repeats, each with significant identity to a consensus β-CA sequence. The structure of the *P. purpureum* β-CA shows a dimer with pseudo 2 2 2 point group symmetry, thus an enzyme composed of monomers would form a tetramer. The active site shows zinc ligation by two cystiene ligands, one histidine ligand, and one aspartic acid, suggesting a departure from the catalytic mechanism proposed for the other two classes of CA, which require a catalytic water molecule bound to the active site. Crystals of Cab have been grown in the primitive orthorhombic space group $P2_12_12_1$. Crystallographic analysis of these crystals suggests the molecular structure is consistent with the structure of *P. purpureum* enzyme. A

molecular replacement solution should provide interesting insights by comparison of the β-CA structure from two different organisms.

EXPERIMENTAL PROCEDEURES

Crystallization.

Cab has been overexpressed in *E. coli* and purified by heat denaturation combined with ion exchange as previously described *(16)*. Crystals of the β-CA from *Methanobacterium thermoautotrophicum* ΔH have been obtained from conditions containing 35% ethanol, 12% methyl pentanediol (MPD) and 50 mM Calcium acetate buffered in 100 mM HEPES pH 7.5 at 22 °C (Fig. A-4.1). Crystals form in the primitive orthorhombic space group $P2_12_12_1$ and appear well ordered, diffracting to 2.7 Å resolution using Cu Kα generated by a Rigaku RHU3RHB rotating anode and collected on an Raxis II image plate (Fig. A-4.2). The diffraction may be limited by crystal size (0.05 X 0.05 X 0.1 mm). Attempts have been made to grow larger crystals using a variety of seeding techniques, however, these techniques have not substantially improved the crystals in a reproducible manner.

Data collection

Cryo cooling of the crystals involved screening of a large variety of potential cryo-protectants including glycerol ethylene glycol, glucose, and low molecular weight polyethylene glycol compounds. The best cryo-protection was achieved by substituting all of the water volume of the crystallization conditions with either ethanol or MPD resulting in concentrations of ~50% ethanol or ~35% MPD, and the resultant diffraction for the crystals in each type of cryoprotectant was approximately equivalent. As small volumes of solutions containing low-boiling point compounds tend to evaporate quickly, crystals were routinely cryo-cooled using 35% MPD to promote ease of handling.

RESULTS AND DISCUSSION

SDS-PAGE analysis of carefully washed and dissolved crystals shown that Cab is the exclusive constituent. A complete data set merging to 2.7 Å resolution has been collected on Raxis IV image plates using a RHU3RHB rotating anode. A summary of the data collection and processing statistics is shown in Table A-4.1. The data were processed using DENZO and scaled using SCALEPACK *(18)*. Systematic absences combined with lattice spacings suggest that the crystals belong to the primitive orthorhombic space group $P2_12_12_1$ with unit cell constants a=54.6 Å b=113.8 Å c=156.8 Å. According to the cell size and symmetry, calculation of the solvent content suggests four molecules are present in the asymmetric unit, with a corresponding Matthew's

coefficient of 2.7 *(19)*. To search for the non-crystallographic axes, a self-rotation function (Fig. A.4.1) was calculated using POLARRFN *(20)*. The rotation function (Fig. A-4.3) indicates a 2-fold axis along x and 2-fold axes in the yz plane 45° from the z-axis. Combined with a 16 σ packing peak in the native Patterson at x,y,z=(0,0,0.36), analysis of the native data indicate the asymmetric unit probably contains a tetramer with 2 2 2 point group symmetry, consistent with the pseudo 2 2 2 symmetry seen in the β-CA from *P. purpureum.*

CONCLUSIONS

Preliminary x-ray analysis of Cab crystals suggests that the enzyme forms a tetramer. Molecular replacement of the data with the model from *P. purpureum* will allow a comparison of the two enzymes that may provide further insight into catalysis.

Fig. A-4.1. Crystals of *M. thermoautotrophicum* ΔH β-carbonic anhydrase (Cab).

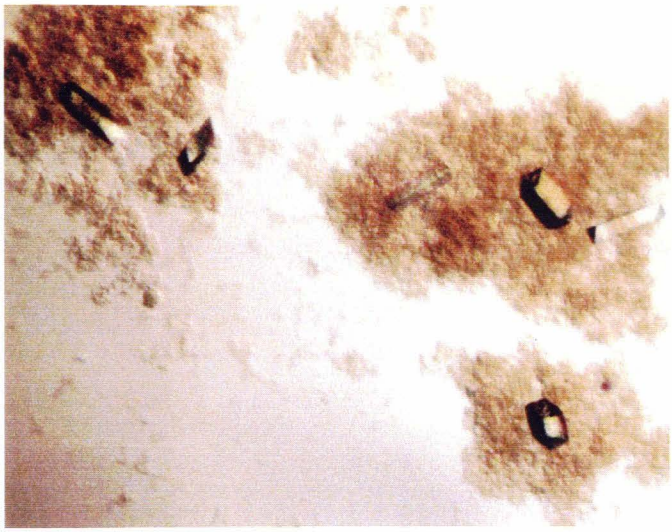

Fig. A-4.2. Typical diffraction pattern of a crystal of Cab. The edge of the image plate corresponds to 2.7 Å resolution.

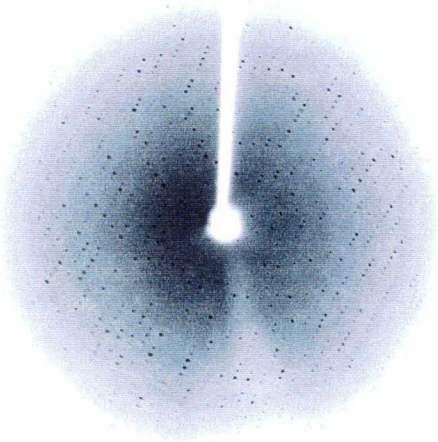

Fig. A-4.3. CAB self rotation function. The left panel show the κ=180° section. The peaks at (ϕ,ω,κ) = (±90°, ±45°, 180°) indicate a 2-fold in the yz plane 45° from the z-axis. Remaining peaks are origin peaks. The right panel shows the κ=90° section. The peak at ϕ=0, ω=0 is consistent with a 2-fold along the x-axis.

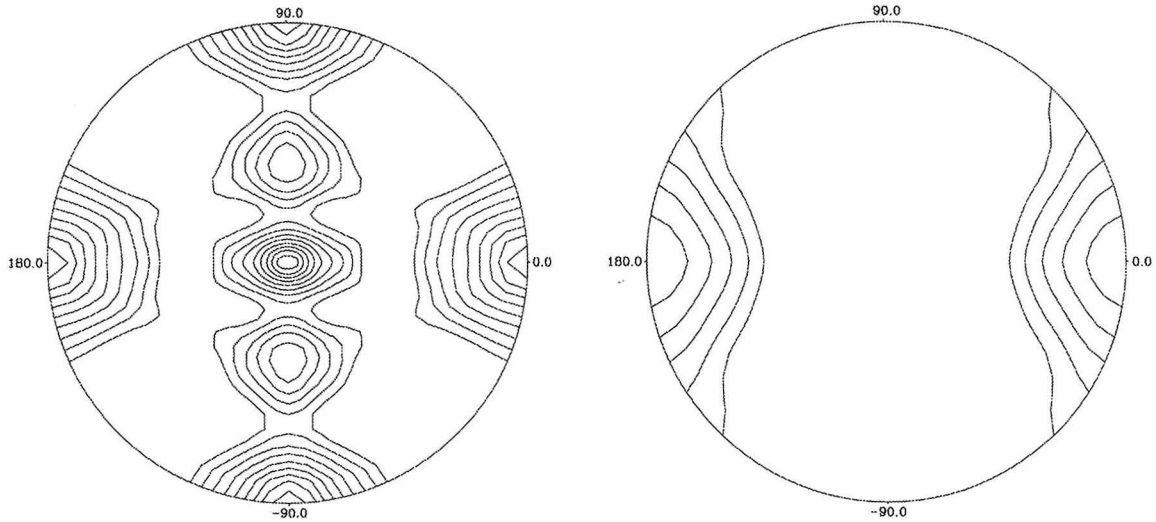

Table A-4.1 Data collection and processing statistics

Crystal Data	
Space group	$P2_12_12_1$
Unit cell dimensions	a=54.6, b=113.8, c=156.8
Data collection	
Resolution (Å)	20 - 2.7
Last resolution shell (Å)	2.8 - 2.7
Completeness	96% (83%)
Number of reflections	206,646
Number of unique reflections	27,526
Redundancy	7.5
R_{sym}	0.086 (0.322)
I/σ	15 (3.4)

Numbers in parentheses indicate values for the last resolution shell.

REFERENCES

1. Smith, K. S., Jakubzick, C., Whittam, T. S., and Ferry, J. G. (1999) *Proc. Nat. Acad. Sci. USA 96*, 15184-15189.

2. Meldrum, H., and Roughton, F. (1933) *J. Physiol. 80*, 113-42.

3. Hewett-Emmett, D., and Tashian, R. (1996) *Mol. Phylogenet. Evol. 5*, 50-77.

4. Soltes-Rak, E., Mulligan, M. E., and Coleman, J. R. (1997) *J. Bacteriol. 179*, 769-774.

5. Boriack-Sjodin, P. A., Heck, R. W., Laipis, P. J., Silverman, D. N., and Christianson, D. W. (1995) *Proc. Natl. Acad. Sci. USA 92*, 10949-10953.

6. Eriksson, A. E., and Liljas, A. (1993) *Proteins 16*, 29-42.

7. Håkansson, K., Carlsson, M., Svensson, L. A., and Liljas, A. (1992) *J. Mol. Biol. 227*, 1192-1204.

8. Kannan, K., Ramanadham, M., and Jones, T. (1984) *Ann. NY Acad. Sci. 429*, 49-60.

9. Stams, T., Nair, S. K., Okuyama, T., Waheed, A., Sly, W. S., and Christianson, D. W. (1996) *Proc. Natl. Acad. Sci USA 93*, 13589-13594.

10. Kisker, C., Schindelin, H., Alber, B. E., Ferry, J. G., and Rees, D. (1996) *EMBO J. 15*, 2323-2330.

11. Alber, B. E., and Ferry, J. G. (1996) *J. Bacteriol. 178*, 3270-3274.

12. Alber, B. E., Colangelo, C. M., Dong, J., Stålhandske, C. M. V., Baird, T. T., Tu, C., Fierke, C. A., Silverman, D. N., Scott, R. A., and Ferry, J. G. (1999) *Biochemistry 38*, 13119-13128.

13. Iverson, T., Alber, B., Kisker, C., Ferry, J., and Rees, D. (submitted) *Biochemistry.*

14. Bracey, M. H., Christiansen, J., Tovar, P., Cramer, S. P., and Bartlett, S. G. (1994) *Biochemistry 33*, 13126-13131.

15. Rowlett, R. S., Chance, M. R., Wirt, M. D., Sidelinger, D. E., Royal, J. R., Woodroffe, M., Wang, Y. F., Saha, R. P., and Lam, M. G. (1994) *Biochemistry 33*, 13967-13976.

16. Smith, K., and Ferry, J. (1999) *J. Bacteriol. 181*, 6247-6253.

17. Mitsuhasi, S., Mizushima, T., Yamashita, E., Yamamoto, M., Kumasaka, T., Moriyana, H., Ueki, T., Miyachi, S., and Tsukihara, T. (2000) *J. Biol. Chem. 275*, 5521-5526.

18. Otwinowski, Z. (1993) in *CCP4 Study Weekend Data Collection and Processing* (Sawyer, L., Isaacs, N., and Bailey, S., Eds.) pp 56-62, SERC Daresbury Laboratory, UK.

19. Matthews, B. W. (1968) *J. Mol. Biol. 33*, 491-497.

20. Bailey, S. (1994) *Acta Cryst. D50*, 760-763.